REVIEW

Check for updates

Thermally activated delayed fluorescence materials: innovative design and advanced application in biomedicine, catalysis and electronics

Ehsan Ullah Mughal, [ID] *[a] Syeda Fariha Kainat,[a] Abdulaziz M. Almohyawi,[b] Nafeesa Naeem, [ID] [a] Essam M. Hussein,[bc] Amina Sadiq,[d] Ahmad Abd-El-Aziz,[e] Ning Ma,[e] Alaa S. Abd-El-Aziz,[e] A. Timoumi,[f] Ziad Moussa, [ID] [g] Nermeen Saeed Abbas[hi] and Saleh A. Ahmed [ID] *[b]

Thermally Activated Delayed Fluorescence (TADF) materials have emerged as a revolutionary class of functional compounds, driven by their unique ability to utilize excitons from both singlet and triplet states for efficient fluorescence emission. This manuscript provides an overview of recent innovations in TADF material design, focusing on molecular strategies to achieve optimal TADF properties, including small singlet–triplet energy gaps (ΔE_{ST}) and high photoluminescence quantum yields. We explore the diverse applications of TADF materials, spanning OLEDs, biomedical imaging, photosensitizers,

[a]*Department of Chemistry, University of Gujrat, Gujrat-50700, Pakistan. E-mail: ehsan.ullah@uog.edu.pk*

[b]*Department of Chemistry, Faculty of Science, Umm Al-Qura University, 21955 Makkah, Saudi Arabia. E-mail: saahmed@uqu.edu.sa*

[c]*Department of Chemistry, Faculty of Science, Assiut University, 71516, Assiut, Egypt*

[d]*Department of Chemistry, Govt College Women University, Sialkot-51300, Pakistan*

[e]*Qingdao Innovation and Development Center, Harbin Engineering University, Qingdao, China, 266400*

[f]*Department of Physics, Faculty of Science, Umm Al-Qura University, Makkah, 24382, Saudi Arabia*

[g]*Department of Chemistry, College of Science, United Arab Emirates University, P.O. Box 15551, Al Ain, United Arab Emirates*

[h]*Department of Chemistry, Faculty of Science, Taibah University, Medina, Saudi Arabia*

[i]*Department of Chemistry, Faculty of Science, Helwan University, Cairo, A. R., Egypt*

Ehsan Ullah Mughal

Ehsan Ullah Mughal obtained his PhD degree in Organic Chemistry from Bielefeld University Germany in 2013. Currently, he is working as Tenured Associate Professor in Department of Chemistry, University of Gujrat, Pakistan. He was a post-doc fellow at Max-Planck Institute for Polymer Research, Mainz, Germany from 2013 to 2014. His current research interests include the design and synthesis of bioactive heterocycles, synthetic flavonoids, transition metal-based terpyridine complexes and their uses in the fabrication of DSSCs and as efficient photocatalysts. His research in the field has resulted in more than 100 published articles (research papers and review papers) in reputable high impact journals. His publications have made a great impact in the field by receiving more than 2330 citations with h-index of 29.

Syeda Fariha Kainat

Syeda Fariha Kainat earned her BS in 2021 and MPhil in 2023 from the University of Gujrat, Pakistan. She has published two research articles and 1 review article in high-impact journals. Her research focuses on the synthesis and photocatalytic applications of terpyridine-based metal complexes.

photocatalysis, UV photodetectors (UVOPDs), electrogenerated chemiluminescence, triplet–triplet annihilation (TTA) sensitizers, organic hybrid microwire radial heterojunctions, multicolor luminescent micelles, mechano-luminescence (ML), light-emitting electrochemical cells (LEECs), and fluorescent probes. The integration of TADF materials in these technologies highlights their potential to enhance performance and efficiency. Through this review, we aim to elucidate the fundamental principles governing TADF behavior and present a forward-looking perspective on the synthetic methodologies and new, versatile applications of materials.

1. Introduction

Since the first report of luminescent materials over four centuries ago, this important class of materials has continued to attract the attention of many research groups in academia and industry.[1–6] Luminescent materials have found a broad range of industrial applications from materials science to biomedical technology.[7,8] Over the past few decades, efficient luminescent emitters, including metal–organic frameworks,[9] lanthanide metal-based nanoparticles,[10] and inorganic quantum dots,[11] have been extensively investigated. However, emitters composed of organic molecules featuring high-order π-conjugation and heteroatoms within their structures have been shown to offer high fluorescence quantum yields, good photostability, improved biocompatibility, and low phototoxicity in biological applications.[12–14] Additionally, numerous π-conjugated luminescent molecules have been investigated for

Nafeesa Naeem received her BS and MPhil degrees from the University of Gujrat, Pakistan, in 2018 and 2020, respectively. She is currently pursuing a PhD in Chemistry under the supervision of Dr Ehsan Ullah Mughal at University of Gujrat, Pakistan. She has published over 40 publications (research papers and review papers) in reputable high impact international journals and receiving more than 1230 citations and an h-index of 21. Her current research focuses on the synthesis, biological evaluation, photophysical studies, and photocatalytic applications of various heterocyclic scaffolds.

Nafeesa Naeem

Alaa S. Abd-El-Aziz is a Full Professor at Harbin Engineering University in China. He currently building an international research program in the field of polymers and materials and their applications in biomedicine and industry. He has extensive experience in the design and synthesis of organic and organometallic polymers and dendrimers with optical and biological properties. His current research is focused on the synthesis of functional polymeric materials as sensors, biosensors or therapeutic agents. He serves on many international advisory and editorial boards.

Alaa S. Abd-El-Aziz

Amina Sadiq is an Associate Professor of Organic Chemistry at the Government College Women University in Sialkot, Pakistan. She earned her PhD in 2013 from Bielefeld University, Germany, under the supervision of Prof. Dr Norbert Sewald, and later conducted postdoctoral research with the same group. She published more than 65 publications in high ranked journals and receiving more than 1580 citations and an h-index of 24. Her research focuses on the design and synthesis of bioactive heterocycles, synthetic flavonoids, and chalcone-based metal complexes, along with evaluating their biological activities.

Amina Sadiq

Prof. Dr Saleh A. Ahmed received his PhD in photochemistry (photochromism) under the supervision of Prof. Heinz Dürr at Saarland University, Germany. He has more than 20 years of experience as a post-doctoral fellow, senior researcher and visiting professor in France, Japan, Germany, Italy and USA. Since 2010 he promoted to full professor of organic photochemistry. He published more than 290 publications in high ranked journals and more than 10 US-patents. His research interests include synthesis and photophysical properties of novel organic compounds, and developments of synthetic methodologies for the synthesis of compounds with unique theoretical and biological applications.

Saleh A. Ahmed

© 2025 The Author(s). Published by the Royal Society of Chemistry
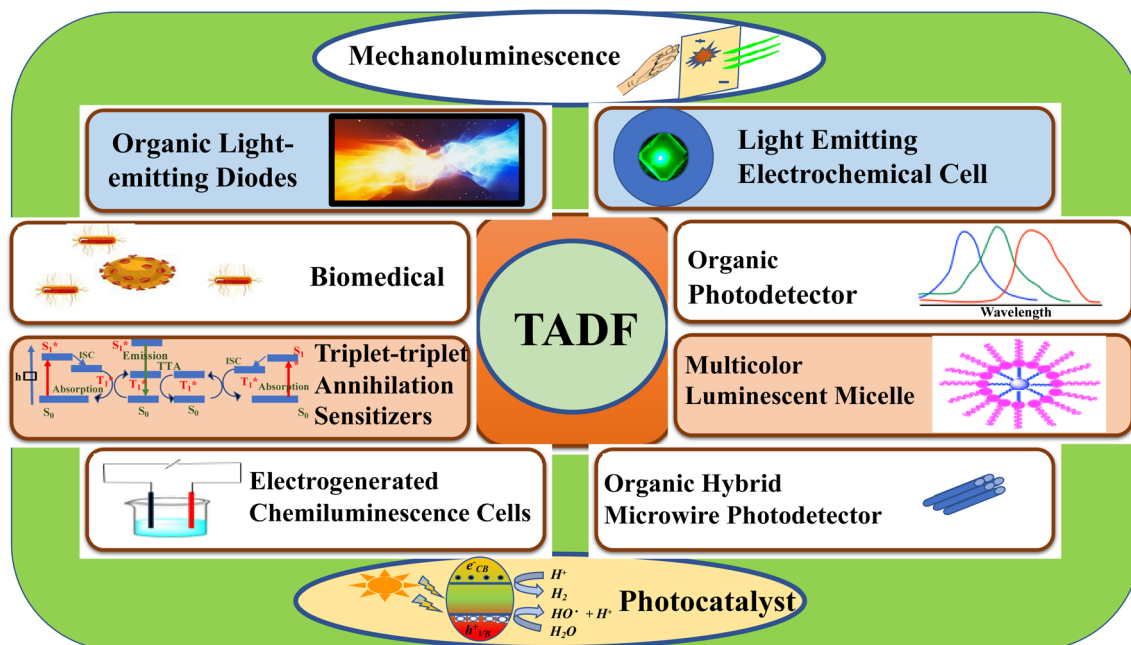
Fig. 1 Applications of TADF materials.

their fluorescence properties in nanoaggregates and thin films, making them valuable in sensing and imaging applications.[15,16] Moreover, organic luminescent materials have gained significant attention due to their tunable luminescence properties, such as the color, duration, and intensity of emissions, which can be adjusted through molecular design. These materials have found advanced applications in fields like biomedicine, electroluminescence, optoelectronics, organic lasers, organic sensors, and organic light-emitting diodes (OLEDs).[17–19] Organic molecules exhibiting thermally activated delayed fluorescence (TADF) properties have become a compelling class of functional materials due to their increasing demand and significant design advancements in recent years.[20] Before using the term TADF, this phenomenon was referred to as "E-type" delayed fluorescence. In the early 1920s, French Nobel Laureate Jean-Baptiste Perrin (Nobel Prize in Physics, 1926) reported the "E-type" delayed fluorescence in "Lumière et réactions chimiques, rapport au 2e Conseil de Chimie Solvay, Bruxelles".[21] Later, Delorme and Perrin reported delayed fluorescence from uranyl salts and solutions in 1929 in an article from "Le Journal de la Physique et la Radium".[22] In early 2024, Huang and Cole generated a database of TADF molecules and made it available through Figshare.[23] The first TADF-based OLED, which was designed using a fluorescein derivative, was described by Adachi et al. in 2012.[17] The increased demand for new TADF materials has been clearly shown in the recent literature. Fig. 1 shows the diverse fields where this class of materials has been utilized, including light emitting devices, photocatalysts and photodetectors, as well as their biomedical applications. As an example, TADF applications of mechanoluminescence from simple organic molecules by positional isomerism were first observed by Xiong et al.[24] TADF-emitting compounds can be used as probes for conventional fluorescence bioimaging or be used for their sensitivity to temperature or oxygen levels.[25] Suleymanova et al. designed a novel liquid-crystal TADF emitter based on substituted carbazoles and terephthalonitrile.[26,27] Also, Chen et al. reported an example of a liquid crystal multi-resonance TADF emitter that showed preferential horizontal orientation.[28] While these examples highlight the importance of this growing field, this review gives a comprehensive description of the design and applications of various types of TADF materials. This will attract a broad interest from many interdisciplinary fields, including materials science, chemistry, physics, biology, and medicine.

1.1. Classification of TADF materials: design strategies and mechanistic insights

TADF materials can be broadly classified into three main categories based on their electronic structures and charge-transfer characteristics.

1.1.1. Metal-enhanced spin–orbit coupling (SOC) TADF. Incorporating metal centers into organic TADF frameworks enhances spin–orbit coupling (SOC), thereby increasing the intersystem crossing (ISC) rate and facilitating efficient RISC. The presence of heavy metal atoms, such as platinum (Pt), iridium (Ir), or gold (Au), introduces strong SOC through relativistic effects, leading to reduced ΔE_{ST} and shorter excited-state lifetimes.[29–34]

Key features:

➢ Faster ISC and RISC rates due to enhanced SOC.

➢ Lower ΔE_{ST}, leading to efficient TADF emissions.

➢ Potential dual-emission behavior from mixed triplet and singlet states.
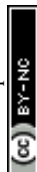
Representative examples: Pt(II) and Au(I) complexes with D–A architectures. Organometallic TADF materials with ligand-field modifications to control emission wavelengths.[33,35–37]

1.1.2. Intramolecular charge transfer (ICT) TADF. ICT-type TADF materials rely on donor–acceptor (D–A) molecular architectures, where charge transfer between the donor and acceptor groups modulates the electronic transitions.[38,39] This category can be further divided into two subtypes based on the extent of charge separation.

1.1.2.1 Long-range charge transfer (LRCT) TADF. In LRCT-TADF systems, the donor and acceptor units are spatially separated by extended π-conjugated linkers, resulting in highly polarized charge-transfer states. While this leads to a significantly small ΔE_{ST}, the reduced spin–orbit coupling often slows down the RISC process.[40–43]

Key features:

➢ Extremely small ΔE_{ST} (∼0.01–0.05 eV), enhancing TADF efficiency.

➢ Increased excited-state lifetimes due to reduced SOC.

➢ High emission stability with minimized aggregation-induced quenching.

Representative examples: multi-resonance boron–nitrogen (BN) embedded systems. Large π-extended D–A systems with steric hindrance to prevent aggregation.[44–48]

1.1.2.2 Short-range charge transfer (SRCT) TADF. In contrast, SRCT-TADF materials have donor and acceptor units in proximity, leading to stronger electronic coupling and moderate charge separation. This configuration ensures a balance between ΔE_{ST} reduction and efficient spin mixing for faster RISC.[49–52]

Key features:

➢ Moderate ΔE_{ST} (∼0.05–0.1 eV), enabling both efficient ISC and RISC.

➢ Shorter excited-state lifetimes than LRCT-TADF, improving device efficiency.

➢ Strong fluorescence-phosphorescence coupling, leads to high photoluminescence quantum yield (PLQY).

Representative examples: carbazole-based D–A molecules with rigidified linkers.[53–55] Polycyclic acceptors paired with nitrogen-rich donors to optimize charge transfer.[56,57]

1.1.3. Space-through charge transfer (STCT) TADF. Unlike ICT-based TADF, STCT-TADF materials rely on through-space charge interactions rather than direct conjugation between donor and acceptor units. These materials are designed with sterically hindered or non-conjugated donor–acceptor pairs, where charge transfer occurs *via* non-covalent interactions.[42,58]

Key features:

➢ Non-bonded through-space interactions control charge-transfer dynamics.

➢ Efficient TADF behavior with tunable emission colors.

➢ Improved molecular stability due to minimized intramolecular vibrations.

Representative examples: twisted or V-shaped donor–acceptor systems with spatial charge confinement.[59–62] Supramolecular host–guest complexes enabling intermolecular TADF.[63,64]

2. Mechanism of TADF

The luminescence process involves the absorption of energy to form excitons, followed by radiative decay from the excited state to the ground state.[65,66] The excited states can possess divergent spin multiplicities, and returning to the ground state therefore results in either fluorescence (from singlet states) or phosphorescence (from triplet states) as shown in Fig. 2. Transitions between two electronic states possessing the same spin multiplicity are possible according to quantum mechanics, but transitions between states with divergent spin multiplicities, *i.e.*, intersystem crossing (ISC) with spin changes, are not allowed. In fluorescence, a radiative transition from singlet excitons to the lowest singlet excited state occurs before being reduced to S_0, a ground state of many types of organic molecules that are generally singlets. This process is extremely rapid, with a life span of nanoseconds. In contrast, the phosphorescence mechanism requires a radiative transition of triplet excitons from the T_1 to the ground states, which can be theoretically achievable.[67]

Organic luminescent molecules with energy gaps above 0.5 eV between the singlet S_1 and triplet T_1 states (ΔE_{ST}) show fluorescence instead of phosphorescence. For example, metal complexes demonstrate large ΔE_{ST} values, due to increased ISC and spin–orbit coupling caused by the presence of metal atoms.[68] TADF materials have strong radiative transitions of excitons from the S_1 state, as evidenced by ISC and a longer delayed emission lifetime compared to phosphorescence. Fig. 2 shows that reverse intersystem crossing (RISC) from the T_1 state back to the S_1 state causes the release of singlet excitons, which is required for the TADF process. RISC can occur after the addition of thermal energy, resulting in the TADF mechanism being an exothermic process because S_1 is a higher-energy state than T_1. Consequently, TADF exhibits stronger emissions at elevated temperatures.

2.1. Influence of molecular design on the excited-state lifetime in TADF materials

The microsecond-level excited-state lifetime is a defining characteristic of TADF materials, as it reflects the efficiency of the RISC process. A prolonged excited-state lifetime typically indicates a slow RISC rate, whereas a shorter lifetime suggests efficient upconversion from the triplet to the singlet state. The molecular design of TADF emitters plays a crucial role in determining this parameter.[64,69]

2.1.1. Donor–acceptor (D–A) strength and spatial separation. The extent of charge transfer (CT) character in TADF materials significantly affects the excited-state lifetime. A strong donor and acceptor combination with large spatial separation results in a small singlet–triplet energy gap (ΔE_{ST}), facilitating RISC but often leading to a longer excited-state lifetime due to reduced spin–orbit coupling (SOC). Conversely, optimizing D–A interactions to achieve moderate charge separation enhances SOC and accelerates the RISC process, leading to shorter excited-state lifetimes.[70–74]

2.1.2. Molecular rigidity and structural confinement. Molecular rigidity is a key factor in controlling non-radiative
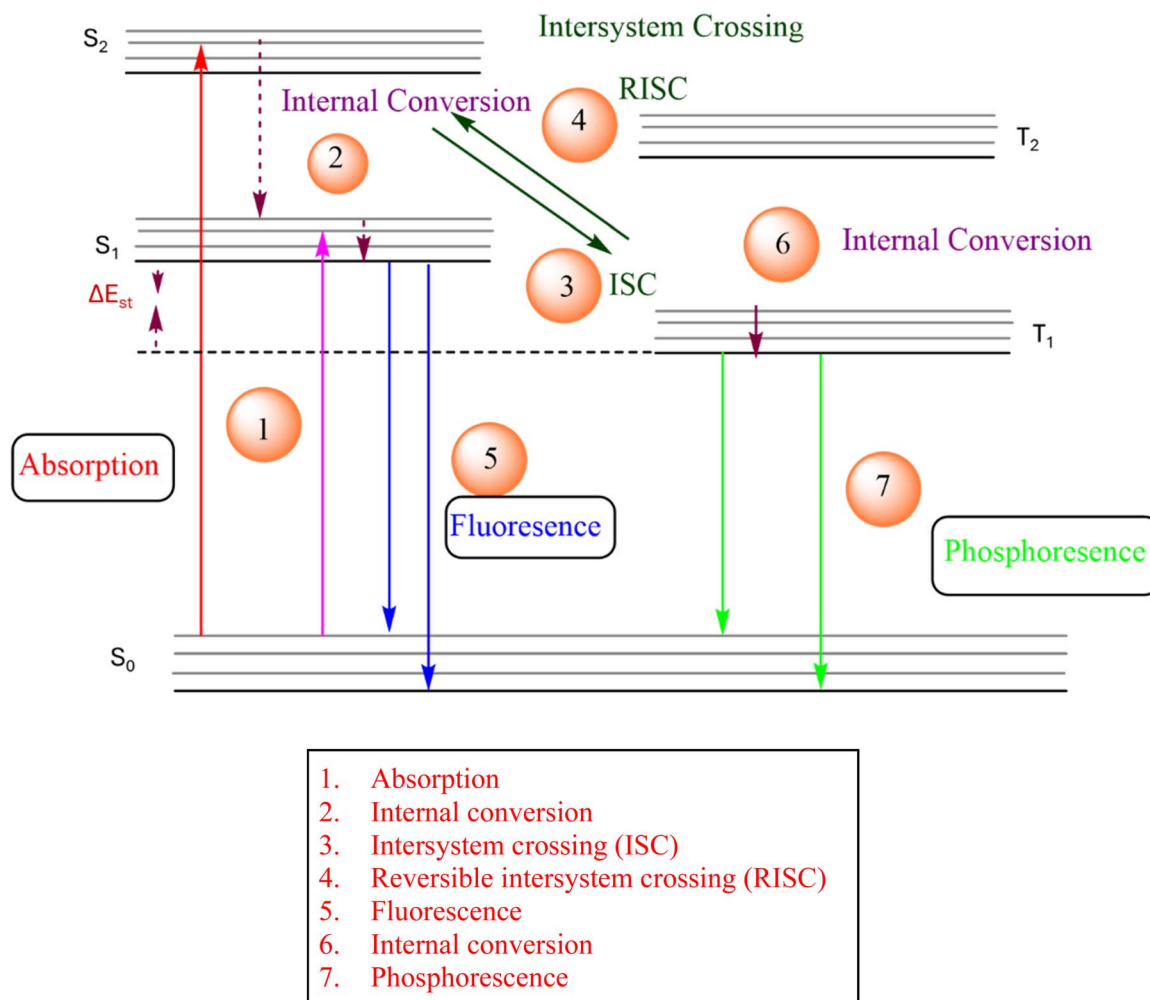
Fig. 2 Process of transitions of photo-excited photons for different phenomena.

decay pathways. Highly rigid frameworks, achieved through steric hindrance or fused-ring systems, reduce molecular vibrations and enhance PLQY. This structural confinement also stabilizes excited-state configurations, modulating the lifetime by minimizing energy dissipation through thermal relaxation.[75,76]

2.1.3. Vibronic coupling and energy level alignment. The efficiency of RISC is directly influenced by the degree of vibronic coupling between singlet and triplet excited states. Molecules with strong electron–phonon interactions exhibit enhanced spin mixing, facilitating rapid RISC and thus reducing the excited-state lifetime. Furthermore, incorporating heteroatoms or resonance structures can fine-tune the energy alignment of singlet and triplet states, further optimizing TADF performance.[77–81]

2.1.4. Host–guest interactions and environmental effects. In OLED devices, the excited-state lifetime can also be modulated by the surrounding host matrix. The polarity and rigidity of the host material affect charge transfer dynamics, influencing the rate of intersystem crossing (ISC) and RISC. A well-matched host material minimizes unwanted triplet quenching

and ensures a balanced charge transport environment, optimizing the overall device performance.[82,83]

By systematically tailoring molecular design parameters, TADF emitters with controlled excited-state lifetimes can be developed, striking a balance between efficient RISC and high quantum yield. These insights provide a deeper understanding of the structure–property relationships governing TADF behavior, guiding the design of next-generation high-performance OLED materials.

TADF was first described in organic molecules in the 1960s, including organic metal complexes and fullerenes **1**.[84] In 1961, the pure organic molecule eosin Y was reported to exhibit TADF, initially termed "E-type" delayed fluorescence (DF). This long-lived emission, identified as a secondary band alongside phosphorescence, exhibited a fluorescence band in the red region of the spectra for eosin Y **2**. Consequently, Parker and Hatchard attributed this emission to DF from the same excited singlet state.[85]

McMillin and coworkers suggested an alternative mechanism from early studies of copper(I) complexes involving two excited states in thermal equilibrium.[86] During initial studies,

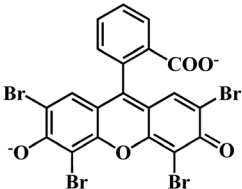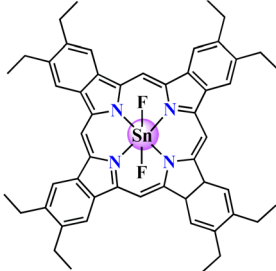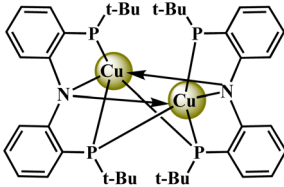**Table 1** Different types of TADF materials
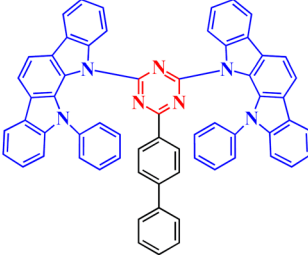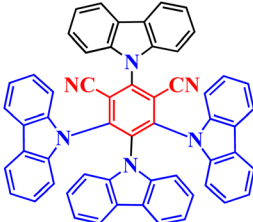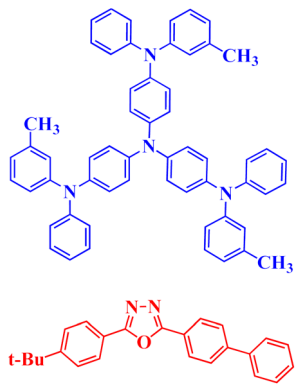
Compound number	Name	Structure	References
1	Fullerene		85
2	Eosin		87
3	Sn(iv)porphyrin complex		88
4	Cu(i) complex		89
5	PIC-TRZ D–A type organic compound		17
6	4CzIPN		90

Review

Table 1 (*Contd.*)

Compound number	Name	Structure	References
7	Organic exciplex		91

the TADF mechanism was only partially impactful due to the relatively large energy gap for eosin 2 ($\Delta E_{ST} = 0.37$ eV). Moreover, no evidence was found for a molecular strategy to enhance TADF efficiency, which posed a significant challenge to the fabrication of TADF materials. Consequently, before 2009, TADF materials had few applications and only their photophysical properties were studied.

In 2009, Endo *et al.* were the first to use TADF to produce singlet and triplet excitons in OLEDs. The excitation was achieved by applying short electrical pulses in an OLED containing a Sn(IV)–porphyrin complex 3, as described in Table 1.[88] In 2010, Peters *et al.* constructed OLEDs with an emissive layer doped with a Cu(I) complex. These OLEDs showed outstanding performance and an external quantum efficiency (EQE) of 16.1%.[89] A major milestone for TADF molecules in OLED applications was documented by Adachi *et al.* in 2011, using purely organic molecules.[92] Through a quantum mechanical analysis, they found that a modest ΔE_{ST} could be achieved by an efficient TADF mechanism that reduced the overlap between the lowest unoccupied molecular orbital (LUMO) and the highest occupied molecular orbital (HOMO). Based on these results, they suggested a molecular design that entailed creating molecules with a twisted electron donor–acceptor (D–A) structure (D shown in blue and A shown in red) (Table 1). This structure was an effective TADF mechanism with a low ΔE_{ST} of 0.11 eV because of the bulky substituents causing steric hindrance. Emitting layers in OLEDs containing were shown to have a high EQE of 5.3%, which is comparable to the theoretical limit of ordinary fluorescent molecules. Adachi and coworkers continued to work on the development of improved TADF-based materials for their applications in OLEDs, focusing on optimizing the radiative decay rate of the final S_1 excitons and exceptionally low ΔE_{ST}. They documented a set of functionalized TADF emitters utilizing carbazolyl dicyanobenzene (CDCB) as the core component in 2012.[17] These emitters exhibited significant photoluminescence (PL) efficiency and could emit a spectrum of colors from orange to sky blue. Applications of the material 4CzIPN 6 in multilayer OLEDs for green OLEDs resulted in a calculated EQE of 19.3%, while orange

OLEDs achieved an EQE of 11.2% and sky-blue OLEDs had an EQE of 8.0%. These results marked a significant advancement over traditional fluorescence-based OLEDs, proving that utilizing organic TADF materials to harvest triplet excitons through DF could achieve high efficiency OLEDs. Around the same time, Adachi and his colleagues also describe the application of exciplexes 7 synthesized using a donor and an acceptor (shown in Table 1 in blue and red, respectively), for a molecule to obtain efficient OLED efficiency *via* efficient DF, with an EQE as high as 10.0%.[91,93] Different types of organic-based TADF materials 1–7 described above are illustrated in Table 1.

Moreover, unlike OLEDs relying on costly noble metals, pure organic materials can be cost-effective alternatives. However, traditional fluorescence-based OLEDs face a critical limitation in their low EQE, with a theoretical maximum of approximately 5%. TADF has therefore introduced an innovative method for generating triplet excitons in OLEDs, greatly enhancing OLED performance using simple and cost-effective organic molecules. Modern OLEDs employing organic TADF materials in their emitting layers, including organic compounds and exciplexes, can achieve EQE values over 20%, and sometimes even exceed 30%.[94–96] TADF materials are now regarded as 3rd-generation emitters, representing a significant advancement in OLED technology.[97]

3. Principles for designing TADF molecules

TADF properties rely on a small ΔE_{ST}, which enables the RISC process (Fig. 3). On the other hand, achieving TADF OLEDs with highly efficient electroluminescence (EL) requires a large radiative decay rate (k_r) of S_1 excitons, which conflicts with the need for a small ΔE_{ST}.

Currently, organic TADF materials reported in the literature can be separated into two classes: organic D–A systems and organic exciplexes consisting of two separate D–A materials.

Huang and colleagues (2015)[98] outlined key principles for the fabrication of D–A type TADF molecules, particularly focusing
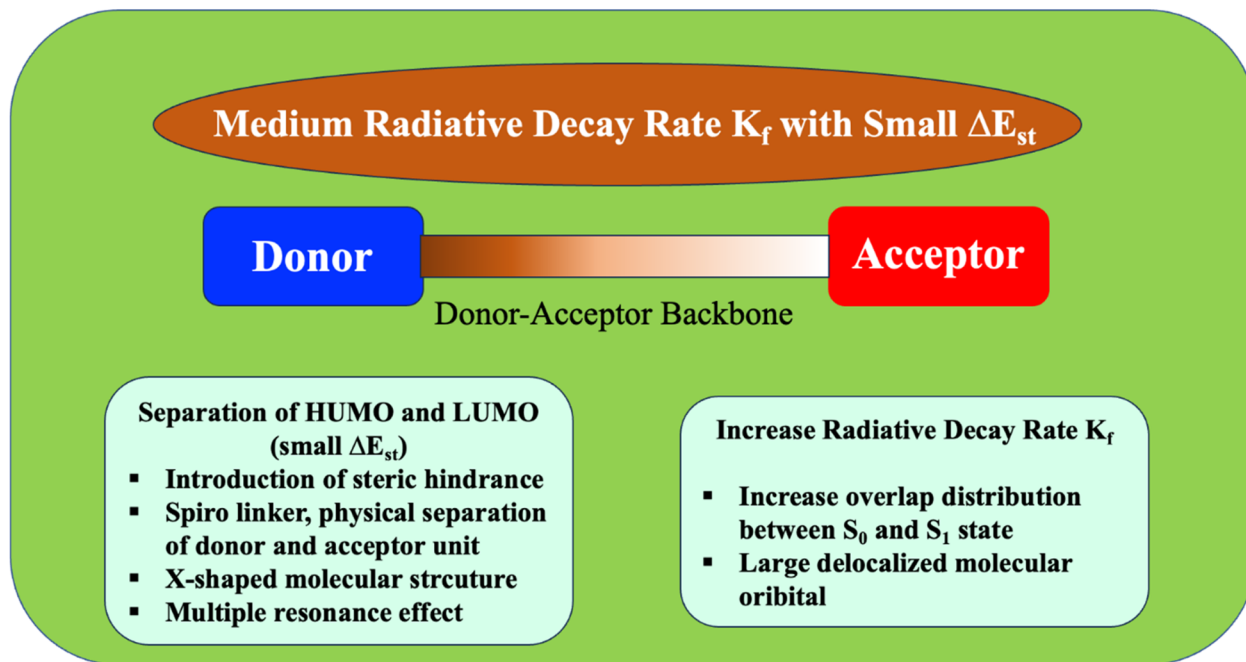
Medium Radiative Decay Rate K_f with Small ΔE_{st}

Donor — Donor-Acceptor Backbone — **Acceptor**

Separation of HUMO and LUMO (small ΔE_{st})
- **Introduction of steric hindrance**
- **Spiro linker, physical separation of donor and acceptor unit**
- **X-shaped molecular strcuture**
- **Multiple resonance effect**

Increase Radiative Decay Rate K_f
- **Increase overlap distribution between S_0 and S_1 state**
- **Large delocalized molecular oribital**

Fig. 3 Principles for designing D–A system of TADF molecules.

on their applications in high-performance OLEDs. These guidelines include:

(i) In order to achieve a smaller ΔE_{ST}, adopting a twisted D–A structure as a result of heavy substituents or a spiro-junction.

(ii) Heavily integrating donor and acceptor groups while enhancing molecular rigidity to improve radiative luminescence efficiency.

(iii) Controlling the length of π-conjugated systems.

(iv) Managing the oxidation-reduction potentials of the donors and acceptors by selectively interrupting conjugation.

In recent years, various innovative methodologies for designing more efficient TADF systems have been introduced. It is desirable to minimize ΔE_{ST} in order to increase the radiative decay rate from the S_1 to the S_0 state. Enhancing the overlap in the density distribution between the electronic wavefunctions of the ground and excited states promotes S_1–S_0 radiative decay, thereby improving the photoluminescence quantum yield (PLQY).[99] To reduce the radiative decay rate of fluorescence (k_f) and the ΔE_{ST}, it is necessary to achieve significant delocalized molecular orbitals with a clear gap between the HOMO and LUMO.[100] The introduction of different molecular systems through physical separation of D–A units,[101] utilizing X-shaped structures,[102] incorporating dual D or A units,[103] or leveraging multiple resonance effects[104] can also lead to separating the HOMO and LUMO and therefore minimization of ΔE_{ST}. A summary of these principles is shown in Fig. 3 and Table 2 shows D–A systems **8–11** used for TADF molecules.[105]

3.1. Organic exciplexes with two separate donor and acceptor materials

Organic exciplexes have received tremendous attention from researchers considering their remarkable properties and luminescent applications. These include organic optical waveguides, lasers, various nonlinear optical devices, OLEDs, and even light-emitting transistors. Extensive research has been conducted on exciplexes. Stable exciplexes are generated when one component of the D–A pair is excited directly or locally from its ground state and forms a complex with the other component, allowing the initial component to maintain stability in its excited state.[106,107]

3.2. Generation of exciplexes by photoexcitation

Two distinct classes of excited-state complexes have been produced by progressively depositing p-type materials containing various electron-donating units and n-type materials containing electron-accepting units in a single layer, a process known as co-doping,[108–110] as shown in Fig. 4. The combination of bipolar and n-type materials could lead to the formation of excited-state complexes which, in turn, gave rise to a sizable hole/electron barrier between the two materials.[111] It was also noted that the radiative electron transitions from the LUMO of the acceptor to the HOMO of the donor resulted in emissions from the excited-state complexes. Similar to exciplexes, electroplexes can arise from the donor carrying a hole or the acceptor carrying an electron. The donor–acceptor gap in an exciplex of planar aromatic compounds is less than that of an electroplex (∼0.4–0.7 nm).[112] Consequently, the structural properties of the materials determine whether exciplexes or electroplexes form. Emissions from exciplexes have been reported for EL as well as PL spectra and could be produced using photoexcitation.[113–115]

3.3. Electrically excited generation of exciplexes

In type II heterojunctions, the generation of exciplexes is intimately linked to the generation of intermolecular charge

Table 2 Different D–A systems of TADF molecules

Compound number	Name	Structure
6	4CzIPN	
8	ACRFLCN	
9	PxPmmBPX	
10	DABNA-2	

transfer (CT) excitons within non-ionic S_0 ground state complexes.[116] During the process of electrical excitation, electrons are introduced into the LUMO of the acceptor, while holes are introduced into the HOMO of the donor. The substantial energy difference between the LUMOs and HOMOs leads to the accumulation of both electrons and holes at the donor–acceptor interface. This accumulation results in the formation of CT excitons, as depicted in Fig. 5.[117]

Once CT excitons are generated, they undergo decay to the ground state either through radiative or non-radiative recombination, which is based on specific mechanisms and time. Exciplex emission phenomena result from a radiative recombination of CT excitons releasing photons. However, exciplexes emit exclusively through the recombination of singlet CT excitons, typically resulting in less efficient PL.[118] Exciplexes may exhibit TADF properties using singlet and triplet excitons by

rapid and DF decay channels. Further, TADF can exceed the internal quantum efficiency (IQE) of about 25% for singlet excitons in the absence of heavy atoms at atmospheric temperature, theoretically allowing the IQE to reach 100%. When the ΔE_{ST} between the lowest triplet and singlet states is minimal, the RISC mechanism is efficiently activated, improving the IQE, as shown in eqn (1) below.

$$\Delta E_{st} = E_s - E_t = 2j \tag{1}$$

where E_s is the energy of the singlet state and E_t is the energy of the triplet state, whereas j indicates energy exchange for electrons related to the overlap of the LUMO and HOMO.[105]

Furthermore, the fabrication of TADF materials based on exciplexes possessed extremely high quantum yields with the following necessary conditions:
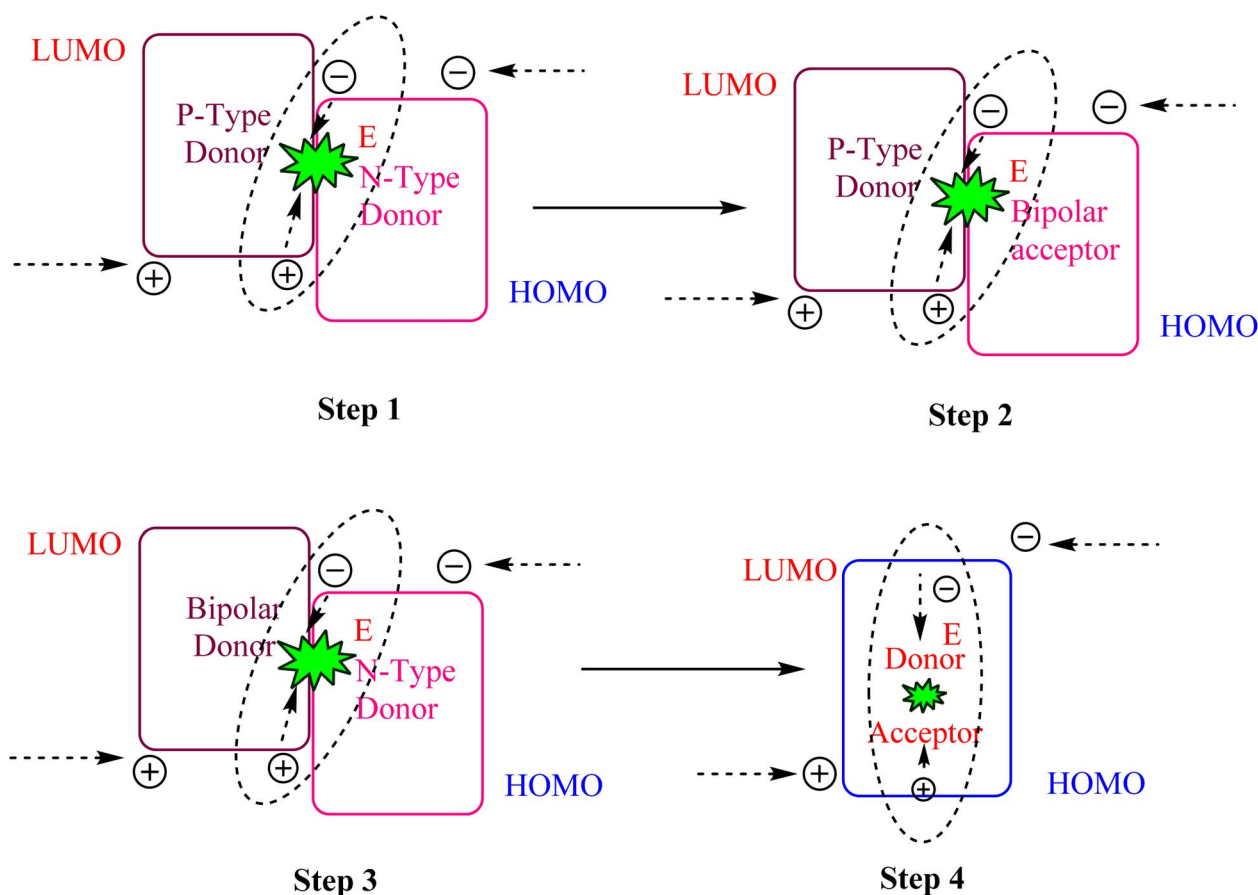
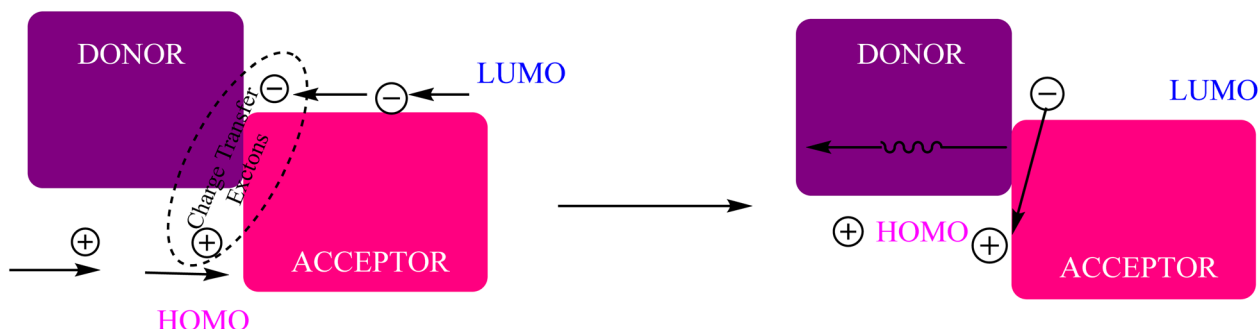Fig. 4 Mechanism for generation of exciplexes by co-doping.

Fig. 5 Electrically excited generation of exciplexes.

To ensure efficient charge injection, D–A materials must exhibit effective electron and hole transport.

(1) The difference in energy between the HOMO and LUMO of the donor and acceptor must be more than 0.4 eV to that cause accumulation of effective charge on the surface.

(2) A D–A unit with higher triplet energy (T_1) levels must be selected to prevent energy transfer back to the exciplex system.[119]

3.4. Design principles for effective TADF exciplex emitters

Both surface and bulk TADF exciplex emitters' EL properties have been enhanced in the presence of an efficient D–A

molecule combination. However, even with these developments, creating effective TADF exciplex emitters remains challenging. As a result, there has been a considerable amount of research done to fully comprehend TADF exciplex systems and several novel ideas have been put out to direct the creation of exciplex emitters with increased efficiency.

3.5. Regulation of excited state energy alignment

For an efficient TADF mechanism, the energy levels of both singlet and triplet states should be nearly equal. However, the system also includes local excited states, which can impact the energy transfer during the formation of the exciplex.

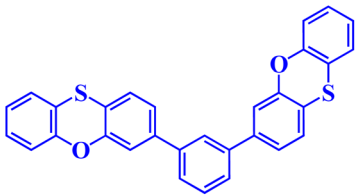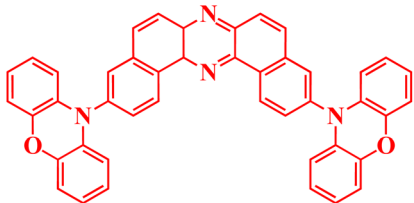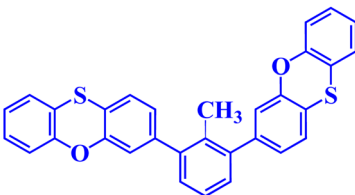**Table 3** List of TADF organic exciplexes donor and acceptor groups[119]
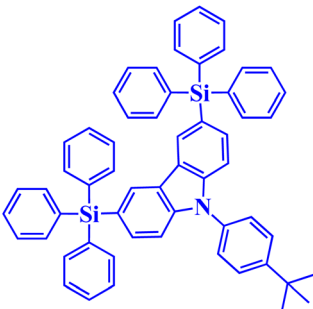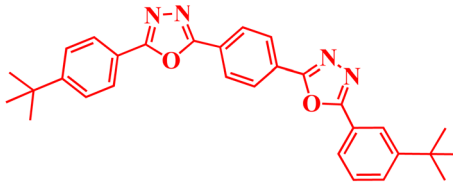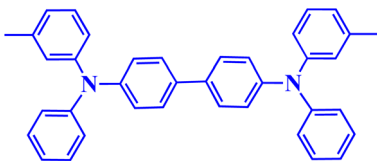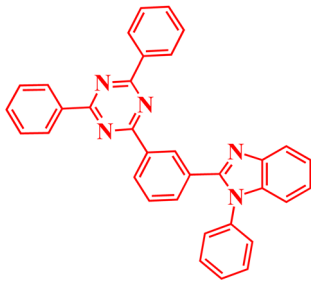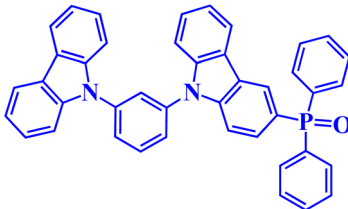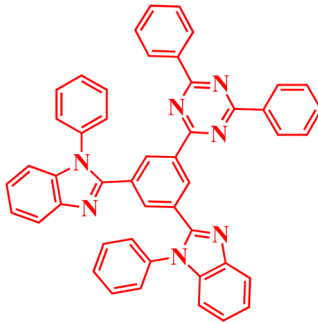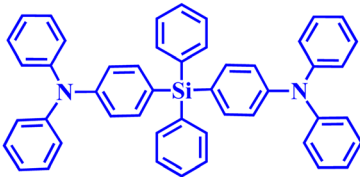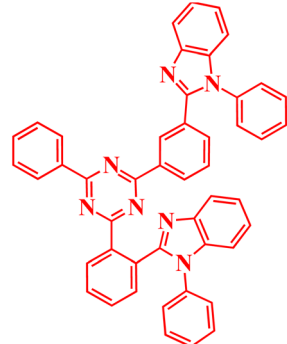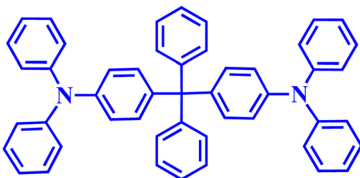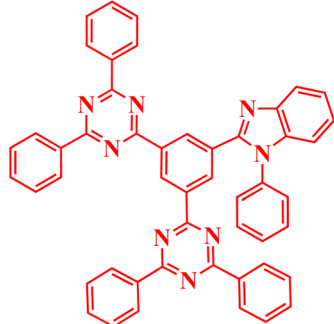
Name	Donor	Name	Acceptor
mPXPT	**11**	POZ-DBPHZ	**18**
mPXTMP	**12**	BFPD	**19**
CzSi	**13**	OXD-7	**20**
	14		**21**

Table 3 (*Contd.*)

Name	Donor	Name	Acceptor
TPD	**15**	PIM-TRAZ	**22**
TASBPA	**16**	A2	**23**
TCBPA	**17**	A3	**24**

Particularly, the local triplet states of the donor and acceptor may have different relative energies compared to the exciplex's CT state. Therefore, to ensure efficient TADF in exciplexes, it is essential to analyze and align the excited triplet states of the donor and acceptor with the excited singlet state of the exciplex to minimize loss of energy and prevent energy leakage.[79,120,121] Several TADF donor and acceptor-based exciplexes **12–25** separated into their donor and acceptor groups are described in Table 3.[119]

4. Applications of thermally activated delayed fluorescence materials

TADF materials have a wide variety of applications in OLEDs and other industries. They are used in a variety of OLEDs, such as dendrimer-based OLEDs, non-doped TADF-based OLEDs, white OLEDs (WOLEDs), solution-processed OLEDs, and doped TADF-based OLEDs. In addition to OLEDs wide range of cutting-edge applications, TADF materials are also used in

electrogenerated chemiluminescence (ECL) cells, fluorescence imaging, organic hybrid microwire radial heterojunctions, organic ultraviolet photodetectors (UVPODs), multicolor luminescent micelles, mechanoluminescence (ML) and mechanoluminochromism (MLC), photocatalysis, photosensitizers, triplet–triplet annihilation (TTA) sensitizers, and biomedical applications.[105] A few representative examples of these applications will be discussed below.

4.1. Biomedical applications of TADF

Metal-free luminophore-based TADF materials have been used in biomedical applications including time-resolved sensing and imaging, generation of singlet oxygen ($^1O_2$) for photodynamic therapy (PDT), and conventional fluorescence imaging in various biological systems (Fig. 6).[18,25,122,123]

4.1.1. Conventional fluorescence imaging. Conventional fluorescence imaging is a well-established technique in the fields of biomedicine and clinical research that can be highly sensitive and exhibits excellent temporal-spatial resolution.[124–130] When comparing metal-free TADF luminophores with traditional fluorophores such as fluorescent polymers or inorganic semiconductors, these organic molecules offer significant advantages. They exhibit PLQY, possess delicate structures with favorable biodegradability, and have low toxicity. These properties make them highly suitable for bioimaging applications, where they have been increasingly utilized over the years.[122,131,132] Organic dyes' ability to provide bright and stable fluorescence with minimal toxicity makes them ideal for detailed and long-term biological imaging, offering a safer and more environmentally friendly alternative to traditional fluorescent materials.

In 2015, Adachi *et al.* explored fluorescent organic nanoparticles, specifically TADF nano-probes based on the anthracene derivative 2,6-bis[4-(diphenylamino)phenyl]anthraquinone (TPAAQ), using self-assembly methods as shown in Fig. 7A and B.[55] They discovered that these nanoparticles emitted strong red light, unlike TPAAQ molecules in THF. In particular, the aggregation-induced emission (AIE) properties of NFO-NPs displayed a significant Stokes shift of 177 nm, which makes them ideal for bioimaging in light of their superior signal-to-noise ratio. The study also assessed the long-term cellular tracing abilities of these nanoparticles, which showed sustained red signals after a single application. They analyzed how TPAAQ solution concentration affected NFO-NP precipitation, finding that TPAAQ **25** did not dissolve in THF beyond a certain concentration. At 1 mg mL^{-1}, the NFO-NPs were uniformly sized at 93.5 nm with a polydispersity index (PDI) of 0.148. These particles had low cytotoxicity and demonstrated AIE in aqueous solutions, indicating a potential for targeting A549 cancer cells *via* endocytosis. Additionally, NFO-NPs exhibited superior resistance to photodegradation and photobleaching compared to dyes like fluorescein sodium, making them promising fluorescent probes for cellular tracing and bioimaging.[131]

In 2016, the same research team explored novel fluorescent organic nanoprobes based on electron-based donor–acceptor (D–A) carbazole derivatives for cellular imaging, aiming to address the shortcomings identified in their 2015 study.[122] The earlier research had revealed issues such as oxygen sensitivity, low water stability, and challenges associated with TADF emitters, which included potential cell or tissue damage from short-wavelength excitation, background interference from
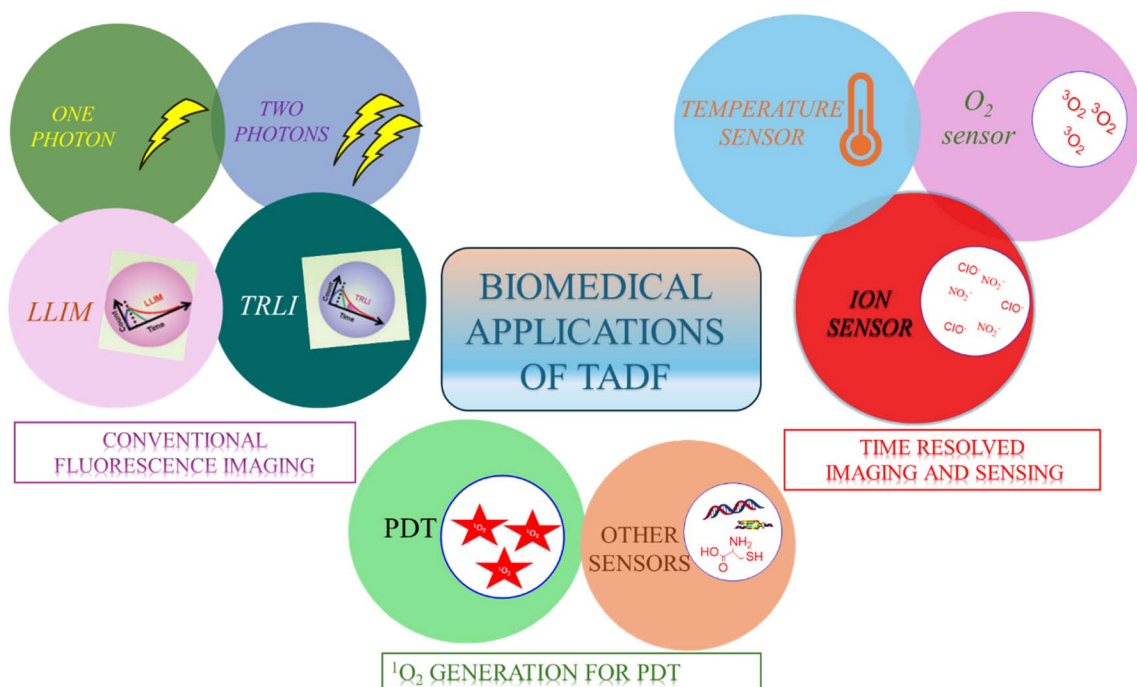

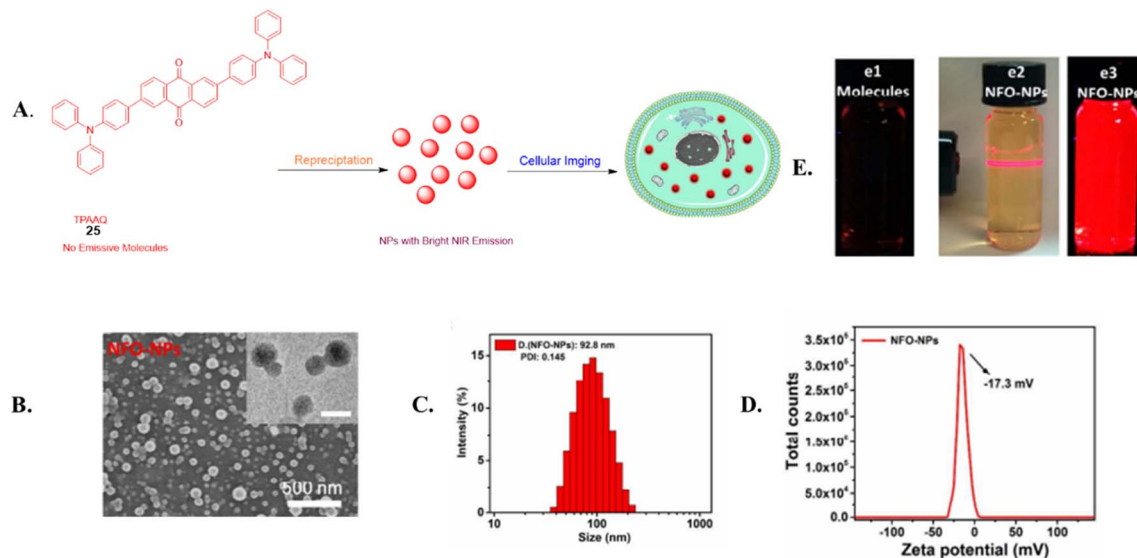Fig. 6 Biomedical application of metal–free TADF luminophores.

Fig. 7 (A) Illustration of the synthesis of NFO nanoparticles (NFO-NPs) using the reprecipitation technique. (B) SEM image of the NFO-NPs and TEM images (C) Dynamic Light Scattering (DLS) measurements and polydispersity index (PDI) of the NFO-NPs. (D) Zeta potential measurement of NFO-NPs. (E) Photographs showing TPAAQ under UV light (e1) and NFO-NPs dispersed in water (e2 and e3). Reproduced from ref. 131 with permission from the Royal Society of Chemistry.

autofluorescence, and limited optical penetration depth. To mitigate these issues, Adachi and his colleagues developed new carbazole-based nanoprobes that emitted red, blue, orange, and green light, suitable for both one- and two-photon cellular imaging techniques, as illustrated in Fig. 8(A and B) 6, 26–27. Despite having identical chemical structures, these TADF
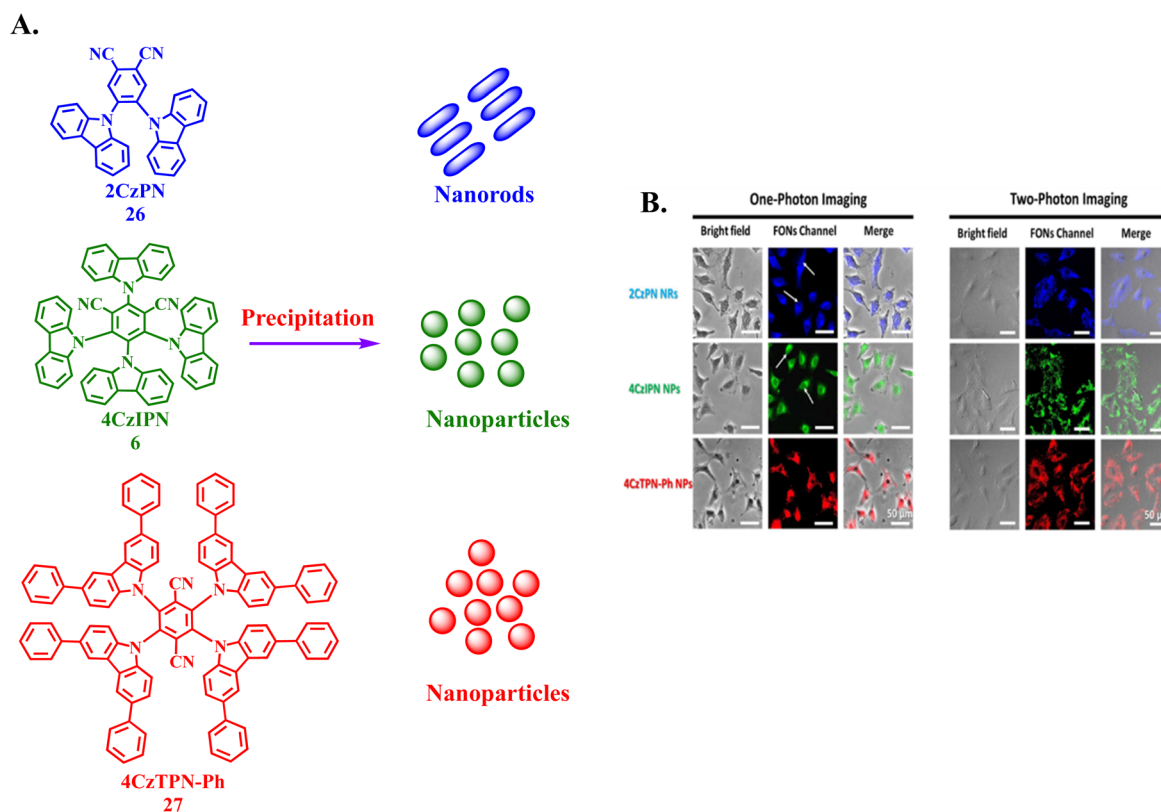

Fig. 8 (A) Schematic diagram for fabrication of blue/red/green fluorescent nanoprobe for cellular imaging in one- and two-photon imaging systems (B) one- and two-photon imaging showing fluorescence and cellular localization of the three-fluorescent organic nanoprobes (FONs) in A549 cells. Reproduced from ref. 122 with permission from American Chemical Society, Copyright © 2016.

materials exhibited diverse structures and optical properties, which were associated with D–A acceptor supramolecular interactions arising from variations in their molecular frameworks.

In 2019, the same research group investigated organic nanoparticles exhibiting a high photoluminescence quantum yield (PLQY) of approximately 94%, along with a long-lived delayed emission of 3.1 µs, originating from TADF.[132] These nanoparticles developed into glassy state particles in oil or water emulsions under pressures below 20 bar. The resulting organic nanoparticles demonstrated remarkable dispersion capabilities, photostability, and excellent uptake properties in living cells. When incorporated into a glassy host matrix, luminophores such as 4CzIPN achieve an impressive photo-luminescence quantum yield (PLQY) of 94%, a substantial enhancement compared to the 13% PLQY observed in pure 4CzIPN O-dots in aqueous solution. This significant improvement highlights their potential as promising agents for both *in vivo* and *in vitro* studies. However, a notable drawback of these TADF-emitting glassy organic nanoparticles is their insensitivity to oxygen. The glassy host matrix restricts oxygen diffusion to the emitters after nanoparticle fabrication, and organic nanoparticles produced under air-saturated conditions did not perform effectively. Fig. 9 illustrates various chemical structures (**6**, **28–30**) used in the preparation of these organic nanoparticles.

In 2020, Li *et al.* developed an economical method using galactose, a glucose isomer, to synthesize Gal-PEG-DSPE. This compound was employed to modify TADF liposomes to target HepG2 cells, enhancing the accumulation of TADF materials within cancer cells. This approach aimed to create a targeted fluorescent probe for detecting malignant cells.[133] The fluorescence intensity of liposomes modified with Gal-PEG-DSPE showed a significant increase compared to Blank-PEG-DSPE liposomes ($P < 0.05$). This enhancement is attributed to the Warburg effect, which involves the overexpression of glucose transporter proteins (GLUT) in malignant cells. The presence of galactose ligands on the liposomes therefore facilitated greater uptake by tumor cells compared to conventional liposomes without this modification, as shown in Fig. 10A. Both Gal-PEG-DSPE- and Blank-PEG-DSPE-modified liposomes encapsulating the TADF probe exhibited excitation at 488 nm and emission at 520 nm, as illustrated in Fig. 10B. Fig. 10C shows that the Gal-PEG-DSPE-modified liposomes showed significantly increased fluorescence intensity compared to Blank-PEG-DSPE-modified liposomes. This finding was consistent with the flow cytometry analysis results showing cellular uptake. Confocal imaging revealed that the liposomes were primarily localized in the cytoplasm, with significant accumulation surrounding the nucleus, but no detectable fluorescence signal was detected in the nucleus itself.[133]

4.1.2. Time-resolved luminescence imaging (TRLI). Luminescence imaging allows for the visualization of biological processes within cells and subcellular compartments.[134–138] Unfortunately, its accuracy and precision are often compromised by variations in the local concentration of the probe, the power of the laser used for excitation, and the challenge of distinguishing autofluorescence backgrounds.[139–146] Luminescence lifetime imaging (LLIM) offers a solution by using luminescence lifetime in place of intensity as a distinct optical property. This technique has been applied for the differentiation of probe signals from background obstruction across different time domains, even with the same emission wavelengths, making it increasingly popular in bioimaging and biosensing.[146–153] Conventional LLIM agents such as lanthanides[139,154,155] and transition metal complexes[117,156] are inorganic

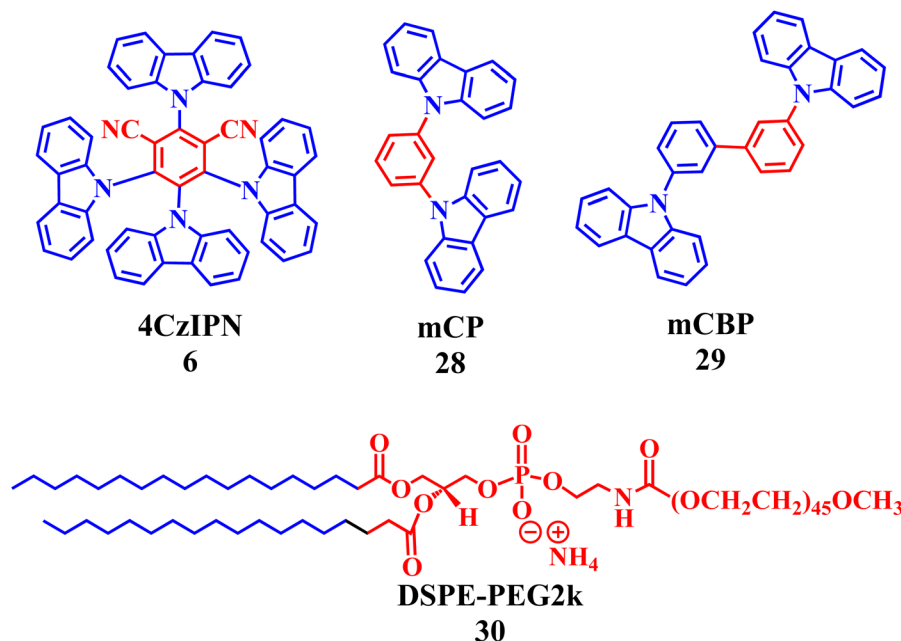
Fig. 9 Chemical structures of molecules **6**, **28**, **29** and **30** used in the preparation of TADF-emitting glassy organic nanoparticles. Reproduced from ref. 132 with permission from the Royal Society of Chemistry.
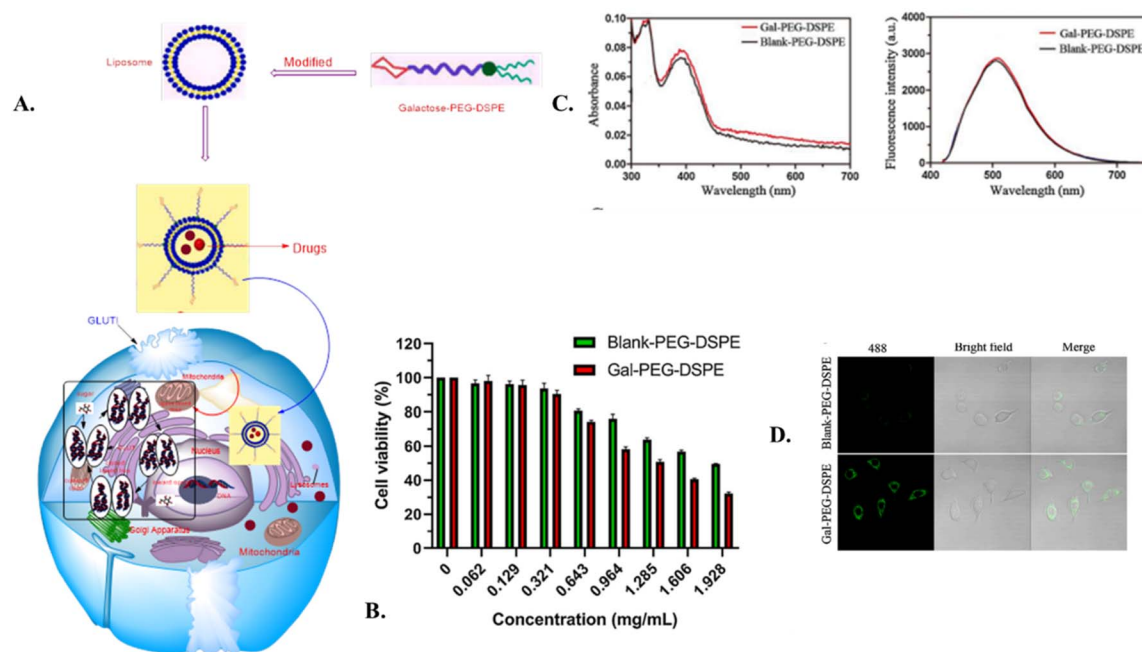
Fig. 10 (A) Schematic representation of galactose-modified liposomes transport *via* GLUT. (B) Cell viability at various concentrations of Gal-PEG-DSPE- and Blank-PEG-DSPE-modified liposomes in HepG2 cells (C) UV-vis absorption spectra for absorbance (left) and fluorescence. (D) Confocal fluorescence images of HepG2 cells after incubation solely with Blank-PEG-DSPE and Gal-PEG-DSPE modified liposomes in PBS for 2 h. Adapted from ref. 133 with permission from Elsevier, Copyright © 2020.
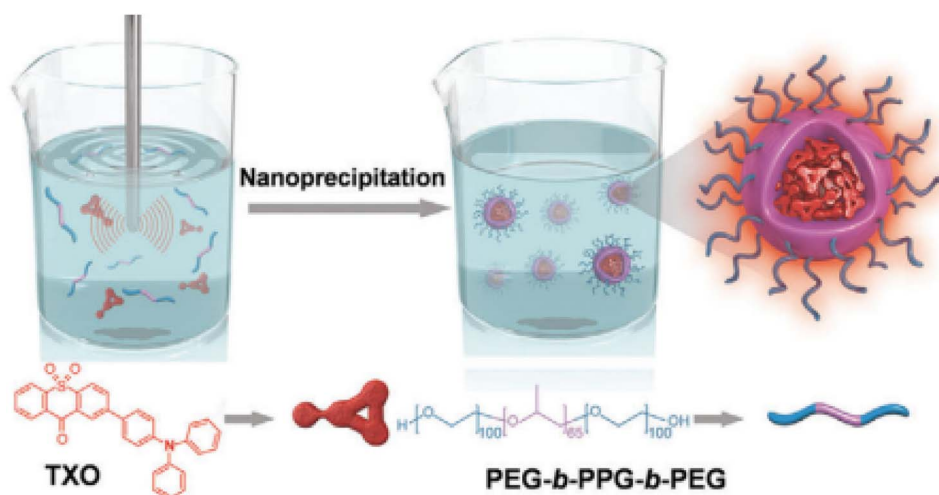

Fig. 11 The fabrication process of TXO NPs through nanoprecipitation. Reproduced from ref. 159 with permission from John Wiley & Sons, Copyright © 2018, Wiley-VCH Verlag GmbH & Co. KGaA, Weinheim.

nanoparticles that can be cytotoxic, prone to removal, and costly to fabricate. On the other hand, TADF fluorophores are metal-free organic probes known for their outstanding biocompatibility and affordability, making them ideal for LLIM applications.[105,122,157,158] For example, Fan and colleagues developed water-soluble organic semiconducting nanoparticles that exhibit both TADF and AIE properties, as illustrated in Fig. 11.[159] Moreover, the oxygen-inert properties of TXO nanoparticles extended their luminescence lifetime to 4.2 μs. The longer luminescence lifetime is advantageous for precise two-photon

fluorescence lifetime imaging (TP-FLIM) applications for use in biological environments rich in oxygen.

Research on TRLI has focused on enhancing optical diagnosis and sensing by focusing on luminescence lifetime, thereby increasing specificity and sensitivity. In biological systems, this technique effectively eliminates short-lived background signals, thus enhancing the signal-to-noise ratio. By using a suitable time-gating mechanism among the excitation laser and luminescence detection, TRLI collects only long-lived
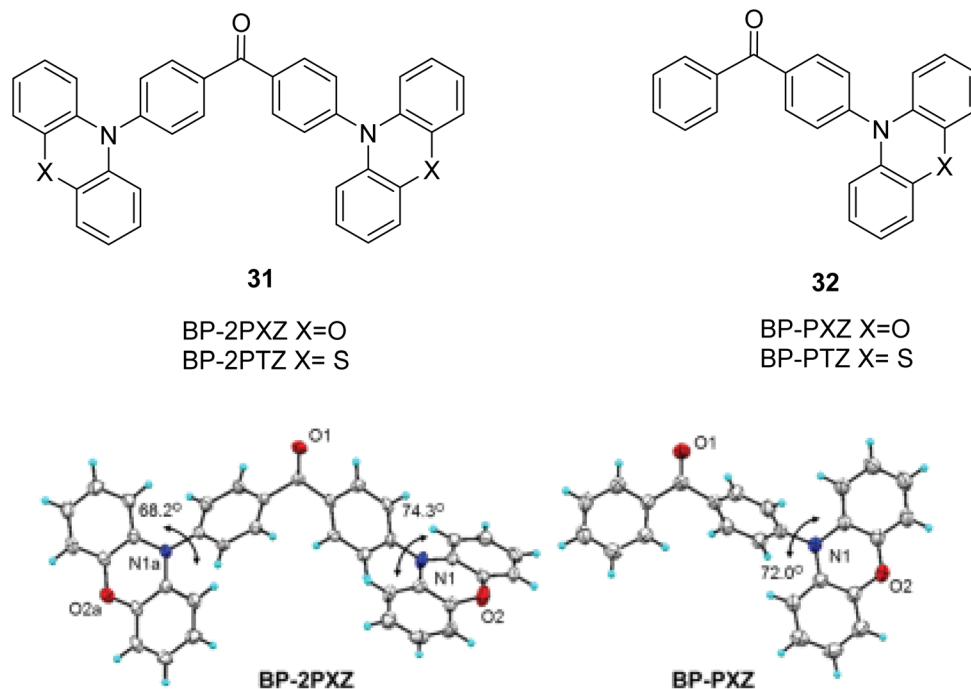
Fig. 12 Molecular structures of the luminogens and crystal structures of BP-2PXZ (**31**) and BP-PXZ (**32**). Reproduced from ref. 168 with permission from the Royal Society of Chemistry.

signals.[134,160,161] TADF dye materials are crucial in advancing TRLI.[159,162–167]

In 2017, Tang and coworkers investigated a set of luminogens based on phenoxazine (PXZ) that displayed both aggregation-induced emission (AIE) and DF.[168] These luminogens, detailed in Fig. 12 as compounds **31** and **32**, exhibit strong emission in their aggregated state and long-lived fluorescence. Both compounds also formed water-soluble nanoparticles (NPs) suitable for bioimaging when encapsulated by a matrix of bovine serum albumin (BSA). These NPs showed low levels of cytotoxicity and efficiently stained living cells, emitting robust fluorescence in the green or yellow regions. Additionally, the NPs performed well in fluorescence lifetime imaging, clearly displaying intracellular viscosity based on varying fluorescence lifetimes. While the use of luminogens with AIE and DF for fluorescence lifetime bioimaging has been relatively unexplored, these results show that they hold significant promise, particularly in addressing the limitations of luminescent metal complexes, such as the presence of toxic heavy metals.

Huang and coworkers developed and studied two small molecular organic TADF probes with specific targeting for organelles.[42] These probes show the longest average fluorescence lifetimes observed in TRFI within cells. Two TADF probes, the mitochondria-targeting AI-Cz-MT (**35**) and the lysosome-targeting AI-Cz-LT (**36**) were synthesized and displayed high biocompatibility and organelle-specificity. This was accomplished by attaching a triphenylphosphonium (TPP) group and 2-morpholinoethylamine to AI-Cz-CA (**34**) to yield AI-Cz-MT (**35**) and AI-Cz-LT (**36**), respectively, as shown in Fig. 13A. To assess the influence of organelle-targeting groups on photophysical properties, the team examined and compared the UV-vis absorption and fluorescence emission spectra of **35** and **36** with those of AI-Cz (**33**). In toluene, all three probes showed similar absorption at 335 nm for the carbazole donor unit and 390 nm due to ICT between the carbazole units and the aromatic imide. The emission spectra displayed identical band shapes, with a maximum emission wavelength at 520 nm, characteristic of TADF compounds with large Stokes shifts, as depicted in Fig. 13B. This strategy sought to mitigate the quenching of TADF fluorophores by oxygen by attaching organelle-targeting groups to TADF probes, thereby preserving their extended fluorescence lifetimes for time-resolved fluorescence imaging (TRFI) in cellular environments. The synthesized **35** and **36** demonstrated high fluorescence quantum yields and precise localization within mitochondria and lysosomes. Their extended fluorescence lifetimes were notable both in solution (6.8 μs for **35** and 6.3 μs for **36**) and in TRFI experiments in HepG2 cells (16.7 μs for **35** and 28.0 μs for **36**) in Fig. 14A and B. This study represents a notable advancement in organelle-specific TADF probes showing average fluorescence lifetimes in the microsecond range, as measured by TRFI. These developments could allow for the expansion of the potential bioimaging applications of TADF compounds.

In 2020, Ni *et al.* introduced an innovative approach utilizing *in situ* aggregation-induced TADF turn-on response for cellular imaging.[159] Unlike previous methods that either required external oxygen exclusion or pre-prepared aggregates to limit oxygen exposure, their strategy leverages *in situ* aggregation to enhance TADF emission. The team synthesized the luminophore PXZT, featuring a D–A structure with PXZ as the donor
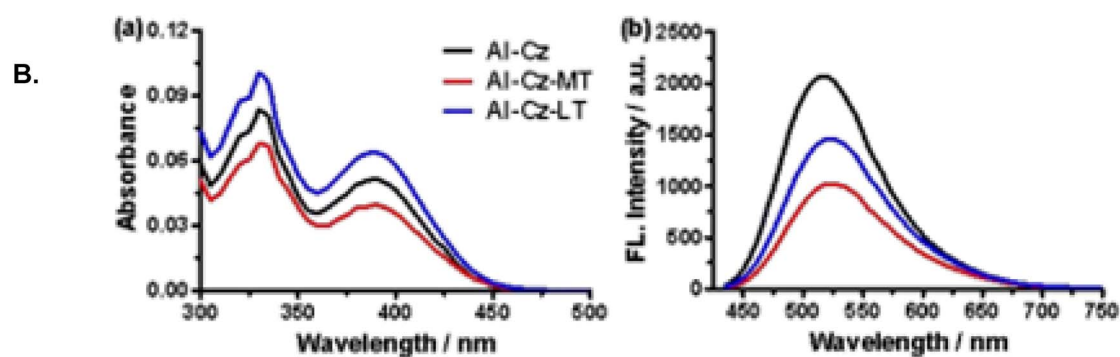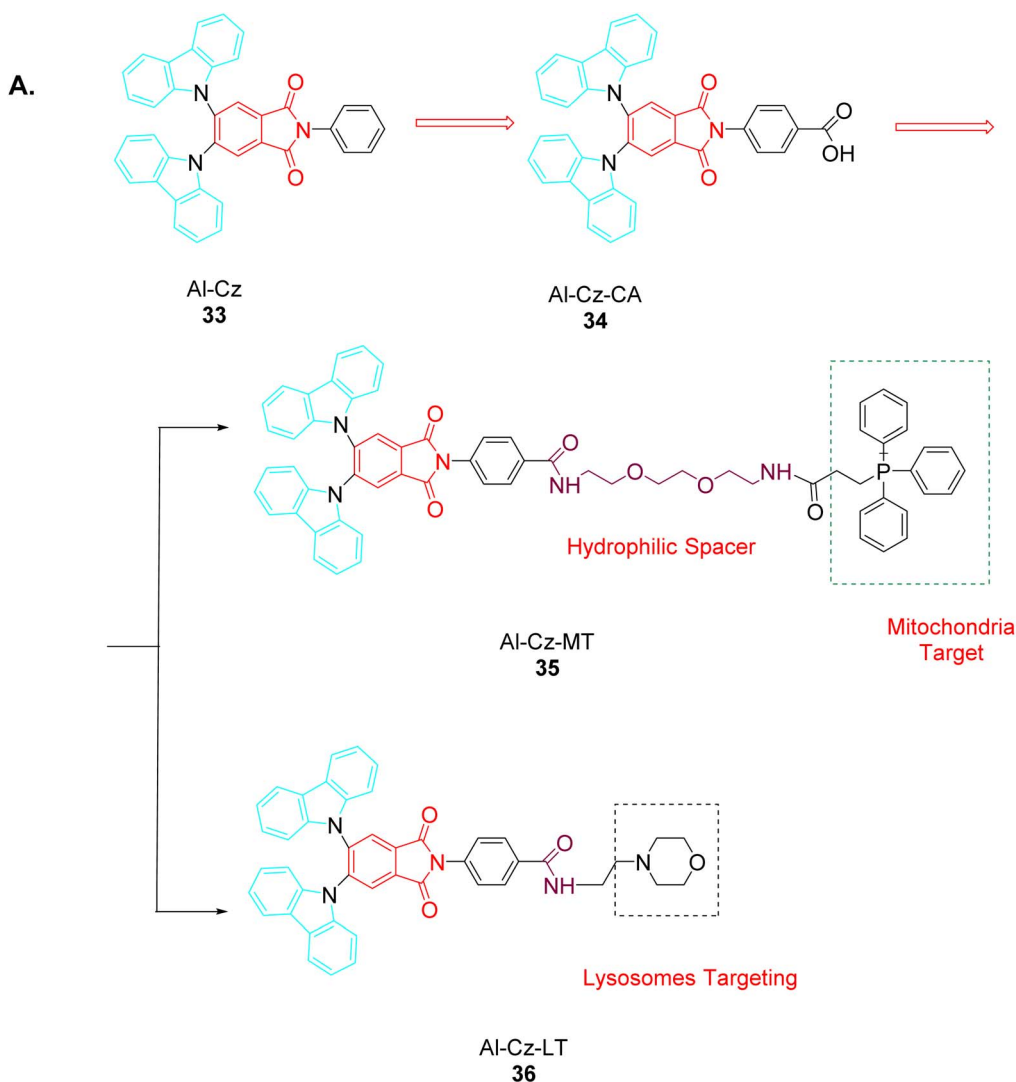
A.

B.

Fig. 13 (A) The synthesis of organelle-specific fluorescent probes **35** and **36**. (B) The absorption and emission spectra of Al-Cz (**33**), Al-Cz-MT (**35**), and Al-Cz-LT (**36**). Reproduced from ref. 42 with permission from American Chemical Society, Copyright © 2023.

and terpyridine as the acceptor. PXZT exhibited promising emission characteristics and characteristic TADF behavior. Coordination of PXZT with Zn allowed for the formation of the ZnPXZT1 complex, which significantly enhanced ICT and quenched PXZT's intrinsic fluorescence, reducing background signals. The water-soluble ZnPXZT1 was utilized for time-resolved imaging in HeLa and 3T3 cells by the release of PXZT through dissociation within the cells. This method showed effective long-lived emission from PXZT during TRLI, demonstrating the practicality of ZnPXZT1 as a cellular imaging probe
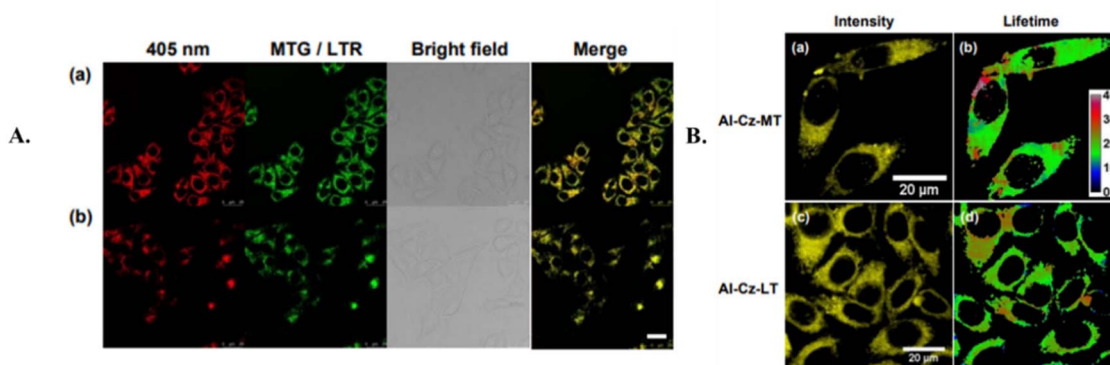
Fig. 14 The subcellular localization of Al–Cz–MT (**35**) (A) and Al–Cz–LT (**36**) (B) in HepG2 cells investigated using fluorescence microscopy. Reproduced from ref. 42 with permission from American Chemical Society, Copyright © 2023.
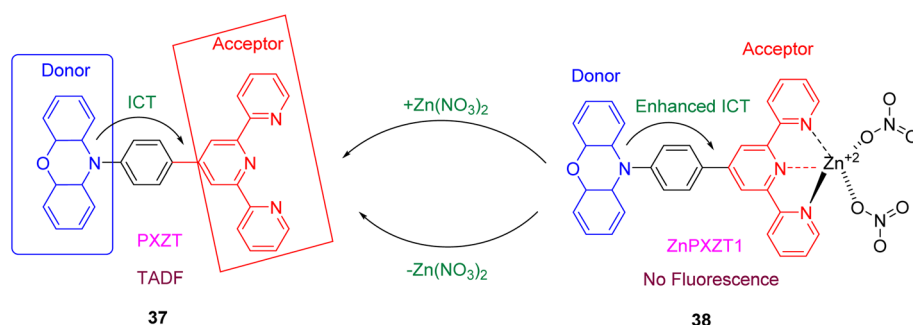
Fig. 15 Proposed mechanism for regulation of TADF using Zn^{2+}. Reproduced from ref. 159, https://doi.org/10.1039/C8SC01485J, under the terms of the CC BY-NC 3.0 license, https://creativecommons.org/licenses/by-nc/3.0/.
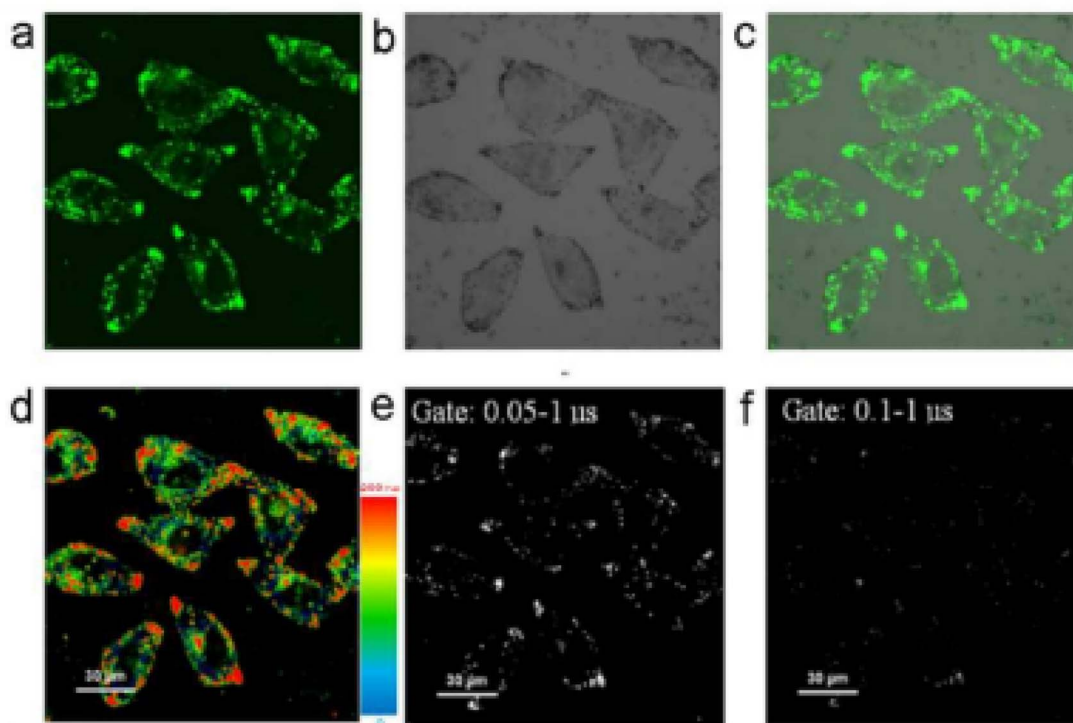
Fig. 16 HeLa cells incubated with 10 μM ZnPXZT1 visualized using (a–c) steady-state imaging, (d) luminescence lifetime imaging, and (e and f) time-gated imaging. Reproduced from ref. 159, https://doi.org/10.1039/C8SC01485J, under the terms of the CC BY-NC 3.0 license, https://creativecommons.org/licenses/by-nc/3.0/.

Fig. 17 Structure of amphiphilic TADF monomer **39** and the synthesis of TADF nanoprobe AI-Cz-NP. Reproduced from ref. 163 with permission from the Royal Society of Chemistry.

(Fig. 15) **37**, **38**. The oxygen sensitivity of PXZT was assessed by comparing its emission spectra in toluene under degassed and aerated conditions. The ZnPXZT1 complex proved to be highly effective in detecting ethylenediaminetetr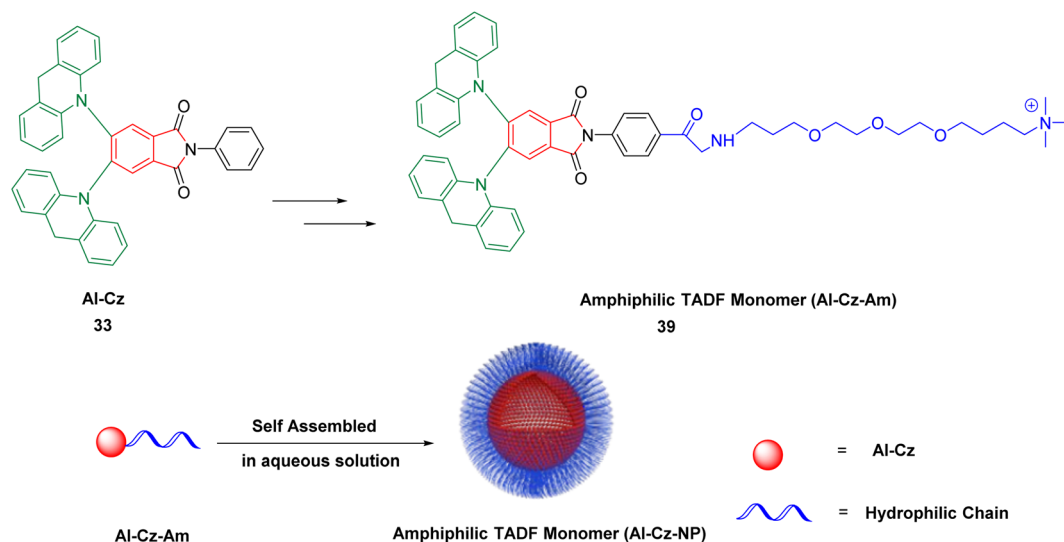aacetic acid (EDTA) with a remarkable 2000-fold increase in fluorescence intensity (Fig. 16). The use of ZnPXZT1 for time-resolved imaging in HeLa and 3T3 cells successfully minimized background signals. This new method, based on dissociation reactions and aggregation processes, offers a practical and efficient platform for time-resolved luminescence imaging compared to previous techniques. This approach, which enhances delayed fluorescence through aggregation, is expected to advance the development of TADF emitters for time-resolved imaging applications.

In 2020, Hu and colleagues developed a novel time-resolved fluorescence nanoprobe, AI-Cz-NP, by self-assembling a single-component amphiphilic monomer, AI-Cz-AM.[163] This monomer integrated a hydrophilic chain with a positively charged terminal into the lipophilic TADF emitter, AI-Cz (Fig. 17) **33–39**. The resulting AI-Cz-NP, formed in aqueous solutions, demonstrated water solubility and biocompatibility due to its amphiphilic nature. The nanoprobe's positive surface charges enhanced cellular uptake, while the aggregation of TADF units within AI-Cz-NP reduced oxygen diffusion to the core, minimizing triplet state quenching. This design aimed to provide prolonged fluorescence lifetimes even in oxygen-rich environments, making AI-Cz-NP suitable for TRLI.

Three new D–A type TADF materials, PXZ-NI (**40**), PTZ-NI (**41**), and Lyso-PXZ-NI (**42**), were synthesized by Nguyen and colleagues in 2020.[165] These materials have aggregation-induced TADF features that make them appropriate for time-resolved imaging and fluorescence in living cells (Fig. 18A) **40–42**. Temperature-dependent time-resolved photoluminescence (TRPL) tests revealed that **40**, **41**, and **42** had exceptionally low activation energy (E_a) values of 8.3, 13.2, and 7.8 meV, respectively (Fig. 18B). This research gave rise to a viable new path

toward the development of TADF materials with delayed fluorescence caused by aggregation.

TADF probes are widely recognized in bioimaging, yet most offer only a single emission signal. This reduces the amount of biological information that can be conveyed as well as compromising fluorescence intensity in complex microenvironments. To overcome this challenge, Zhu and colleagues fabricated a dual M–1 TADF probe featuring an asymmetrical D–A–D′ configuration.[169] This innovative design provides complementary dual TADF-band characteristics, significantly reducing twists in TRLI (Fig. 19a). Dual-TADF emission is effective in both monomeric solutions and aggregated states. Encapsulation of the M–1 TADF probe in the amphiphilic block copolymer Pluronic F-127 resulted in nanoprobes that mitigate oxygen quenching, enhancing TRLI (Fig. 19b). HeLa cells treated with the nanoprobe showed mean PL lifetimes of 33 μs in the DAPI channel and 36 μs in the FITC channel, respectively (Fig. 19c). This dual-channel capability allows for adjusting signal intensities through TRLI parameters. Dual-channel mean lifetime mapping showed a 30–40% decrease in TRLI distortion compared to single-channel mapping, thereby improving the use of TADF materials in medicine (Fig. 19d).

In 2020, Huang's team incorporated organic afterglow emission properties into the TADF framework, achieving up to 45% afterglow efficiency and enhancing the photophysical properties of TADF compounds for biological imaging, as shown in Fig. 20a and b. They developed a twisted D–A system with DCzB by combining difluoroboron β-diketonate with carbazole. This structure enabled a tri-modal organic afterglow that depends on the thermally activated afterglow (TAA) mechanism, which includes: (1) organic ultralong room temperature phosphorescence (OURTP) from the T_1^* state; (2) delayed phosphorescence (DP) through thermally activated exciton release (TAER) due to a narrow exciton trapping depth (ETD); and (3) trapping of S_1 excitons by DP via RISC with

A.

PXZ-NI
40

PTZ-NI
41

Lyso-PXZ-NI
42

B.
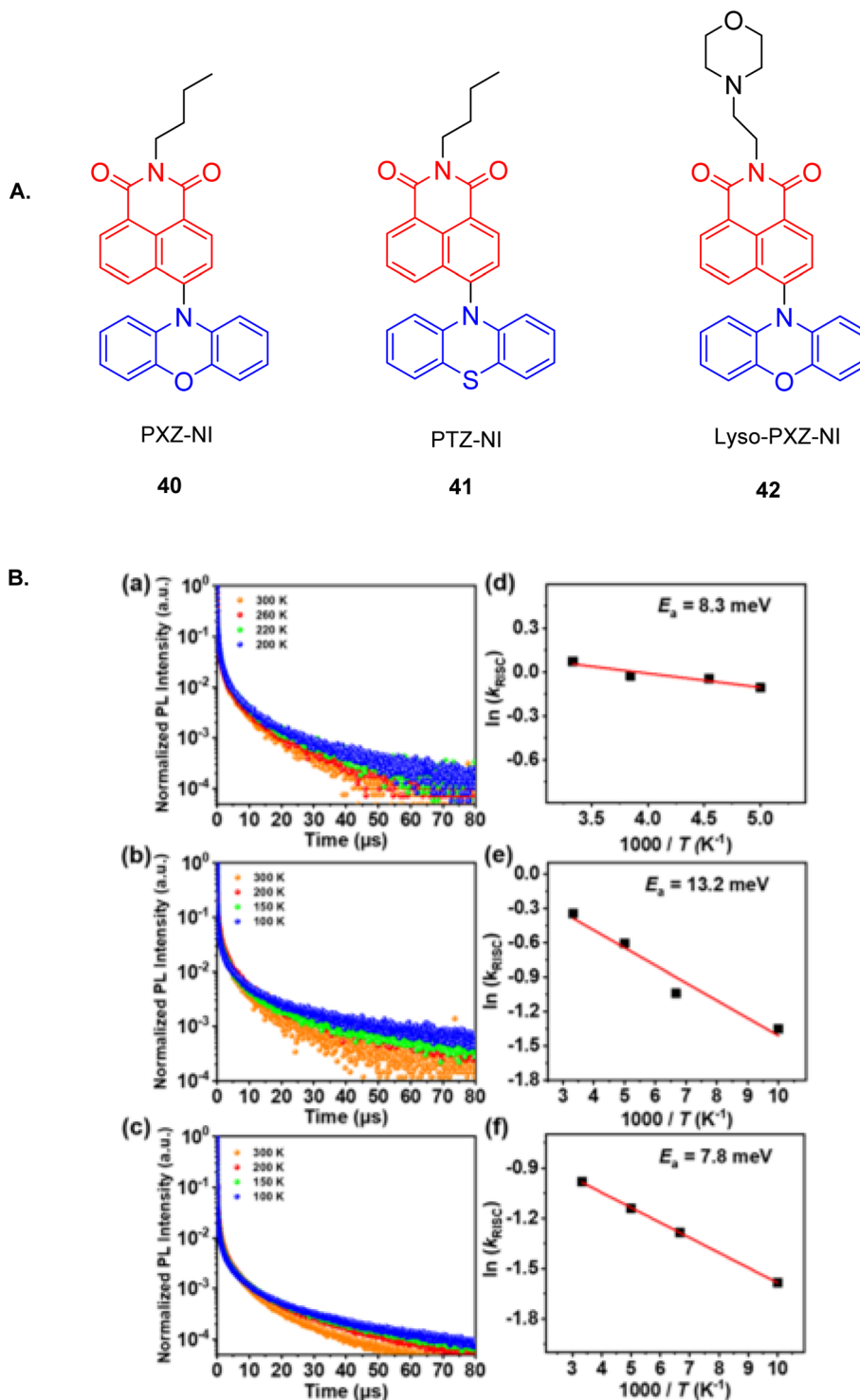
Fig. 18 (A) Structures of TADF organic materials PXZ-NI (**40**), PTZ-NI (**41**), and Lyso-PXZ-NI (**42**). (B) Temperature-dependent TRPL signals for (a) PXZ-NI (**40**), (b) PTZ-NI (**41**), and (c) Lyso-PXZ-NI (**42**), and corresponding Arrhenius plots for the TRPL signals for (d) PXZ-NI (**40**), (e) PTZ-NI (**41**), and (f) Lyso-PXZ-NI (**42**). Reproduced from ref. 165 with permission from American Chemical Society, Copyright © 2020.

a small ΔE_{ST}. DCzB nanoparticles were created by encasing DCzB in the phospholipid F127 (Fig. 20c and d). Phosphorescence lifetime imaging (PLIM) and TRLI revealed that the DCzB nanoparticles were well-suited for higher specificity for cell imaging, exhibiting a longer lifetime for phosphorescence,

approximately 500 μs (Fig. 20e). Additionally, DCzB's temperature-sensitive afterglow color change was explored for visual temperature detection, showing a transition from blue-green to green-yellow in crystals upon cessation of UV light

Fig. 19 (a) The molecular scaffold of M−1 showcases dual TADF emission in the monomeric and aggregated states. (b) Pretreatment involves encapsulating M−1 within NPs (c) TRLI imaging in HeLa cells (d) Integration of TRLI data from dual channels significantly reduces distortion by 30–40%, improving imaging precision. Reproduced from ref. 169 with permission from John Wiley & Sons, Copyright © 2020, Wiley-VCH Verlag GmbH & Co. KGaA, Weinheim.

Fig. 20 (a) Illustration of TAA emission mechanism involving TAER RISC processes. (b) Structure of DCzB. (c) DCzB NPs prepared by encapsulating DCzB. (d) DLS & TEM images of the DCzB NPs. (e) Treatment of PLIM and TRLI of cells in the presence of DCzB NPs. (f) Images of DCzB in powdered form after UV irradiation (365 nm) at various temperatures. Reproduced from ref. 170, https://doi.org/10.1038/s41467-020-14669-3, under the advances of the CC BY 4.0 license, https://creativecommons.org/licenses/by/4.0/.
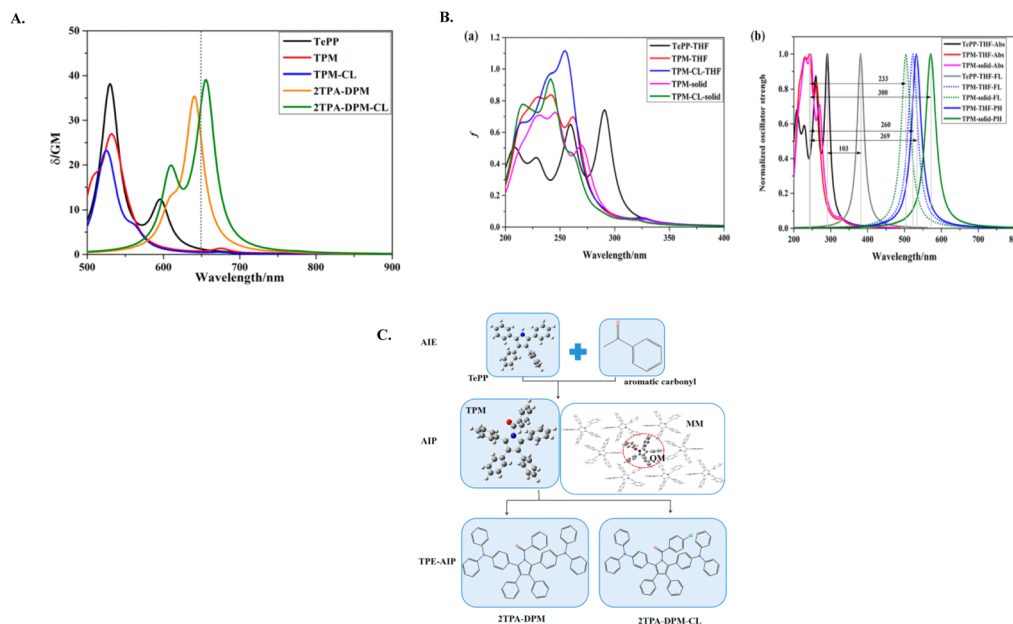
Fig. 21 (A) Two-photon absorption spectra of TePP, TPM, TPM-CL, 2TPA-DPM, and 2TPA-DPM-CL. (B) (a) One-photon absorption spectra, as well as (b) the one-photon absorption (Abs), fluorescence (FL), and phosphorescence (PH) spectra, with arrows showing the Stokes shift for compounds TPM and TPM-CL in various states. (C) Structures of the investigated compounds. Reproduced from ref. 171 with permission from American Chemical Society, Copyright © 2022.

emission, while the DCzB powder exhibited minimal color change from 300 K to 77 K (Fig. 20f).[170]

Zhou and colleagues have made significant advancements in the field of pure organic two-photon excited room temperature phosphorescent (RTP) materials with extended emission lifetimes and high resolution, which were desirable properties for time-resolved imaging (Fig. 21).[171] These aromatic carbonyl-containing materials exhibit both AIE and RTP properties. The incorporation of aromatic carbonyl groups alters the LUMO, resulting in a substantial Stokes shift and enhanced spin–orbit coupling, which facilitates intersystem crossing. For aggregation-induced phosphorescence (AIP), aggregation increases the ΔE between S_1 and T_1 states, thereby reducing the rate of RISC in the solid state. This aggregation also suppresses nonradiative decay and promotes the emission of phosphorescence. This research affords crucial insights for the synthesis of AIP materials. These compounds show promise as two-photon excitation–aggregation-induced phosphorescence (TPE-AIP) materials for time-resolved two-photon excited luminescence imaging applications.

Yang and colleagues introduced a novel in situ aggregation-induced delayed fluorescence (AIDF) technique for time-resolved luminescence sensing (TRLS).[172] They developed a new luminophore, FAc-Py, which exhibits a highly twisted structure and AIDF properties, enabling emission with a long lifetime suitable for time-resolved applications (Fig. 22A) 43–48. A derivative, FAc-Py-Ester, was also synthesized. While non-emissive and liposoluble, it can be used for DF via turn-on sensing of carboxylesterase. This enzyme facilitates the hydrolysis of FAc-Py-Ester, releasing the hydrophobic FAc-Py, which in turn activates the AIDF emission that is insensitive to air. FAc-

Py-Ester was used as a luminophore in living cells to assess both the carboxylesterase sensing capability and recovery of delayed fluorescence. HeLa cells treated with various concentrations of FAc-Py-Ester for two hours exhibited significant green luminescence. Given that cellular autofluorescence lifetimes are typically under 8 ns, short-lived fluorescence was excluded using delay times of 20 and 30 ns. Luminescence signals with lifetimes exceeding these thresholds were concluded to be due to the long-lived DF of aggregated FAc-Py, which is likely a result of carboxylesterase-mediated release of FAc-Py of FAc-Py-Ester during cellular imaging (Fig. 22B).

Although DF research has grown in importance for biological imaging, it is still difficult to develop small molecule DF probes sensitive to certain analytes. To create analyte-responsive DF probes, Zhang et al. presented a novel technique called excited-state intramolecular proton transfer-delayed fluorescence (ESIPT-DF), as shown in Fig. 23A.[42] By using different donor moieties with the ESIPT-based fluorophore 2-(2′-hydroxyphenyl)benzothiazole (HBT) as an acceptor and creating twisted donor–acceptor pairs inside each molecule, their method allowed them to develop ESIPT-DF luminophores. The compounds HBT-PXZ and HBT-PTZ were particularly noteworthy since they showed strong ESIPT and DF properties. Their solid-state lifetimes were 3.65 μs and 5.37 μs, respectively. Furthermore, as seen in Fig. 23B, a caged probe was created by including an ESIPT-DF blocking agent together with a hydrophilic D-galactose group, resulting in the probe HBT-PXZ-Ga, which was used for the specific identification of the enzyme β-galactosidase (β-gal). Using this probe, the impact of metal ions on the activity of surface β-gal in the bacteria Streptococcus pneumoniae was examined. According to the study,
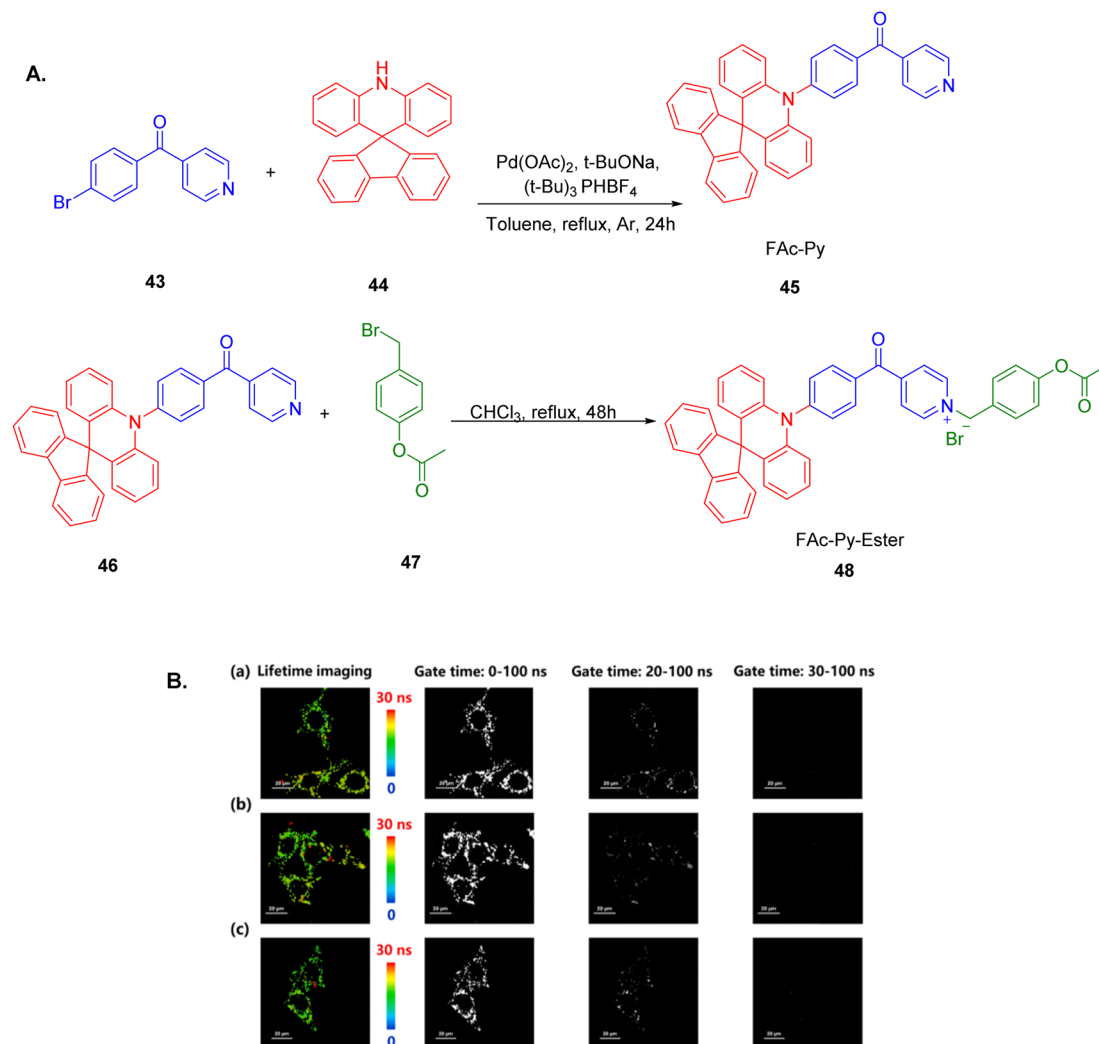
Fig. 22 (A) Preparation of FAc–Py (**45**) and FAc–Py–Ester (**48**). (B) Time-gated imaging of carboxylesterase activity in HeLa cells incubated with varying concentrations of FAc–Py–Ester (**48**). Reproduced from ref. 172 with permission from Elsevier, Copyright © 2022.

Zn^{2+} ions reduced β-gal activity by 68%. Through modification of the functional group, while retaining the main structure, this TADF "turn-on" method may be modified for the detection of different analytes.

Wu and colleagues prepared red TADF nanoparticles designed for real-time TRLI, overcoming challenges related to low efficiency and short lifetimes.[173] The study involved doping TPAAQ into a CBP (4,4′-bis(carbazol-9-yl)biphenyl) host matrix, as demonstrated in Fig. 24A. At low TPAAQ concentrations, the nanoparticles displayed significant TADF characteristics, achieving luminescence lifetimes greater than 0.1 ms and a PLQY of up to 35% (Fig. 24B). These nanoparticles substantially improved both luminescence efficiency and lifetime, with TADF lifetimes extending to several hundred microseconds. This enabled rapid LLIM using a time-resolved luminescence microscope. The efficient luminescence facilitated *in vivo* time-gated luminescence imaging, effectively eliminating interference from biological autofluorescence, as illustrated for an example zebrafish subject (Fig. 24C–E). This technique allowed for both long-lived luminescence and cost-effective imaging,

which provides opportunities for real-time detection of biological processes in various organisms, even in the presence of high autofluorescence.

Zhou and colleagues investigated aggregation-regulated TADF. They proposed new methodologies and strategies for designing two-photon fluorescent TADF materials tailored for time-resolved biological imaging, as depicted in Fig. 25.[174] They found that aggregation impacted the internal conversion decay rate and affected both the ΔE_{ST} and rate of ICS. By carefully selecting substituent groups, they suggested that materials with conventional fluorescence could be engineered into long-lifetime TADF or phosphorescent materials, offering a method for creating extended-afterglow materials. To improve TADF properties for *in vivo* time-resolved imaging, they developed a new two-photon excited TADF material, NI-metaCz, incorporating π-extension in its fluorophore structure. NI-metaCz exhibited a significant two-photon absorption cross-section of 112 GM at 775 nm, which is suitable for biological applications, as well as nearly 100% TADF efficiency, a significant Stokes shift (153 nm), and an extended fluorescence lifetime (50.75 μs).
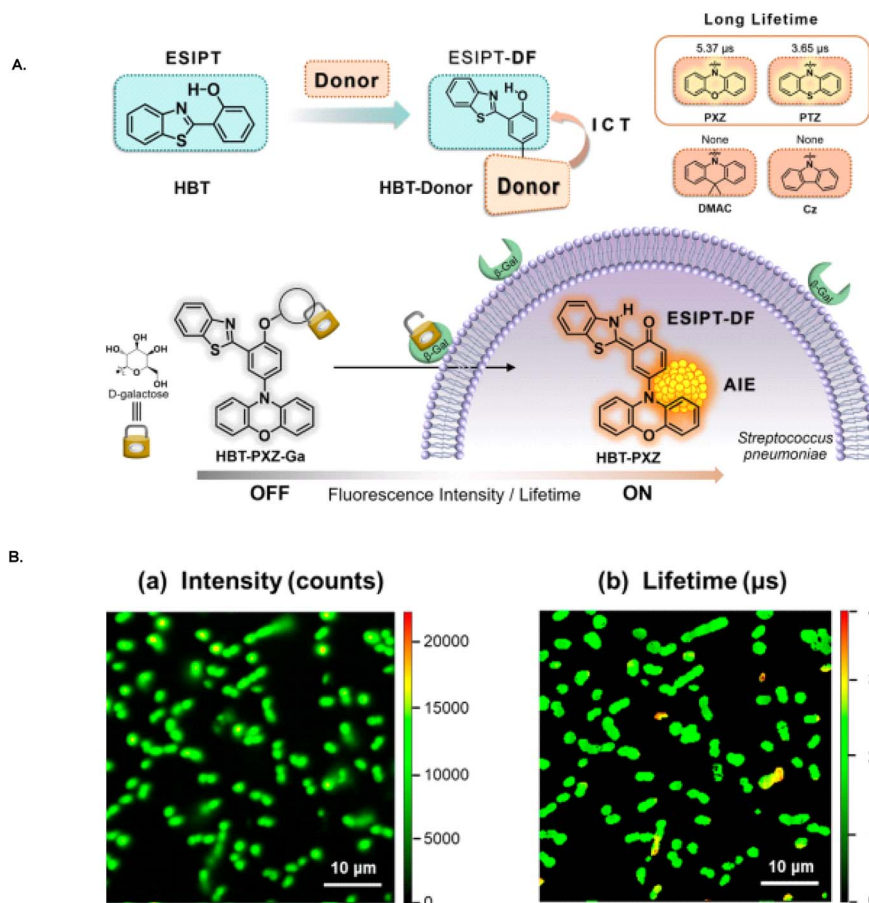
Fig. 23 (A) Schematic illustration of the synthesis and β-gal sensing mechanism of HBT-PXZ-Ga. (B) Fluorescence lifetime imaging of HBT-PXZ-Ga-treated *S. pneumoniae* by (a) fluorescence intensity and (b) lifetime. Excitation wavelength $\lambda_{ex} = 405$ nm (25 000 Hz) Reproduced from ref. 42 with permission from American Chemical Society, Copyright © 2023.
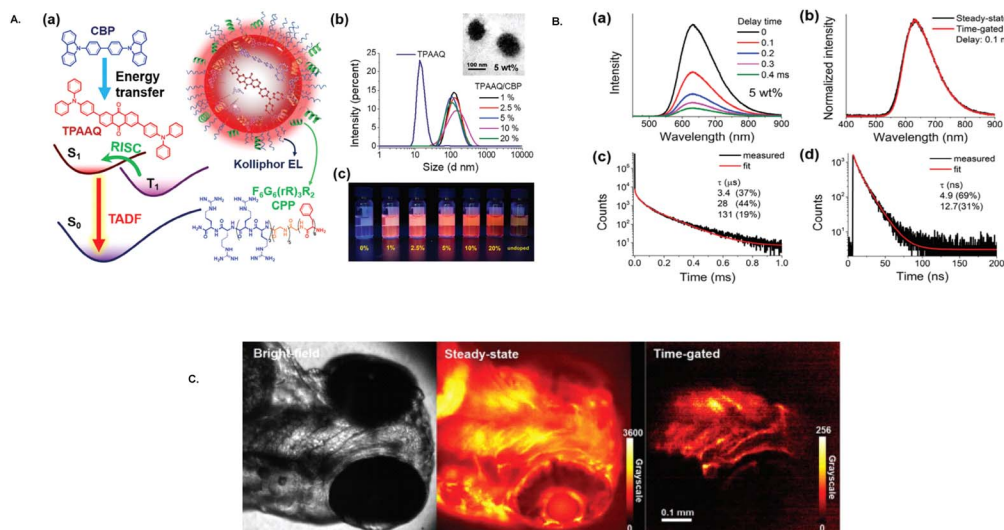

Fig. 24 (A) (a) Representation of TPAAQ/CBP/CPP TADF nanoparticles (b) DLS histograms showing the size of the nanoparticles and inset TEM images showing their morphology. (c) Photographs of the nanoparticle solutions under UV irradiation. (B) Time-gated emission spectra of the nanoparticles at various delay times. (C) Imaging of zebrafish incubated with TPAAQ/CBP/CPP nanoparticles, where the bright field is displayed on the left side of the figure, the steady-state luminescence is shown in the middle, and the time-gated luminescence is displayed on the right. Reproduced from ref. 173 with permission from John Wiley & Sons, Copyright © 2024, Wiley-VCH Verlag GmbH & Co. KGaA, Weinheim.
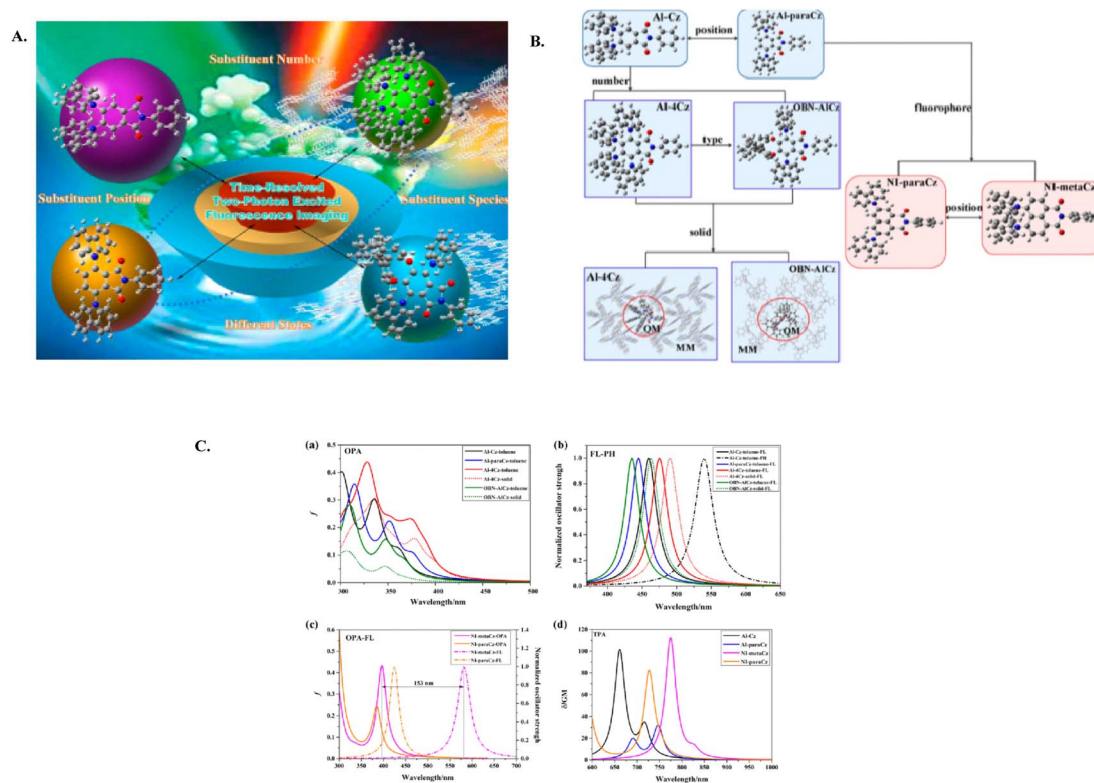
Fig. 25 (A) Design of aggregation-regulated TADF materials (B) diverse architectures of aggregation-regulated TADF materials (C) spectra for (a) one-photon absorption and (b) one-photon fluorescence (c) one-photon absorption and fluorescence of the fluorophores and (d) two-photon absorption. All investigated scaffolds were measured in aqueous solution. Reproduced from ref. 174 with permission from American Chemical Society, Copyright © 2023.

These features make NI-metaCz a highly promising candidate for time-resolved two-photon fluorescence imaging for biological detection.

Hudson and coworkers synthesized luminescent glassy organic dots (g-Odots), as potential bioimaging nanoparticles due to their exceptional luminescence intensity and stability afforded by their rigid glassy structure (Fig. 26A).[175] The emission wavelength of g-Odots can be easily adjusted by encapsulating different hydrophobic fluorophores within the glassy matrix. This versatility is particularly beneficial in combination with phosphorescent or TADF dyes, enabling time-gated fluorescence imaging while protecting the emitters from oxygen. However, controlling the size of g-Odots, a critical factor for cellular uptake and metabolism, has not been thoroughly explored. In this study, methods for controlling g-Odot size while maintaining their glassy interior were investigated. The approaches included precipitation into "aggregated Odots" (a-Odots), then annealing the glassy host material post-synthesis to maintain the glass transition temperature (T_g) of the particles, and adjusting the host-to-surfactant ratios to achieve tunable particle sizes. These findings enhanced the tunability of g-Odot sizes for bioimaging experiments, where narrow size distributions and small average sizes are crucial (Fig. 26B). Additionally, these probes have potential applications beyond cellular imaging, including imaging vascular structures or in

lateral flow assays for point-of-care diagnostics, where robust bright particles are required.

4.1.3. Time-resolved fluorescence biosensing. RISC processes have shown sensitivity to heat and oxygen, which has led to the emergence of TADF materials for applications in temperature and oxygen sensing.[176–179]

Platinum(II) and palladium(II) benzoporphyrin complexes with alkylsulfone groups have been synthesized from inexpensive materials by Borisov *et al.* (2017).[176] Attaching alkylsulfone groups to *meso*-tetraphenyltetrabenzoporphyrin (TPTBP) significantly improves its solubility in organic solvents, photostability, and electron-deficiency, resulting in a redox potential increase of up to 0.65 V compared to the unmodified porphyrin. These modified dyes show strong absorption in the blue (440–480 nm) and red (620–650 nm) regions and exhibit intense room-temperature phosphorescence in the near-infrared (NIR) spectrum, with quantum yields reaching up to 30% in solution, as illustrated in Fig. 27. Palladium(II) complexes of these dyes display efficient TADF at room temperature, with TADF efficiency rising with temperature to a maximum of 27% at 120 °C for the Pd–O–S and Pd–T–I complexes. The TADF observed is notably stronger than that of advanced porphyrin complexes due to a reduced singlet–triplet energy gap. The ratiometric temperature dependence of the TADF emission allows for dual temperature and oxygen sensing using a single emitter. The photophysical properties of these porphyrins render them
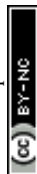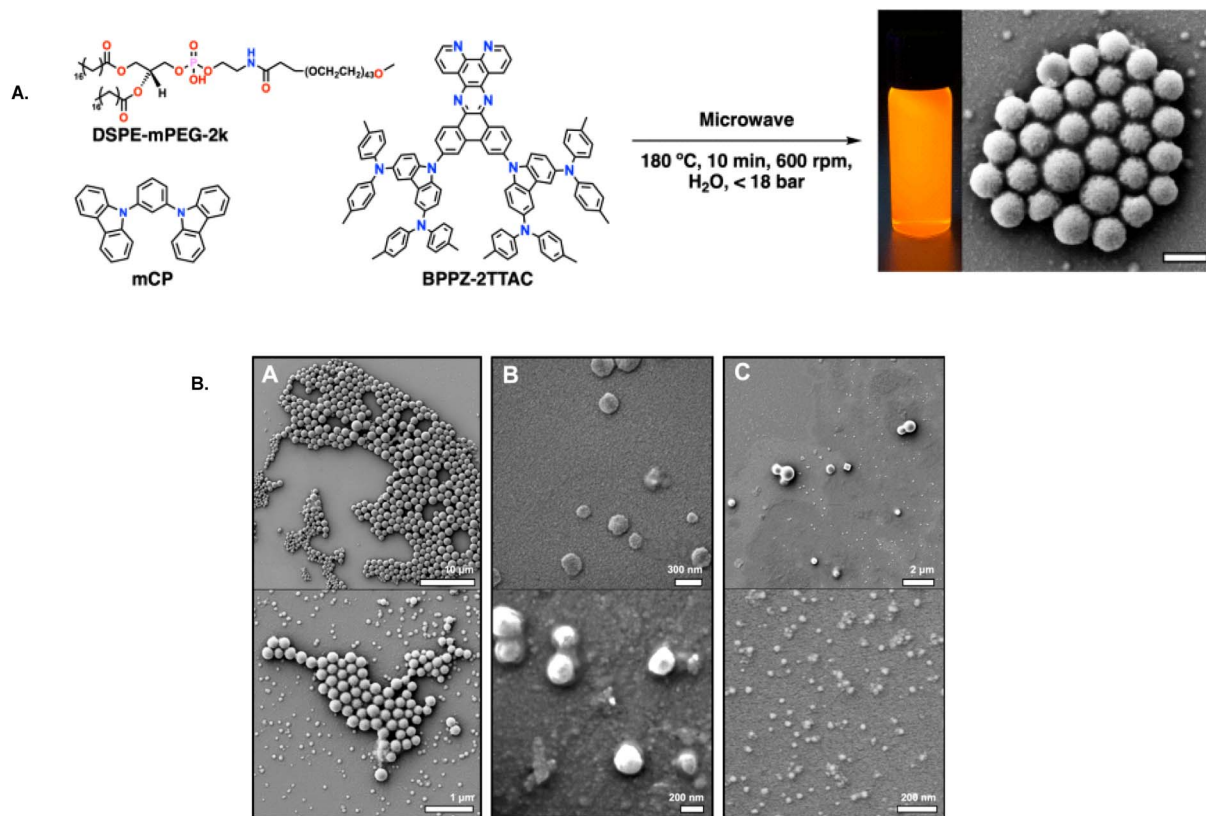
Fig. 26 (A) (Left) Synthetic procedure for g-Odots, showing a suspension of particles under 365 nm excitation in water (5.3 × 10⁹ particles per mL). (Right) SEM image of obtained particles: 2.00 kV accelerating voltage, 402 40× magnification, 300 nm scale bar (B) SEM images of (A) g-Odots synthesized by the standard oil-in-water emulsion method, (B) a-Odots prepared by nanoprecipitation, and (C) annealed a-Odots. Reproduced from ref. 175 with permission from American Chemical Society, Copyright © 2024.

suitable for various photonic applications, including organic light-emitting diodes (OLEDs), photovoltaics, and two-photon imaging of oxygen in biological samples. The TADF feature is particularly advantageous for imaging, as it separates the emission spectrum from the NIR excitation spectrum. This prevents overlap between the excitation and emission spectra, which is a limitation of current phosphorescent probes.

Hudson and coworkers developed a series of TADF-emitting monomers, achieving quantum yields up to 96% and a range of colors from blue to orange (see Fig. 28).[177] These monomers contained an oxadiazole core as the acceptor and were polymerized using Cu(0)-mediated reversible deactivation radical polymerization (Cu(0)-RDRP). This technique resulted in copolymers with low dispersity (1.10–1.45) and high molecular weights (Mn > 20 kDa) using a copper wire catalyst at room temperature. The design incorporated structural constraints to reduce donor–acceptor orbital overlap, which facilitated TADF in the materials. Among the synthesized dendrimer materials, dimethylacridine, phenothiazine, phenoxazine, and carbazole exhibited strong delayed fluorescence, while methylphenazine showed weaker emissions. The phenothiazine-based emitter demonstrated dual emission properties suitable for ratiometric oxygen sensing at 516 nm relative to 396 nm for varying oxygen concentrations. The results demonstrate how the emission intensity at 516 nm changes with different levels of oxygen,

showcasing the material's sensitivity to oxygen concentration. The researchers also created water-soluble polymer dots by coprecipitation with amphiphilic surfactants. The photophysical properties of these polymer dots in the precipitated state were similar to those in the solid state, displaying ratiometric oxygen sensing and longer fluorescence lifetimes. Overall, these oxadiazole-based polymers present a flexible platform for developing multicolor TADF materials using a simple, scalable approach.

Hudson and collaborators also developed a TADF monomer by integrating a naphthalimide (NAI) acceptor along with a DMAC (dimethylacridine) donor, resulting in TADF emission ranging from orange to deep red.[179] The copolymerization of NAI-DMAC monomer (shown in red) with tBuODA (shown in blue) and a matrix of N-isopropylacrylamide (NIPAM) was employed to prepare a series of thermoresponsive polymers (Fig. 29A). Using Cu(0)-RDRP, they produced TADF-emitting polymers with quantum yields up to 31% in the solid state and 58% in the solution. These dual-emission polymers were capable of switching from red TADF to blue fluorescence by changing the temperature from room temperature to 70 °C, with a ratiometric thermal sensitivity of 32 ± 4% K⁻¹ (Fig. 29B). These characteristics make these red TADF polymers suitable for applications in temperature sensing, drug delivery vehicles, biosensing and bioimaging.
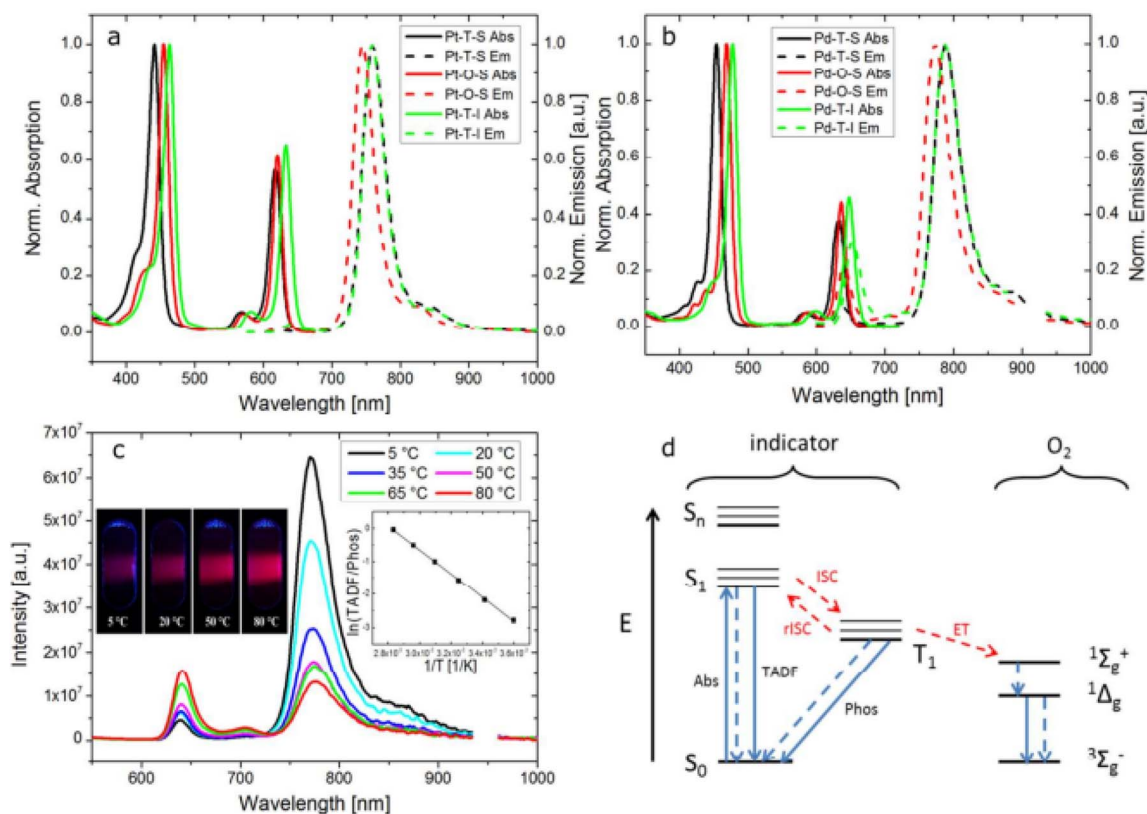
Fig. 27 Absorption and emission spectra of (a) Pt(ii) and (b) Pd(ii) complexes. (c) Pd−O−S emission spectra in anoxic toluene. (d) Schematic illustration of the photoluminescence processes of the tested complexes. Reproduced from ref. 176 with permission from American Chemical Society, Copyright © 2017.
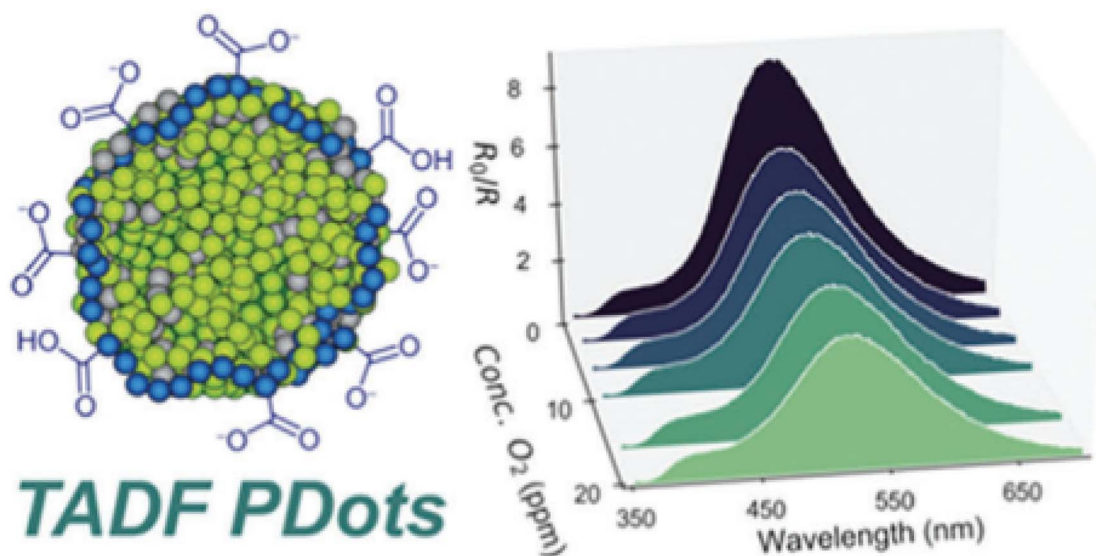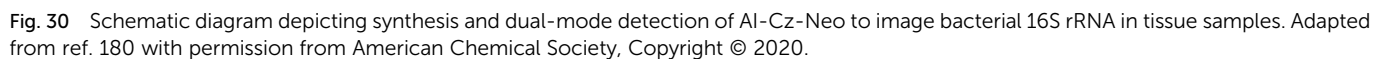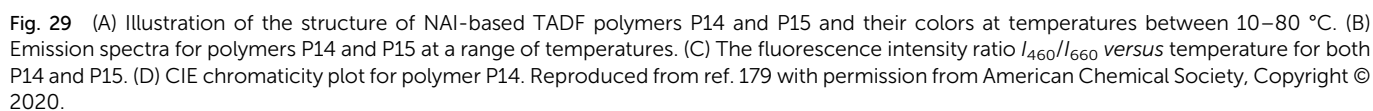

Fig. 28 (Left) TADF polymer dots (PDots) with the green-emitting PTZ-ODA0.15 (in green) and blue-emitting PSMA components (in blue). (Right) The emission intensity of PTZ-ODA0.15 at 516 nm relative to 396 nm was measured under varying oxygen concentrations. Reproduced from ref. 177 with permission from American Chemical Society, Copyright © 2020.

Hu and colleagues created a water-soluble TADF probe named AI-Cz-Neo by attaching a TADF emitter to neomycin, which specifically targets bacterial 16S ribosomal RNA.[180] This probe (**49**) was effectively used for dual-mode detection of bacterial 16S rRNA, employing both conventional fluorescence imaging and fluorescence lifetime imaging. The probe could be

Fig. 29 (A) Illustration of the structure of NAI-based TADF polymers P14 and P15 and their colors at temperatures between 10–80 °C. (B) Emission spectra for polymers P14 and P15 at a range of temperatures. (C) The fluorescence intensity ratio I_{460}/I_{660} *versus* temperature for both P14 and P15. (D) CIE chromaticity plot for polymer P14. Reproduced from ref. 179 with permission from American Chemical Society, Copyright © 2020.

Fig. 30 Schematic diagram depicting synthesis and dual-mode detection of Al-Cz-Neo to image bacterial 16S rRNA in tissue samples. Adapted from ref. 180 with permission from American Chemical Society, Copyright © 2020.

detected in *Staphylococcus aureus* bacteria *via* confocal fluorescence microscopy and TRFI in cells and tissues (Fig. 30). This innovation provides a dependable method for diagnosing bacterial infections through dual-mode imaging.

Zhu and colleagues recently developed a 3D ratiometric luminescent sensor by incorporation of a D–A–D′ moiety.[181] These TADF molecules are capable of emitting both fluorescence and DF phenomena. This sensor distinguishes environmental polarity by varying the TADF wavelength and lifetime while keeping fluorescence constant. To assess the sensor's practical diagnostic potential, they fabricated simulated membranes with self-assembly into micelle nanostructures by phospholipids (PLs) and cholesterol (Chol) with TADF-3, while varying the Chol content to alter the polarity. The luminescence of TADF-3 in these micelles enabled quantitative detection of polarity changes, as illustrated in a 3D plot diagram (Fig. 31). This TADF-based sensing approach was also validated at the cellular level, demonstrating its potential for detecting cholesterol-related membrane abnormalities.

4.1.4 $^1O_2$ **generation for PDT.** Photodynamic therapy (PDT), which is a clinical method first approved by France, Germany, The Netherlands, Japan, Canada, and the United States in 1993, offers a non-invasive, highly specific treatment approach with negligible drug resistance and low side effects.[182] It has since become a leading technique in cancer therapy due to these significant advantages.[183–190] In photodynamic therapy (PDT), photosensitizers (PSs) absorb photons, leading to their excitation. This energy is then transferred to ground-state triplet oxygen ($^3O_2$), converting it into singlet oxygen ($^1O_2$), which induces damage to tumor cells.[191–194]

Lee and colleagues have pioneered organic nanostructures incorporating TADF emitters featuring a small ΔE_{ST}, which facilitates efficient ISC and were employed to generate photo-excited singlet oxygen ($^1O_2$).[195] They prepared donor–acceptor composite NPs by combining two non-TADF donors with an acceptor. While both NPs exhibited high exciplex emission, only one demonstrated TADF, leading to enhanced $^1O_2$ production. This research shows that D:A composite NPs with TADF properties can be derived from non-TADF components, expanding the range of available TADF materials without additional synthesis. *In vitro* MTT assays confirm the potential of these TADF-based nanostructures for photodynamic therapy (PDT). These findings suggest that water-dispersible TADF
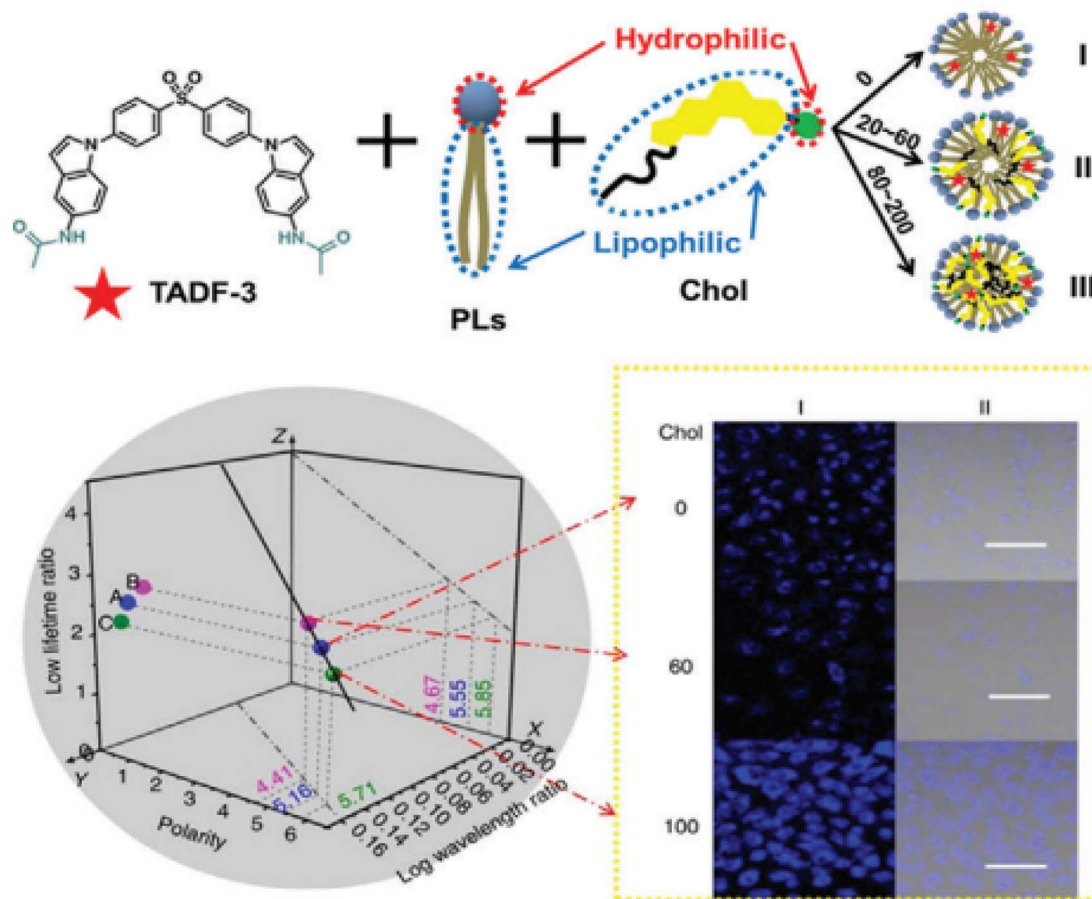

Fig. 31 (Top) Design of TADF-3-based nanostructured membranes with varying cholesterol contents to self-assemble into micelles containing phospholipids (PLs) and cholesterol (Chol). (Bottom) A 3D plot diagram of sensing using TADF-3-based micelles within simulated membrane environments. Reproduced from ref. 181, https://doi.org/10.1038/s41467-019-08684-2, under the terms of the CC BY 4.0 license, https://creativecommons.org/licenses/by/4.0/.
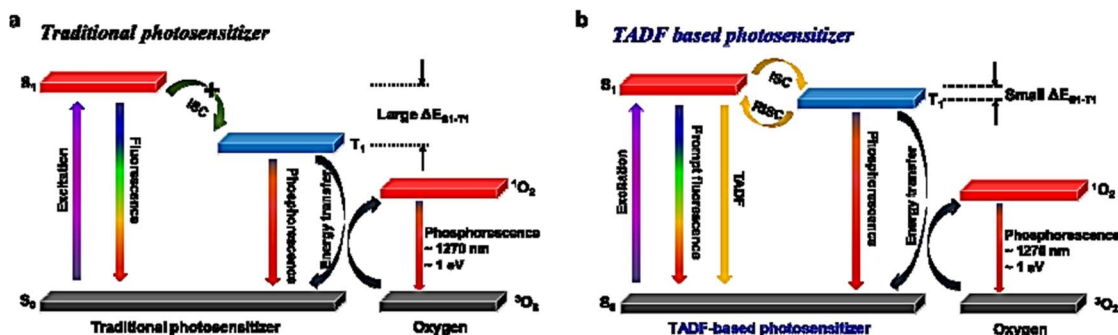
Fig. 32 Modified Jablonski diagram illustrating singlet oxygen production by (a) conventional photosensitization and (b) TADF photosensitization. Reproduced from ref. 195 with permission from the Royal Society of Chemistry.
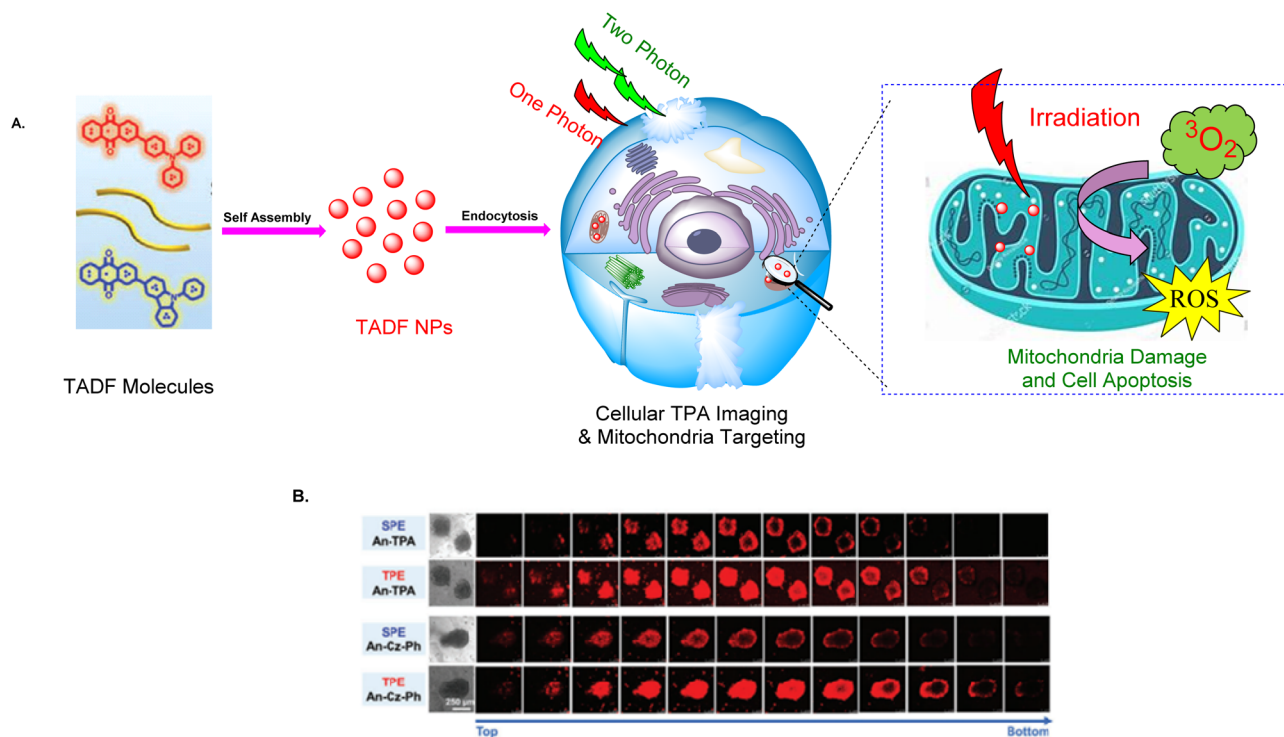

Fig. 33 (A) Diagram depicting the design of TADF NPs for TPE fluorescence imaging and PDT (B) single-photon excitation and TPE penetration depth images of A549. Adapted from ref. 196 with permission from American Chemical Society, Copyright © 2019.

nanostructures could significantly advance the development of novel photosensitizers for biomedical applications (Fig. 32a and b).

To address challenges such as inadequate singlet oxygen ($^1O_2$) quantum yields, limited optical penetration depth, and insufficient organelle targeting in photodynamic therapy (PDT), Lee and colleagues explored TADF emitters with small ΔE_{ST} for developing high-performance, metal-free photosensitizers.[196] Their research introduced two types of TADF emitter-based nanoparticles (TADF NPs) specifically designed for two-photon PDT and fluorescence imaging, as illustrated in Fig. 33A. These TADF NPs offer several key advantages: (1) a high quantum yield (52%) for $^1O_2$, (2) enhanced penetration of NIR due to two-photon activation and (3) effective targeting of mitochondria without additional modifications. These properties enable significant production of reactive oxygen species (ROS) localized to the mitochondria and effective cancer cell cytotoxicity at low light intensities. The development of multifunctional single molecule-based NPs with TADF emission represents a significant advancement in PDT, offering new avenues for creating potent photosensitizers for biomedical applications. As shown in Fig. 33B, two-photon excitation (TPE) imaging of TADF NPs in A549 lung tumor cells exhibited enhanced NIR light penetration relative to single-photon excitation imaging. Additionally, the ability of the TADF NPs to specifically target mitochondria enhances the effectiveness of PDT in cancer therapy.
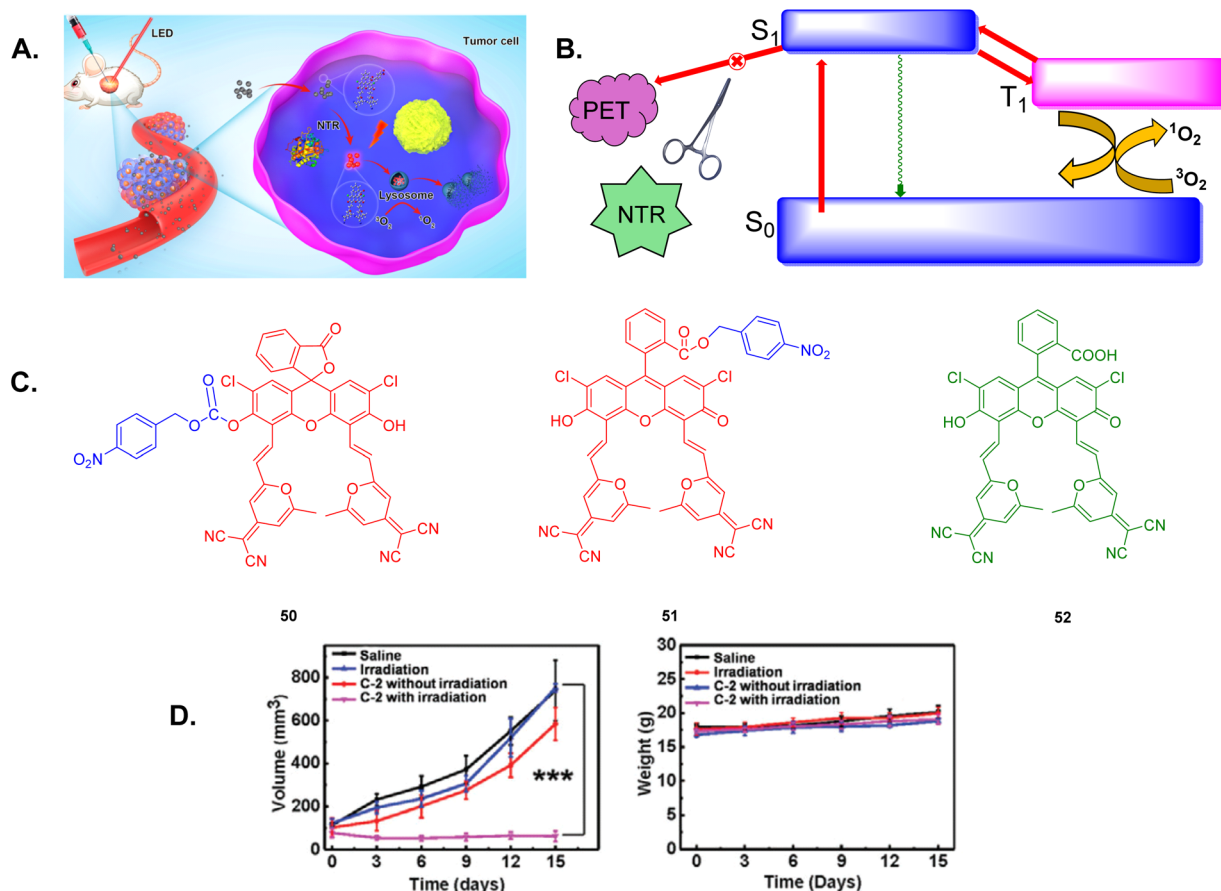
Fig. 34 (A) Diagram depicting TADF fluorescein scaffolds for fluorescence imaging and PDT. (B) PDT process of the TADF in theranostics molecule. (C) Structure of the chemical scaffolds of **50**, **51**, and **52**. (D) PDT effectiveness of **51** in mice.[198] Reproduced from ref. 198 with permission from American Chemical Society, Copyright © 2019.

Lysosomes have emerged as a significant target for improving the effectiveness of PDT. The ROS produced during PDT can damage lysosomes, causing the release of various acid hydrolases. This disruption triggers programmed cell death known as apoptosis in cancer cells, enhancing the overall therapeutic impact of PDT.[197–199] The Peng group synthesized two TADF fluorescein scaffolds, **50** and **51**, for targeted fluorescence imaging and PDT as shown in Fig. 34A and B.[198] These TADF compounds, which specifically target lysosomes, exhibited markedly higher PDT efficacy compared to traditional porphyrin-based photosensitizers even under mild hypoxic conditions. In the absence of NTR inhibition by dicoumarin, **51** is enzymatically converted by nitroreductase (NTR) into **52**, which then activates fluorescence in tumor cells. Additionally, **51** demonstrated remarkable PDT performance and high biosafety in HeLa tumor-bearing mice, as seen in Fig. 34D.

By optimization of exciton dynamics for adjustment of energy distribution in TADF NPs with D–A configurations, their photochemical characteristics can be improved to balance fluorescence imaging and PDT. Lee and colleagues developed two types of TADF nanoparticles, PT NPs and AT NPs, each of which possessed different electron donating groups for modification of ΔE_{ST} and oscillator strength (f). When incorporated

into nanotheranostic agents, PT and AT NPs demonstrated distinct efficiencies in two-photon excitation ($^1O_2$) generation and fluorescence emission (Fig. 35A–C). Specifically, PT NPs, with a smaller ΔE_{ST} and higher f, exhibited superior PDT effectiveness due to more efficient ISC compared to AT NPs, which displayed stronger fluorescence intensity. These nanoparticles could be used to design TADF nanotheranostics optimized for either high-performance PDT or enhanced fluorescence imaging by adjusting ΔE_{ST} and f in TADF materials.[200]

For improvement in the efficacy of TADF materials in PDT, Lee and his team incorporated the effect of heavy atoms in TADF molecule AQCz to create AQCzBr$_2$ photosensitizers, as depicted in Fig. 36.[201] Both AQCz **53** and AQCzBr$_2$ **54** exhibit a small ΔE_{ST} of 0.11 eV. However, AQCzBr$_2$ **54**, due to the heavy-atom effect, had a spin–orbit coupling constant approximately three times that of AQCz. This increased spin–orbit coupling enhanced the ISC process, resulting in a much higher $^1O_2$ quantum yield for AQCzBr$_2$ **54** NPs compared to AQCz NPs (91% vs. 21%). The AQCzBr$_2$ **54** NPs achieved a remarkable 91% $^1O_2$ quantum yield and demonstrated safety and effectiveness as both an in vitro and in vivo PDT agent. These findings highlighted that the incorporation of heavy atoms into TADF
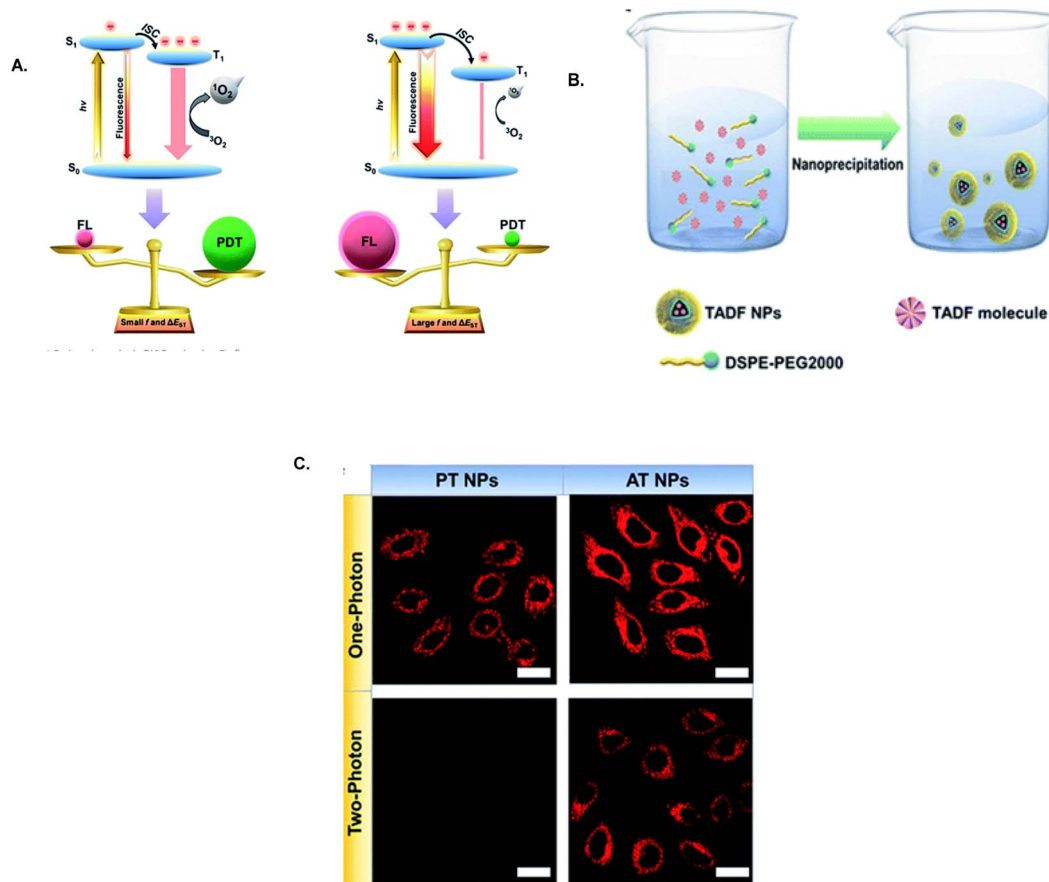
Fig. 35 (A) Illustration of exciton dynamics in TADF-NPs. (B) Preparation of TADF nanoparticles (NPs). (C) SPE and TPE images. Reproduced from ref. 200, https://doi.org/10.1039/C9SC05817F, under the terms of the CC BY 4.0 license, https://creativecommons.org/licenses/by/4.0/.

photosensitizers with inherently small ΔE_{ST} gap is a successful strategy for developing highly efficient photosensitizers, offering valuable insights for future advancements in PDT.

Yan and colleagues designed a new TADF material, BCzSFB, by combining the electron acceptor difluoroboron β-diketonate with the electron donor carbazole, linked through a π-bridged styrene unit, as illustrated in Fig. 37.[202] This D–π–A–π–D structure, approximately 2.4 nm in length, features an exceptionally small ΔE_{ST} of 0.08 eV, a wide absorption spectrum ranging from 350 to 650 nm, and an extended near-infrared (NIR) TADF lifetime when dispersed in aqueous nanoparticles. The singlet oxygen ($^1O_2$) quantum yield of BCzSFB was calculated to be 62%, surpassing that of commercial photosensitizers such as eosin blue and methylene blue. Additionally, it effectively targets and destroys Gram-positive bacteria such as *S. aureus*, with ~100% of cells within 10 minutes under low-intensity white light (60 mW cm^{-2}).

Type I photosensitization addresses the challenge of reduced photodynamic therapy (PDT) efficacy in hypoxic tumors by enhancing electron transfer capabilities. Song and colleagues have demonstrated that encapsulating a TADF photosensitizer (PS) with bovine serum albumin (BSA) significantly boosts Type I PDT, leading to increased generation of superoxide anions ($O_2^{\cdot-}$) as depicted in Fig. 38.[203] In this approach, BSA acts as an

"electron reservoir" while the PS functions as an "electron pump." By combining these functions into a single system, they developed the nano photosensitizer PS@BSA. This Type I PDT system effectively targets tumors under hypoxic conditions and shows promising results in tumor-bearing mice. This strategy provides a significant advancement in improving PDT efficiency for hypoxic tumors.

Tang and colleagues developed a TADF-based zirconium(IV) complex, Zr(^{Mes}PDP^{Ph})$_2$, which exhibited unexpected aggregation-induced emission enhancement (AIEE).[204] This complex demonstrated long-lived luminescence even in air, likely due to reduced oxygen exposure caused by its aggregation, as described in Fig. 39. This theory was supported by DFT calculations, which indicated that the oscillator strengths remained consistent despite variations in the dihedral angles between the benzene groups and the central plane of the ligands. The emission intensity and lifetime of Zr(^{Mes}PDP^{Ph})$_2$ NPs were further improved after deoxygenation. Additionally, DFT calculations showed that the favorable ΔE_{ST} and spin–orbit coupling (SOC) rendered Zr(^{Mes}PDP^{Ph})$_2$ an effective sensitizer. The study confirmed that Zr(^{Mes}PDP^{Ph})$_2$ NPs could function in both Type I and Type II PDT and also act as a photoredox catalyst for NADH oxidation. This catalytic cycle, assisted by the protein cytochrome c, facilitated oxygen-free PDT under hypoxic
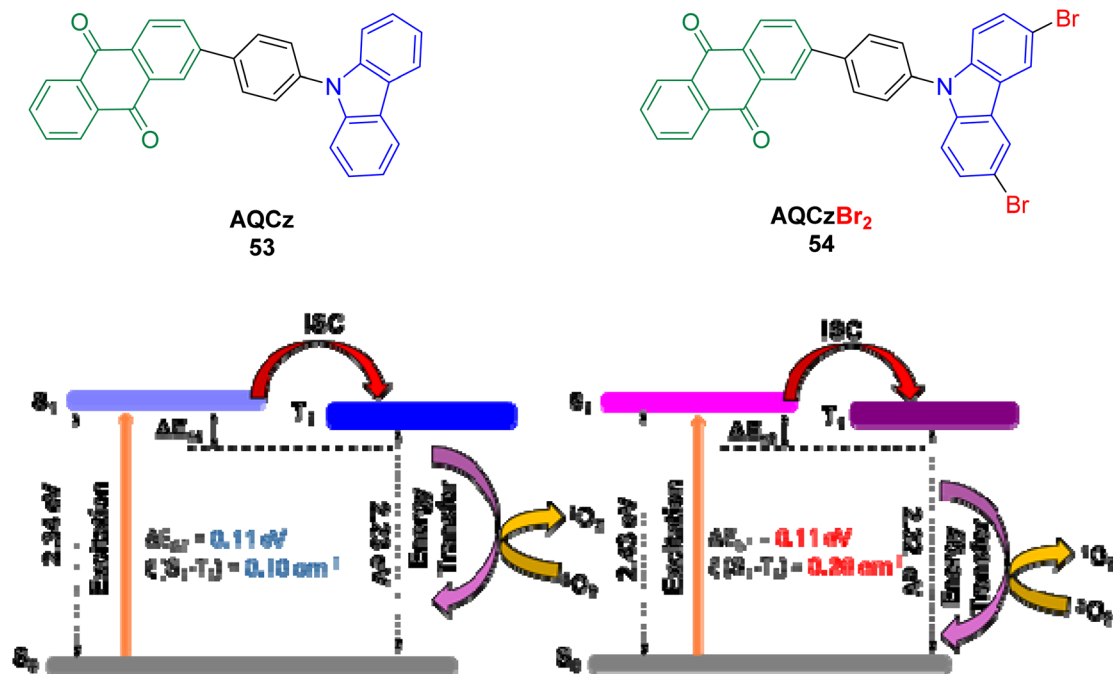
Fig. 36 Chemical structures and $^1O_2$ generation process diagrams of AQCz and AQCzBr$_2$. Adapted from ref. 201 with permission from the Royal Society of Chemistry.
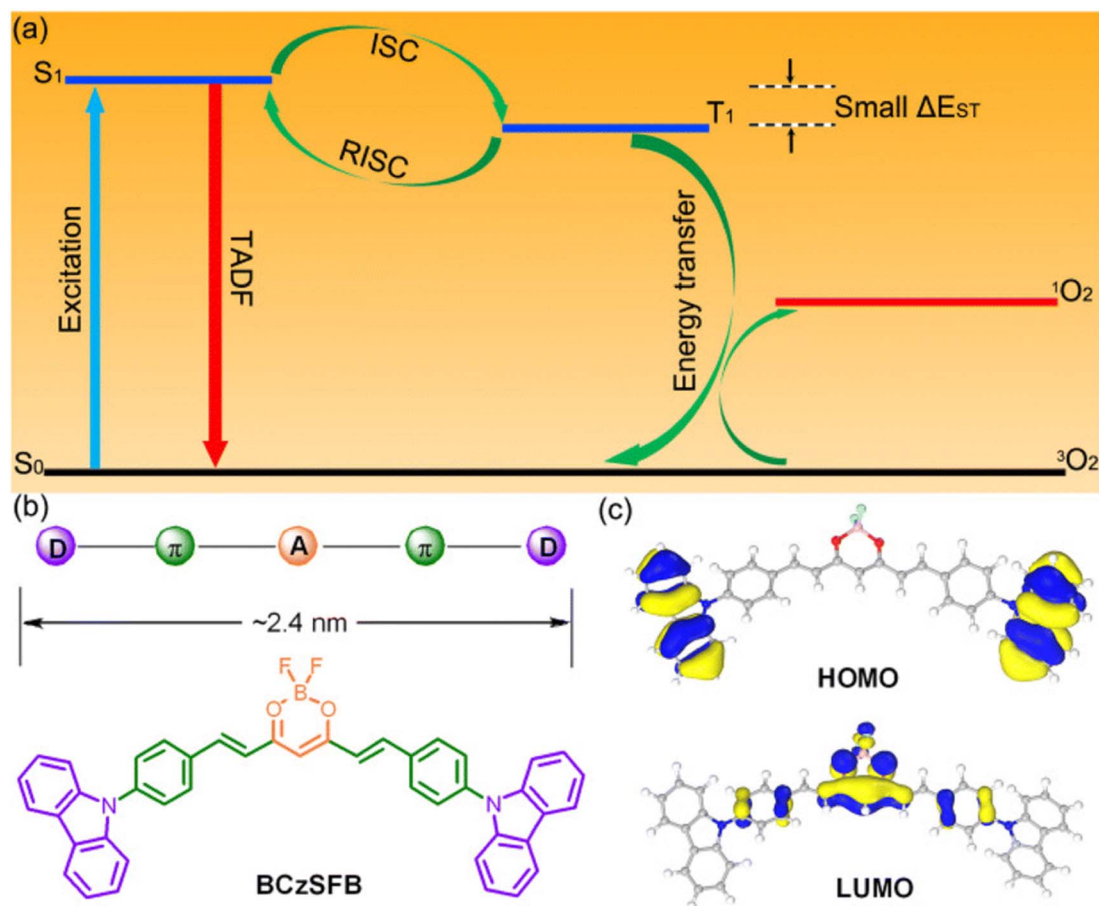

Fig. 37 (a) Schematic representation of a TADF-based photosensitizer for the generation of $^1O_2$. (b) Structure of the BCzSFB nanomolecule. (c) Computationally derived HOMO and LUMO distributions. Reproduced from ref. 202 with permission from the Royal Society of Chemistry.
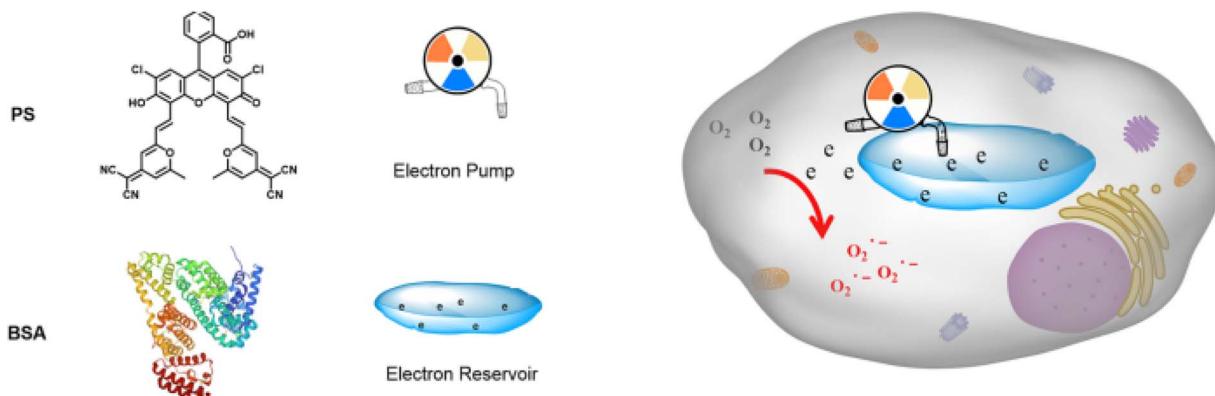
Fig. 38 Illustration of the Type I PDT process. Reproduced from ref. 203 with permission from American Chemical Society, Copyright © 2023.
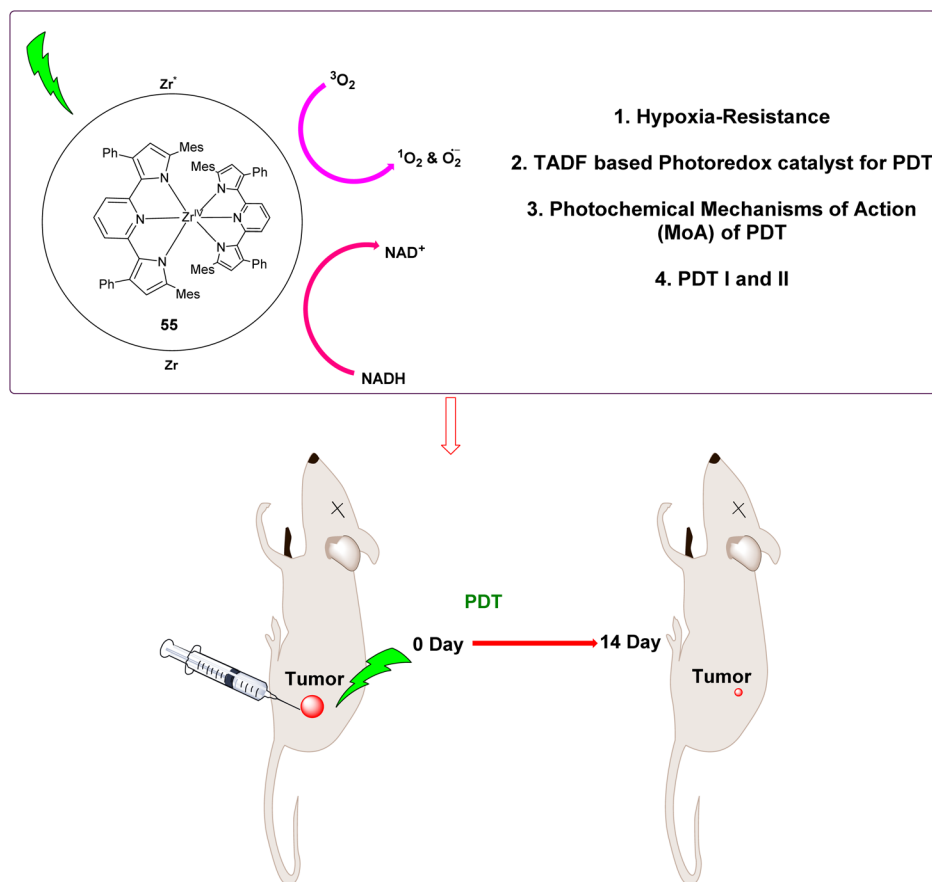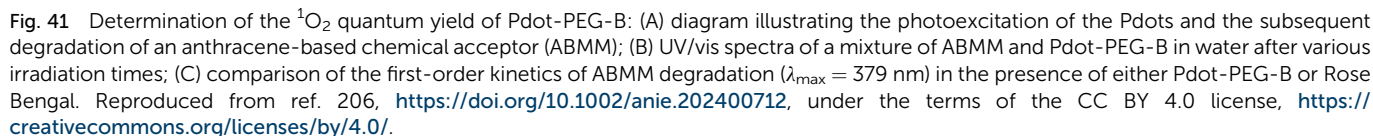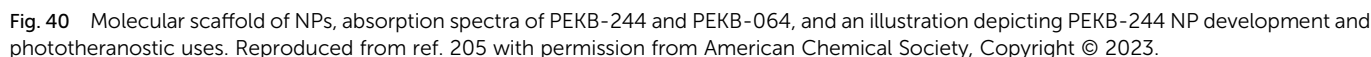

Fig. 39 Schematic representation of the TADF-based photocatalyst Zr(^{Mes}PDP^{Ph})$_2$ NPs and its use in PDT. Reproduced from ref. 204 with permission from American Chemical Society, Copyright © 2023.

conditions. *In vivo* studies demonstrated that Zr(^{Mes}PDP^{Ph})$_2$ NPs effectively inhibited tumor growth with good biocompatibility. This work highlights Zr(^{Mes}PDP^{Ph})^2 as a promising TADF-based photoredox catalyst for overcoming hypoxia in PDT and offers new insights for clinical applications.[204]

Photothermal therapy (PTT) with NIR-emitting conjugated polymers has shown significant capability for tumor treatment, but these polymers exhibited inadequate therapeutic efficacy in light of their weak NIR absorbance and low photothermal conversion efficiency (PCE). Zhou and colleagues developed an innovative approach to enhance the performance of NIR polymeric photosensitizers by integrating TPAAQ into the polymer backbone (Fig. 40).[205] The resulting polymers, known as PEKBs, demonstrate improved PCE and strong NIR absorbance. Among

Fig. 40 Molecular scaffold of NPs, absorption spectra of PEKB-244 and PEKB-064, and an illustration depicting PEKB-244 NP development and phototheranostic uses. Reproduced from ref. 205 with permission from American Chemical Society, Copyright © 2023.

Fig. 41 Determination of the $^1O_2$ quantum yield of Pdot-PEG-B: (A) diagram illustrating the photoexcitation of the Pdots and the subsequent degradation of an anthracene-based chemical acceptor (ABMM); (B) UV/vis spectra of a mixture of ABMM and Pdot-PEG-B in water after various irradiation times; (C) comparison of the first-order kinetics of ABMM degradation ($\lambda_{max} = 379$ nm) in the presence of either Pdot-PEG-B or Rose Bengal. Reproduced from ref. 206, https://doi.org/10.1002/anie.202400712, under the terms of the CC BY 4.0 license, https://creativecommons.org/licenses/by/4.0/.

these, PEKB-244, with an optimal proportion of TPAAQ units, exhibits the highest NIR absorbance and a PCE of 64.5%. Both *in vitro* and *in vivo* studies confirm that these NPs can efficiently destroy cancer cells after irradiation by an NIR laser. This new molecular design strategy promises to advance the design of effective NIR photosensitizers for photothermal therapy of cancer.

Hudson and colleagues described the first synthesis of multifunctional copolymers containing both a TADF luminophore (DMAc) and an oxygen sensitizer (BDP) for theranostics applications.[206] To tune the biological behavior of these materials, "stealthy" polyethylene glycol (PEG) and cell-penetrating guanidinium (BGN) repeat units were incorporated as hydrophilic corona blocks *via* ring-opening metathesis polymerization (ROMP) as shown in Fig. 41. This allowed for the straightforward combination of these components through sequential addition during polymerization. These amphiphilic copolymers can self-assemble into polymer dots (Pdots) that
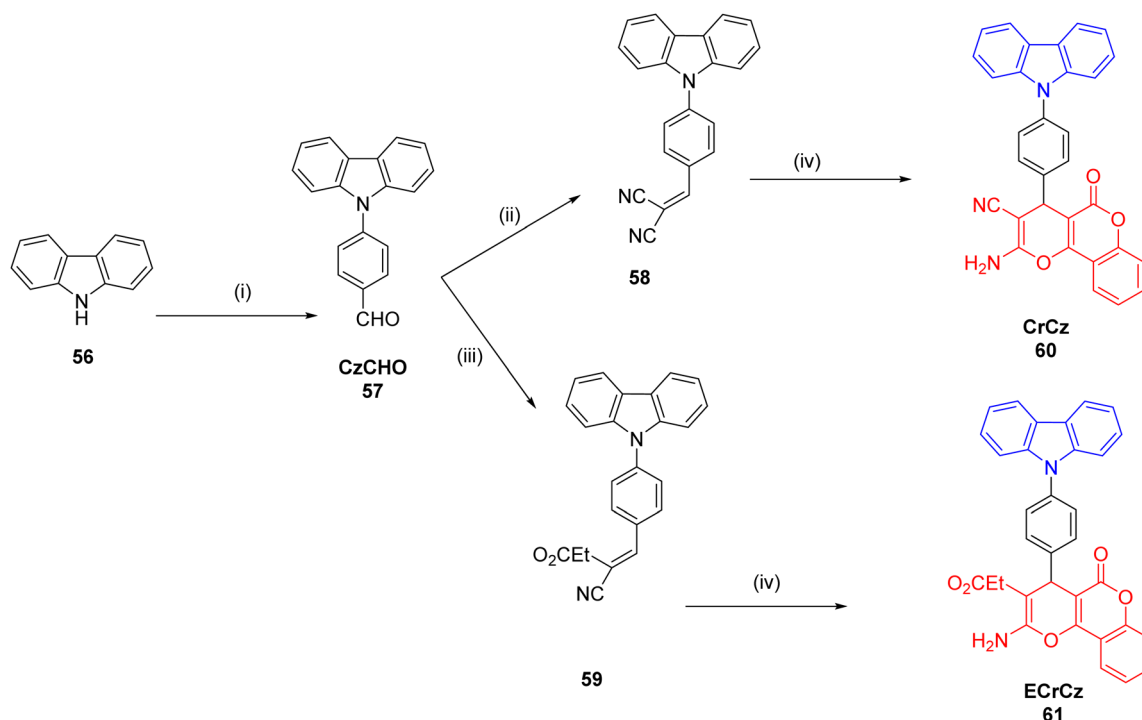
Fig. 42 Synthesis of CrCz and ECrCz starting from 9H-carbazole: (i) 4F-Ph-CHO, K_2CO_3, N,N-dimethylformamide (DMF), 130 °C (ii) $CH_2(CN)_2$, EtOH, reflux; (iii) ethyl cyanoacetate, EtOH, reflux; (iv) 4-hydroxycoumarin, Ni–Np, EtOH.[207]
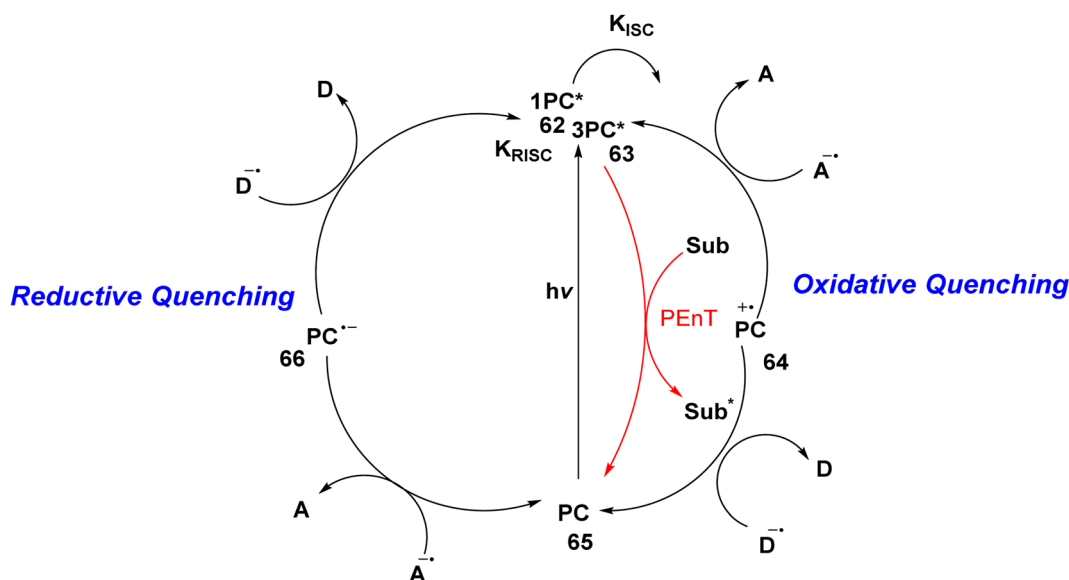

Fig. 43 Photocatalytic cycles of a typical PC with general donor D and acceptor A. Reproduced from ref. 208, https://doi.org/10.1039/D1CS00198A, under the terms of the CC BY-NC 3.0 license, https://creativecommons.org/licenses/by-nc/3.0/.

simultaneously shield the TADF luminophore from the environment while exposing the sensitizer, enabling both delayed emission and singlet oxygen generation. By localizing the BDP sensitizer ($^1O_2$ quantum yield = 76%) in the hydrophilic corona of the Pdots, this design achieves an IC_{50} with only ∼0.05–0.13 μg mL^{-1} of photosensitizer loading and can lead to over 96% cell death upon irradiation (30–50 min, 23 mW cm^{-2}), while maintaining negligible dark toxicity for both PEG- and BGN-

based Pdots. Remarkably, Pdots with PEG *versus* BGN coronas exhibited completely different cellular uptake results, despite the high efficiency of both types in killing cancer cells. Furthermore, the presence of the oxygen sensitizer did not affect the TADF properties of DMAc in the core of the Pdots, achieving orange-red delayed emission (Φ_{PL} = 8–18%) even when exposed to air. The multifunctional BGN Pdots could be used to image HeLa cells following cellular uptake and showed
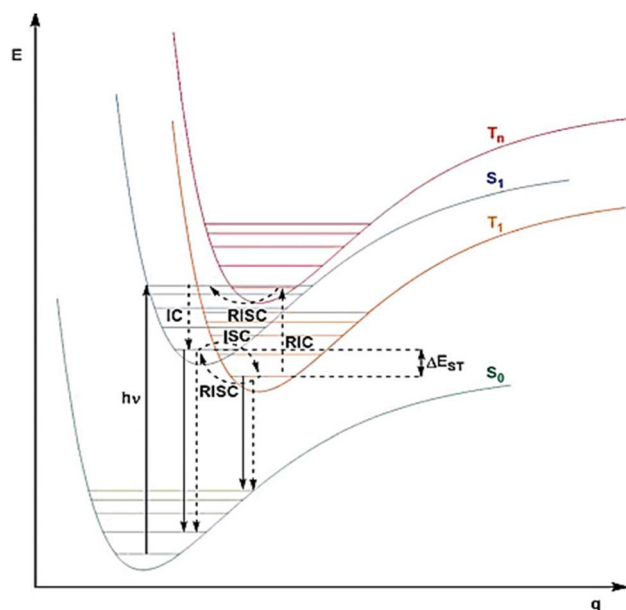
Fig. 44 Jablonski-type graph along Morse potentials illustrating the photophysical mechanism in TADF molecules. Reproduced from ref. 208, https://doi.org/10.1039/D1CS00198A, under the terms of the CC BY-NC 3.0 license, https://creativecommons.org/licenses/by-nc/3.0/.

the potential of these Pdots in time-gated spectroscopy to effectively eliminate the influence of background auto-fluorescence in bioimaging. The use of ROMP also provided a modular synthetic approach where both the emitter and photosensitizer can be selected to absorb and emit at wavelengths best suited for particular clinical applications. Future avenues for exploration include immunolabeling the PEG Pdots to target specific cells or tissues and altering the chemical composition of the parent copolymers to allow for the imaging probe and the oxygen sensitizer to be excited independently.

Barman and colleagues developed a donor–acceptor system featuring a carbazole donor and a 2H-chromene coumarin derivative as the acceptor, which exhibits both AIE and TADF in the solid state, as illustrated in Fig. 42.[207] This system also included a core with a selective affinity for the coronavirus spike protein for antiviral activity against SARS-CoV-2. The team conducted comprehensive photophysical studies to explore the structure–activity relationship structure of this system, focusing on the effect of a cyclic sp^3 spacer between the carbazole and the chromene. This spacer-induced TADF phenomenon had not been extensively investigated previously. Additionally, they modified the molecular framework to incorporate an emissive AIEgenic rotor donor, using cyano (–CN) and ester (–CO₂Et) groups in the acceptor while preserving the overall structure. Their experimental and theoretical work revealed that TADF
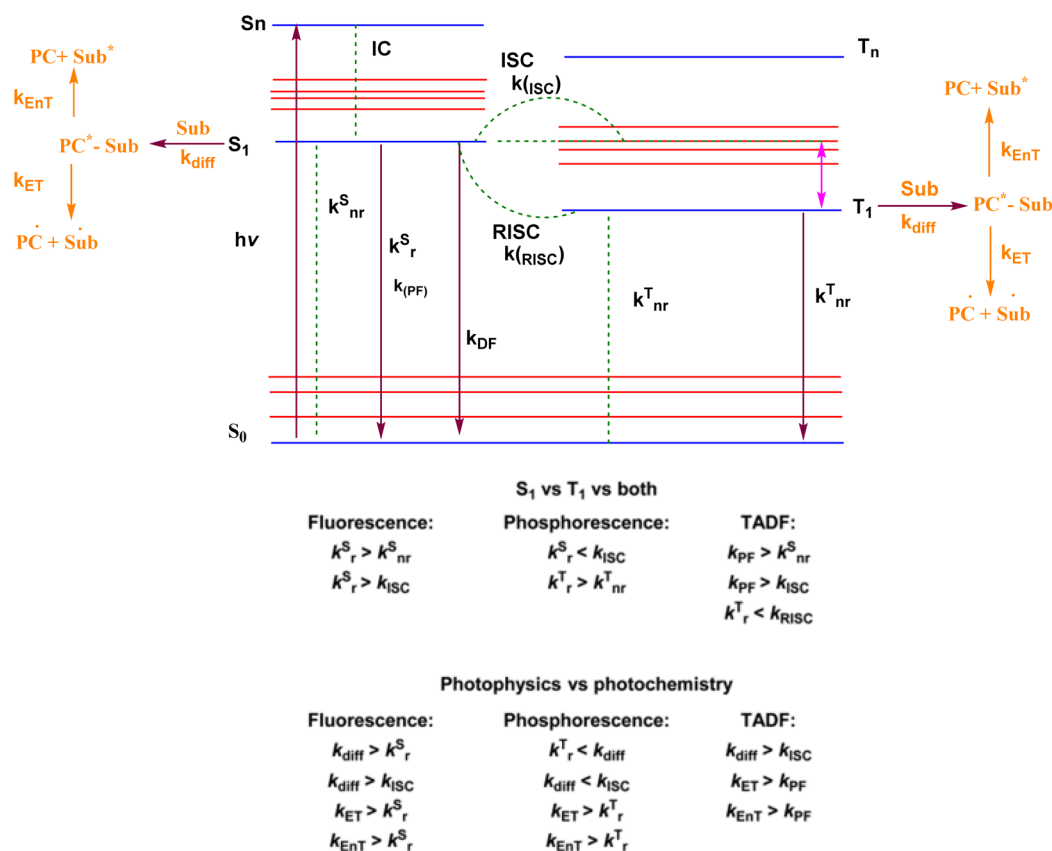

Fig. 45 Jablonski diagram and potential photochemical pathways for excited states of luminescent compounds such as TADF materials. Reproduced from ref. 208, https://doi.org/10.1039/D1CS00198A, under the terms of the CC BY-NC 3.0 license, https://creativecommons.org/licenses/by-nc/3.0/.

A.

4CzIPN
6

B.

[Ir(dF(CF$_3$)ppy)$_2$(dtbbpy)]PF$_6$
67
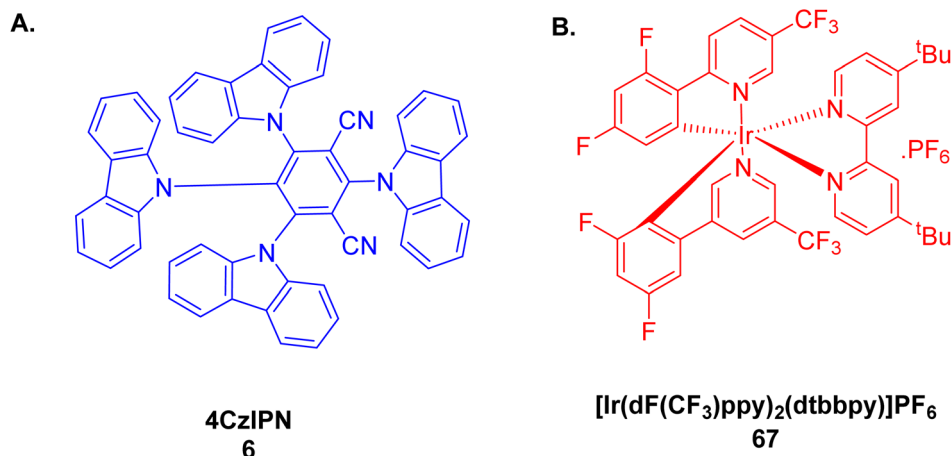
Fig. 46 Chemical scaffold of (A) 4CzIPN and (B) [Ir(dF(CF$_3$)ppy)$_2$(dtbbpy)]PF$_6$.

τ_d = (4CzIPN) = 1.39 μs
τ(Ir) = 2.3 μs

E*$_{red}$ = (4CzIPN) = 1.35 V
E*$_{red}$ (Ir) = 1.21 V

E*$_{ox}$ = (4CzIPN) = -1.04 V
E*$_{ox}$ (Ir) = -0.89 V

Reductive Quenching

Oxidative Quenching

E_{red} = (4CzIPN) = -1.21 V
E_{red} (Ir) = -1.37 V

E_{ox} = (4CzIPN) = 1.52 V
E_{ox}(Ir) = 1.69 V

$E_{0,0}$ = (4CzIPN) = 2.67 eV
$E_{0,0}$(Ir) = 2.58 eV
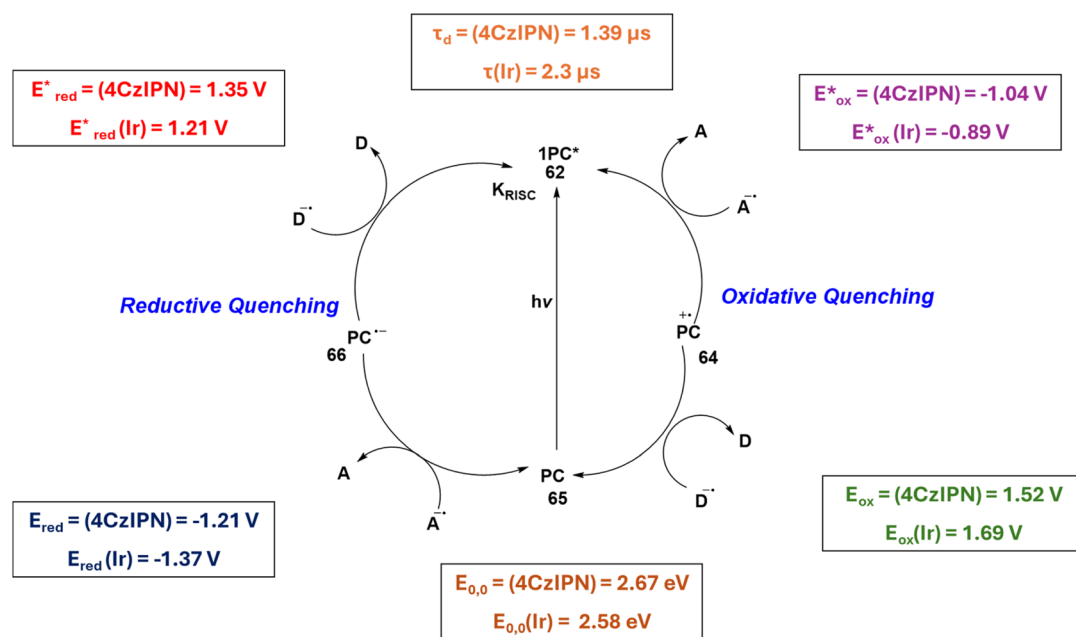
Fig. 47 Photocatalytic cycle comparison of redox and photophysical properties of 4CzIPN. Adapted from ref. 208, https://doi.org/10.1039/D1CS00198A, under the terms of the CC BY-NC 3.0 license, https://creativecommons.org/licenses/by-nc/3.0/.

occurs through two isoenergetic states: ^{1}CT–^{3}CT and ^{1}CT–^{3}LE–^{3}CT. To explore antiviral potential against SARS-CoV-2, they performed molecular docking simulations and selected the fused 2H-chromene coumarin core due to its strong binding with the virus spike protein. This research offers a novel approach to designing AIE-TADF-based antiviral agents by utilizing advanced concepts of aggregation and triplet-state harvesting in purely organic materials.

4.2. Thermally delayed fluorescence materials as photocatalysts

Detailed applications of TADF material as a photocatalyst have previously been described by Zysman-Colman et al. in a comprehensive review in 2021.[208] In this section, we will

instead describe new research into applications of TADF materials as photocatalysts from 2021 to 2024.

4.2.1. Photocatalysis. Photocatalysis harnesses light energy to drive chemical reactions, utilizing materials that are light-absorbing to enhance the rate of reaction. From 2007, a resurgence of interest in this field, was driven by key contributions from researchers like MacMillan, Yoon, and Stephenson.[209–211] Their groundbreaking work demonstrated that photoactive organometallic complexes could effectively catalyze valuable organic transformations. This renewed focus has expanded the applications of photocatalysis, leveraging advancements in photoactive materials to achieve innovative and efficient reaction processes. The advancement of photocatalysis has transformed it from a specialized technique into a broadly adopted
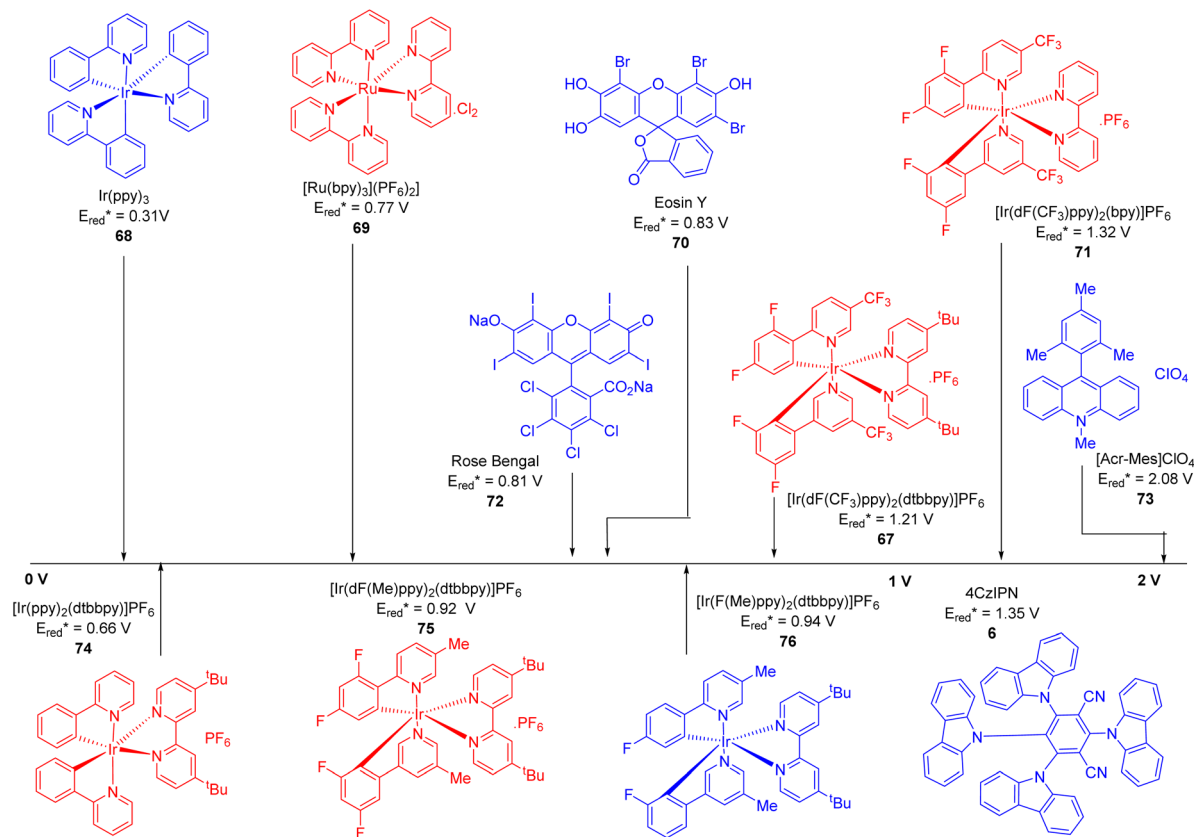
Fig. 48 E_{red}^* of common visible light PCs. Reproduced from ref. 208, https://doi.org/10.1039/D1CS00198A, under the terms of the CC BY-NC 3.0 license, https://creativecommons.org/licenses/by-nc/3.0/.

and valuable synthetic strategy. This approach enables the fabrication of greener, cost-effective reactions that operate under mild conditions, providing a substantial advantage over conventional catalytic methods. Photocatalysis also facilitates the generation of products that are otherwise inaccessible through thermal methods and produces reactive intermediates under mild conditions. This capability allows for novel transformations and enhances overall reaction efficiency.

Upon light absorption, the photocatalyst transitions to the excited state PC*, allowing photoinduced electron transfer (PET) and photoinduced energy transfer (PEnT) between the excited photocatalyst and reactant, with the PET and single electron transfer (SET) mechanisms involved as shown in Fig. 43 for photocatalysts 62–66. When PET is active, the process is known as photoredox catalysis. Photocatalysts (PC) undergo selective photoexcitation in the presence of organic reactants, which leads to the formation of products. As many organic substrates are transparent in these regions, it is preferred to use a PC that absorbs in the visible or near-UV regions. Using PCs that require higher energy for photoexcitation increases the risk of direct homolytic bond cleavage in the PC as well as organic substrates, leading to undesired side reactions and reduced process efficiency. Maximizing the yield of excited state formation requires consideration of both the quantum yield and the absorption cross-section of the photocatalyst, which is influenced by its concentration as well as its molar extinction

coefficient (ε). For the reactions that do not involve the radical chain mechanism, their quantum yield $\Phi(\lambda)$ ideally approaches 1 (100%) for a photocatalytic process as given in eqn (2).[212]

$$\Phi = \frac{(\text{mol of product formed})}{(\text{mol of photons absorbed})} \quad (2)$$

Additionally, the excited state PC* should have a lifetime on the nanosecond scale or greater to overcome the diffusion processes which lead to the formation of encounter complexes in biomolecular reactions.[213–217]

4.2.2. TADF compounds as photocatalysts. TADF compounds are a significant class of inorganic, organic, and organometallic photocatalysts.[218,219]

Upon photoexcitation, the S_1 state is quickly filled. Radiative decay then takes place with the assistance of DF, defined as prompt fluorescence (PF) with a lifetime on the nanosecond scale, similar to typical fluorescent compounds. The competing pathways include ISC or the triplet layer non-radiative decay back to the S_0 to populate the T_0 to T_1 states. Phosphorescence from the triplet state is spin-forbidden and not observed at room temperatures due to a large $\Delta E_{S_0-T_1}$ energy gap (eqn (3)).

$$\lambda \propto \frac{H_{so}}{\Delta E_{ST}} \propto \frac{Z^4}{n^3} \quad (3)$$

However, RISC from T_1 to S_1 can occur at atmospheric temperatures as a result of low ΔE_{ST}, which can be thermally overcome, resulting in DF that manifests on a timescale similar to phosphorescent complexes, usually in the microseconds range.[17] The RISC mechanism is facilitated by spin-vibronic coupling as depicted in Fig. 44. Fig. 45 shows that the rate constant for prompt fluorescence (k_{PF}) is larger compared to those for ISC (k_{ISC}) and non-radiative decay from the singlet
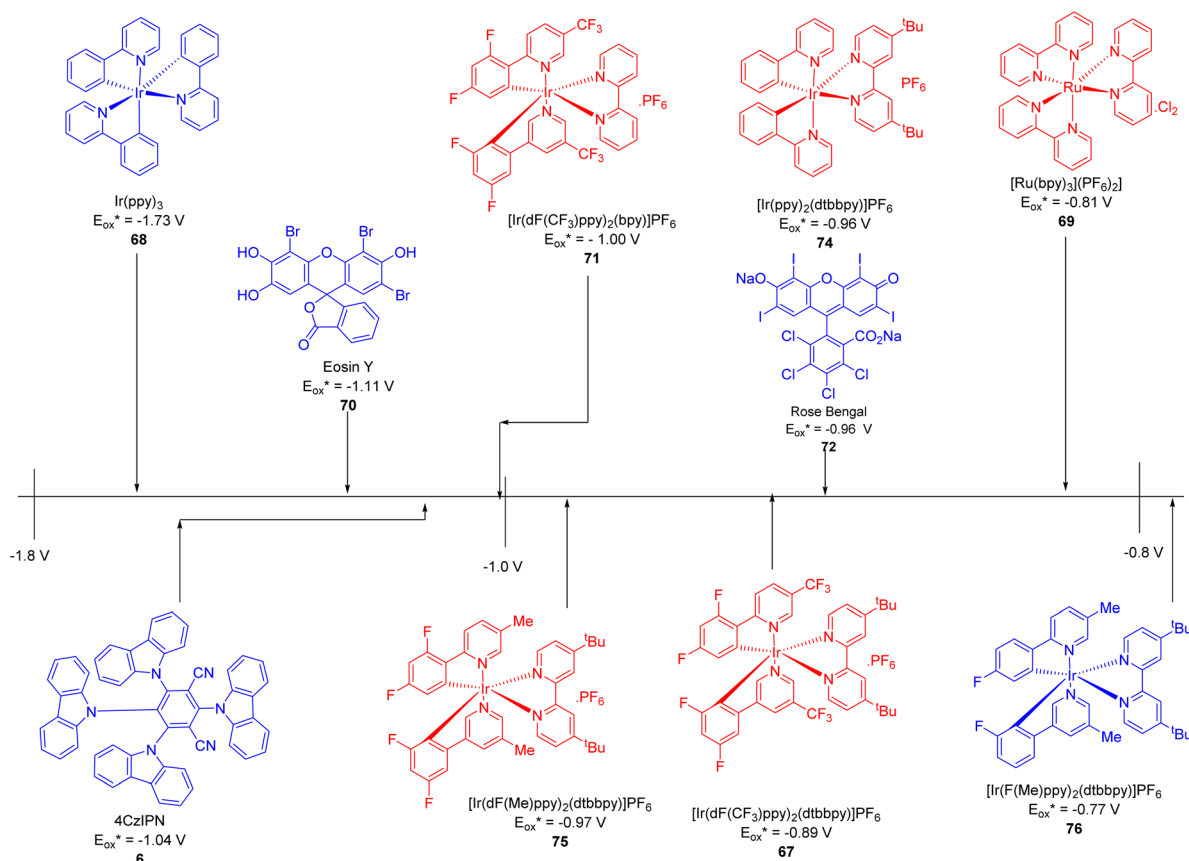

Fig. 49 E_{ox}^* of common visible light PCs. Reproduced from ref. 208, https://doi.org/10.1039/D1CS00198A, under the terms of the CC BY-NC 3.0 license, https://creativecommons.org/licenses/by-nc/3.0/.
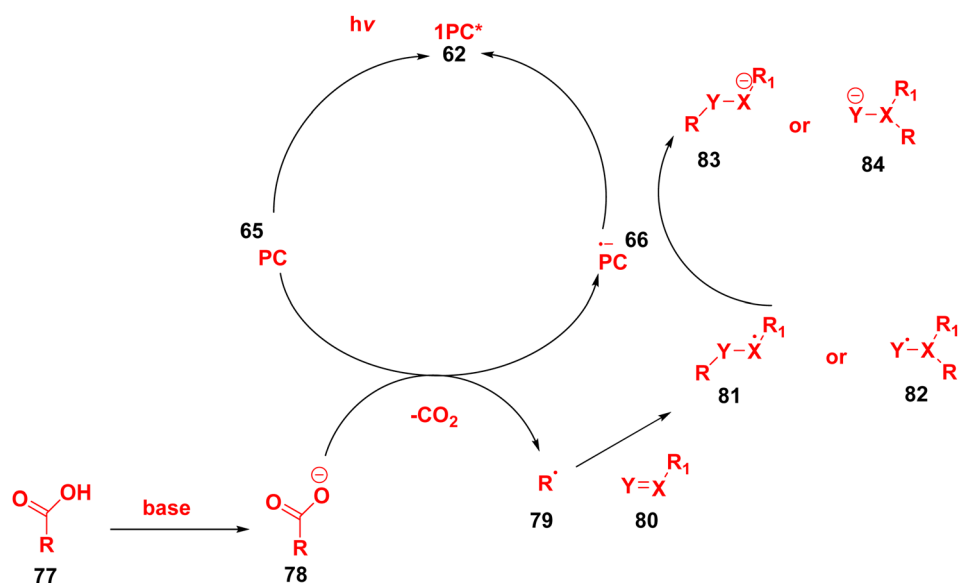

Fig. 50 The catalytic cycle for photoinduced oxidative decarboxylation *via* a radical addition mechanism.[232]

state (k_{nr}^S). DF occurs because k_{RISC} is more rapid than both the radiative (k_r^T) and non-radiative (k_{nr}^T) decay rates from the triplet state.[208]

For organic TADF compounds, the k_{ISC} is generally below 10^{-7} s^{-1}. However, k_{ISC} can vary significantly depending on the specific compound. In these materials, k_{ISC} is typically slower than the diffusion rate constant (k_{diff}), which enhances the likelihood of PET and PEnT from the S_1. In TADF compounds with a faster rate of k_{ISC}, the triplet state manifold can also contribute to photocatalytic processes. In such scenarios, the quantum yields for PF (Φ_{PF}) and DF (Φ_{DF}) are crucial for assessing the availability of S_1 and T_1 excited states and thereby determining the probabilities of PET and PEnT from each state.[208]

Photocatalysis occurs from an excited state that depends on the k_{ISC} and k_{RISC} in TADF PCs. The reaction rates that are related to ISC/RISC are defined by the given mathematical eqn (3), where the rate constants depend on both the ΔE_{ST} and spin–orbit coupling. Organic TADF compounds are characterized by ΔE_{ST} values lower than 0.3 eV,[220] which influence the extent of state mixing.[221] The ΔE_{ST} is directly related to the J (exchange integral) between the excited singlet and triplet states, as expressed in eqn (4).[220,221] The dependence of J on the orbital overlap of the FMO involves transitions to S_1 and T_1, as shown in eqn (5). Here, Ψ and Φ typically represent the HOMO and LUMO wavefunctions and integration into S_0–S_1 and S_0–T_1 transitions, respectively, and e represents the charge on the electron.
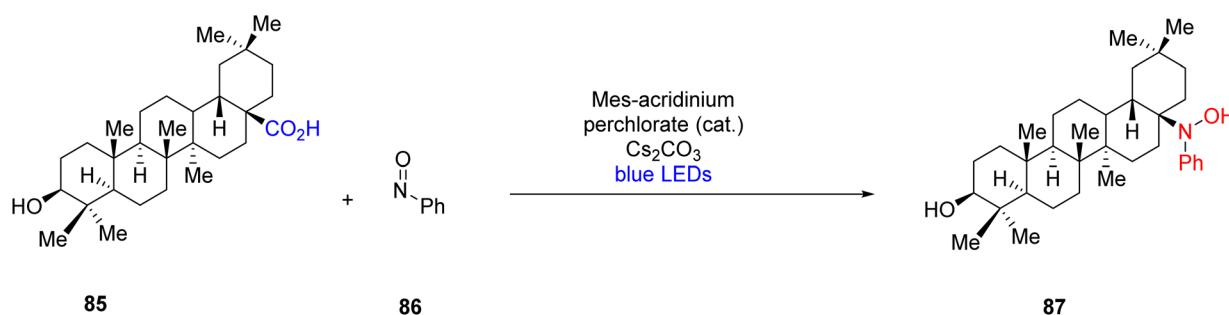

Fig. 51 The synthesis of arylhydroxylamines *via* photoredox catalysis. Reproduced from ref. 233 with permission from Georg Thieme Verlag KG, Copyright © 2018.
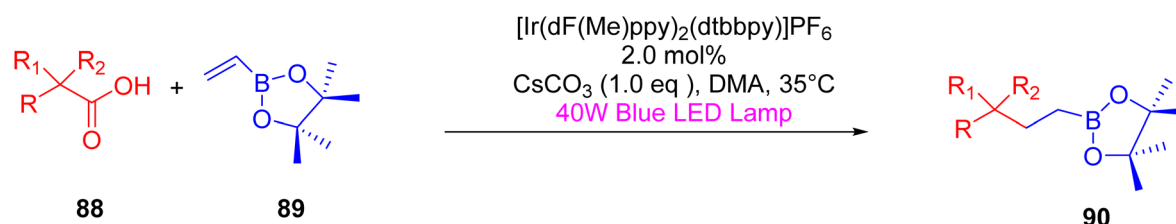

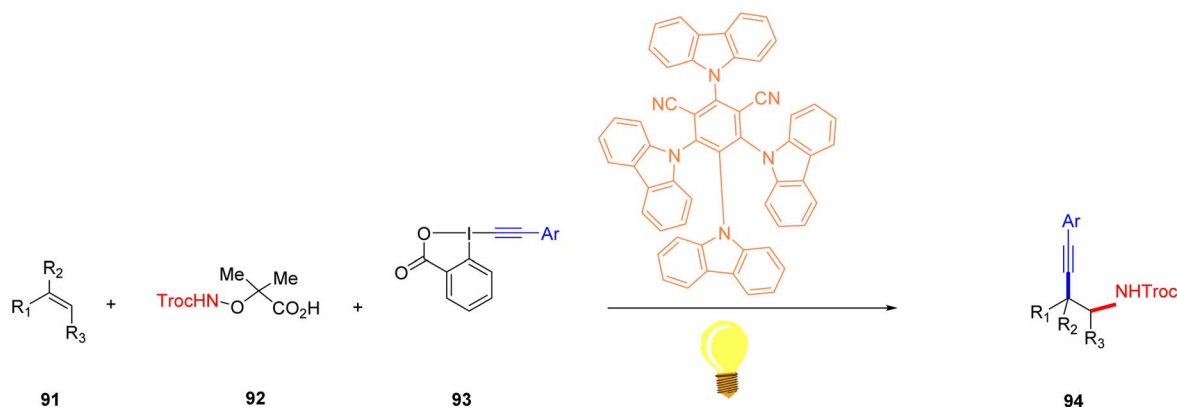**Fig. 52** Synthesis of γ-amino boronic esters.[234]

Fig. 53 1,2-Amidoalkynylation of alkenes. Adapted from ref. 235 with permission from John Wiley & Sons, Copyright © 2018, Wiley-VCH Verlag GmbH & Co. KGaA, Weinheim.

$$\Delta E_{ST} = E_S - E_T = 2J \qquad (4)$$

From eqn (5), it is evident that a reduction in the J will occur by minimizing the overlap between the HOMO and the LUMO. Consequently, this will result in a smaller ΔE_{ST}.[220] Decoupled donor–acceptor and spatially separated compounds, characterized by significant torsion between the donor and acceptor units, are typically used to design TADF emitters.[222]

$$J = \iint \Phi(r_1)\Psi(r_2)\left(\frac{e^2}{r_1 - r_2}\right)\Phi(r_2)\Psi(r_1)\mathrm{d}r_1\mathrm{d}r_2 \qquad (5)$$

4.2.3. Significance of 4CzIPN in photocatalysis. Eosin Y was the first TADF material evaluated as a photocatalyst.[85] As an early organic dye, it was among the first compounds recognized for exhibiting TADF properties. Historically described as E-type fluorescence, the phenomenon now recognized as TADF underscores the key role of eosin Y in radiative decay processes. Eosin Y's affordability and availability as a dye have made it a common choice for photocatalysis.[223] The TADF properties of eosin Y have not currently been investigated for photocatalytic applications. However, it is well-documented that single electron transfer (SET) processes could be initiated from the triplet state of Eosin Y[213] due to its larger intersystem crossing yield (F_{ISC}) and extremely short-lived singlet excited state with a 2 ns lifetime in methanol,[224] which reduced the possibility of interaction between the excited state and the reactant in the PC.

A notable TADF compound used as a PC was 2,4,5,6-tetra(carbazol-9-yl)benzene-1,3-dicarbonitrile (4CzIPN), which was first synthesized by Adachi *et al.* in 2012 (Fig. 46A) **6**.[17] 4CzIPN consisted of four carbazole donors with an iso-phthalonitrile acceptor. Fig. 46B shows the structure of [Ir(dF(CF$_3$)ppy)$_2$(dtbbpy)]PF$_6$ **67**, where (dF(CF$_3$)ppy) stands for 2-(2,4-difluorophenyl)-5-trifluoromethylpyridinato and dtbbpy stands for 4,4′-di-*tert*-butyl-2,2′-bipyridine, which has been

utilized. The mixed charge transfer from ligand to ligand or metal to ligand features a radical cation associated with dp(dF(CF$_3$)ppy). Here, the iridium center was oxidized to Ir(iv), and the ligand (dtbbpy) was reduced to a radical cation.

As illustrated in Fig. 47, all compounds **62–66** showed charge-transfer (CT) excited states. The excited-state redox properties of 4CzIPN are noteworthy, as it is a strong photo-oxidizing and photo-reducing PC compared to other commonly used visible-light PCs, such as [Ir(dF(CF$_3$)ppy)$_2$(-dtbbpy)]PF$_6$ **67**, Ir(ppy)$_3$ **68**, [Ru(bpy)$_3$](PF$_6$)$_2$ **69**, Eosin Y **70**, [Ir(dF(CF$_3$)ppy)$_2$(bpy)]PF$_6$ **71**, Rose Bengal **72**, [Acr-Mes]ClO$_4$ **73**, [Ir(ppy)$_2$(dtbbpy)]PF$_6$ **74**, [Ir(dF(Me)ppy)$_2$(dtbbpy)]PF$_6$ **75**, [Ir(F(Me)ppy)$_2$(dtbbpy)]PF$_6$ **76**, and 4CzIPN **6**, as shown in Fig. 48 and 49. The main advantage of 4CzIPN is its low-cost synthesis.[208]

The effectiveness of a PC is typically evaluated based on the highest product yield achieved.[225] However, it is not always confirmed whether the reaction reaches complete conversion, leading to potential variations in yield due to differences in reaction kinetics and reactivity. To address this, a threshold is established for yield comparison, where variations of less than 5% are considered statistically insignificant across different PCs.[208] Additionally, isolated yields, often reported, can be more variable due to experimental discrepancies, whereas NMR yields provide a more precise measure of product formation.

A quantitative approach to measuring the effectiveness is the $\Phi(\lambda)$ eqn (2); however, these are separately documented from the product yield.[226] Quantum yields are often used to infer the presence of a radical chain mechanism in a reaction. When the quantum yield exceeds one, it suggests that one mole of photons can produce more than one mole of product, indicative of a radical chain mechanism. Conversely, a quantum yield of less than one suggests the radical chain mechanism may not function, although this interpretation is simplistic. Reactions
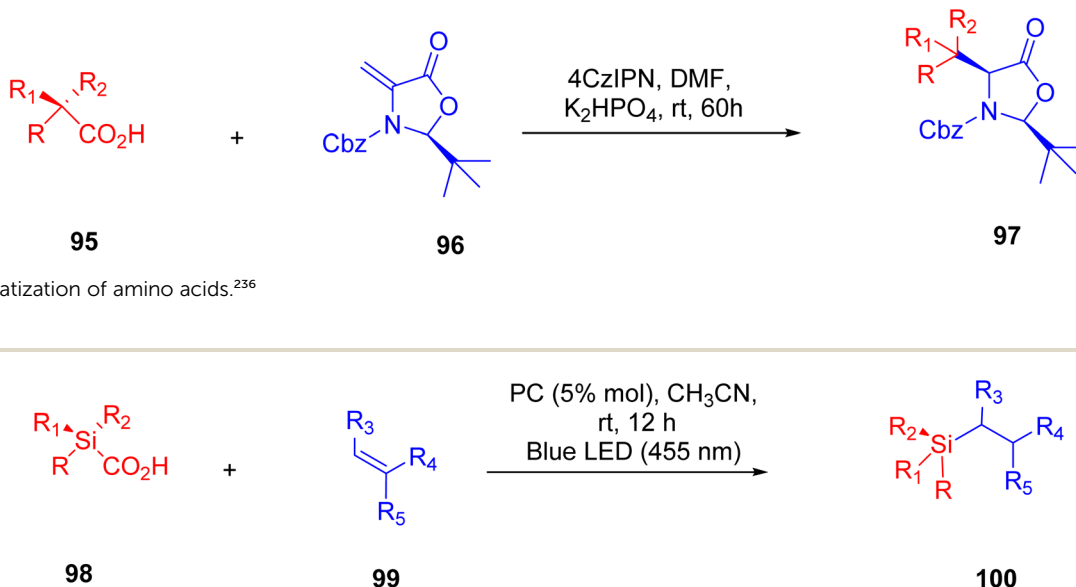

Fig. 54   Derivatization of amino acids.[236]
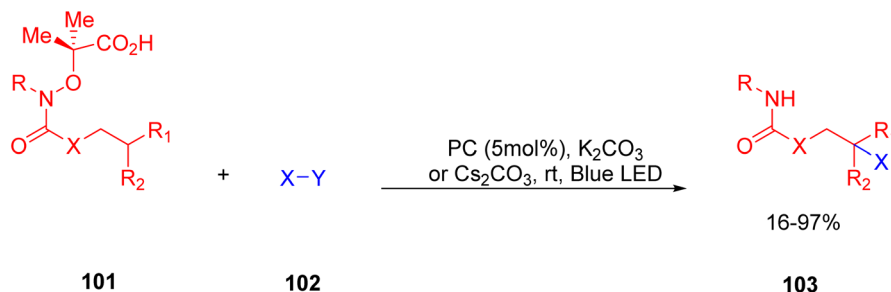

Fig. 55   Hydrosilylation of alkene.[237]

Fig. 56 Reaction illustration for the functionalization of amines and amides.[239]

can still involve radical mechanisms even if their quantum yields are below one. In cases where the initiation step of the chain mechanism is highly inefficient, estimating the length of the radical chain may be possible by analyzing the quenching fraction, though such analyses are infrequently reported in photocatalysis studies.[227]

Throughout the fabrication or formation of a PC, various sources of excitation may be used, ranging from traditional compact fluorescent lightbulbs to high-powered LED lamps.[228] Furthermore, photoreactors can catch and reflect all photons from the source of excitation towards the reaction vessel to enhance reaction efficacy.

It is crucial to recognize that the proposed mechanisms for the reactions discussed in this review are largely speculative and frequently lack robust supporting evidence. Mechanistic proposals frequently rely on comparing the thermodynamic properties of PCs and reactants. While this provides an overall assessment of PC effectiveness, it often neglects the importance of reaction kinetics. For example, Wolf and colleagues studied how photoexcited state lifetime influences the yield of product in the trifluoromethylation of quinoline.[229] They discovered that longer lifetimes for the excited state of PCs led to faster SET, but the second SET was also discovered to be the rate-limiting step rather than the first SET. Similarly, Scaiano and coworkers[230] noted that, although suitable redox potentials were required for the PCs to start the target SET, the success of photocatalysis was determined by reaction kinetics, which are less frequently studied. Lamentably, kinetics studies like these are infrequently conducted.

4CzIPN is a highly investigated TADF-based PC, predominantly involved in photoredox catalysis reactions through PET. However, there are a few instances, which will be discussed below, where the photocatalysis occurs through PEnT.[208]

4.2.4. Photoinduced decarboxylation of carboxylic acids by reductive quenching mechanism. 4CzIPN can function as a PC in the decarboxylation of substrates, typically through reductive quenching. The application of carboxylic acids for the generation of C(sp³) radicals with the assistance of photoinduced oxidative decarboxylation has facilitated diverse synthetic strategies for C–C and C–X bond formation.[231] Activation of carboxylic acids or their scaffolds involves SET to the PC, for the generation of haloalkyl radicals. It has been noted that, for this process to occur efficiently, the PC should be a potent photo-oxidant that allows for carboxylate oxidation, as carboxylates

typically have E_{ox} between 1.2 and 1.5 V.[232] A radical addition mechanism for photoinduced oxidative decarboxylation is shown in Fig. 50 (using compounds **62, 65, 66, 77–84**).

Examples of radical addition include the synthesis of aryl-hydroxylamines (**87**) through photoredox catalysis. This process involves the reaction between carboxylic acids (**85**) and nitro-soarenes (**86**), as illustrated in Fig. 51.[233] Another example is the addition of vinyl boronic esters (**88**) to radicals generated from α-amino carboxylic acids (**89**) to produce γ-amino boronic esters (**100**), which is outlined in Fig. 52.[234] 1,2-Amidoalkynylation of alkenes can be performed using the addition of alkenes (**91**) to amidyl radicals derived from 2,2,2-trichloroethoxycarbonyl-protected α-aminoxy acids (**92**) and ethynylbenziodoxolone (**93**) to yield the alkynylated products (**94**) as shown in Fig. 53.[235] The addition of alkyl radicals generated from amino acids or peptides (**95**) to a methyleneoxazolidinone analogue of dehydroalanine (**96**) has been employed to produce peptide derivatives (**97**) as illustrated in Fig. 54.[236] Finally, a hydrosilylation reaction can be achieved by the addition of silyl radicals formed
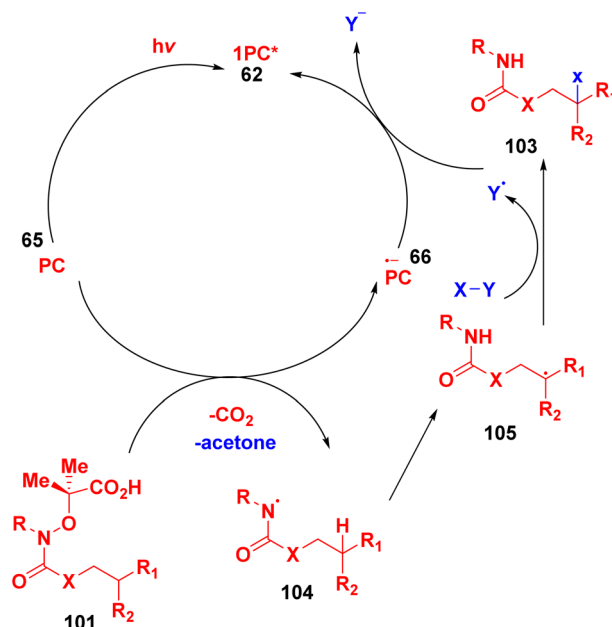

Fig. 57 Generalized cycle for group transfer in C–H functionalization and decarboxylation.[239]

from silacarboxylic acids (**98**) to alkenes (**99**) to yield hydrosilylated alkanes (**100**) as seen in Fig. 55.[237]

In other reactions utilizing organic PCs, no products were formed when eosin Y and 9-mesityl-10-methylacridinium perchlorate ([Mes-Acr]ClO$_4$) were used.[238] The 1,2-aminoalkynation of alkenes (Fig. 53), with 2-methylpent-1-ene as the alkene, produced a 77% yield using 4CzIPN as a PC. Other organic PCs produced yields of 7% to 33%, such as eosin Y which is effective and produces a yield of about 33%.[235] The difference in yield was correlated with the ground-state reduction potential of the PCs 4CzIPN, eosin Y, and [Mes-Acr]ClO$_4$.[238] This suggests that the reduction potential of the PC significantly influences its success.

In alkene hydrosilylation (Fig. 55), 4CzIPN outperformed ruthenium and iridium PCs, achieving an 82% yield.[237] This superior performance was attributed to the exceptional photo-oxidizing competence of 4CzIPN, which had an E_{red}^* of 1.35 V compared to [Ir(dF(CF$_3$)ppy)$_2$(dtbbpy)]PF$_6$, which had an $E_{red}^* = 1.21$ V. This is crucial for the oxidation of Ph$_2$MeSiCO$_2^{\cdot}$/Ph$_2$MeSiCO$_2^-$. This high efficiency was notably observed in the derivatization of amino acids (Fig. 54).[236] 4CzIPN and [Ir(dF(Me)ppy)$_2$(dtbbpy)]PF$_6$ provided almost equal yields (such as 89% and 90%, respectively), prompting the selection of 4CzIPN as the PC for further investigation.

Unfortunately, 4CzIPN and [Ir(dF(CF$_3$)ppy)$_2$(dtbbpy)]PF$_6$ is an ineffective PC for synthesizing the hydroxylamine product (Fig. 51), but [Mes-Acr]ClO$_4$ and [Mes-Acr]BF$_4$ proved to be an effective PC for this reaction, due to their exceptional oxidizing ability in the excited state with a reduction potential of approximately 2.06 V.

Fig. 52 shows the preparation of γ-amino boronic esters using four PCs: [Ir(ppy)$_2$(dtbbpy)]PF$_6$, [Ir(dF(CF$_3$)ppy)$_2$(dtbbpy)] PF$_6$, [Ru(phen)$_3$]Cl$_2$, and 4CzIPN. Among these, [Ir(ppy)$_2$(dtbbpy)]PF$_6$ was low-cost and produced a yield of about 88% of the final product in the presence of Boc-Pro-OH and the addition of Cs$_2$CO$_3$. In contrast, the yield of 4CzIPN is 66% without Cs$_2$CO$_3$, and its yield with the additive was not reported, making direct comparison challenging. The superior performance of [Ir(ppy)$_2$(dtbbpy)]PF$_6$ over 4CzIPN was likely due to their relative ground-state reduction potentials. The lower E_{red} of the iridium PCs led to the formation of the intermediate α-boryl radical. A mechanistic approach-related example secluded the functionalization of amides and amines (**101**) with the help of electrophilic nitrogen radicals (**102**) to form the functionalized amides/amines (**103**) (Fig. 56).[239] This reaction generates an electrophilic amidyl radical through the decarboxylation of carboxylic acid scaffolds. The resulting radical then undergoes a 1,5-hydrogen atom transfer (HAT), leading to the formation of a distal alkyl radical as shown in Fig. 57.[239] This radical subsequently undergoes radical cleavage or group transfer in the presence of polarized SOMOphile (SOMO = singly occupied molecular orbital), resulting in the formation of remotely
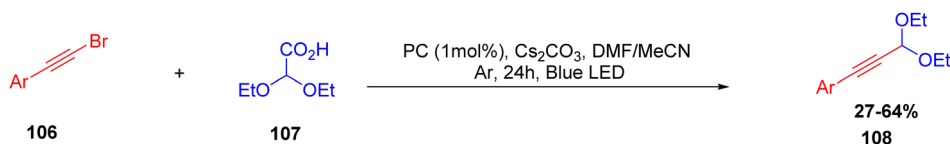

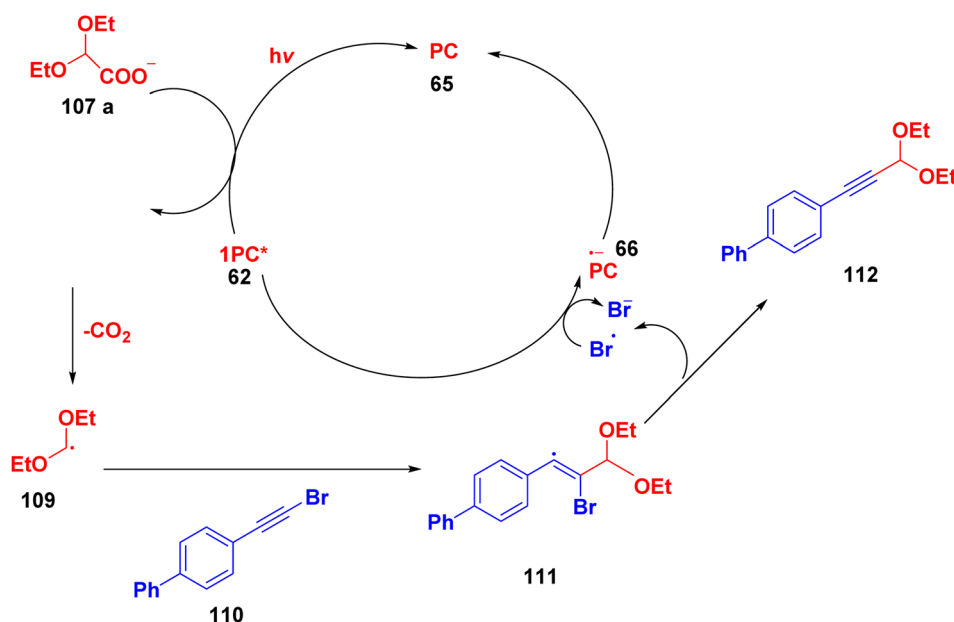**Fig. 58** Synthetic approach for acetalation of alkynyl bromides.[240]

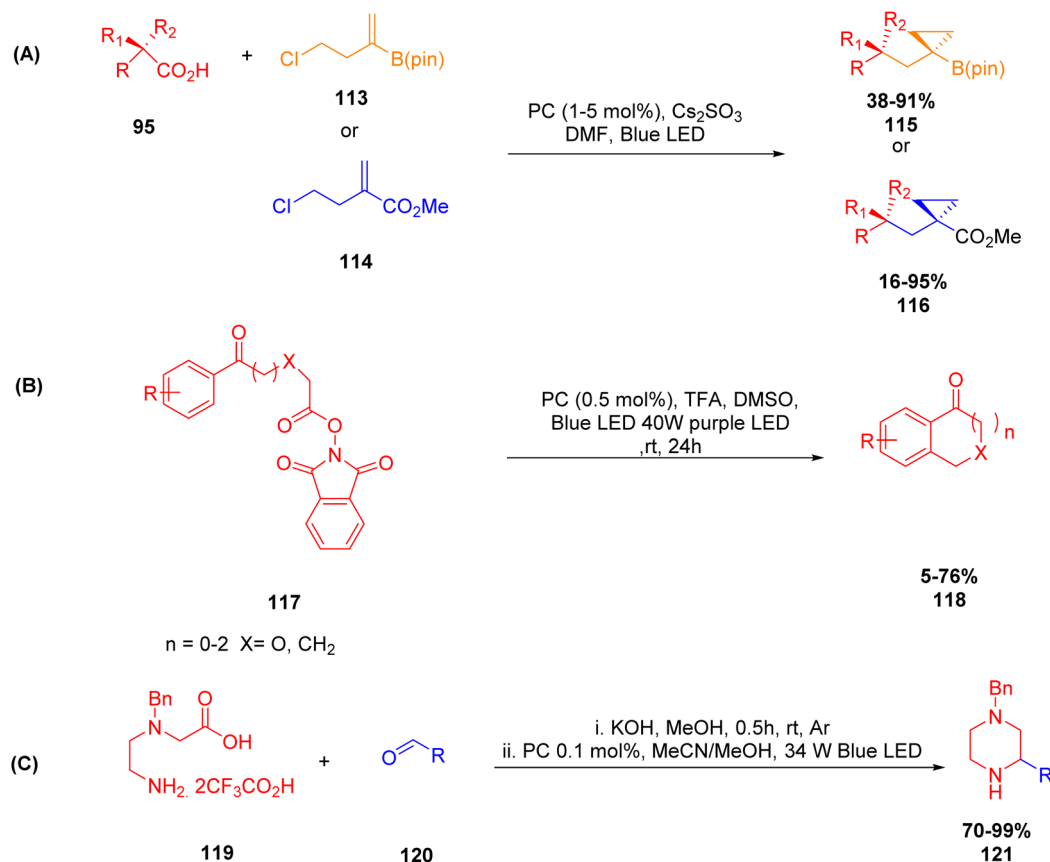**Fig. 59** Synthetic approach for the photocatalytic acetalation of alkynyl bromides.[240]

Fig. 60 Schemes for cyclization reactions involving photoinduced decarboxylation mechanism used to synthesize (A) functionalized cyclo-propanes,[242] (B) synthesis of intramolecularly alkylated arenes[243] and (C) synthesis of 2-substituted piperazines.[244]
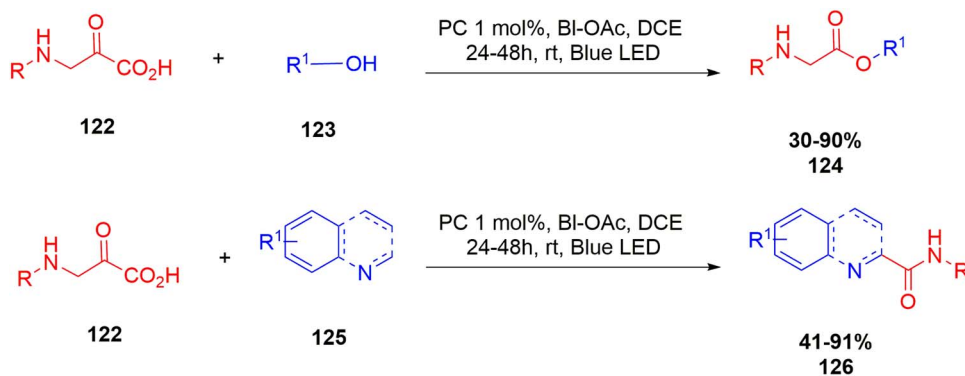

Fig. 61 Synthetic approach by oxidative decarboxylation of oxamic acids.[245]

substituted amines or amides. 4CzIPN demonstrated higher yields in various reactions, including γ-chlorination, thio-etherification, cyanation, and alkynylation, although there was no comparative data for an iridium photocatalyst in the final reaction.

Carboxylic acids can serve as radical precursors for acetyla-tion of alkynyl bromides (**106**) (Fig. 58).[240] The reaction proceeds *via* decarboxylation, generating an acetal radical (**109**) that subsequently forms a bromoalkenyl radical (**111**) by addition to the alkynyl bromide (Fig. 59).[240] The removal of a bromyl

radical, which is removed by the PC (**66**), leads to the formation of the product.

Radical capturing experiments revealed the inclusion of the acetal radical, and further radical suppression studies sup-ported the radical-based nature of the process. Among the PCs tested, 4CzIPN and [Ir(dF(CF$_3$)ppy)$_2$(dtbbpy)]PF$_6$ yielded only 5% and 36%, respectively, while [Ru(bpy)$_3$](PF$_6$)$_2$ and eosin Y did not produce any product. Wang *et al.* attributed this to the photooxidizing abilities of the PCs. The cesium salt of 2,2-diethoxyacetic acid, with E_{ox} of 0.95V, was studied[241] and the
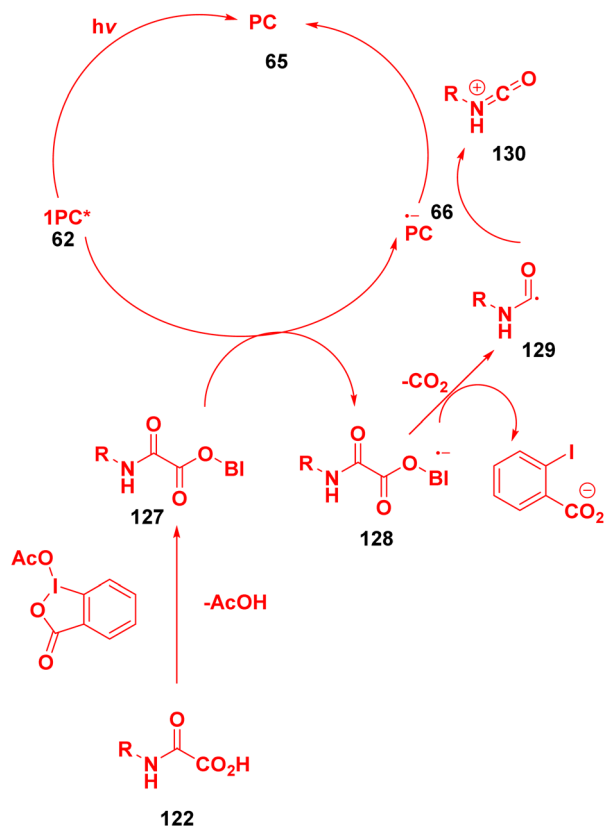
Fig. 62 Oxidative decarboxylation of oxamic acids using photocatalysis.[245]

results indicate that for a reaction to be thermodynamically feasible, the PCs should have a more positive reduction potential than that of substrate.[241] Both [Ir(dF(CF$_3$)ppy)$_2$(dtbbpy)]PF$_6$ and 4CzIPN exhibited sufficiently high photooxidizing abilities, which likely accounted for the efficient performance of 4CzIPN, but [Ru(bpy)$_3$](PF$_6$)$_2$ and eosin Y were not effective for this single-electron transfer process. Additionally, oxidative decarboxylation has been employed in cyclization reactions, such as the synthesis of functionalized cyclopropanes (**115** and **116**) from carboxylic acids (**95**) and a carboxylate ester (**113**) or

boronic ester (**114**) (Fig. 60A),[242] intramolecular arene alkylation from N-(acyloxy) phthalimides (**117**) to alkylated arene (**118**) (Fig. 60B),[243] and the fabrication of 2-substituted piperazines (**121**) by addition of a glycine-based diamine (**119**) to aldehydes (**120**) (Fig. 60C).[244]

4.2.5. The photoinduced decarboxylation of carboxylic acids through oxidative quenching mechanism. Carboxylic acids can be used to generate carbon radicals in reactions that cause the formation of C–C and C–X bonds. This includes applications in synthesizing urethanes and urea, where oxidative quenching mechanisms with PCs are employed (Fig. 61A) **122–124**.[245] Reduction of oxamic acids due to an excited PC triggers decarboxylation and synthesis of a carbamoyl radical. This radical undergoes oxidation to generate an isocyanate while the PC is concurrently regenerated (Fig. 62).[245] 4CzIPN was selected as the PC for its environmentally friendly profile, but its rate of reaction is slow and requires one day to achieve a 91% yield, compared to [Ru(bpy)$_3$]Cl$_2$. The selection of 4CzIPN was motivated by its potential for greener synthesis of urethanes and urea, offering a more sustainable alternative to transition metal PCs. Additionally, subsequent research confirmed that the carbamoyl radical generated in this process can react with heteroarenes (Fig. 61B) **122–126**.[245] Among the PCs evaluated, 4CzIPN achieved the highest yield of 95% as compared to other PCs including eosin Y, [Mes-Acr]ClO$_4$ and Rose Bengal. The variation in performance is attributed to its excellent E_{ox} of about 1.52V in its ground state compared to eosin Y and Rose Bengal.[246]

The excited PC can also be used for the Minisci reaction.[247] This reaction begins with oxidative quenching in the presence of N-(acyloxy)phthalimides (NAPs) (**131**), which leads to the generation of an alkyl radical. The addition of the radical to a heteroarene (**132**) leads to the functionalized compound (**133**), as described in Fig. 63.[247] Ir PCs and 4CzIPN produced similar yields in the reaction but 4CzIPN was chosen as the PC to prevent potential toxicity associated with the use of Ir-based PCs by utilizing an organocatalyzed process.

An analogous synthetic approach includes the formation of carbon-fluorine bonds with N-hydroxyphthalimide esters (**134**) to form alkyl fluorides (**135**) (Fig. 64) **134–135**.[248]
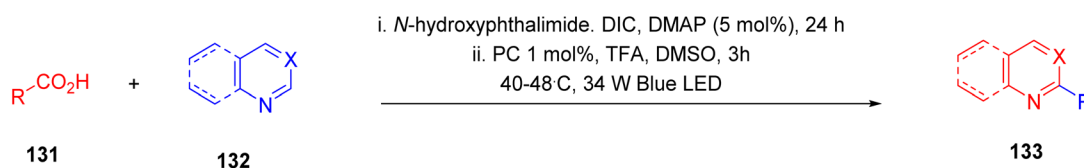

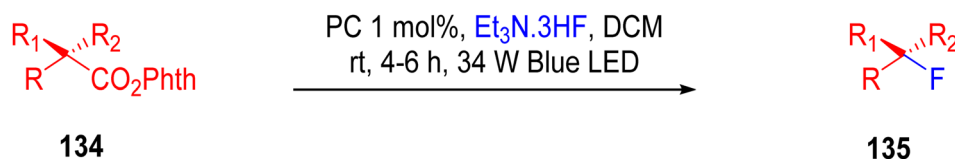**Fig. 63** Minisci reaction in the use of carboxylic acids in the presence of NAPs.[247]

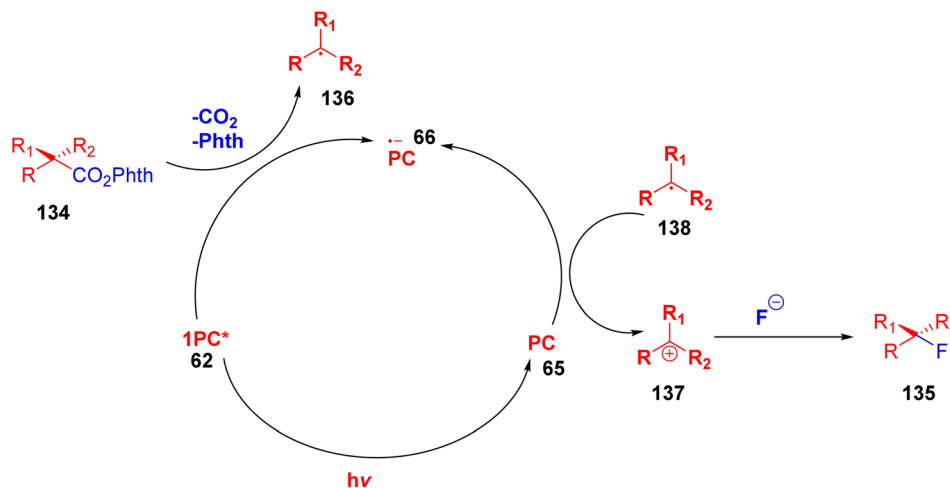**Fig. 64** Nucleophilic fluorination of redox-active esters.[248]

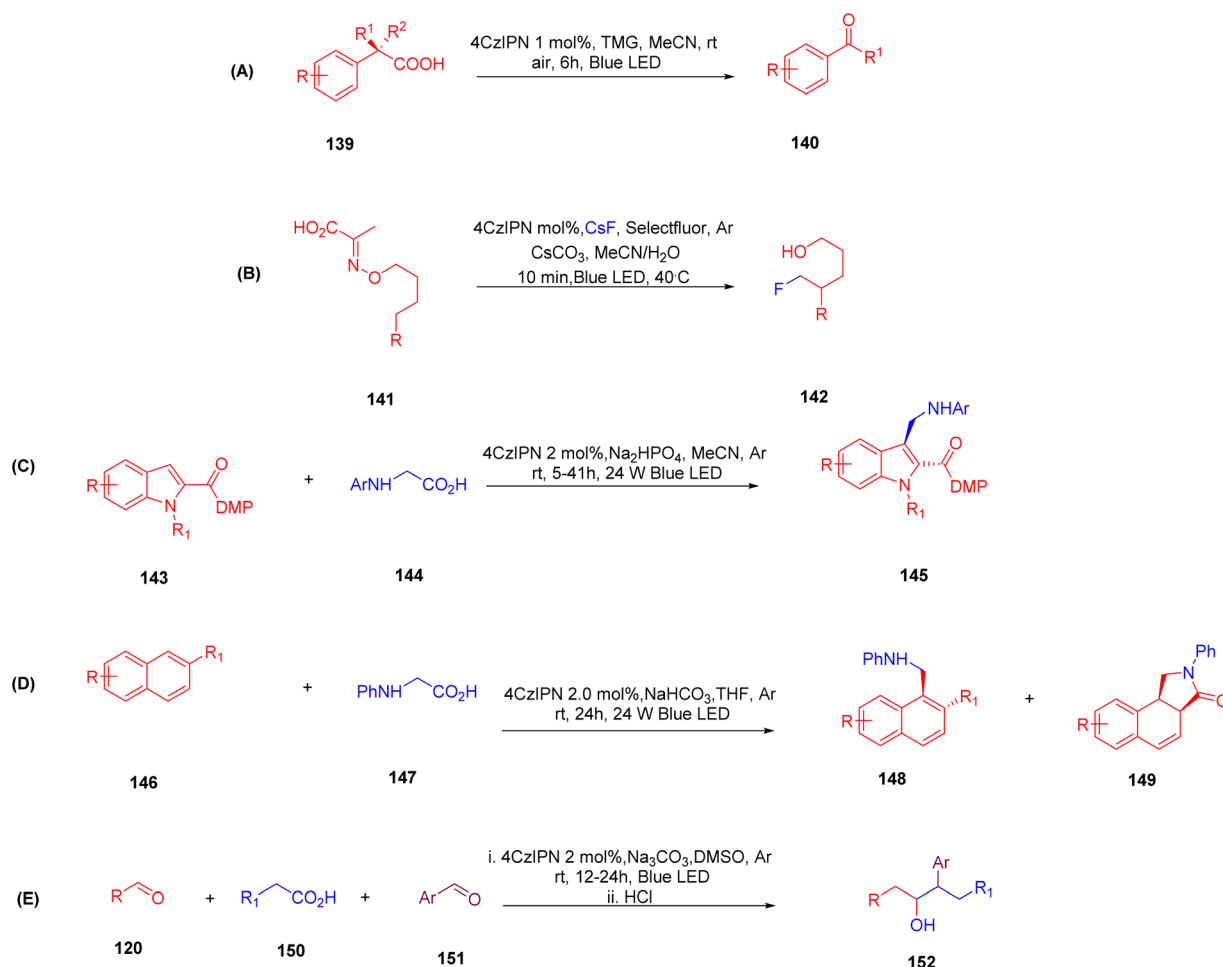**Fig. 65** Detailed mechanism of nucleophilic fluorination of redox-active esters using a photocatalyst.[248]

Fig. 66 Examples of different photocatalytic reactions: (A) synthesis of aldehydes and ketones,[249] (B) δ-fluorination,[250] (C) dearomatization of indoles,[251] (D) dearomatization of naphthalene,[252] and (E) synthesis of 1,4-amino alcohols.[253]

The mechanism of this reaction used a PC* oxidative quenching of redox-active ester **134**, which results in an alkyl radical **136** (Fig. 65).[248] In this reaction, the alkyl radical is oxidized in the presence of PC*. This results in a carbocation (**137**) instead of the addition of a double bond or coupling to another radical. This carbocation is then captured by a fluoride
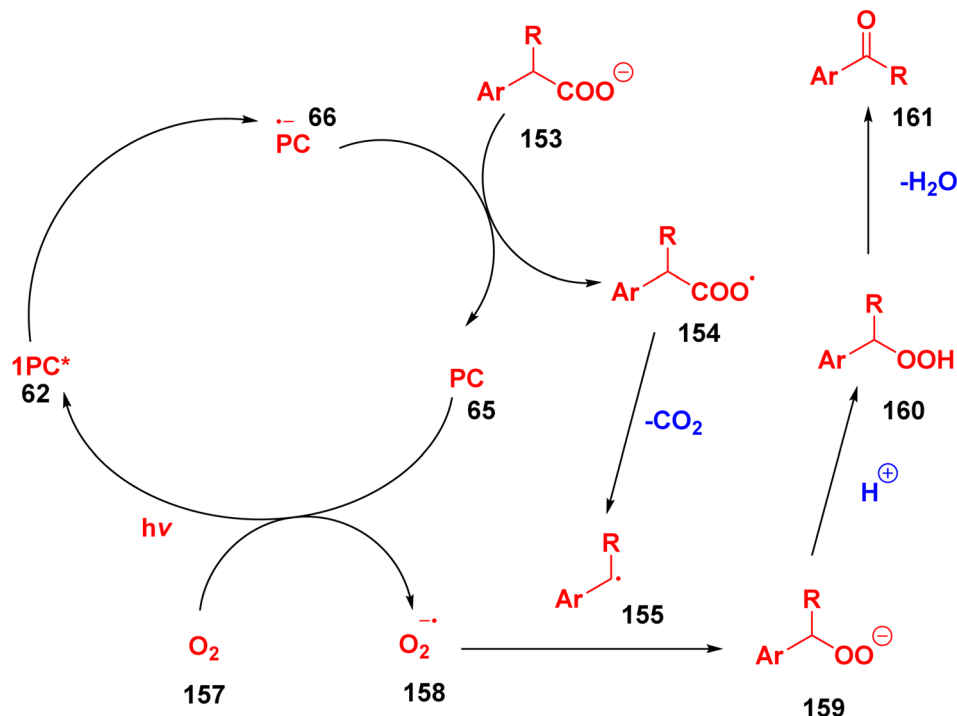
Fig. 67 Photocatalytic formation of ketones and aldehydes in the presence of carboxylic acids.[249]

ion, leading to the formation of an alkyl fluoride (**135**). The quantum yield of the reaction was 37%, revealing that this process does not have any involvement in the radical chain mechanism. Stern–Volmer quenching studies revealed effective quenching of the excited photocatalyst by the phthalimide ester. The presence of the alkyl radical was validated by the inhibition of product formation by adding TEMPO (2,2,6,6-tetramethylpiperidin-1-oxyl), leading to the TEMPO adduct. Additional radical capturing experiments with different precursors such as styrene and methyl acrylate supported the presence of alkyl radical. The formation of the carbocation was further validated by capture experiments in the presence of different nucleophiles such as alcohols and 1,3,5-trimethoxybenzene. Among the tested photocatalysts, 4CzIPN achieved a 91% yield, which is comparable to that of Ir PCs.

Excitation of the PC is typically performed by oxidative quenching with carboxylic acid derivatives, resulting in alkyl radicals. Alternatively, the generation of alkyl radicals can be attributed to the oxidized photocatalyst itself. This mechanism is evident in different types of photocatalytic reactions such as synthesis of aldehydes and ketones (**140**) from arylacetic acids (**139**) (Fig. 66A),[249] a δ-C–H mono- and difluorination reaction of an alkoxy radical precursor (**141**) to form the difluorinated products **142** (Fig. 66B) **141–142**,[250] intermolecular hydroalkylative dearomatization of electron-deficient indole scaffolds (**143**) via reaction with phenylglycine (**143**) to yield the dearomatized product (**145**) (Fig. 66C),[251] 1,2-hydroalkylation for the intermolecular dearomatization of naphthalene scaffolds (**146**) via reaction with phenylglycine (**147**) to yield the dearomatized products (**148** and **149**) (Fig. 66D),[252] and the synthesis of 1,4-

amino alcohols (**152**) by decarboxylative radical addition using a reaction between aliphatic aldehydes (**120**), carboxylic acids (**150**) and aromatic aldehydes (**151**) (Fig. 66E) **120, 150–152**.[253] In the given examples 4CzIPN is employed as a PC because it is commercially available TADF material, wide functional group captability and reactions under mild conditions. In these examples, a 99% yield is obtained as compared to other transition metal-based PCs such as iridium PCs which is why 4CzIPN is used as the best photocatalyst in these reactions.

The fluorination reaction of the radical **163** was achieved using Selectfluor (**164**), leading to the formation of **142** and reduction of the Selectfluor radical cation (**165**) by the excited PC* (**62**). The fluorination process was completed in just 10 minutes in the presence of PC with a 1% molar concentration compared to the chlorination reaction that involved 18 hours with a molar concentration of PC of 3 mol%. Quantum yield experiments indicated values of 7.0% for fluorination and 1.6% for chlorination, suggesting the unavailability of a radical chain mechanism. The greater efficiency of the fluorination reaction, even with lower PC loading, was corroborated by radical clock experiments, which showed that the quenching of alkoxy radical was 53 times faster in fluorination as compared to chlorination. Among the tested PCs, the yields were 67% for 4CzIPN and 71% for [Ir(dF(CF$_3$)ppy)$_2$(dtbbpy)]PF$_6$, respectively. Despite the comparable results, 4CzIPN was favored for its superior efficiency.

In the dearomatization of the indole scaffolds reaction mechanism (Fig. 66C), the PC* was essential for oxidative quenching, which formed a new radical.[251] The α-amino radical is then formed through oxidative decarboxylation of the scaffold
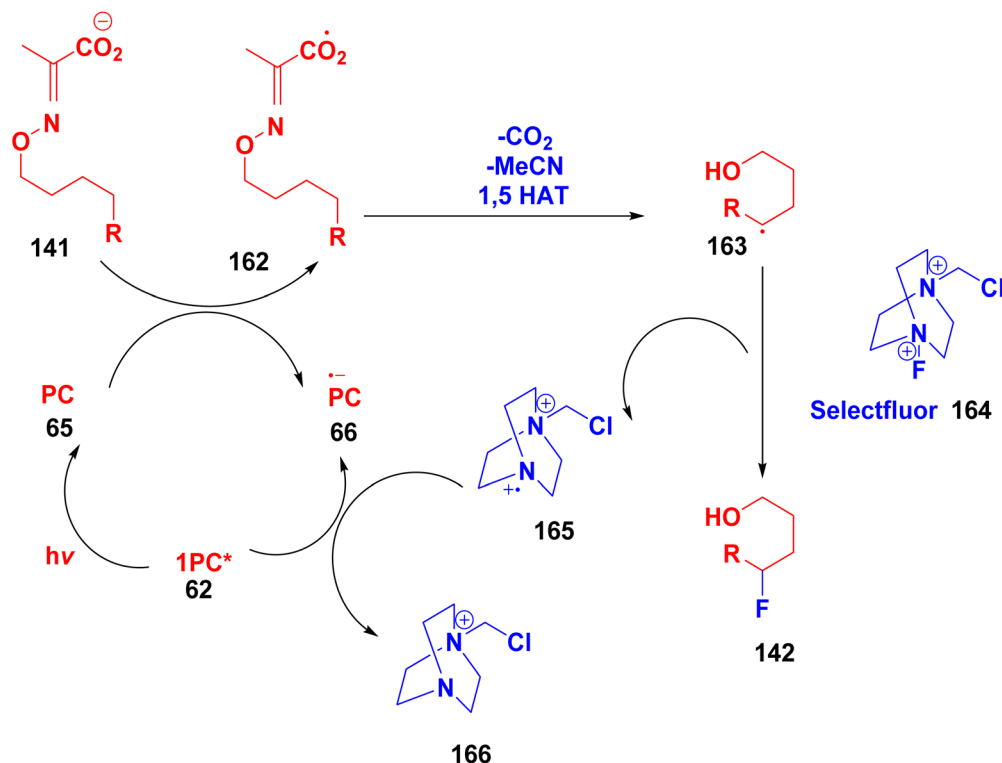
Fig. 68 Fluorination of carboxylic acid scaffolds in a photocatalytic reaction.[250]
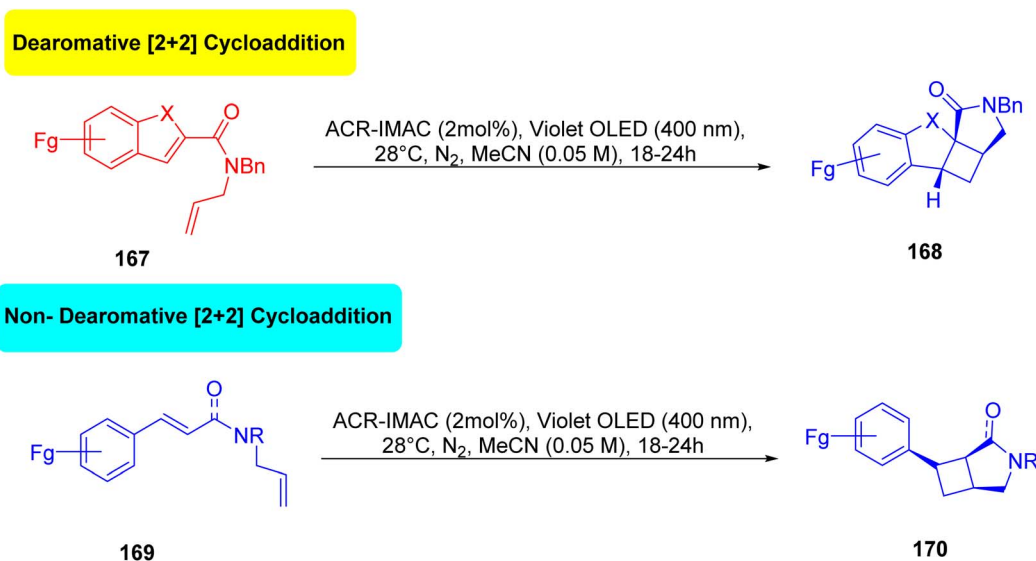

Fig. 69 Non-dearomative and dearomative intramolecular [2 + 2] photocycloaddition reactions.[254]

(**144**) catalyzed in the presence of the oxidized PC, which then couples with a protonated intermediate to form the final product. Stern–Volmer quenching experiments showed that indole quenched the PC* with more efficacy than glycine, with constants of 1460 and 173, respectively. Among the photocatalysts tested, 4CzIPN achieved a yield of nearly 99%, surpassing transition metal-based photocatalysts such as *fac-*

Ir(ppy)$_3$, [Ru(bpy)$_3$]Cl$_2$ and [Ir(ppy)$_2$(dtbbpy)]PF$_6$ due to their oxidation potential in the excited state.

For the 1,2-hydroalkylation reaction used for intermolecular dearomatization of naphthalene derivatives (Fig. 66D), 4CzIPN was the most effective among the tested PCs, achieving a 90% yield with a 2:1 ratio of uncyclized to cyclized products.[252] In contrast, [Ir(ppy)$_2$(dtbbpy)]PF$_6$ achieved only a 60% yield with a 3.7:1 ratio. The discrepancy in yield remains unexplained, as
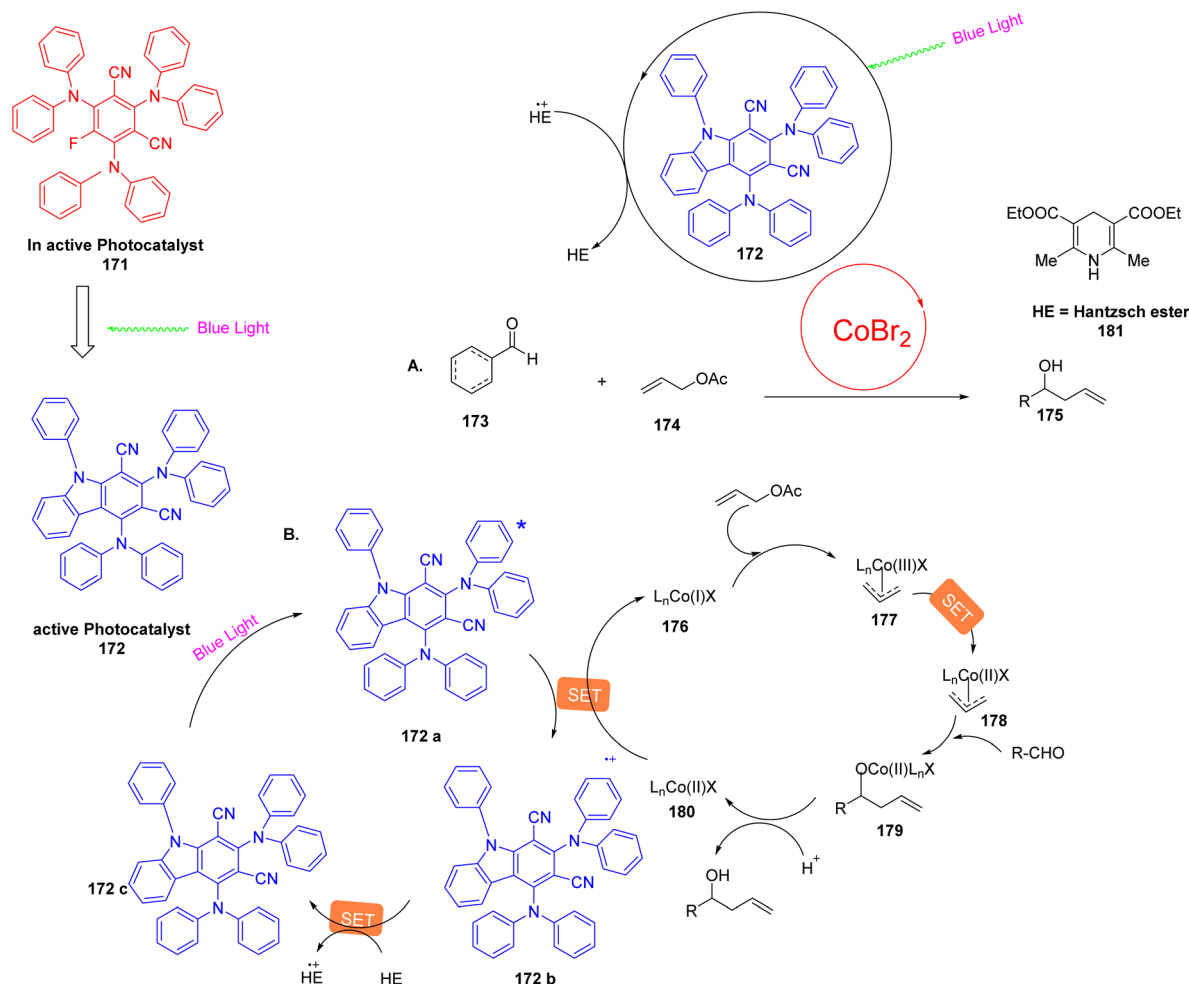
Fig. 70 (A) TADF PC for cobalt-mediated allylations and (B) its proposed mechanism.[255]

both catalysts have similar $E_{red} = -1.45$ V for the naphthalene derivative.

Finally, for producing 1,4-amino alcohols by the decarboxylative radical addition bifunctionalization process, as shown in Fig. 66E.[253] In this process formation of ketyl radical occurred through oxidative quenching of aldehyde in the presence of PC*. The oxidized PC produces the alkyl radical from the carboxylate in a similar fashion to the previous examples. The reaction of an alkyl radical with olefins generated a new radical that subsequently coupled with a ketyl radical. Radical protonation leads to the formation of the final product (**152**). The proposed photocatalytic cycle was confirmed by experiments using the radical scavenger TEMPO and deuterium labeling. Among the eight PCs tested, the yield was 90% for 4CzIPN and was 42% for [Ir(dF(CF₃)ppy)₂(dtbbpy)]PF₆. This is attributed to their strong photoreducing abilities compared to [Ru(bpy)₃]Cl₂, which did not produce any product. The authors also suggest an alternative reductive quenching mechanism. However, the absence of a clear mechanistic understanding makes it difficult to explain why 4CzIPN demonstrated superior performance compared to the other photocatalysts.

The preparation of aldehydes and ketones from arylacetic acids was achieved *via* the coupling of the alkyl radical with a superoxide radical causing the generation of SET by the excited PC*.[249] This coupling led to dehydration and protonation, resulting in the synthesis of the final product (Fig. 67). Stern–Volmer quenching studies demonstrated higher luminescence quenching of the PC by oxygen, highlighting its function. Electron paramagnetic resonance (EPR) spectroscopy confirmed the superoxide radicals' presence during the reaction. The introduction of TEMPO interrupted the reaction, suggesting the involvement of radical intermediates. Among the organic PCs tested, the yield of 4CzIPN was 91% but eosin Y and Rose Bengal yielded significantly less product. This disparity was attributed to their oxidation potentials. For example, Eosin Y and Rose Bengal, with oxidation potentials of 0.78 V and 0.84 V, respectively, are insufficient for oxidizing the carboxylate. In contrast, 4CzIPN, with a higher oxidation potential of 1.52 V, effectively facilitates the reaction. Additionally, by reducing the concentration of PC slightly results increased the yield of product from 91% to 98%.

For δ-C–H mono- and dehalogenation reactions (Fig. 66B), the oxidation of PC facilitates the decarboxylation of carboxylic
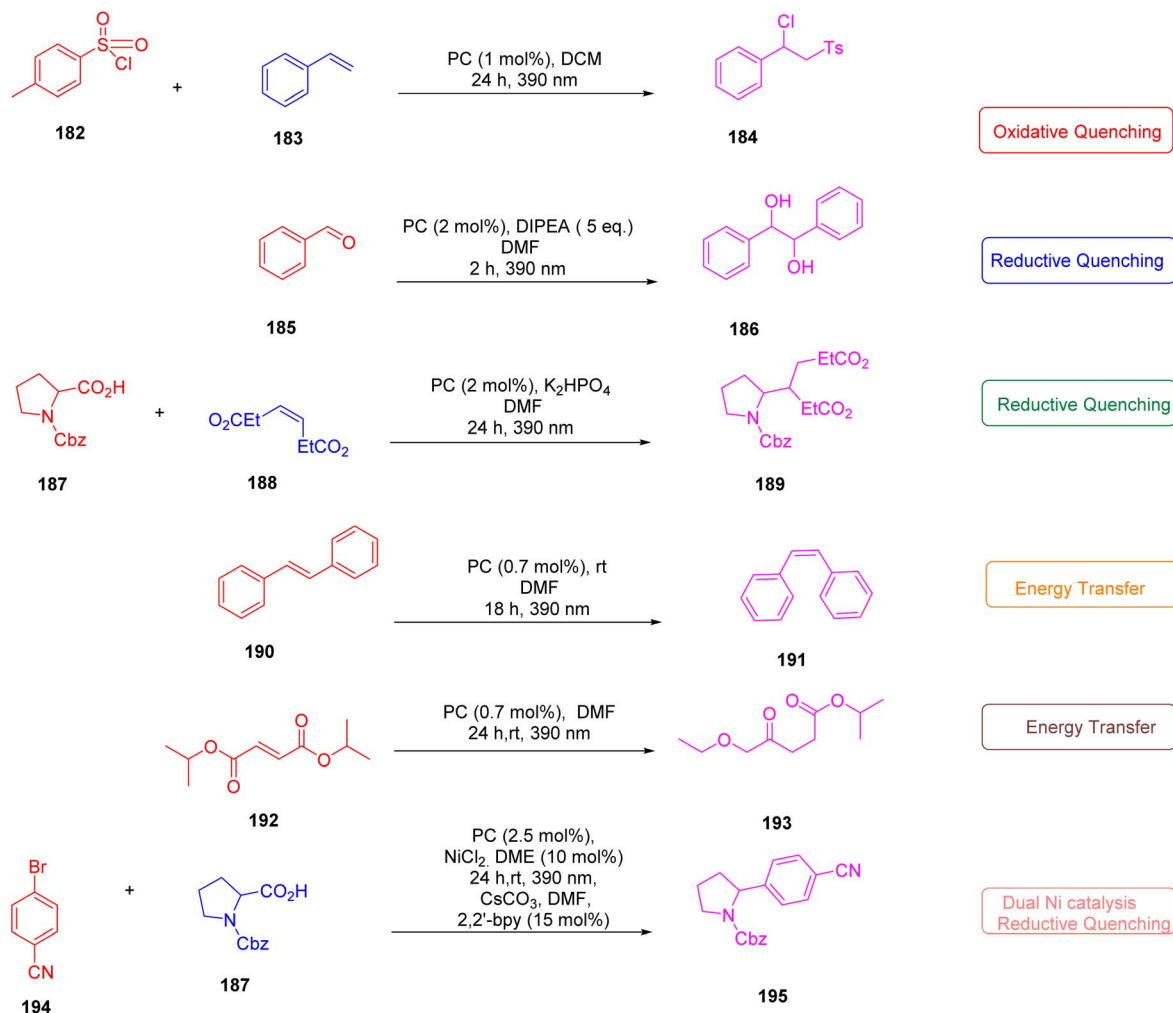
Fig. 71 Investigated photocatalysis reactions including energy transfer, oxidative quenching, dual metallaphotocatalysis and reductive quenching *via* Ni(II) cocatalyst.[256]

acid substrates, resulting in the loss of CO_2 and MeCN. This process involves alkoxy radical formation by a 1,5 hydrogen atom transfer (HAT) mechanism (Fig. 68).[250]

4.2.6. Other photocatalytic reactions. Hudson *et al.* (2022) described the highly efficient and versatile triplet sensitizer ACR-IMAC, based on an imidazoacridine scaffold, which was developed to replace the much more expensive iridium-based PC for use in [2 + 2] cycloadditions with illumination approaches that use common light sources as well as commercial wavelengths (Fig. 69).[254] The conversion efficacy of organic PCs such as ACR-IMAC is almost similar to that of Ir-based PCs in intramolecular [2 + 2] cycloaddition reactions. The synthesis of this catalyst was in a very small quantity and was prepared with easily available precursors. Its effectiveness in acetonitrile (MeCN), a solvent frequently used in cross-coupling reactions, suggests its potential application beyond [2 + 2] cycloadditions. Mechanistic investigations, including microsecond time-resolved transient absorption spectroscopy and Stern–Volmer luminescence quenching analyses, showed a triplet–triplet energy transfer (EnT) sensitization mechanism. This research highlights the potential for wider use and

advancement of TADF materials as organic PCs, most importantly for complexes in which high-energy chemical transformation occurs with the assistance of visible light. Future research will aim to explore further applications of similar materials in organic synthesis that also include ACR-IMAC.

The photodegradation of TADF-active halo-isophthalonitriles is a crucial aspect to address for their application as photocatalysts and for designing appropriate photoredox-promoted chemical transformations. Cozzi *et al.* (2022) showed that the photoconversion of the halo-isophthalonitrile 3DPAFIPN produces an isolable carbazole-1,3-dicarbonitrile derivative with significant photophysical properties, such as TADF, as depicted in Fig. 70A.[255] These properties include a prolonged delayed fluorescence lifetime and modulated redox potentials in both ground and excited states, which are advantageous for photocatalysis using $CoBr_2$. Dual metal and photoredox catalysis were utilized for the effective allylation of aldehydes, yielding homoallylic alcohols with good efficiency.

Zysman-Colman *et al.* (2022) have discovered a donor–acceptor TADF compound, pDTCz-DPmS, that could rival the
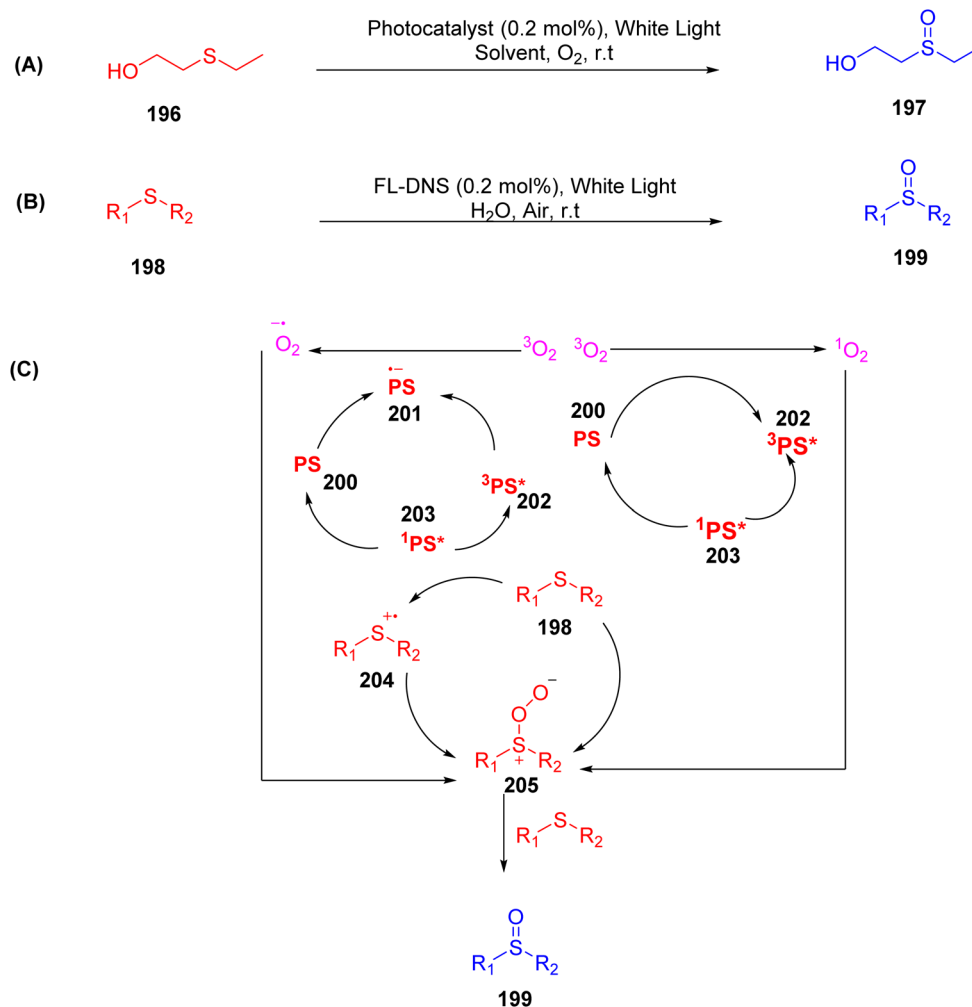
Fig. 72 (A) Oxidation of sulfide to sulfoxide *via* photocatalysis using white light. (B) Oxidation of sulfides *via* FL-DNS. (C) Photocatalytic mechanism of oxidation of sulfide into sulfoxide *via* FL-DNS.[257]

commonly used 4CzIPN in various photocatalytic reactions, as illustrated in Fig. 71.[256] Their results consistently highlight the photocatalytic potential of *p*DTCz-DPmS in comparison to 4CzIPN. Due to its significantly stronger photoreducing ability, *p*DTCz-DPmS is expected to be a more effective photocatalyst in oxidative quenching mechanisms, especially when reductive quenching pathways are not feasible. Furthermore, due to its higher triplet energy (ET) of approximately 0.4 eV greater than that of 4CzIPN, *p*DTCz-DPmS is expected to perform well in photoinduced energy transfer reactions involving substrates with high ETs. This is comparable to benzophenone (ET = 3.00 eV), a well-established efficient energy transfer PC. Furthermore, under the studied reaction conditions, *p*DTCz-DPmS showed much better photostability than 4CzIPN. Thus, our work shows that TADF donor–acceptor compounds that are not limited to 4CzIPN or the carbazolyl dicyanobenzene (CDCB) family could be used and could even outperform this widely used organic photocatalyst in terms of efficiency.

As seen in Fig. 72, Song *et al.* (2023) prepared two PCs based on an organic TADF molecule for the oxidation of sulfides into sulfoxides in aqueous media.[257] Cross-linking between the two

PCs was thought to be responsible for their catalytic activity. By forming hydrophobic domains by cross-linking, the photocatalyst FL-DNS was able to increase its catalytic activity and prolong the duration of its triplet state. In addition, FL-DNS is both recyclable and reusable, making it suitable for aquatic settings or other applications for green chemistry. Mechanistic investigations demonstrated that superoxide ($O_2^{\cdot-}$) and singlet oxygen ($^1O_2$) were both involved in the catalytic process. The study highlighted the value of delayed fluorescence and the advantages of photocatalysts based on TADF for catalytic applications.

Hudson *et al.* (2023) synthesized a set of TADF compounds by incorporating a new imidazo-phenothiazine (IPTZ) acceptor to enhance spin–orbit coupling and excited-state lifetimes by structural constraints and the heavy atom effect.[258] These materials were employed as PCs in various visible light-driven energy transfer reactions. These included [2 + 2] cycloaddition, etherification, disulfide–ene reactions, Ni-mediated esterification, and amination. They generally displayed superior activity to ACR-IMAC and 2CzPN, as illustrated in Fig. 73 and 74. The high concentration of locally excited triplet states in these
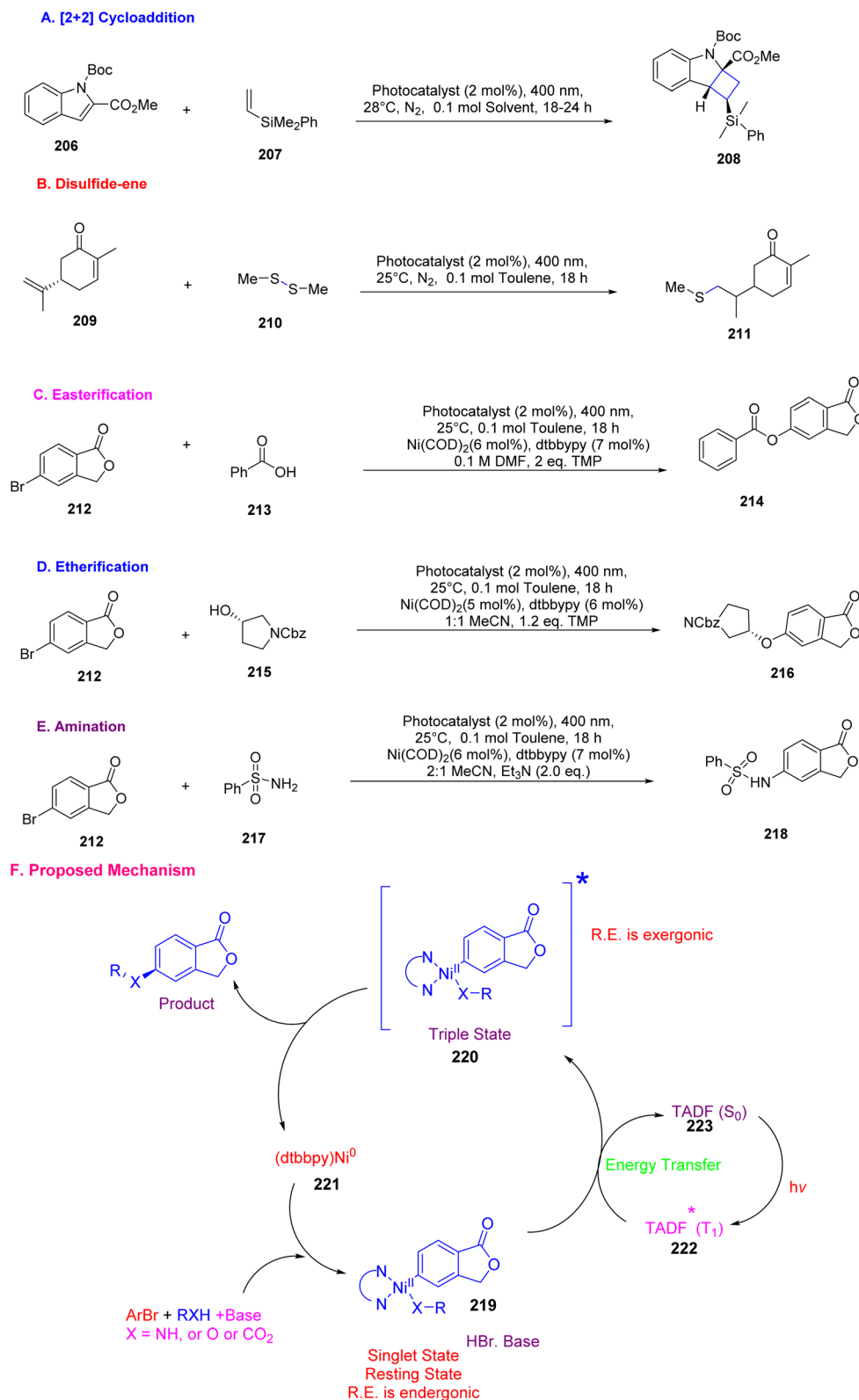
Fig. 73 (A) Reaction [2 + 2] cycloaddition. (B) Reaction scheme for disulfide−ene and (C) amination in the presence of IPTZ PCs. (D) Esterification, (E) etherification, and (F) generalized mechanism for energy transfer occurring in the Ni-catalyzed cross-coupling reaction.[258]

materials was key to effective photocatalysis in MeCN, as it minimized solvatochromic effects responsible for lower triplet energy. SACR-IPTZ emerged as an especially effective triplet

sensitizer, noted for its high energy transfer efficiency, significant locally excited triplet state character, long-lived excited states in polar solvents, broad visible-range absorption, and

Fig. 74 (A–C) Optimizing Ni cross-coupling reactions (D) Ni-catalyzed amination through SACR-IPTZ with reduced loading of catalyst.[258]
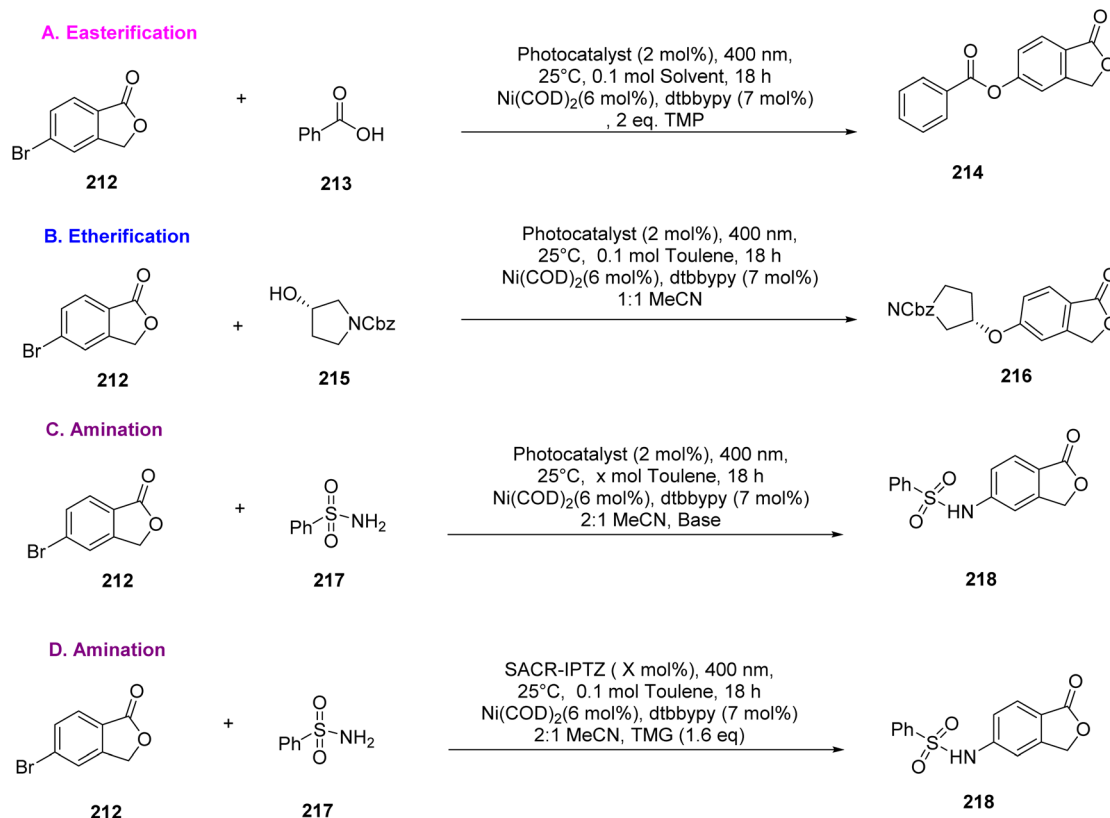
excellent photostability. This study highlighted the potential of the effect of heavy atoms in creating TADF materials with exceptional photocatalytic capabilities. Future research should focus on further optimizing TADF PCs with enhanced visible-range absorption, minimized solvatochromic shifts, and improved photostability and solubility in polar solvents. Additionally, IPTZ-based materials could be used in SET-mediated reactions to expand their applications, leveraging the success of phenothiazine-based PCs in sulfur-centered radical photoredox reactions.

Wang *et al.* (2024) developed a technique for producing α-fluoracrylates (**226**) from *gem*-difluorostyrenes (**224**) utilizing formate salts (**225**) as a carbon source, as shown in Fig. 75.[259] This method produces the (Z)-type α-fluoracrylate framework without using transition metals and with high regioselectivity. Mechanistic investigations found that the carbon sources for the defluorinative carboxylation include sodium formate and potassium carbonate, with successive photoexcitation presumably performing a part in the SET defluorination of *gem*-difluoroalkene. Furthermore, 4DPAIPN and its chloro- or bromo-substituted variants were efficient photocatalysts in this process. Future studies will focus on researching photocatalytic reactions using halogen-containing dyes.[259]

Strehmel *et al.* (2024) worked on the confinement of carbon dots (CDs), which resulted in light-sensitive materials capable of forming triplet states, evidenced by the prolonged afterglow of TADF and RTP.[260] This enabled metal-free photo-ATRP (afterglow room temperature phosphorescence) based on

a reductive mechanism as shown in Fig. 76. Triplet states play a crucial role in the mechanistic setup, as their spin orientation delays electron back-transfer reactions. Photo-CIDNP (photo-chemically induced dynamic nuclear polarization) studies could enhance understanding in this area. Notably, this approach worked well with confined carbon dots derived from cellulose, while materials without confinement, such as CMCCDs, did not exhibit either TADF or RTP. No heavy atoms were involved in triplet formation. Future work could focus on altering the confinement matrix to increase TADF and RTP efficiency. Materials with ordered structures, whether from synthetic or biomaterials, might be promising candidates. Photopolymerization experiments also demonstrated the distinct behavior of these heterogeneous systems compared to those in homogeneous environments. More exploratory studies are needed to understand the surface morphology of particles used for polymer synthesis. Unwanted chain growth could be mitigated by adding small amounts of CuBr$_2$/L, which improved selectivity during polymerization. However, this compromised the advantage of a metal-free photo-ATRP system, which could be beneficial for some electronic applications, even though small amounts of CuBr$_2$/L drastically alter the system. Future research should clarify how this metal cocatalyst interacts with the confined material at the surface, explaining the reactivity differences between a metal-free system and one containing CMCCDs@SiO$_2$/CuBr$_2$/L. Additionally, strategies should be developed to keep the photocatalyst surface active throughout the process. Recycling is another intriguing feature offered by
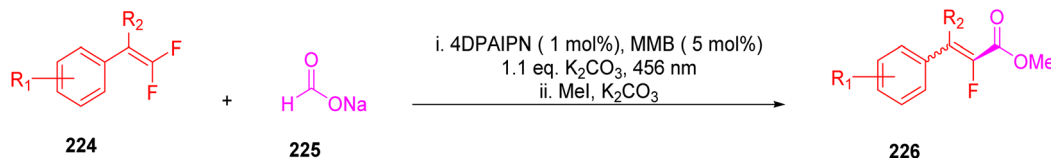
Fig. 75 Production of α-fluoracrylates (**226**) *via* a redox photocatalytic process.[259]
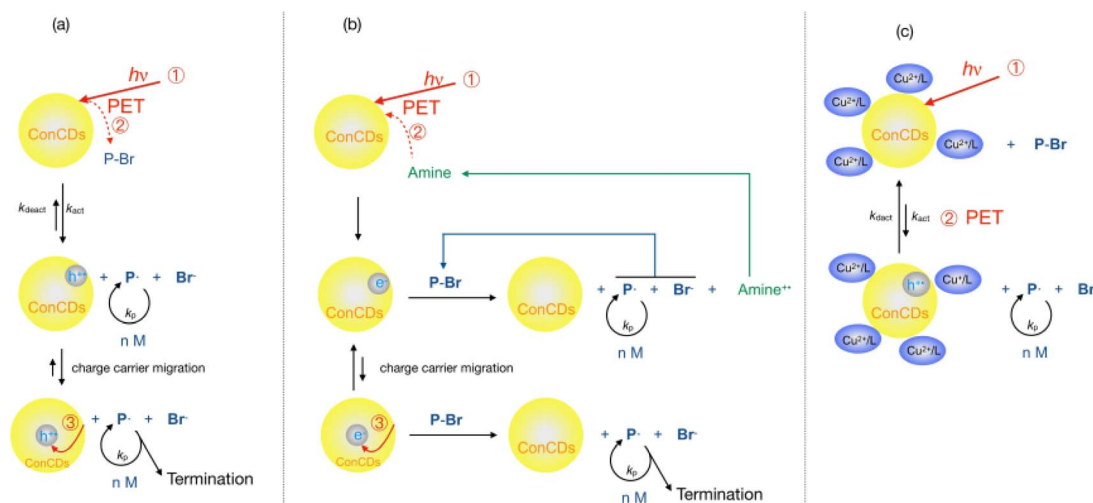

Fig. 76 Participation of confined CMCCDs@SiO$_2$ (ConCDs) in a metal-free photopolymerization following (a) an oxidative mechanism or (b) a reductive mechanism in an ATRP setup. (c) The addition of Cu^{2+} to ConCDs.[260]

these confined materials. CDs do not offer this feature due to their much smaller size, making this aspect worthy of more attention in future work to design greener systems.

4.3. Applications of TADF materials in OLEDs

The TADF emitter component of OLEDs is generally distributed at a low concentration in an appropriate substrate matrix. This technique is aimed at reducing aggregation-caused quenching (ACQ) and TTA, resulting in improved EL performance. As a result, it is vital to construct host materials with specific properties:

(i) A high triplet energy (E_T) in the host material is crucial to inhibit energy transfer from the TADF emitter back towards the host, not dependent on emission color.

(ii) Proper alignment of HOMO and LUMO is essential to confirm efficient charge transfer from adjacent layers.

(iii) Maximizing direct charge capture on the doped emitter, by increasing the energy gap between the HOMO and LUMO.

(iv) Both positive and negative charge transport properties are critical for achieving an equitable balance of electrons and holes in the emitting layer.

(v) Exhibiting high structural stability and excellent film properties.[104]

Numerous materials, notably bipolar host materials, have attracted substantial interest for their potential in efficient TADF-based OLEDs and have become a key aspect of OLED research.[261]

TADF materials have gained significant attention due to their ability to harness triplet excitons for high-efficiency OLEDs. A progressive approach to their application necessitates a structured classification based on emission color, quantum yield enhancement strategies, and mechanisms facilitating efficient RISC.

4.3.1. Classification of light colors in TADF emitters. TADF materials can be systematically categorized based on their emission wavelengths, which are governed by the molecular structure and D–A configuration. Blue TADF emitters typically feature strong electron-withdrawing acceptors to maintain a large singlet–triplet energy gap (ΔE_{ST}), whereas green and red TADF emitters often incorporate extended conjugation or heavy-atom effects to modulate emission properties. Recent advancements have focused on the development of deep-blue TADF emitters with narrowband emissions, essential for high-purity OLED displays.[262–264]

4.3.2. Strategies for quantum yield improvement. The EQE of TADF-OLEDs is heavily influenced by the PLQY of the emitter. Several approaches have been employed to optimize PLQY, including:

➢ Rigidity enhancement through π-extended frameworks to reduce non-radiative decay.

➢ Host–guest interactions in OLED devices to suppress aggregation-induced quenching.

➢ Excited-state engineering *via* intramolecular charge-transfer tuning to balance radiative and non-radiative pathways.[265,266]
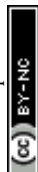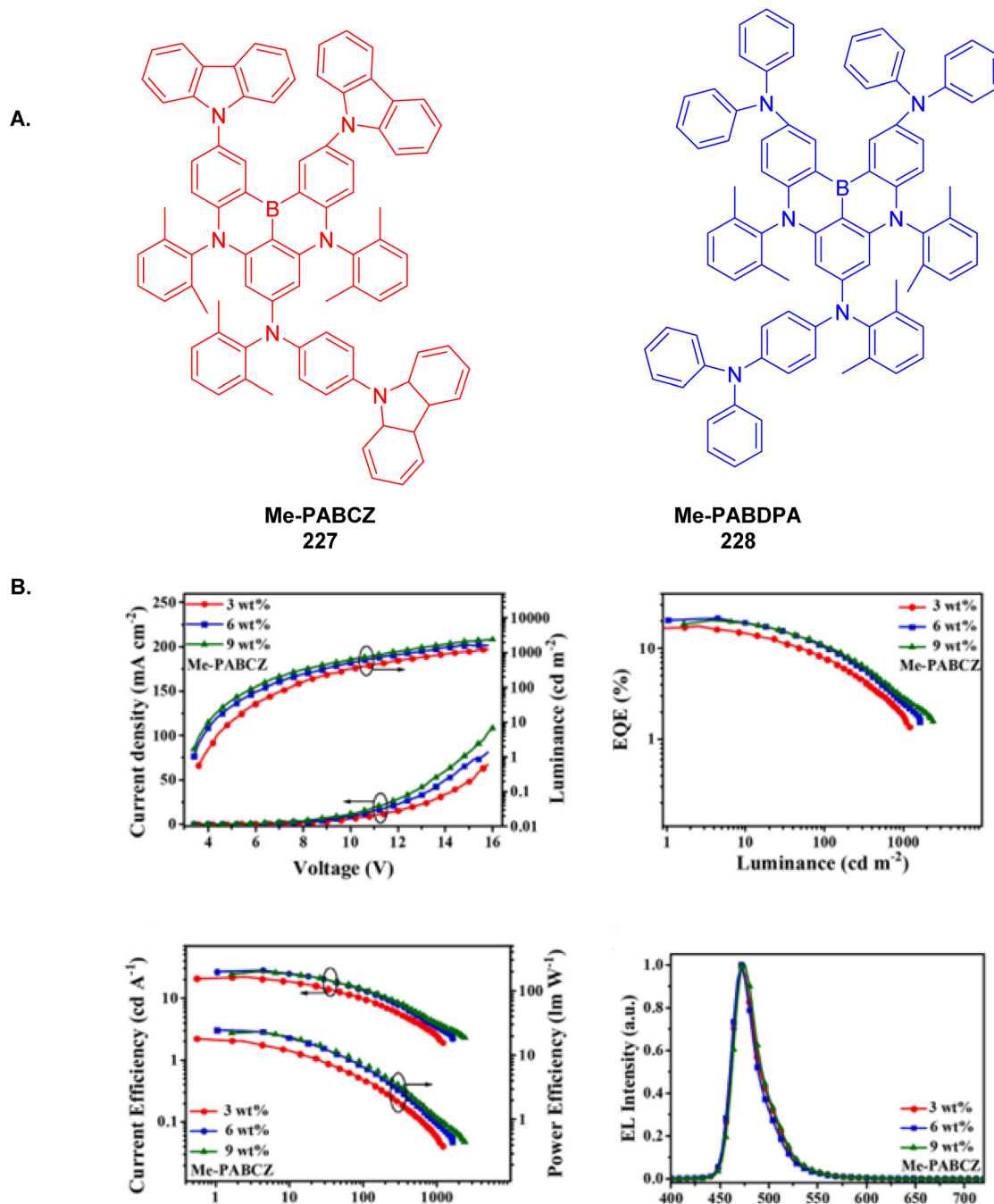
Fig. 77 (A) Chemical structures of PAB, Me-PABCZ, and Me-PABDPA (B) EL characteristics of Me-PABCZ based OLEDs using different doping concentrations: current J–V–L characteristics; EQE–luminance curves; current efficiency–luminance–power efficiency curves; normalized EL spectra at 6 V.

4.3.3. Promotion of RISC processes. Efficient RISC is crucial for high-performance TADF materials, as it facilitates the upconversion of triplet excitons to the emissive singlet state. Strategies for RISC promotion include:

➢ Minimizing ΔE_{ST} through optimal D–A spatial separation while maintaining strong orbital overlap.

➢ Utilizing high-spin–orbit coupling (SOC) elements or second-order vibronic coupling to accelerate the intersystem crossing dynamics.

➢ Designing multi-resonance TADF molecules to achieve fast and efficient RISC *via* intermediate charge-transfer states.[267]

By integrating these progressive aspects into TADF material design, researchers continue to refine the structure–property relationships governing OLED efficiency, paving the way for next-generation display and lighting technologies.

In 2017, Chi *et al.* reviewed the applications of TADF-emitting molecules in OLEDs.[105] In this section, the
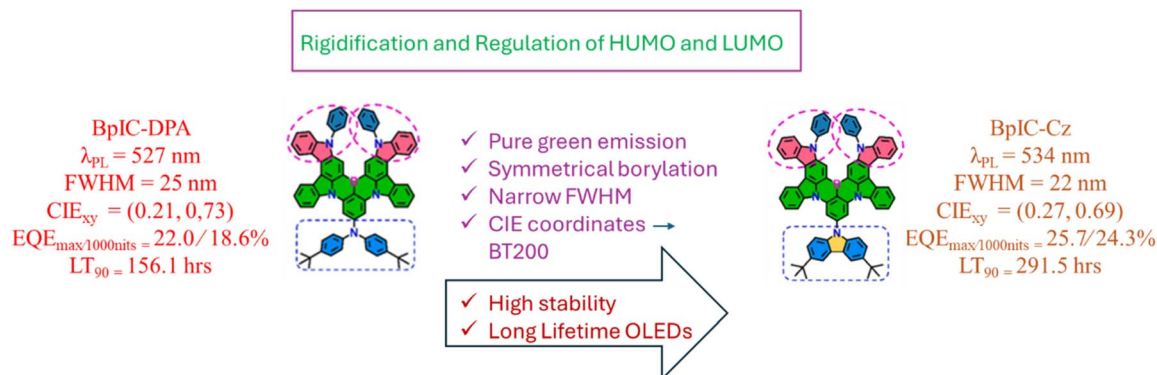
Fig. 78 The molecular structures of green emissive B/N type MR emitters and designed polycyclo-heteraborin MR-TADF materials BpIC-DPA and BpIC-Cz.
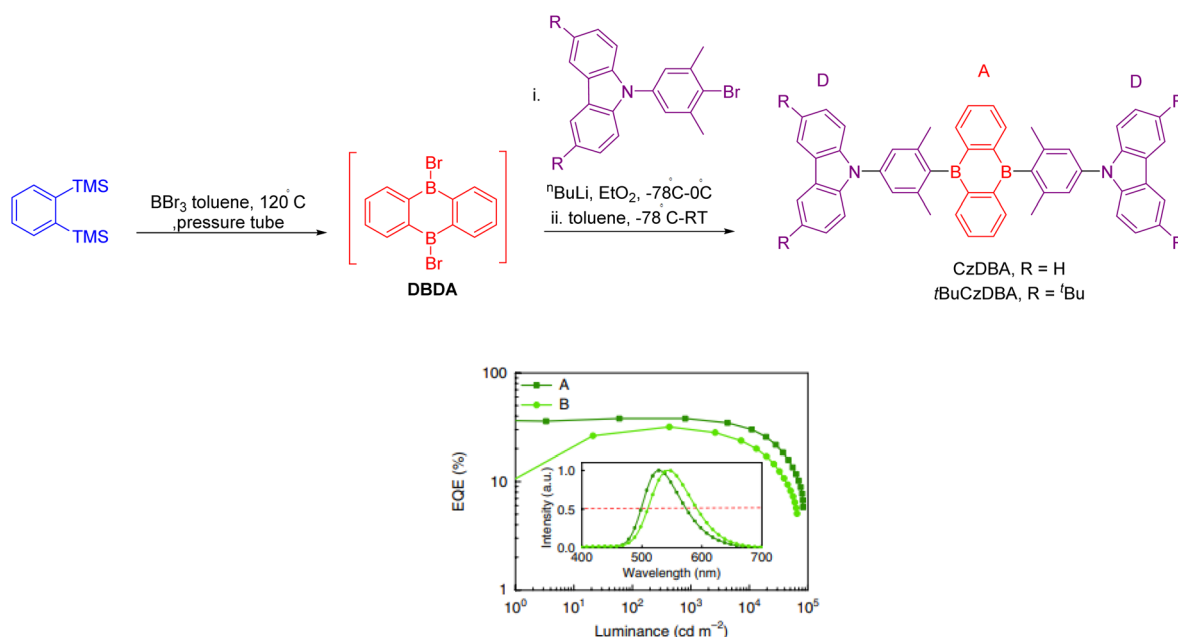

Fig. 79 Synthetic route of CzDBA and tBuCzDBA and along with external quantum efficiency *versus* luminance electroluminescent spectra.[270]

applications of TADF molecules in OLEDs from 2019 to 2024 are examined.

Wang and his coworkers (2024) studied multiple resonance TADF materials which represent remarkable applications such as high color purity and high-resolution OLEDs display. They worked on two new MR-TADF emitters Me-PABCZ **227** and Me-PABDPA **228** with PLQYs of 94.6% and 91.8% respectively, that are synthesized by using one-shot electrophilic C–H borylation reaction. The ideal device had narrow emission spectra with an FWHM of 36 nm, CIE coordinates of 0.14, and 0.57, and a maximum EQE of 27.9% as shown in Fig. 77. This study extends the versatile use of MR-TADF luminogens in electroluminescent devices and offers a novel concept for their molecular structure construction.[268]

In this study, Kwon and colleagues (2024) employed a molecular design strategy focused on rigidifying the boron-embedded polycyclic heteraborin core and regulating

molecular orbitals to achieve ultra-pure green emission. Two MR emitters, BpIC-DPA and BpIC-Cz, were produced by combining fused curvilinear indolocarbazoles with peripheral *tert*-butyl substituted carbazole/diphenylamine donors. The produced symmetrical heteraborins had incredibly narrow FWHMs of 25 and 22 nm, respectively, along with exceedingly rigid molecular structures and pure green emission at 527 and 534 nm. With matching CIE coordinates of (0.21, 0.73), BpIC-DPA demonstrated the purest green emission of the two materials, meeting the BT2020 green color criteria. A high PLQY of more than 84% is displayed by both emitters. The designed OLEDs based on these emitters have optimum efficiencies of over 22.0% and ultra-roll-off characteristics. The BpIC-Cz-based device had an operational lifetime (LT_{90}) of 291 hours at an initial brightness of 1000 cd m^{-2}. This is the longest lifetime achieved for pure green narrowband OLEDs. In the future these design tactics will continue to steer the investigation of
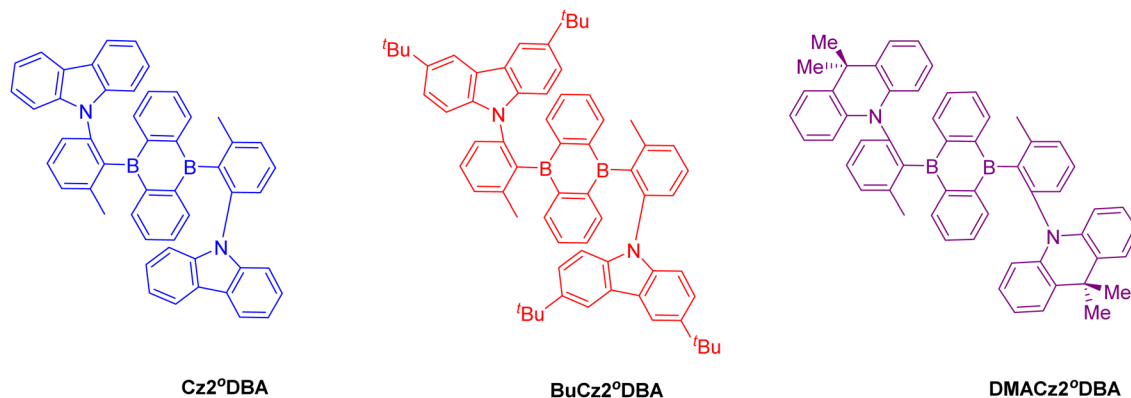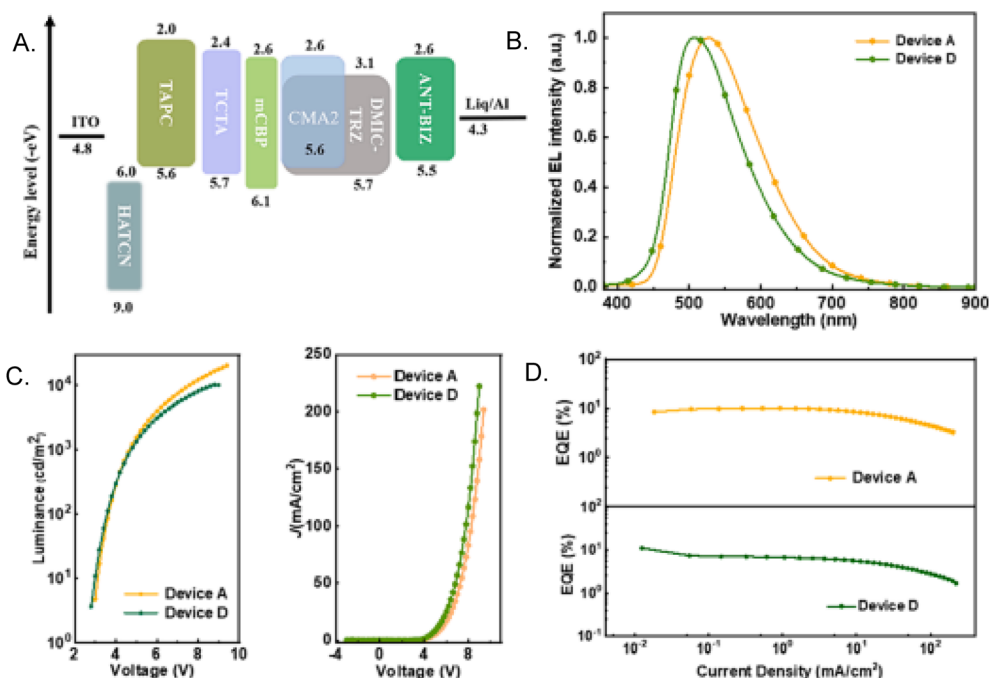
Fig. 80 Different diboron-based D−A TADF systems.[271]

Fig. 81 (A) Device structure and energy level diagram. (B) EL spectra of devices A and D. (C) Luminance−voltage, current density−voltage, and (D) EQE−current density curves of devices A and D.

extremely efficient and reliable MR-TADF heteraborins with full-color narrowband emissions, resulting in highly efficient OLEDs with great color purity (Fig. 78).[269]

Cheng *et al.* (2018) worked on two rod-like D–A–D-type DBA derivatives with carbazole groups, CzDBA and *t*BuCzDBA, which were produced through a facile two-step method for DBA compounds (Fig. 79). Excellent PLQYs and TADF properties, such as very tiny ΔE_{ST}, short, delayed fluorescence lifespan τ_d, and high horizontal emission dipole orientations, are displayed by the two DBA derivatives. Green electroluminescent device A (CIE 1931 coordinates (0.31, 0.61)) has achieved a record-low efficiency roll-off (only 0.3% roll-off of the EQE at 1 000 cd m^{-2}) and a record-high EQE of 37.8 $\pm$ 0.6% as shown in Fig. 79. For TADF materials, the DBA core is an exceptional electron-accepting group that can provide excellent PLQY. It offers

a foundation for the next molecular designs of extremely effective TADF-based OLEDs.[270]

Lee *et al.* (2020) demonstrated that *ortho*-donor–acceptor–donor (D–A–D) compounds, incorporating a 9,10-diboraanthracene (DBA) acceptor functionalized with *ortho*-donor groups (Cz, BuCz, and DMAC), can exhibit strong TADF with emission spanning from green to red. Computational studies corroborated the crystal structure study, which showed twisted conformations between donors and DBA moieties as well as the presence of weak intramolecular N···B nonbonding interactions. While DMAC-substituted compound DMACz2^{o}DBA was somewhat emissive (PLQY = 44%) in a stiff state, compounds Cz2^{o}DBA and BuCz2^{o}DBA containing Cz displayed significant PLQYs that approached 100%. Highly effective green-to-red TADF-OLEDs were achieved by using *ortho*-D–A–D compounds

as emitters. Above 100 lm W^{-1}, the device with a green emitter Cz2^{o}DBA demonstrated exceptional power efficiency and a very high ECE of 26.6%. With an EL peak at 615 nm, a red OLED device based on emitter DMACz2^{o}DBA attained a maximum EQE of 10.1%, which was like that of red OLEDs doped with boron that has been reported. The creation of extremely effective green-to-red TADF-OLEDs that utilize emitters containing boron (Fig. 80).[271]

For the first time, a new class of Cu(I) exciplexes was created by combining Cu(I) CMA complexes with DMIC-TRZ studied by Gong *et al.* (2024). Because of the intermolecular through-space charge transfer process, these Cu(I) exciplexes displayed unique TADF characteristics. The emission colors and exciton durations of the Cu(I) exciplexes can be controlled by adjusting the donor ligands of Cu(I) CMA complexes. The copper atom is essential to the production of these exciplexes, as demonstrated by experimental research and theoretical computations. This is because the core copper atom subtly participates in border molecular orbitals. Additionally, it has been shown that certain named conformations of CMA complexes promote the creation of exciplexes. Both emitters and hosts for OLEDs can be found in the class of Cu(I) exciplexes. The OLED that used Cu(I) exciplex as the emitter among them produced a high EQE of 10.9%. With low driving voltages of less than 3 V, the OLEDs that used MR-TADF molecules as guest emitters and Cu(I) exciplexes as host materials produced remarkable EVEs of up to 24.9% as shown in Fig. 81. In the future, this work opens up a wide range

of possible uses for coinage-metal-based exciplexes in addition to presenting a novel design approach for the creation of Cu(I)-based emitters using intermolecular charge transfer.[272]

The ink optimization for printing *t*BuCzDBA as an emitting layer in OLEDs has been documented in this study by Mariano *et al.* (2024). To get the ideal printed thin film, a suitable blend of three solvents (toluene, chloroform, and *o*-dichlorobenzene) with varying surface tensions was used. This created Marangoni flows in the wet film and facilitated a consistent and quick drying process. Since chlorinated solvents and other widely used printing solvents are hazardous to both humans and the environment, they can undoubtedly hinder industrial scalability. However, they are still a necessary component of industrial processes and the creation of organic materials for optoelectronic devices. With the optimized solvent formulation, the printed *t*BuCzDBA emissive layer demonstrated excellent morphology and minimal roughness. This film exhibits TADF features, according to the time-resolved photophysical analysis. The thin film produced by inkjet printing was used as an emissive layer in an OLED structure, adjusting the *t*BuCzD concentration in the ink to achieve the ideal film thickness and device functionality. The device with 18 nm of *t*BuCzDBA demonstrated an EQE of 10%, a maximum luminance of 32 000 cd m^{-2} at 13 V, and a max-CE of 27.5 cd A^{-1} as shown in Fig. 82. The presented findings show that the ideal ink formulation can be regarded as a potent instrument for effortless inkjet printing small molecule active layers in OLEDs, attaining superior
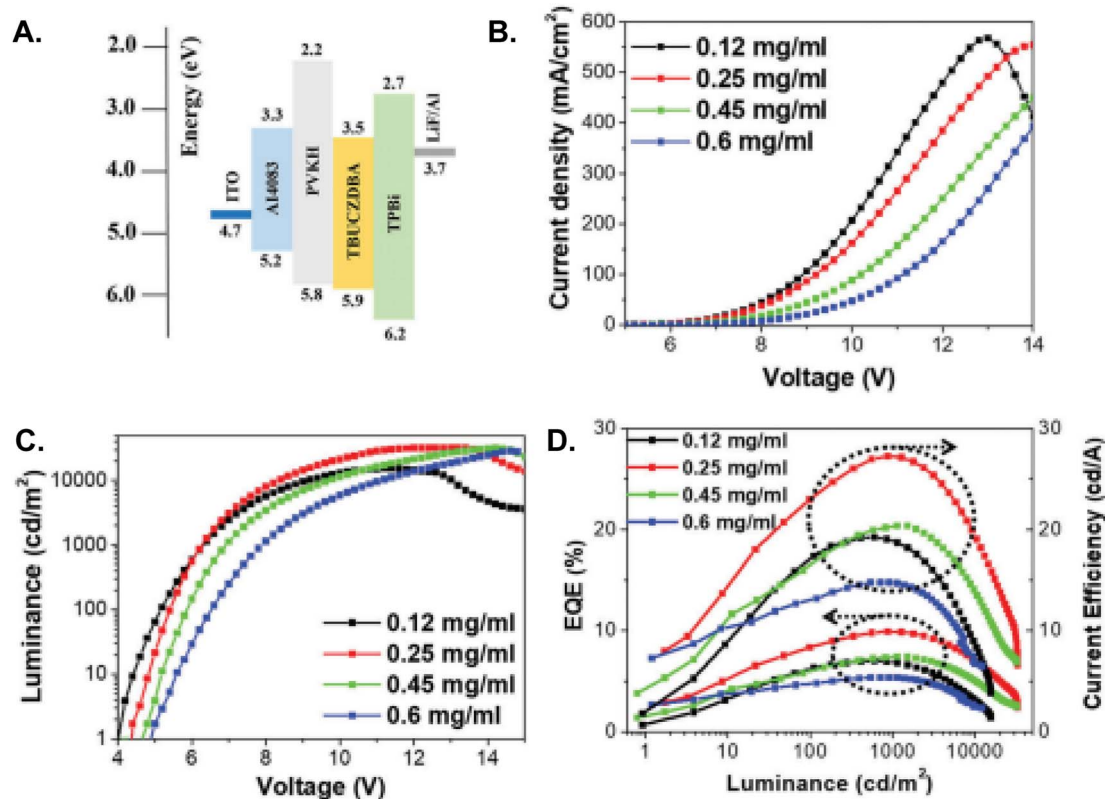
Fig. 82 Characterization of OLED device with different thicknesses of inkjet printed *t*BuCzDBA film as the active layer (A) device architecture and energy level diagram of the prepared OLEDs (B) current density *versus* voltage, (C) luminance *versus* voltage, and (D) efficiency *versus* luminance characteristics.

229

X= 0.01   PCzDBN1 **229 a**
X= 0.02   PCzDBN2 **229 b**
X= 0.03   PCzDBN3 **229 c**
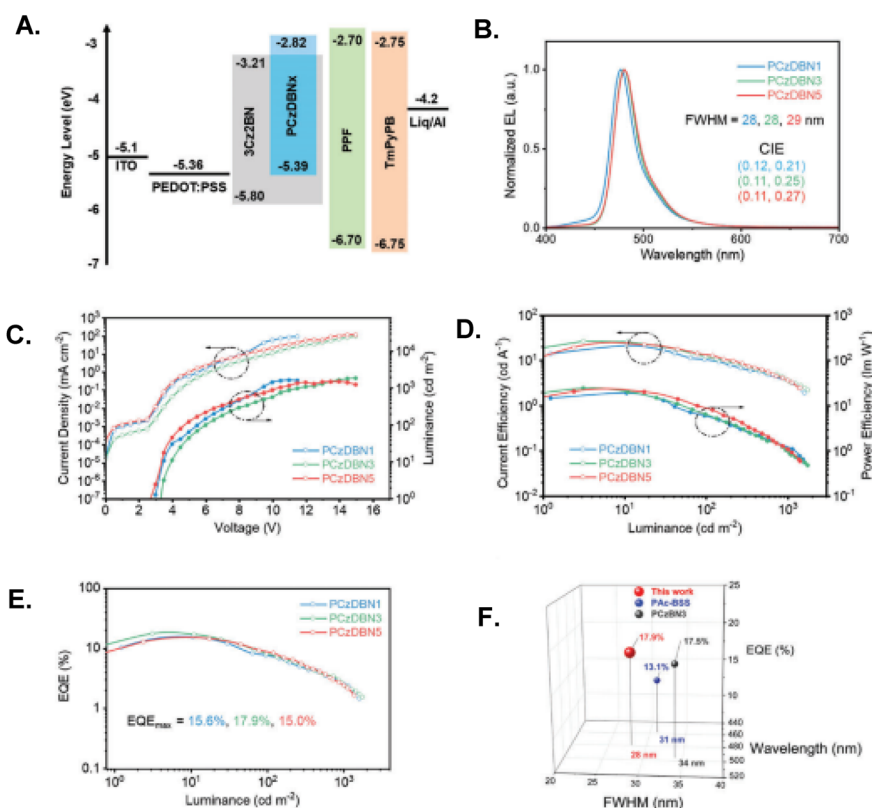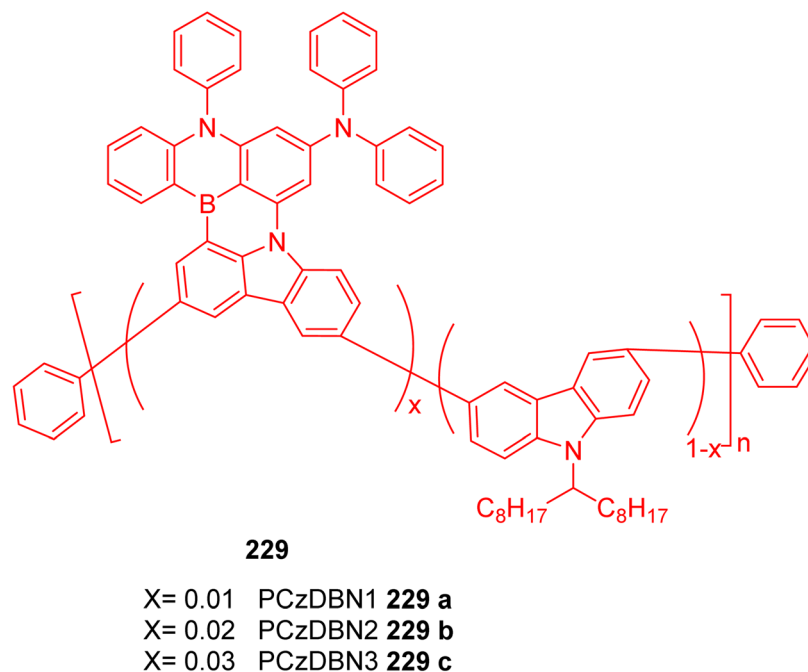
Fig. 83 Chemical structure of (A) device architecture and energy level diagram of the prepared OLEDs (B) current density *versus* voltage, (C) luminance *versus* voltage, and (D) current efficiency–luminance–power efficiency characteristics (CE–L–PE) (E) external quantum efficiency luminance plots (F) summary of the EQE *versus* EL peak wavelength and FWHM plots for the reported narrowband emissive TADF polymer OLEDs.

optical, electro-optical, and morphological characteristics. The design of an OLED can be made simpler by the potential use of a self-hosted material in the emissive layer. Furthermore, OLED technology can now be used in a wider range of industries at much lower costs because of solution-based, inexpensive, and industrially scalable manufacturing procedures.[273]

✓ Red shift PL and EL
✓ Green narrowband emission
✓ Increased Φ_{DF}
✓ Improved Performance

PCzTBN5
230

PCzTBN5 λ_{PL} = 517 nm   FWHM = 46 nm
λ_{EL} = 511 nm   FWHM = 44 nm
EQE_{max} = 22.2%
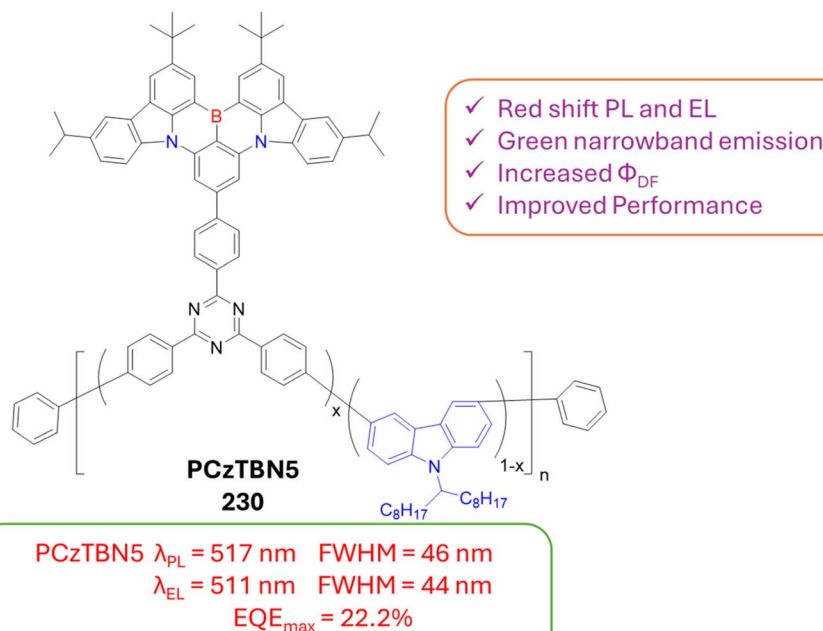
Fig. 84 Green MR-TADF and its attachment with MR emitting moiety acts as a pendant to an acceptor triphenyltriazine and simultaneously embeds acceptor moiety into polycarbazole backbone.

By integrating a blue MR-TADF unit into the main poly-carbazole chain, a general and efficient method for creating blue narrowband TADF conjugated polymers was studied by Yang *et al.* (2024). In the toluene solution, the conjugated polymers PCzDBNx **229** effectively produced narrowband blue emissions with emission peaks at 474 nm and FWHMs of

Enhanced the Molecular orientation via a peripheral decoration strategy

Decorating Unit

Connecting
232

Diphenyltriazine Group
Planar Structure
Electron-withdrawing ability
Good Optoelectronic Properties

N-para Decoration
Maintained Blue Emission
Narrowband Preservation
Planar Expansion

MR Core

$\Theta// = 73\%$

DPACzBN2
231

$\Theta// = 98\%$

3QCzBN
233

λ_{PL} = 464 nm
FWHM = 22 nm

Fig. 85 Chemical structure and molecular design strategy of 3QCzBN.

Fig. 86 Molecular design strategy of BN–Cz-based MR-TADF emitters and chemical structures of BN-R1, BN-R2 and BN-R3.

23 nm. With an EQE$_{max}$ of 17.9% and an FWHM of only 28 nm, the devices based on these polymers demonstrated outstanding EL cha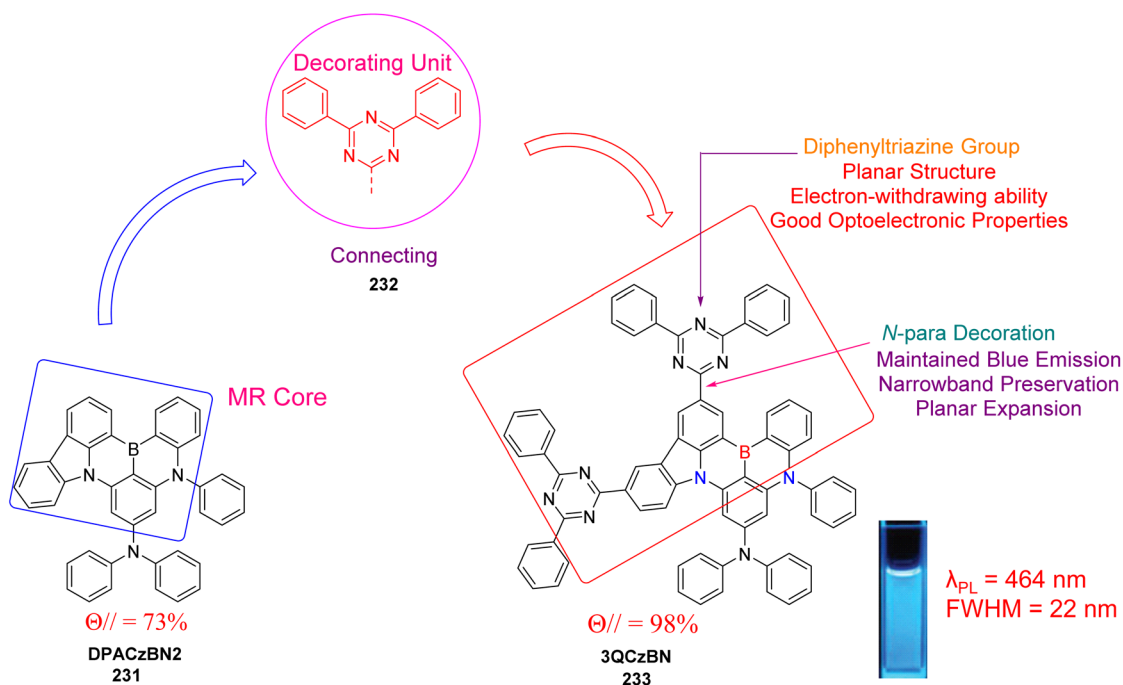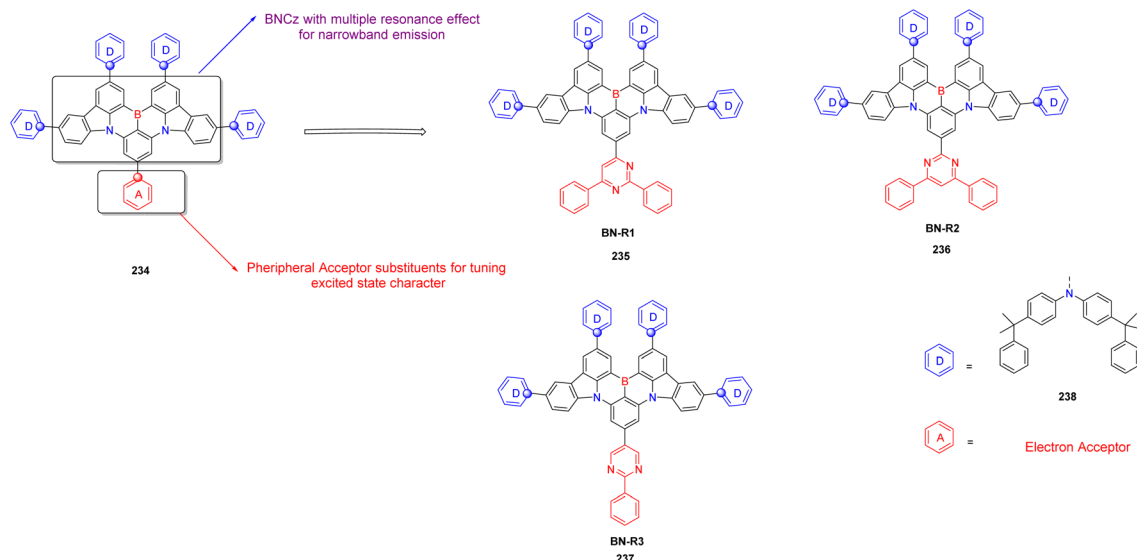racteristics, leveraging the narrowband emission and good TADF features as shown in Fig. 83. This is the first instance of a narrowband TADF conjugated polymer in the blue area that they are aware and think that intriguing outcomes and the molecular design idea will direct the development of narrowband emissive TADF polymers in the future, leading to high-performance solution-processable OLEDs.[274]

Yang *et al.* (2024) showed that creating green MR-TADF **230** conjugated polymers is possible as shown in Fig. 84. This method entailed embedding the acceptor moiety into the conjugated backbone and concurrently attaching a bluish-green MR emitting moiety as a pendant to an acceptor triphenyltriazine. Gaining from the improved ICT interaction with the addition of triphenyltriazine to the B atom's *para* carbon in the MR unit, as well as prolonged. All produced polymers showed red-shifted PL spectra in comparison to the pendant MR emitting moiety, indicating a conjugation effect along the polymeric backbone. These polymers' narrowband green emissions were indicated by their PL emission peaks, which ranged from 505 to 517 nm, and corresponding FWHMs, which were in the 46–48 nm range. With a record-high EQEmax of 22.2% among the MR-TADF polymer-based narrowband OLEDs, the EL devices based on these polymers demonstrated exceptional EL performance. It is anticipated that this work will encourage further researchers to investigate the MR-TADF polymers, which are incredibly effective.[275]

The effective implementation of a molecular design strategy for high-performance blue MR-TADF materials involved affixing a planar electron-acceptor group to the MR framework's HOMO-distributed carbon atom designed by Yang *et al.* (2024) as shown in Fig. 85. The produced emitter 3QCzBN was provided with narrowband blue emission, high PLQY, and good TADF qualities inherited from the parent MR molecule due to the special capabilities of the decorating DPTRZ group. Additionally, it

achieved increased molecule planarity, which resulted in an almost perfect Θ// of 98%. The outcome was a blue emission with a peak at 476 nm, a high EQE$_{max}$ value of 25.2%, and an efficient suppression of efficiency roll-off in the manufactured non-sensitized binary OLED using 3QCzBN as an emitter. Notably, 3QCzBN-based HF OLED achieved a notable improvement in EQE with the help of a TADF sensitizer, reaching 34.8% at its maximum and sustaining 26.5% at a brightness of 1000 cd m^{-2}. The 3QCzBN-based devices' two EQE$_{max}$ values significantly outperformed their parent MR molecule equivalent. This work presents a straightforward yet effective method for creating high-performance MRTADF materials and emphasizes the critical role that molecule orientation plays in determining the EQE of OLEDs.[276]

Bi *et al.* (2024) suggested using the FMOE strategy to control several pyrimidine derivatives to create orange-red MR-TADF emitters with decreased aggregation-caused quenching simply and practically. Consequently, the newly designed emitters successfully prevented spectrum and aggregation quenching. Because of their twisted molecular topologies caused by the addition of large terminal substituents on the MR framework, they exhibit broadening characteristics in the solid state. Furthermore, by altering the electronic structure to varied degrees with the electron-withdrawing ability of peripheral acceptor substitutes, the emitter's PL spectra could be realized with precise orange-red emission while maintaining the narrowband emission and small ΔE$_{ST}$S characteristics. Solution-processed OLEDs with sensitizers showed good EL performance, with maximum ECEs of 19.0%, 20.4%, and 20.4% for BN-R1 **235**, BN-R2 **236**, and BN-R3 **237** respectively, as well as high color purity orange-red light with CIE coordinates of 0.663, 0.337, 0.606, 0.393, and 0.553, 0.44 as shown in Fig. 86. To satisfy the requirements of ultra-high-definition displays, our work offers an effective route for creating orange-red MR-TADF emitters and is anticipated to stimulate more research efforts
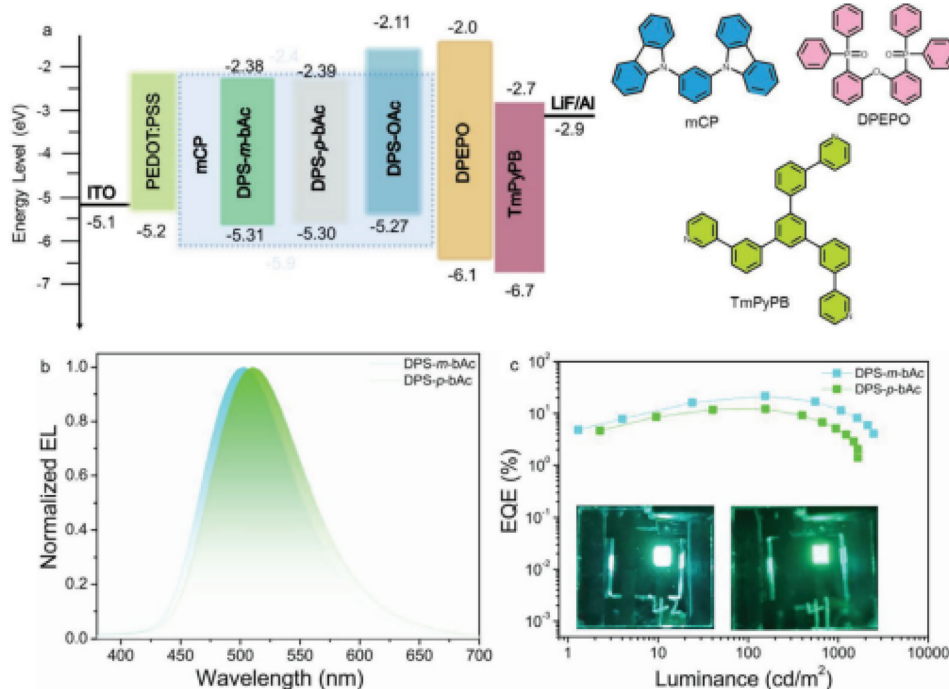
Fig. 87 The energy levels, molecular structures in the device, and device performance. (a) energy levels of the device; (b) molecular structures; (c) EL spectra of the devices; (d) EQE–current density curves. (Inset) The images of the devices (left is DPS-*m*-bAc, and right is DPS-*p*-bAc).

toward the production of a wider spectrum of narrowband emitters.[277]

Zhu *et al.* (2024) resolved the question of why certain emitters appear to exhibit a negative singlet–triplet energy gap. Three carefully tailored organic emitters—DPS-*m*-bAc, DPS-*p*-bAc, and DPS-OAc—were created and thoroughly characterized for this purpose. The TADF and AIEE characteristics of all three compounds were evident. While DPS-*m*-bAc and DPS-*p*-bAc have
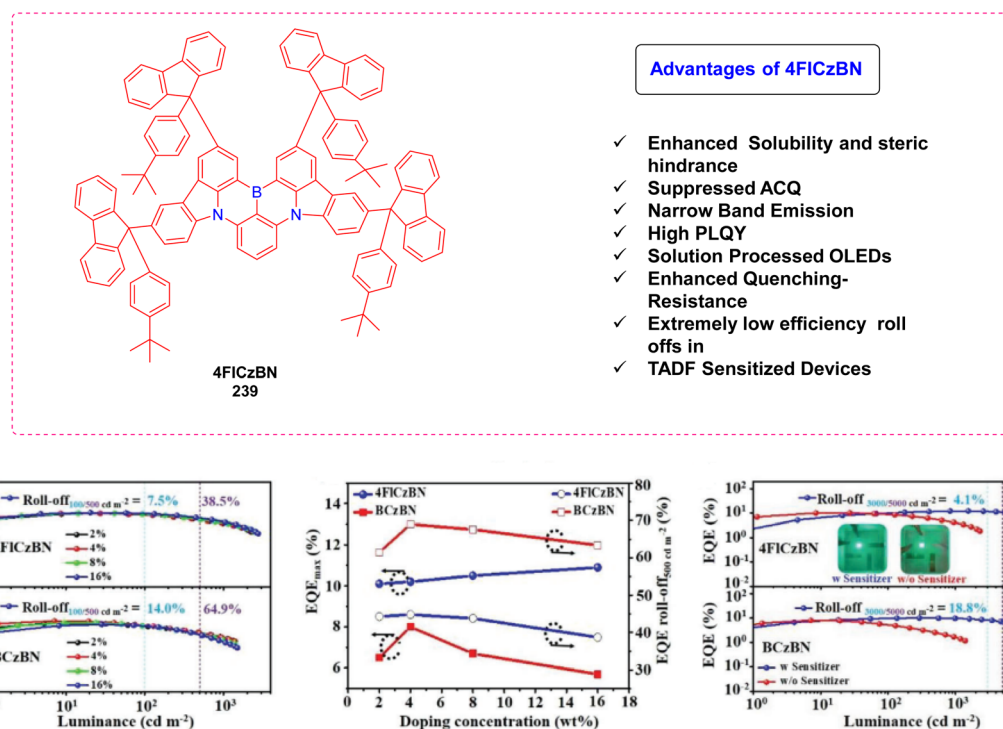
Fig. 88 Chemical representation and advantages of 4FICzBN and EQE electroluminescence characteristics of the material.
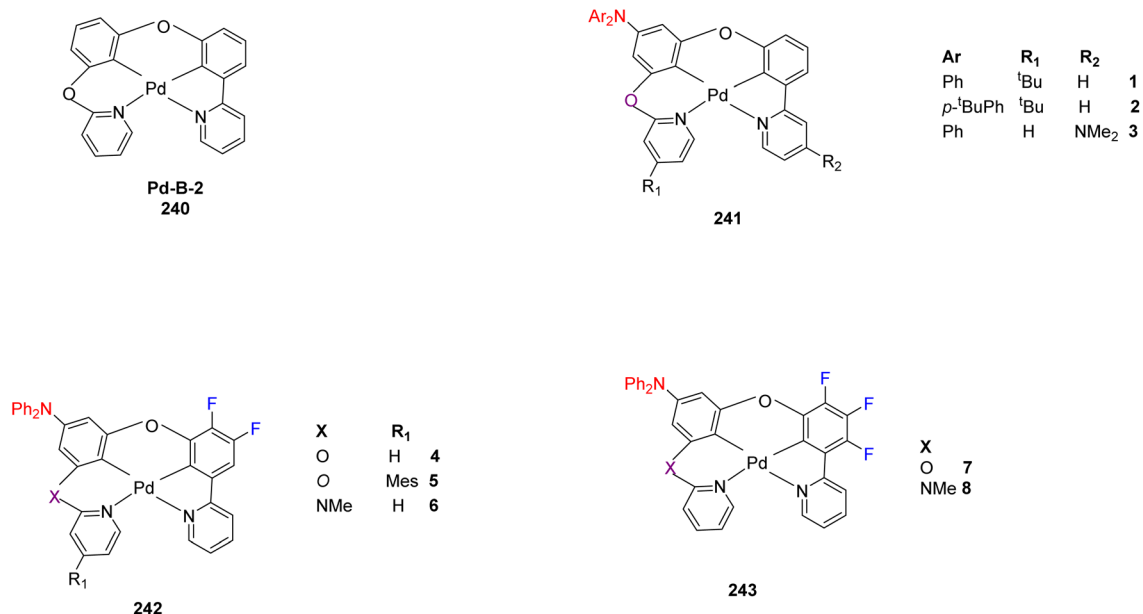
Fig. 89 Chemical representation of Pd−B-2 and tetradentate Pd(II) emitters.

two ICT states—the ICT_{high} and ICT_{low} states—DPS-OAc only has the ICT_{high} state, making it a reference for the $^1ICT_{high}$ and $^3ICT_{high}$ energies, according to an examination of the absorption spectra in solution. The through-bond nature of this ICT state results in a relatively large gap between the $^1ICT_{high}$ and $^3ICT_{high}$ states, whereas time-resolved photoluminescence
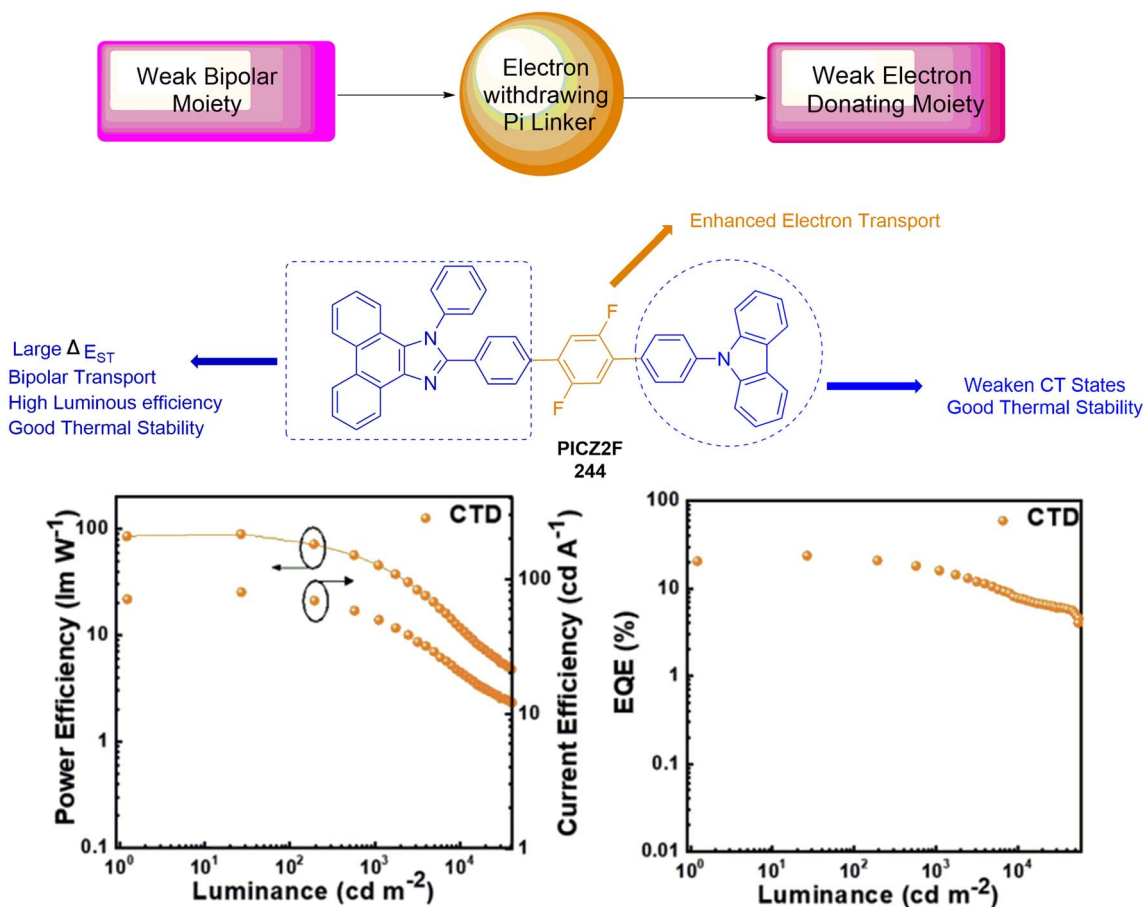
Fig. 90 Molecular representation and design concept of PICZ2F along with EL characteristics.

studies (conducted at both 5 and 80 K) show that $^3ICT_{low}$ and $^1ICT_{low}$ are nearly isoenergetic due to some through-space contribution to this ICT state. Crucially, internal conversion between the higher and lower ^3ICT states is slower than phosphorescence from $^3ICT_{high}$, and the $^3ICT_{high}$ state has a larger energy total than both $^1ICT_{low}$ and $^3ICT_{low}$. Therefore, in addition to the fluorescence from $^1ICT_{low}$, 77 K measurements also show phosphorescence from $^3ICT_{high}$. This could be mistakenly interpreted as a negative singlet–triplet gap, even though all of the compounds have very small but positive singlet–triplet gaps, as demonstrated by thorough time-resolved photoluminescence measurements conducted at 5 K. Because of its large TSCT impact and relatively modest TBCT effect, solid-state photophysical investigations reveal that DPS-*m*-bAc exhibits the greatest k_{RISC}, with a value on the order of 107 s^{-1}. Accordingly, with a slight efficiency roll-off, the solution-processed OLEDs based on DPS-*m*-bAc had the greatest EQE of 21.7% as shown in Fig. 87.[278]

Park *et al.* (2024) studies Encasing the planar MR core (CzBN) with large phenyl-fluorene (Fl) units effectively produced a solution-processable, ACQ-free MR emitter with strong PLQY and narrowband emission.

Even in highly doped films, it was discovered that the MR core of the target chemical, 4FlCzBN **239**, effectively inhibited interchromophore interactions. The spectrum broadening of 4FlCzBN in doped films, the red shift of emission spectra, and the ACQ were all greatly decreased because of this sterically shielded design. At different doping concentrations (2–16 weight percent), 4FlCzBN-based OLEDs produced by the solution technique demonstrated narrowband emission (28–30 nm) and EQE$_{max}$ values of 10.1–10.9%. Additionally, it was discovered that 4FlCzBN-based devices with TADF sensitizer greatly

reduced the efficiency roll-off and raised the EEQE$_{max}$ by up to 12.2% as shown in Fig. 88. In the future present approach involves creating solution processable and ACQ-free MR emitters offers important insights into the creation of several novel compounds with related functions.[279]

For the first time Cheng *et al.* (2024) worked on donor–acceptor type tetradentate Pd(II) emitters that exhibit strong TADF emission in solution and thin film, with quantum yields as high as 99% and k_r as high as 7.3 × 10^5 s^{-1} at ambient temperature as shown in Fig. 89. Such Pd(II)-TADF emitters are very efficient and adaptable, producing sky-blue TADF OLEDs and blue TADF-sensitized OLEDs with maximum EQEs of 24.8% and 23.1%, respectively. They also have low-efficiency roll-off at 1000 cd m^{-2}. Tetradentate Pd(II)-TADF complexes are a viable option for producing stable blue OLED emitters with great performance.[280]

Yan *et al.* (2024) have developed a novel deep blue hybridized local and charge-transfer (HLCT) fluorophore, PICZ2F **244**, characterized by high oscillator strength, a fast radiative decay rate (k_r), and bipolar charge transport properties. The doped device had an EQE of 7.10% with the desired CIE coordinate (0.155, 0.068), while the non-doped device had an EQE of 6.16% with reduced roll-off at a high brightness level of 15 000 cd m^{-2} (EQE 15000: 5.80%). A high-performance single-cell all-fluorescent CT-WOLED with a single-doped single-emissive-layer structure was accomplished by using PICZ2F as both a blue emitter and a universal host for the yellow TADF emitter. Along with a huge CCT span of 3749–18279 K, this device demonstrated remarkable efficiencies of 89.5 lm W^{-1}, 79.8 cd A^{-1}, and 23.73%, respectively as shown in Fig. 90. This work not only shows the significant potential of HLCT-type deep-blue materials as all-fluorescent WOLED emitters and hosts, but it
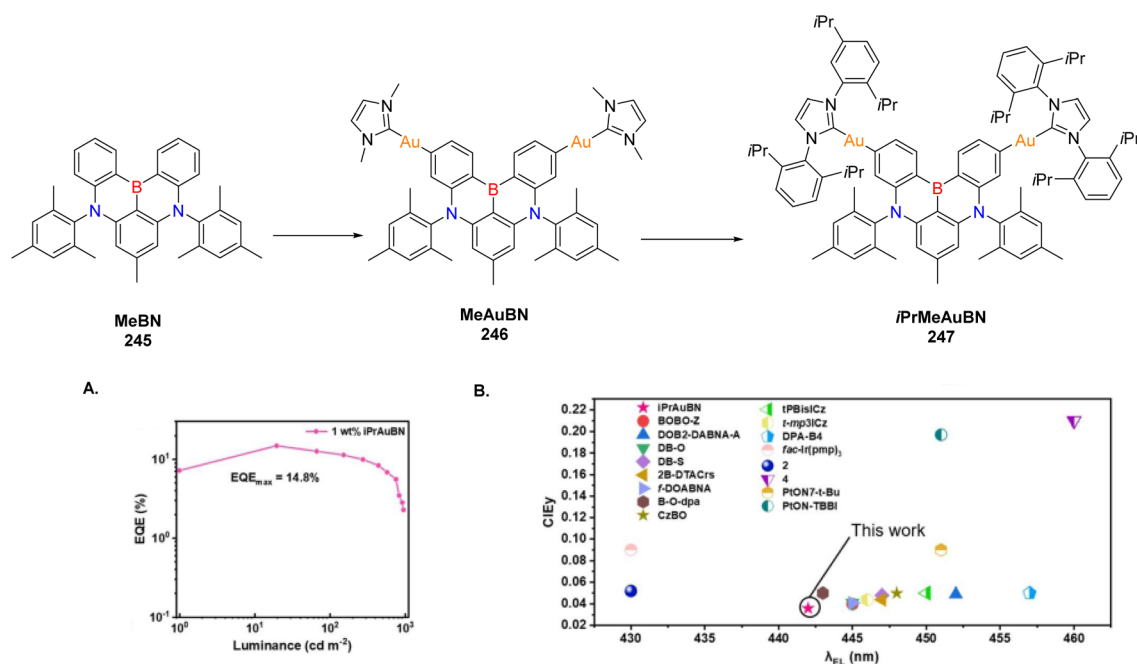
Fig. 91 Chemical representation of MeBN and di-nuclear Au(II) complexes (A) electroluminescence curve (B) CIEy coordinate *vs.* emission wavelength which indicates deep blue phosphorescent and MR-TADF OLEDs.
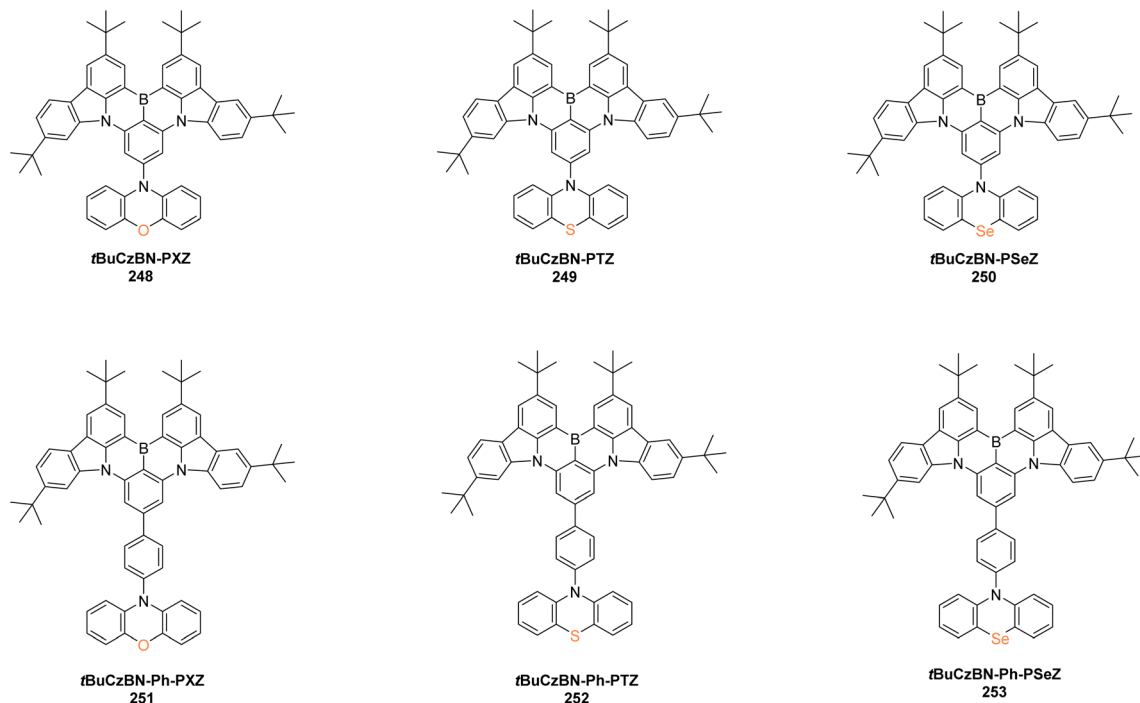
Fig. 92 Chemical representation of different TADF emitters.
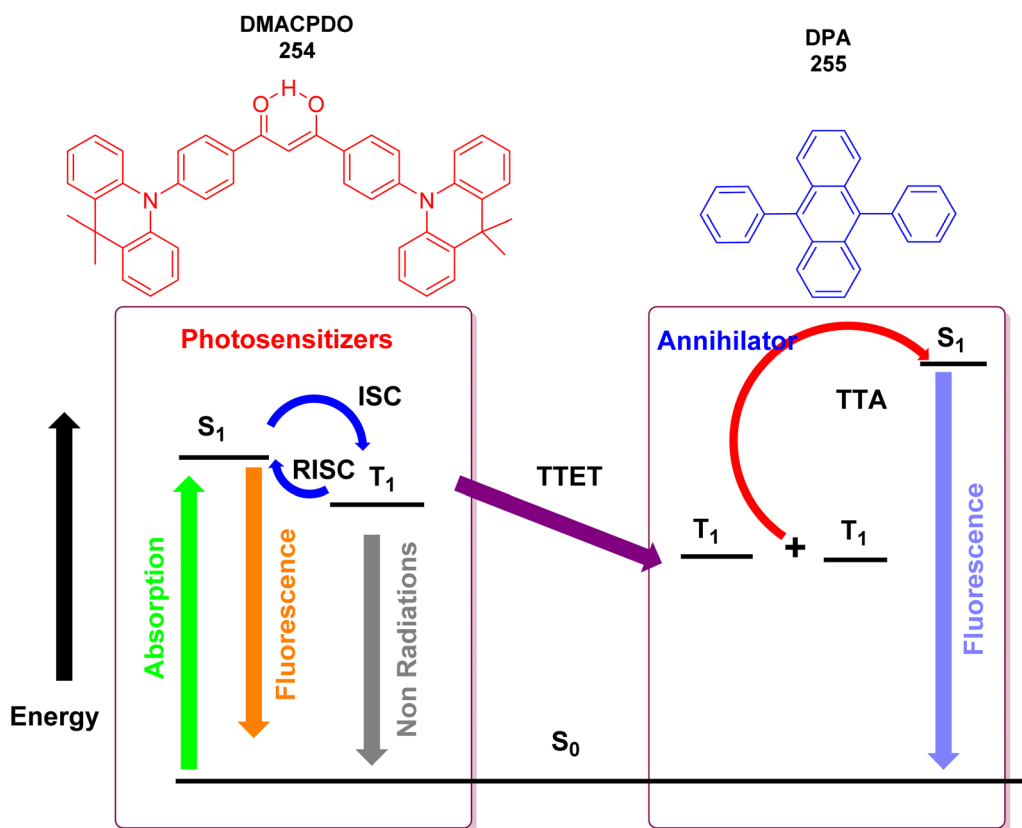
Fig. 93 Diagram depicting the TTA upconversion process between the TADF photosensitizer DMACPDO (**254**) and the annihilator DPA (**255**). Adapted from ref. 297 with permission from the Royal Society of Chemistry.

also offers a workable design approach for achieving straightforward and effective CT-WOLEDs, which could open the door for the use of all-fluorescent WOLEDs with color tuning in real-world applications.[281]

Yang *et al.* (2024) produced two deep blue-emitting dinuclear TADF-Au(I) complexes **246–247** using an MR-type B/N ligand. On the one hand, the participation of Au Orbitals in the S_1 state. Significantly improves the SOC effect between S_1 and T_1 states. The complexes had 8-fold lower delayed fluorescence lifetimes than the parent molecule. However, adding two Au atoms to the B/N MR skeleton's periphery positions does not affect color purity. The OLED with iPrAuBN emitter produces pure blue light with a maximum at 442 nm and FWHM of 19 nm, combining the CIE coordinates (0.154, 0.036) and EQE_{max} of 14.8% as shown in Fig. 91. This research suggests that combining MR skeletons with heavy metal atoms can create non-sensitized, high-performance ultrapure blue emitters.[282]

Yan *et al.* (2024) designed MR-TADF emitters with diverse electron-donating components to study the impact of LRCT and heavy-atom effects on excited states as shown in Fig. 92. They developed MR-TADF emitters by combining electron-donating units with the MR skeleton to study the impact of LRCT and heavy-atom effects on excited-state properties and energy levels. Photophysical properties, including quantum states and energy levels. Photophysical properties and quantum chemistry computations show that radiative decay and exciton-up conversion can be modulated. MR-TADF emitters have covalently bonded MR segments that donate electrons. The electron-donating ability of moieties allows for precise control over their excited-state properties. Enhanced LRCT in *t*BuCzBN-PXZ allows for spin-flipping of triplet excitons, quickening the RISC process while retaining narrow emission of the S_1 state. Research shows that LRCT is more effective than heavy-atom effects in influencing exciton dynamics in MR-TADF emitters with strong electron-donating units.

Adding a phenyl bridge between the MR segment and donor moiety weakens LRCT strength. The photophysical properties and quantum chemical simulations show that increasing the number of atoms leads to a significant increase in k_{RISC} values, indicating that the heavy-atom effect can accelerate the spin-flip of triplet excitons in MR-TADF emitters without modulatory LRCT states. Both *t*BuCzBN-PXZ **248** and *t*BuCzBN-Ph-PSeZ **253** have significantly higher k_{RISC} values (>2.0 × 10^5 s^{-1}) and near-unity photoluminescence quantum yields. The EQE_{max} values of *t*BuCzBN-PXZ and *t*BuCzBN-Ph-PSeZ-based solution-processable OLEDs reach 21.3% and 19.4%, respectively, placing them in the top tier of reported solution-processable MR TADF binary OLEDs without additional sensitizers. This study suggests a method for controlling the photoelectric characteristics of MR-TADF emitters by carefully managing LRCT and heavy-atom effects.[283]

4.4. Miscellaneous applications of TADF materials

Because TADF-based materials can effectively convert triplet excitons into singlet excitons, they are mainly utilized in OLEDs to improve performance. In addition to OLEDs, these materials find use in a few cutting-edge applications, including organic hybrid microwire radial heterojunctions, TTA sensitizers, ECL cells, UVOPDs, LEECs, multicolor luminous micelles, ML, and MLC. This adaptability highlights the wide range of applications for TADF-based materials in cutting-edge technological domains, which will be outlined below.

4.4.1. Triplet–triplet annihilation sensitizers (TTA). TTA involves two types of molecules: a sensitizer responsible for the absorption of low-energy photons for generation of triplet excitons, and an annihilator molecule that receives these excitons *via* Dexter energy transfer, thereby enabling the TTA process.[284] During the 1960s, there were numerous reports of delayed fluorescence in solutions containing aromatic hydrocarbons such as pyrene, phenanthrene, and anthracene. This phenomenon was linked to the formation of excited dimers, with the intensity of the fluorescence being proportional to the square of the rate of absorbed stimulating light. After the mechanism involving TADF was elucidated, the term "delayed luminescence resulting from quenching of triplet states" was introduced. This process is now commonly referred to as P-type or pyrene-type delayed fluorescence, or more specifically, triplet–triplet annihilation (TTA).[285] TTA sensitizers have found extensive applications in organic materials, including the development of organic light-emitting diodes (OLEDs) and solar cells. Triplet-polaron annihilation (TPA) and TTA between triplet excitons or between a triplet exciton and a polaron are easily observed due to the relatively long lifetimes of triplet excitons in phosphorescent and TADF-based emitters. These interactions can lead to the generation of highly energetic excited states, which in turn have the potential to cause molecular degradation. However, the use of TTA emitters, which exhibit delayed fluorescence, can prevent the formation of these high-energy states. The excited states produced in TTA emitters result in light emission, thereby reducing the risk of chemical degradation and potentially enhancing the device's operational stability.

Due to their beneficial properties, many TTA-based materials have been investigated as OLED emitters.[286] Beyond their role in OLED technology, TTA materials also show promise in biomedical applications and sensing.[287] Their tunable excitation and emission wavelengths, strong visible light absorption, and high upconversion quantum yields make them particularly useful in energy-related applications such as photocatalysis and solar cells.[288]

There is existing literature discussing the role of TADF molecules in TTA mechanisms.[105,289–296] This section provides an overview of recent studies on the role of TADF molecules in TTA mechanisms from 2023–2024.

Chen *et al.* (2023) introduced a novel TTA upconversion system using the newly developed TADF molecule DMACPDO **254** as a triplet photosensitizer, paired with diphenylanthracene (DPA) **255** as an annihilator (Fig. 93).[297] Efficient upconversion of fluorescence was reported in toluene, benzene, and chlorobenzene, with upconversion quantum yields (Φ_{UC}) of 22.3%, 21.9%, and 8.1%, respectively. Further, the effect of solvent properties on ISC and triplet–triplet energy transfer (TTET)
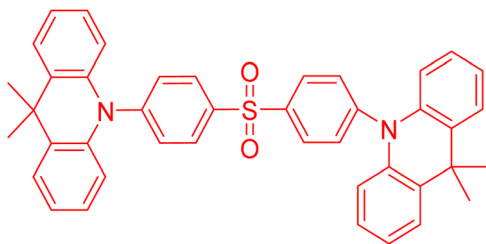
256

Fig. 94 Molecular representation of 3,4′-SOAD (**256**).[298]

processes was explored. The critical factor for TTA upconversion was determined to be the solvent polarity, as it could alter the energy of the T_2 triplet state.

Li *et al.* (2023) created the asymmetrically structured diphenylsulfone derivative 3,4′-SOAD (**256**), as shown in Fig. 94, to efficiently use triplet excitons through the RISC process. A combination of low ΔE_{ST} and increased singlet–triplet spin-orbital coupling was caused by an asymmetrical packing of 3,4′-SOAD that resulted in alternating strengths of intermolecular interactions. As a result, the triplet excitons could be promoted from TADF to TTA upconversion. A sky blue device based on 3,4′-SOAD was produced and showed high electroluminescence efficiencies and low-efficiency roll-off, with
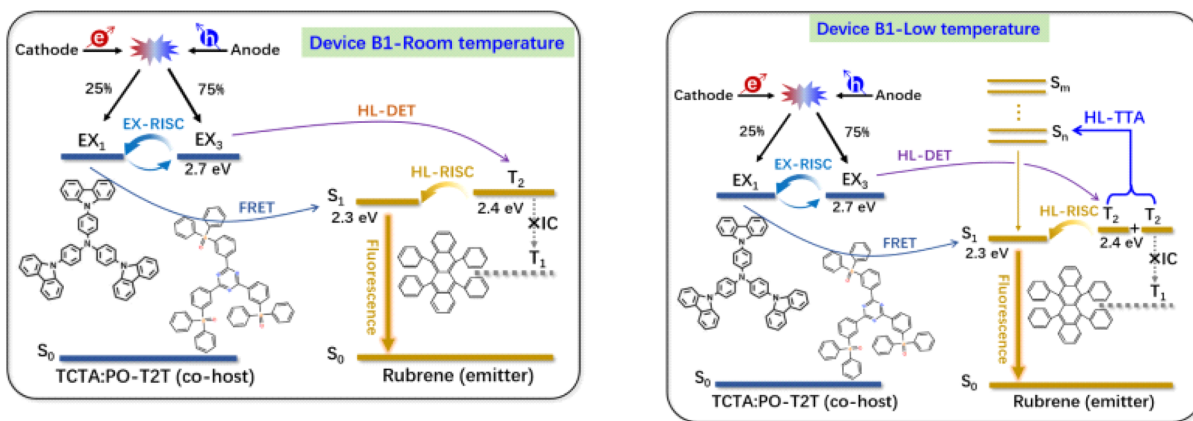
Fig. 95 Diagram showing room-temperature energy transfer mechanisms in device B1 without a CzDBA sensitizer. Schematic illustration of low-temperature energy transfer mechanisms in device B1 without a CzDBA sensitizer. Adapted from ref. 299, with the permission of AIP Publishing.
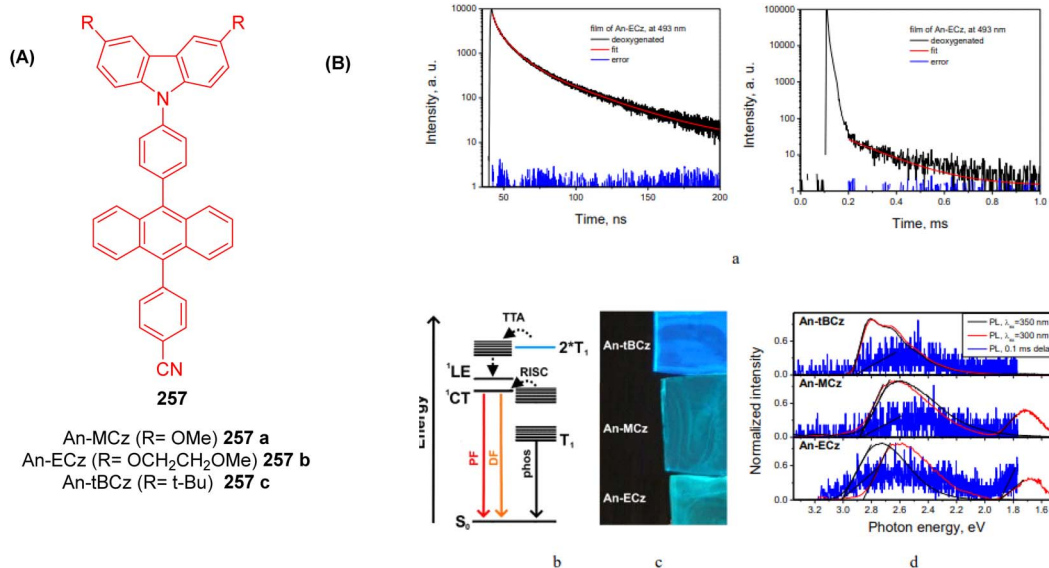
Fig. 96 (A) Molecular structure of An-MCz (**257a**), An-MCz (**257b**), and An-*t*BCz (**257c**) (B) (a) PL decay curves of the films (b) diagram illustrating the electronic states and transitions of the molecules (c) a photograph of the films of the compounds produced by deposition on drop casting on FTO substrates (d) PL spectra with varying delays. Reproduced from ref. 273, https://doi.org/10.1021/acsaelm.4c00533, under the terms of the CC BY 4.0 license, https://creativecommons.org/licenses/by/4.0/.
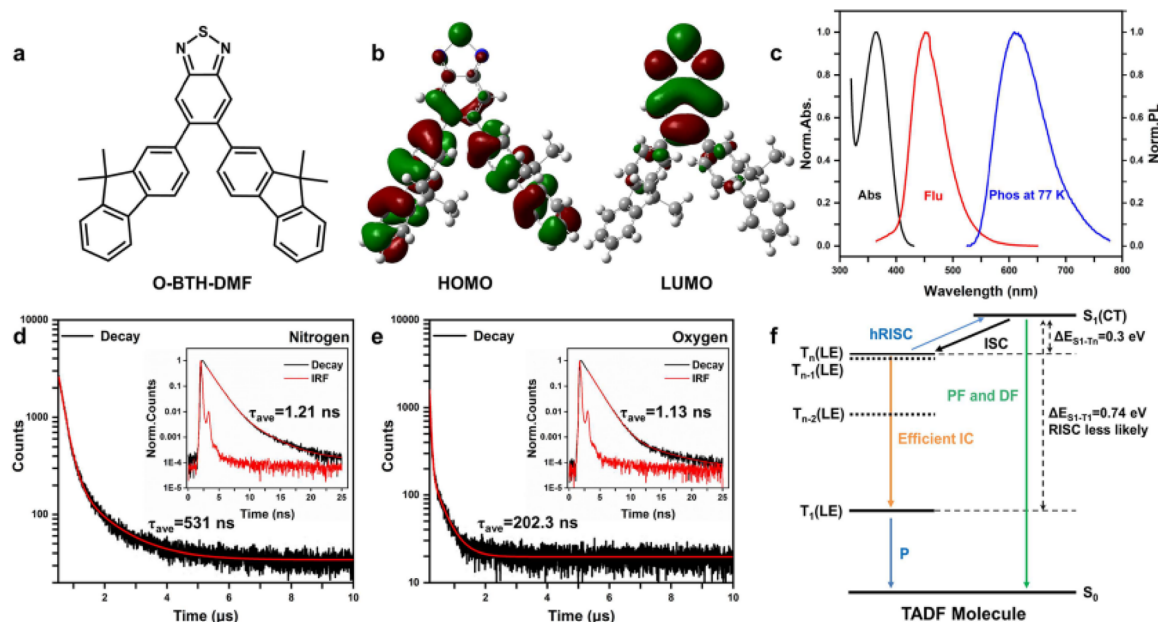
Fig. 97 (a) Molecular structure of *o*-BTH-DMF. (b) Theoretical calculations showing the HOMO and LUMO distributions of *o*-BTH-DMF. (c) UV-vis absorption and PL spectra along with phosphorescent spectra of *o*-BTH-DMF/PMMA doped thin film. (d and e) Delayed fluorescence lifetime measurements of *o*-BTH-DMF (d) nitrogen conditions and (e) oxygen conditions. (f) Simplified photophysical diagram illustrating the photophysical processes in *o*-BTH-DMF, including PF, DF, and phosphorescence. Reproduced from ref. 301 with permission from American Chemical Society, Copyright © 2024.

a maximum power efficiency (PE_{max}) of 33.5 lm W^{-1}, a maximum EQE_{max} of 14.7%, and a maximum current efficiency (CE_{max}) of 32.0 cd A^{-1}.[298]

Tang *et al.* (2024) employed magneto-electroluminescence to study a "hot exciton" channel in OLEDs doped with 1% rubrene and a TADF sensitizer, CzDBA, at room temperature, as depicted in Fig. 95.[299] This high-level triplet–triplet annihilation (HL-TTA) process involves transitions from T_2 to S_1. The presence of CzDBA enhances Dexter energy transfer pathways between two sets of triplets: the host-sensitizer and sensitizer-guest triplets, thereby increasing excitons in the T_2 state to promote HL-TTA. Similar to the conventional TTA process, the HL-TTA process is enhanced by a higher bias current, but unlike the conventional TTA process, the HL-TTA process is diminished by decreased temperature. These findings provide valuable insights into the mechanisms of HL-TTA processes, also referred to as "hot exciton" channels A deeper understanding of these processes could contribute to the development of high-performance OLEDs.

Using Stille coupling reactions between bromoanthracene and corresponding stannanes, Bezvikonnyi *et al.* (2024) synthesized three carbazolyl phenyl anthracenyl benzonitriles with distinct substituents (*tert*-butyl, methoxy, and methoxyethoxy) at the C-3 and C-6 positions of the carbazole moiety, as shown in Fig. 96A.[300] The planar anthracene with π-conjugation enhanced molecular packing in the solid state and the resulting π-stacking interactions favored TTA. The compounds emitted DF on photoexcitation, which improved their thermal stability and PLQY values, and the *t*-butyl substituent was the most efficient. The *t*-butyl compound was therefore used to fabricate host-free and guest–host emitting layers in OLEDs. With the use

of TTA upconversion and a bicomponent host–guest system, a hyperfluorescent OLED could also be produced without the requirement for a sensitizer. As can be observed in Fig. 96B, the non-doped TTA OLEDs achieved a 5.9% maximum EQE, while the hyperfluorescent OLEDs using TTA upconversion achieved a 7.1% maximum EQE, and a long-lived emission characteristic of TTA was detected for the device using the *t*-butyl-substituted emitter.

Zhao *et al.* (2024) examined the TADF molecule *o*-BTH-DMF (seen in Fig. 97a), using both time-resolved spectroscopy and computational modeling employing DFT calculations, to study
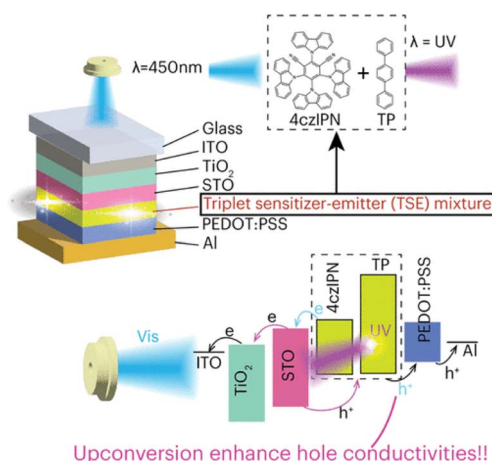

Fig. 98 Visible light-assisted charge extraction in high bandgap SrTiO$_3$ through the integration of triplet sensitizer-emitter thin film. Reproduced from ref. 302 with permission from American Chemical Society, Copyright © 2024.
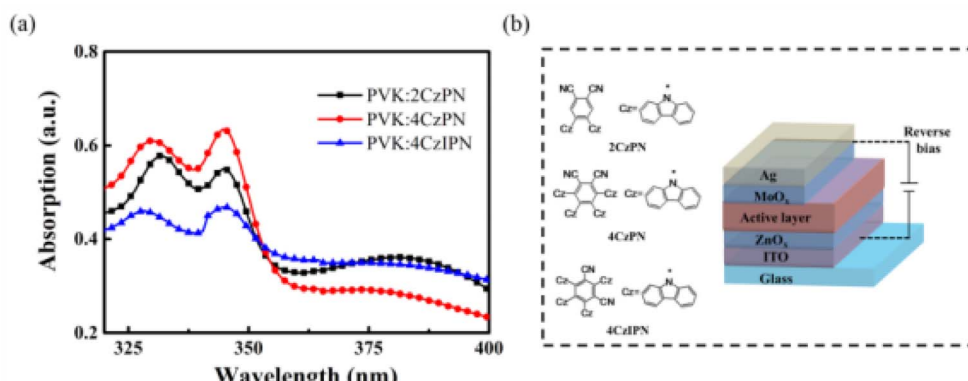
Fig. 99 (a) Absorption spectra of PVK:2CzPN, PVK:4CzPN, and PVK:4CzIPN blend films. (b) Molecular scaffolds of 2CzPN, 4CzPN, and 4CzIPN and device architecture. Reproduced from ref. 303 © IOP Publishing. Reproduced with permission. All rights reserved.

the dynamics of both the singlet and triplet excited states.[301] Transient absorption (TA) spectroscopy was done using two different timescales: femtoseconds (fs-TA) and nanoseconds (ns-TA). The fs-TA spectra indicated that the S_1 state has a lifetime similar to that of transient fluorescence as well as a long-lived triplet state. On the other hand, the ns-TA spectra showed that the larger energy gap between the singlet excited state S_1 and excited triplet states above T_1 (T_n), in addition to the local emission properties between triplet states, meant that the internal conversion from T_n to T_1 was favored over RISC. The accumulation of excitons in the T_1 state was then confirmed using sensitization experiments confirmed that the observed triplet state in ns-TA is the T_1 state as shown in Fig. 97d and e. The RISC processes in the o-BTH-DMF molecules were validated using transient fluorescence emission spectroscopy. These findings were supported by the DFT calculations for HOMO and LUMO shown in Fig. 97b. This research provides greater insight into the o-BTH-DMF luminescence mechanism, which could be useful in applications of this TADF molecule for OLEDs.

Ahmad *et al.* (2024) integrated strontium titanate (STO) into the triplet sensitizer-emitter (TSE) system composed of a 4CzIPN/*p*-terphenyl thin film to form the TSE/STO photovoltaic cell. The STO significantly enhanced the EQE under visible light, as depicted in Fig. 98, which was further enhanced by increased irradiance intensity.[302] The TSE upconversion was dependent on the thickness of the film, resulting in higher efficiency without saturation in EQE/EQE$_0$, potentially allowing these cells to maximize absorption of the high photon flux. The efficiency of the cells was further optimized by preparation and characterization in an inert gas environment with N_2 bubbling

to deoxygenate the TSE solution. Overall, the TSE system demonstrated promise as a thin film for photovoltaic cells for effectively using photon absorption from longer wavelengths while suppressing "parasitic absorption" processes from the electron transport layer of the cell.

4.4.2. Organic ultraviolet photo detectors (UVOPDs). Wang *et al.* (2018) developed solution-processed UVOPDs using three TADF materials such as 2CzPN, 4CzPN, and 4CzIPN as acceptors as shown in Fig. 99b.[303] These devices showed exceptional photodetection performance. As can be observed from the graph in Fig. 99a, the highest detectivity (D^*) under 0.5 mW cm^{-2} of 350 nm UV light was exhibited by the device based on 4CzPN, which had a D^* of 1.09×10^{12} Jones. These detectivity values were associated with the properties of the active layers, including the film morphology, carrier mobility, and energy levels. When these UVOPDs were fabricated with ultrathin silver anodes, the semitransparent devices produced had an average transmittance of 43% and an enhanced D^* of 2.09×10^{11} Jones. Finally, an optical simulation of light-harvesting suggested that the illumination of the indium tin oxide-coated side of the device resulted in higher absorption and generation of excitons. In summary, this study highlighted a fullerene-free method for the preparation of low-cost UVOPDs using TADF materials.

To develop materials that could be used in devices with activity as both OLEDs and UVOPDs, Wang *et al.* (2023) synthesized two blue-fluorescent emitters, TPA-AN and 2mTPA-AN. These emitter molecules were composed of an acceptor unit, benzonitrile, and a donor unit, triphenylamine (TPA) or 4-methyl-*N*-phenyl-*N*-(*p*-tolyl)-aniline (MeTPA), with anthracene (AN) as a bridge as shown in Fig. 100.[304]
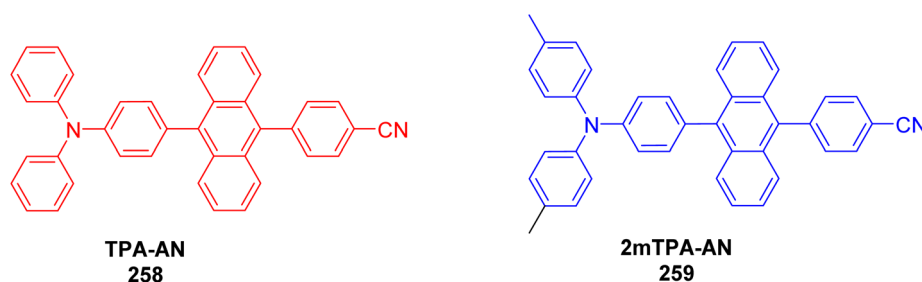
Fig. 100 Molecular structures of the employed materials.[304]
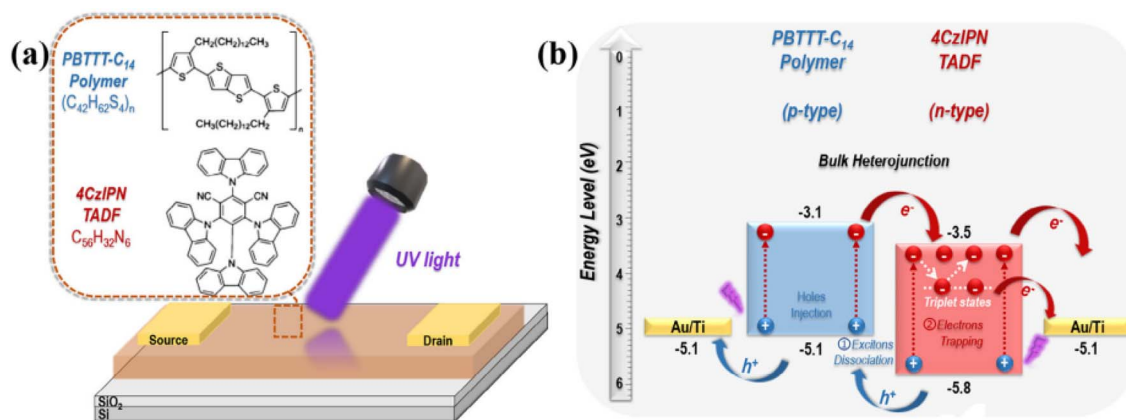
Fig. 101 (a) Diagram of the device structure and (b) energy level diagram in PBTTT-C14 polymer and 4CzIPN bulk heterojunction photo-transistor. Reproduced from ref. 305 with permission from John Wiley & Sons, Copyright © 2024, Wiley-VCH Verlag GmbH & Co. KGaA, Weinheim.

Zeng and coworkers (2024) demonstrated that TADF triplet state excitons generated by 4CzIPN can significantly enhance the performance of organic photodetectors (OPDs). These OPDs were prepared by a combination of 4CzIPN with a high-mobility PBTTT-C14 polymer *via* a bulk type-II heterojunction, as illustrated in Fig. 101a.[305] The long-lived spin-triplet excitons of 4CzIPN, which are nearly isoenergetic with the spin-singlets, improve free carrier extraction and photogating effect, leading to a fast response and high gain, as illustrated in the energy level diagram in Fig. 101b. The PBTTT-C14/4CzIPN UVOPD device was able to operate at a low dark current (~pA) with a detectivity of ~10^{11} Jones while demonstrating a quick reaction time of ~79 ms, a high EQE of ~1.0×10^4, and a high

Fig. 102 Molecular structures of four TADF molecules with ECL emission.[307]

photogain ($\sim 10^3$). In addition, the gate photoresponse range was broad (250–600 nm) and tunable.

4.4.3. Electrogenerated chemiluminescence (ECL) cells. ECL involves electrogenerated radical species undergoing electron transfer near a biased electrode, leading to the formation of excitons (excited states). The relaxation of these excitons produces ECL emission. ECL cells are constructed from a liquid emitter sandwiched among tw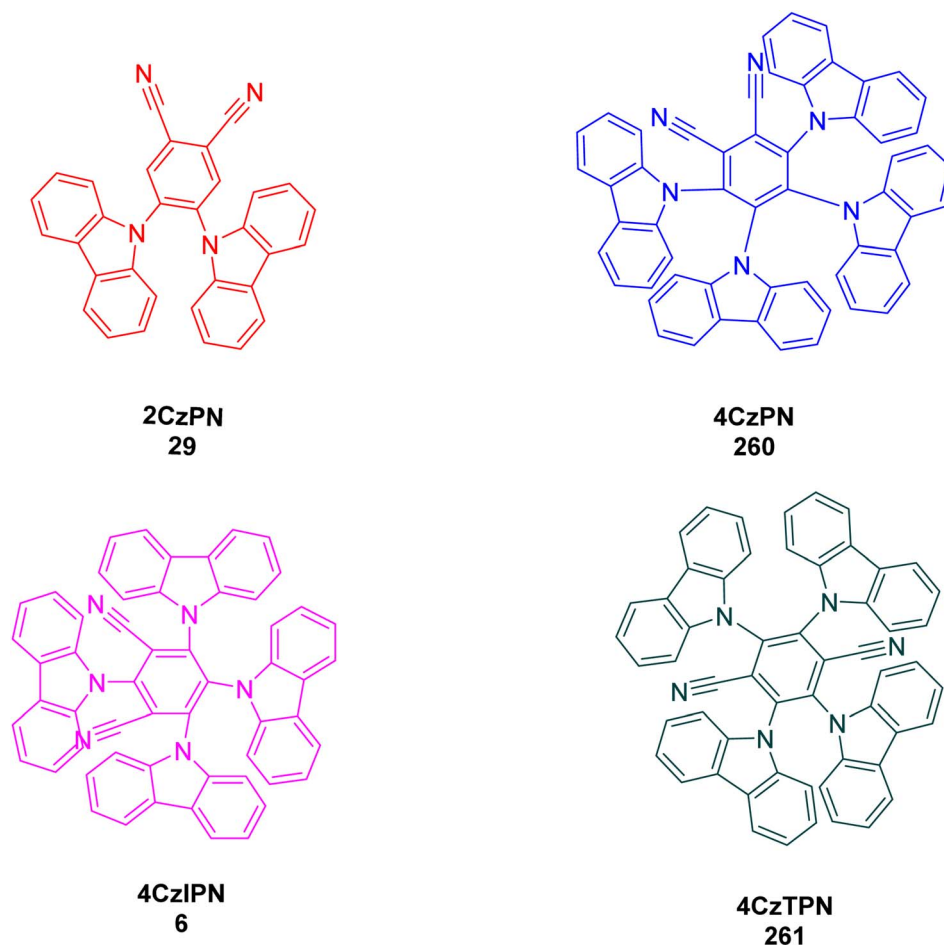o glass layers with electrodes present in the structure. The fluid properties of liquid emitters ensure flexible, crack-resistant light-emitting layers, even under repeated bending. While fluorescent and phosphorescent dyes have been commonly used in ECL studies, challenges remain in the creation of patterned liquid emitters and achieved multi-color light emission. However, the incorporation of TADF molecules as emitters in ECL systems has been theorized to enhance ECL efficiency by facilitating spin upconversion from the T_1 to S_1 state.[306]

Adachi and colleagues 2014 researched TADF molecules, such as 2CzPN, 4CzPN, 4CzIPN, and 4CzTPN, that emit ECL with high efficiency, producing light ranging from green to red.[307] Notably, 4CzIPN in MeCN achieved an ECL efficiency of approximately 15%, which is about three times higher than the efficiency observed for the $[\text{Ru(bpy)}_3]^{2+}$ system and significantly exceeds its PLQY. This result indicates the significant advantage
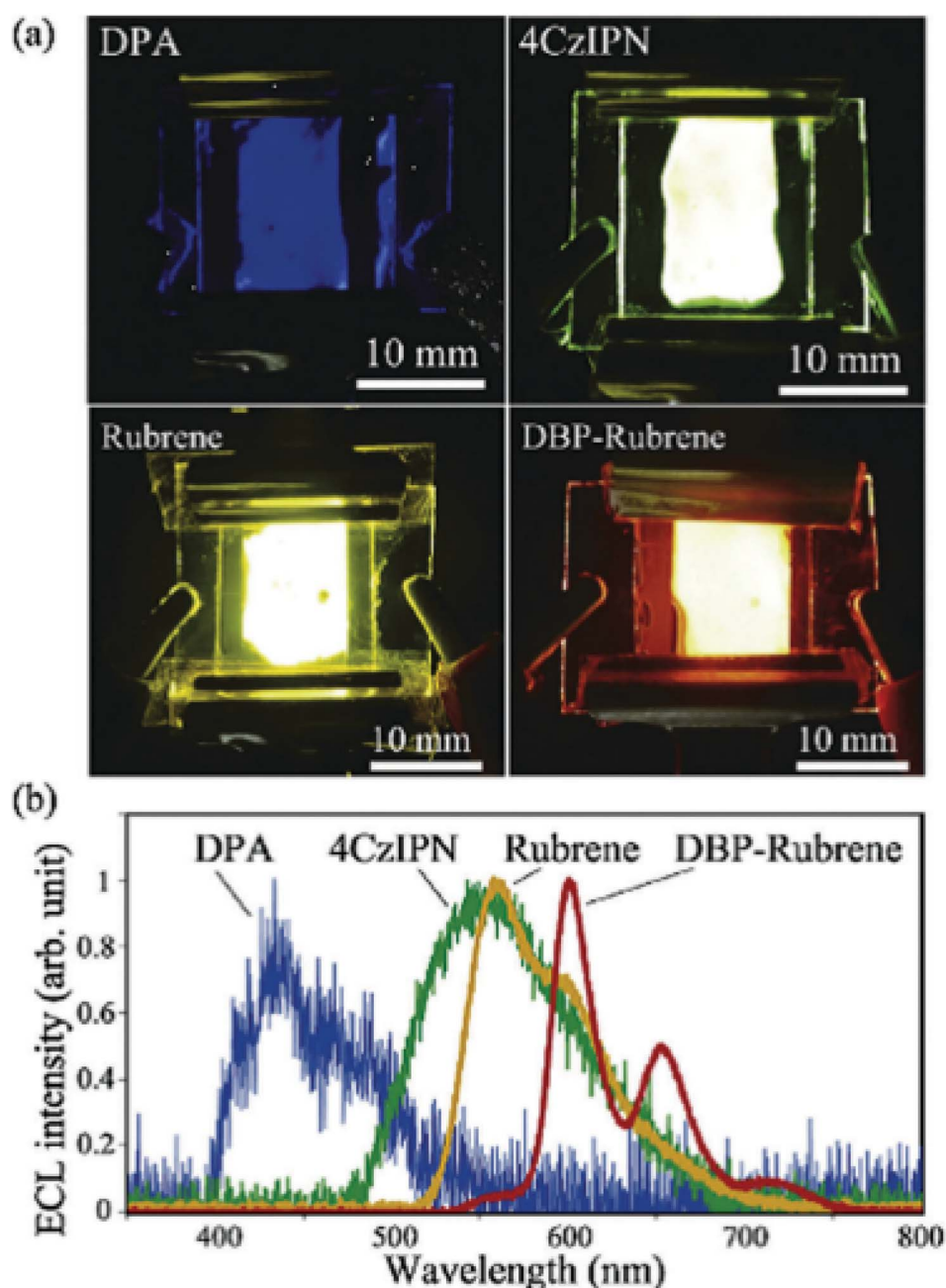

Fig. 103 (a) Photographs for emission of light and emissions of light from DPA, 4CzIPN, rubrene and DBP-doped rubrene in simple ECL cells (b) ECL spectra from the simple-structured ECL cells. Reproduced from ref. 308 with permission from Elsevier, Copyright © 2014.
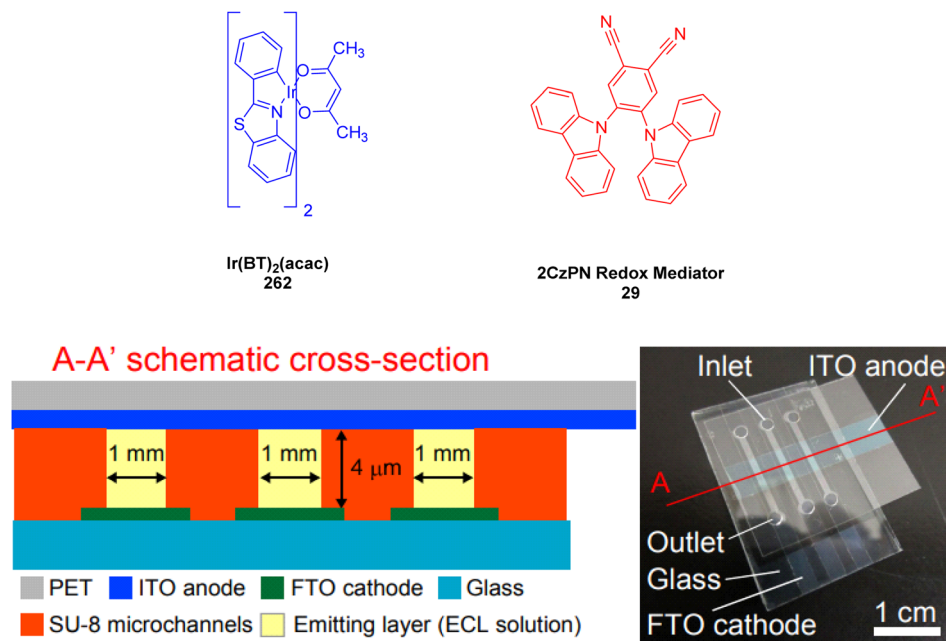
Fig. 104 Molecular representation of 2CzPN (**29**) and Ir(BT)$_2$(acac) (**262**) along with the microfluidic ECL cell with a schematic cross-section. Reproduced from ref. 309, https://doi.org/10.5796/electrochemistry.23-00147, under the terms of the CC BY 4.0 license, https://creativecommons.org/licenses/by/4.0/.

of spin upconversion through thermal activation for ECL as shown in Fig. 102. Therefore, TADF molecules show great promise for use in ECL applications such as immunoassays and liquid light-emitting devices due to their high ECL efficiency.

A study by Mizuno and coworkers in 2014 described a four-color microfluidic ECL system using straightforwardly designed ECL cells, capable of both single and multi-color emission as shown in Fig. 103.[308] In this configuration, the TADF compound 4CzIPN was utilized for green ECL. For the fabrication of yellow, blue, and red ECLs, conventional fluorescent materials were employed including rubrene, DPA, and DBP-doped rubrene, respectively. This study underscores the considerable potential of this multicolor microfluidic device for applications in liquid-based light emission.

Kasahara *et al.* designed a yellow phosphorescent ECL cell prepared using a mediator in solution, namely the carbazolyl dicyanobenzene derivative 2CzPN **29**, as shown in Fig. 104.[309] 2CzPN **29** has deeper HOMO and LUMO levels compared to Ir(BT)$_2$(acac) **262**. This configuration achieved the highest maximum luminance (L_{max}) of 113 cd m^{-2} and efficiency CE$_{max}$ of 2.84 cd A^{-1} reported for iridium complex-based cells. The study suggested that the developed ECL system could be suitable for both fluorescent and phosphorescent materials. The authors suggested potential future improvements for this system, including using combinations of iridium complexes with these mediators to form multicolor phosphorescent cells, encapsulating the ECL cells to inhibit phosphorescence quenching caused by oxygen molecules with a triplet ground state, and coating the electrodes with conductive films to enhance the ECL performance.

4.4.4. Organic hybrid microwire radial heterojunction. In 2016, Li and colleagues employed a solvent-assisted self-

assembly methodology to construct a ternary organic hybrid microwire radial heterojunction, as shown in Fig. 105.[310] This solution-based process is more efficient and convenient for device fabrication. The process consisted of three steps: solvent evaporation to form 4,4′,4″-tri(*N*-carbazolyl) triphenylamine (TCTA) microwires, adsorption of [6,6]-phenyl-C61-butyric acid methyl ester (PCBM) nanoparticles to creating a binary hybrid microwire with a "corn cob" structure, and surface adsorption of 4CzIPN to the hybrid microwires, resulting in a ternary hybrid microwire radial heterojunction. Bottom-contact devices fabricated from the ternary microwires demonstrated high photoconductivity. The photoconductivity of the ternary microwire under illumination by ~79.4 mW cm^{-2} simulated white light resulting in an on/off ratio of about 320 at a 30 V bias. This was over three times greater compared to the photoconductivity of the binary hybrid microwire (TCTA/PCBM). The TADF material 4CzIPN increased the production of free charge carriers by upconversion of triplet excitons into singlet excitons. The hybrid microwire's conductivity was then increased by a conducting channel that was formed by these photogenerated charge carriers at the heterojunction interface. Additionally, experiments under a nitrogen atmosphere showed that oxygen in the air slightly reduced photoconductivity due to its quenching effect on triplet excitons. This novel radial heterojunction ternary microwire has great promise for cutting-edge optoelectronic applications by providing an efficient way to increase the photoconductivity of one-dimensional organic materials.

4.4.5. Multicolor luminescent micelle. Zhu *et al.* (2016) developed micelles based on diphenyl-diacetylene to enhance IQE and fully utilize radiative decay during excitation.[311] These micelles can be used to produce multicolor luminescent
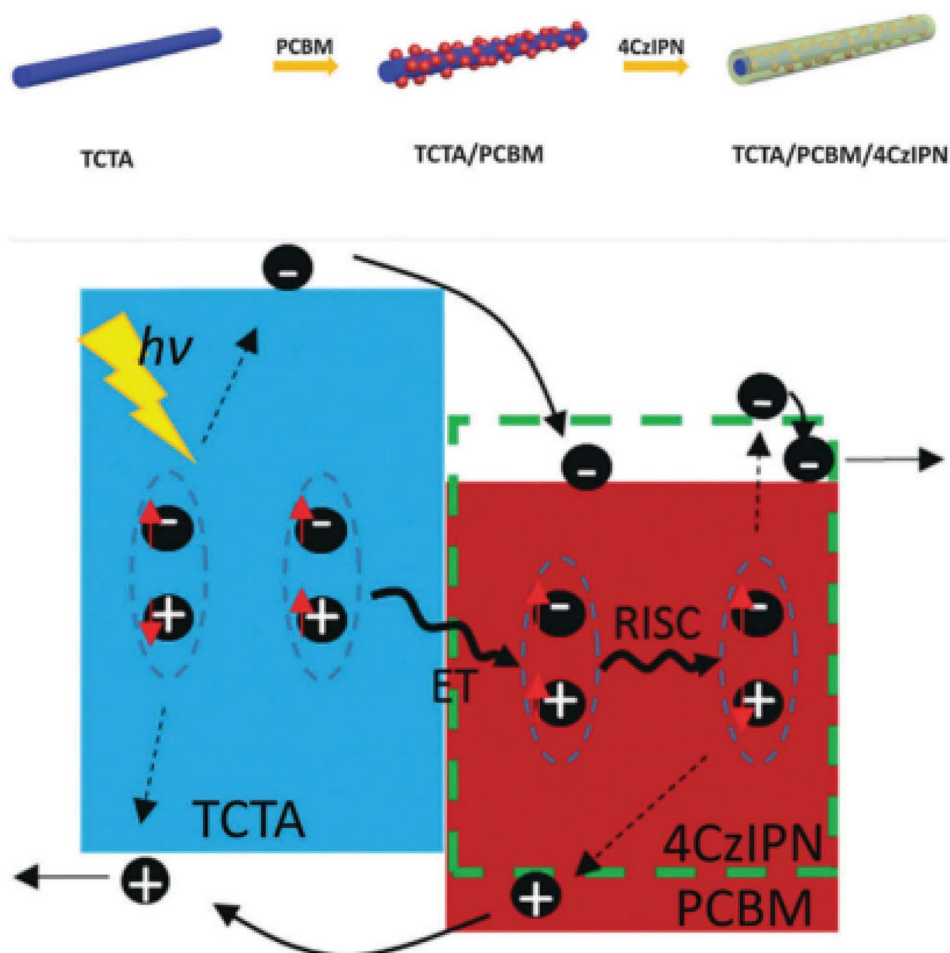
Fig. 105 (top) Diagram representing the process for the synthesis of ternary radial heterojunction microwires and (below) photoconductivity process in TCTA/PCBM/4CzIPN. Reproduced from ref. 310 with permission from the Royal Society of Chemistry.
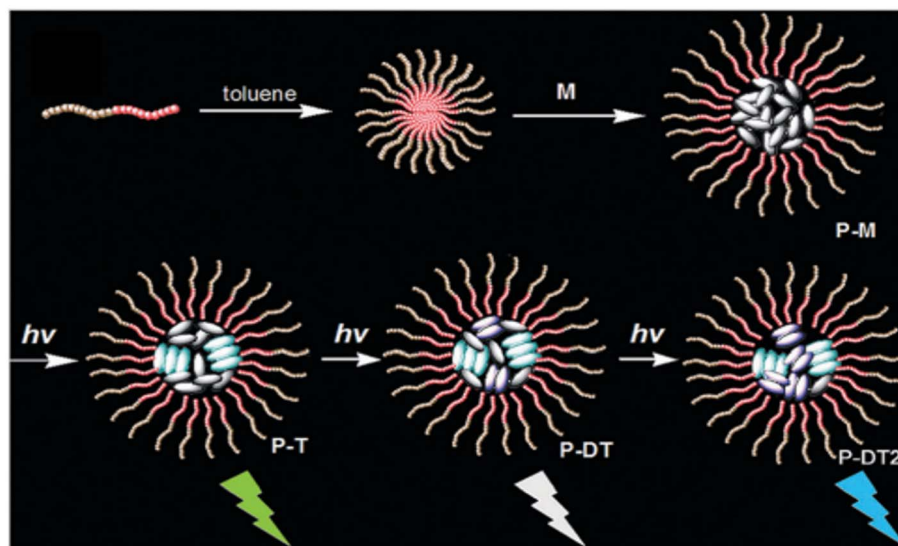
Fig. 106 Synthetic route of micellar ensemble P-M, with the encasement of the block copolymer P by diphenyl-diacetylene monomer M to form oligodiacetylene trimers (P-T) and dimers (P-DT and P-DT2). Reproduced from ref. 311, https://doi.org/10.1039/C5SC04253D, under the terms of the CC BY 4.0 license, https://creativecommons.org/licenses/by/4.0/.
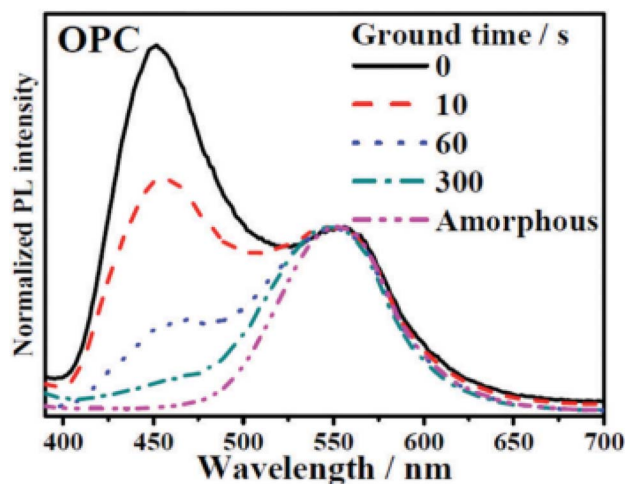
Fig. 107 PL spectrum of OPC in the solid state before and after grinding. Reproduced from ref. 316 with permission from John Wiley & Sons, Copyright © 2015, Wiley-VCH Verlag GmbH & Co. KGaA, Weinheim.

systems by finely tuning the radiative decay processes of triplet states. The diphenyl-diacetylene-based co-micellar nano-assemblies (Fig. 106) could undergo successive photo-crosslinking reactions, creating trimeric and dimeric oligodia-cetylenes with individual emissive bands spanning the visible-light spectrum. This adjustable dual-band capability caused the micelle system to exhibit a dynamic color transition from light green to white to purple-blue. With extremely rapid ISC and a small ΔE_{ST}, this system was capable of exhibiting both TADF and phosphorescence. This leads to long-lived, broad-band emissions without color distortion. This innovative design aims to create high PLQY emitters, making it suitable for sophisticated controllable optoelectronic devices.

**4.4.6. Mechanoluminescence (ML) and mechanolumino-chromism (MLC).** Mechanically responsive luminescence (MRL), also known as mechanofluorochromism (MFC) when involving fluorescence, is a significant and reversible change in PL color, or the ability to switch luminescence on and off, in response to mechanical processes such as pressing, grinding, crushing, rubbing, and stretching. MRL materials have received

attention from many research groups because of their potential applications in many fields such as optical storage, miniature photonic devices, security papers, mechano-sensors, and logic gates.[312–315] The luminescence properties of such materials in their solid form are significantly affected by factors such as conformation, molecular packing and intermolecular interactions of materials. Alterations in these factors can impact the HOMO and LUMO energy levels, thereby modifying the luminescence properties. Thus, dynamic control of highly functioning MRL materials can be achieved by manipulating these physical factors, providing easy control of luminescence properties and reversibility. However, such MRL materials are rare due to two primary challenges.[314] The first is a lack of a defined fabrication process. The second is that many luminescent materials suffer from aggregation-caused quenching (ACQ), which leads to very low luminescence in their solid form. There has therefore been research into the design of MRL materials that can overcome these issues using TADF.

In 2015, Chi and Xu's group fabricated an asymmetric D–A–D′ type TADF material by modification of the acceptor unit with benzophenone, resulting in the synthesis of carbazolyl- and phenothiazinyl-substituted benzophenone (OPC).[316] OPC possessed characteristics such as dual emission, aggregation-induced emission (AIE) TADF and mechanofluorochromic properties. In its crystalline form, OPC emitted white light with dual photoluminescence peaks in the blue and yellow regions of the spectrum, but after grinding, only the yellow peak remained, as shown in Fig. 107. This study demonstrated that these asymmetric molecules present a promising approach for creating novel organic materials that emit white light with dual emission properties and mechanofluorochromic behavior, which makes them suitable for various applications.

Cheng and coworkers demonstrated a TADF material in 2016 that possessed two *meta*-carbazolyl groups on the phenyl ring of benzoyl-4-pyridine mDCBP (**263**). The MLC properties and chemical structure of mDCBP (**263**) are shown in Fig. 108.[317] Upon grinding, the material's luminance color was changed from blue to green. The original blue color could be returned by exposing the material to dichloromethane vapor, demonstrating the reversible nature of mDCBP's emission properties.
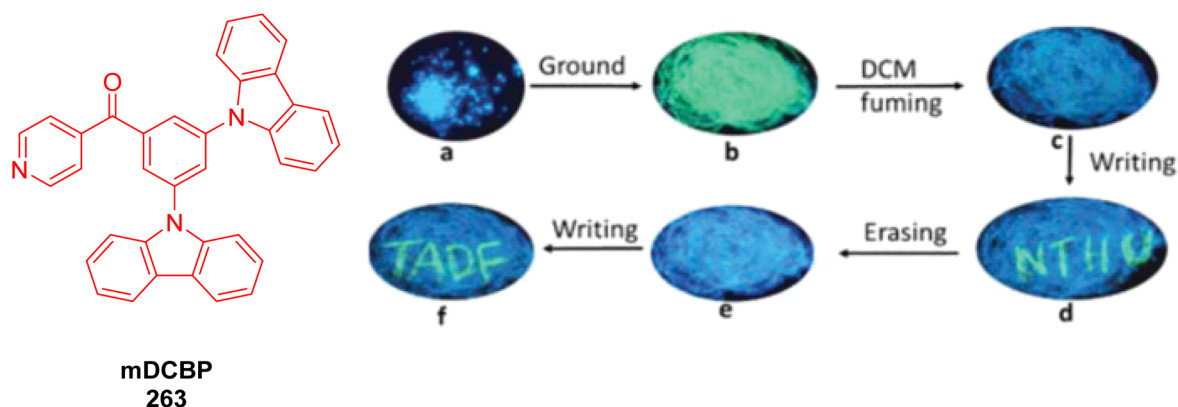

mDCBP
263

Fig. 108 Chemical structure and photographs of the material in different states. Adapted from ref. 317 with permission from the Royal Society of Chemistry.
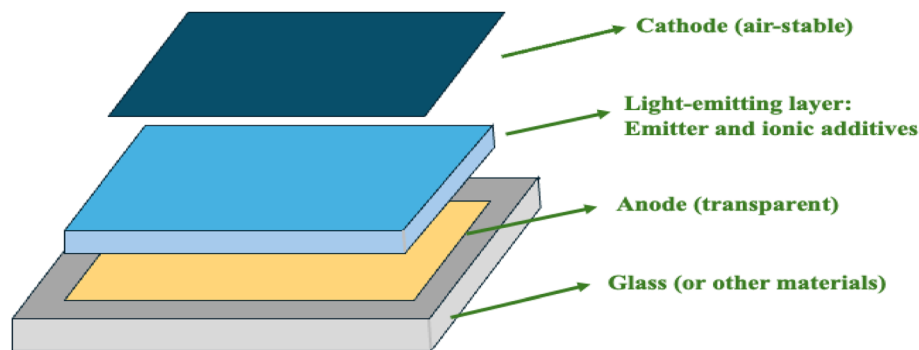
Fig. 109 Schematic diagram of a general LEEC device.

4.4.7. Light-emitting electrochemical cells (LEECs). LEECs are considered the epitome of simplicity among thin-film lighting devices. As illustrated in Fig. 109, LEECs consist of a single active layer positioned between a transparent anode and an air-stable cathode. The active layer is typically comprised of a blend of emitters.[318,319]

There has been a great deal of research into describing the role TADF materials can play in LEECs.[320–329]

Wong *et al.* (2015) introduced charged organic TADF-based OLEDs and LEEC devices. This TADF material could function both as a charge transporter and emitter, as depicted in Fig. 110.[330] The cyano (–CN) group, commonly used as an electron acceptor, plays a crucial role in lowering the Lowest Unoccupied Molecular Orbital (LUMO) energy level, enhancing the charge-transfer characteristics. By incorporating strong acceptor groups like cyano, the energy gap between the singlet and triplet excited states (ΔE_{ST}) is minimized. This facilitates reverse intersystem crossing (rISC), where triplet excitons are converted back to the singlet state, enabling delayed fluorescence. The donor groups, on the other hand, such as carbazole, triphenylamine, or other electron-rich moieties, raise the Highest Occupied Molecular Orbital (HOMO) energy level. This

Fig. 110 The chemical structure of the TADF compound superimposed on a photograph of its LEEC. Reproduced from ref. 330, https://doi.org/10.1021/acs.chemmater.5b03245, under the terms of the CC BY 4.0 license, https://creativecommons.org/licenses/by/4.0/.

donor–acceptor configuration ensures efficient charge separation in the excited state, promoting TADF. The maximum EQE of the LEECs was improved by lowering the current density, leading to a value of 0.39% for this emitter. The OLEDs produced from this emitter were color-stable and able to be processed in solution. In addition, OLEDs using pristine films of the emitter demonstrated superior performance compared to OLEDs using a doped EML, which is consistent with the findings for the LEECs, demonstrating the potential of these emitters for non-doped TADF devices.[330]

Pei and coworkers (2017) presented a single-layer LEEC based on a TADF host, illustrated in Fig. 111.[331] The single active layer of the LEEC is comprised of a solution-processed mixture of a TADF host material (PIC-TRZ, **5**), three dopants **264**, **265**, and **266** that were used to emit green, yellow and red phosphorescence, respectively, polyvinylcarbazole (PVK, **267**) to improve the morphology of the layer, and an electrolyte (**268**). By varying the ratios of the dopants, different color emissions could be achieved, including green, yellow, red, and warm white light, as well as blue-green in the non-doped device. However, the non-doped device only emitted less than 300 cd m^{-2} with a maximum efficiency of 0.5 cd A^{-1}, while the green, yellow, red, and white LEECs reached 6000, 4200, 2300, and 1200 cd m^{-2} with a peak efficiency of 7.1 cd A^{-1}. The green LEEC even achieved an exceptional luminance of 35 000 cd m^{-2} for a short period, although the effect was short-lived. These LEECs were able to leverage the optical and transport properties of TADF materials, which allowed them to surpass the efficiency and brightness of conventional LEECs using phosphorescent hosts. Further, the simple single-layer solution-processed structure would be more cost-effective for the production of lighting sources with high luminance.

Moore *et al.* (2018) synthesized and investigated three first-generation carbazole (Cz)-based ionic host materials for usage in LEEC devices.[332] The carbazole (Cz)-based ionic host materials were shown to have broad band gaps characterized by reversible oxidations and irreversible reductions. PL experiments showed that the luminescence of films containing the carbazole (Cz)-based host materials and an ionic transition metal complex (iTMC) guest was enhanced compared to pristine films of the host materials alone. The LEECs were therefore made with thin films of the pristine hosts, pristine guests, and
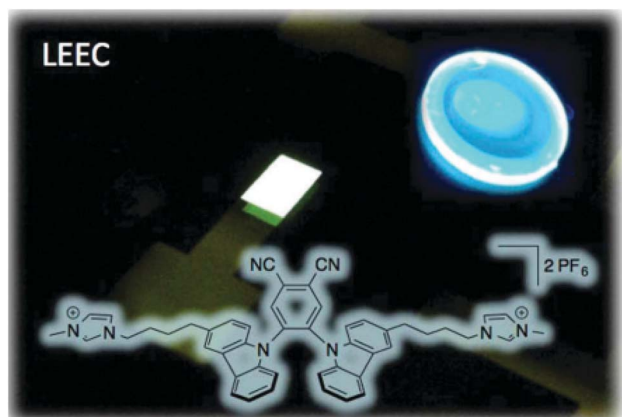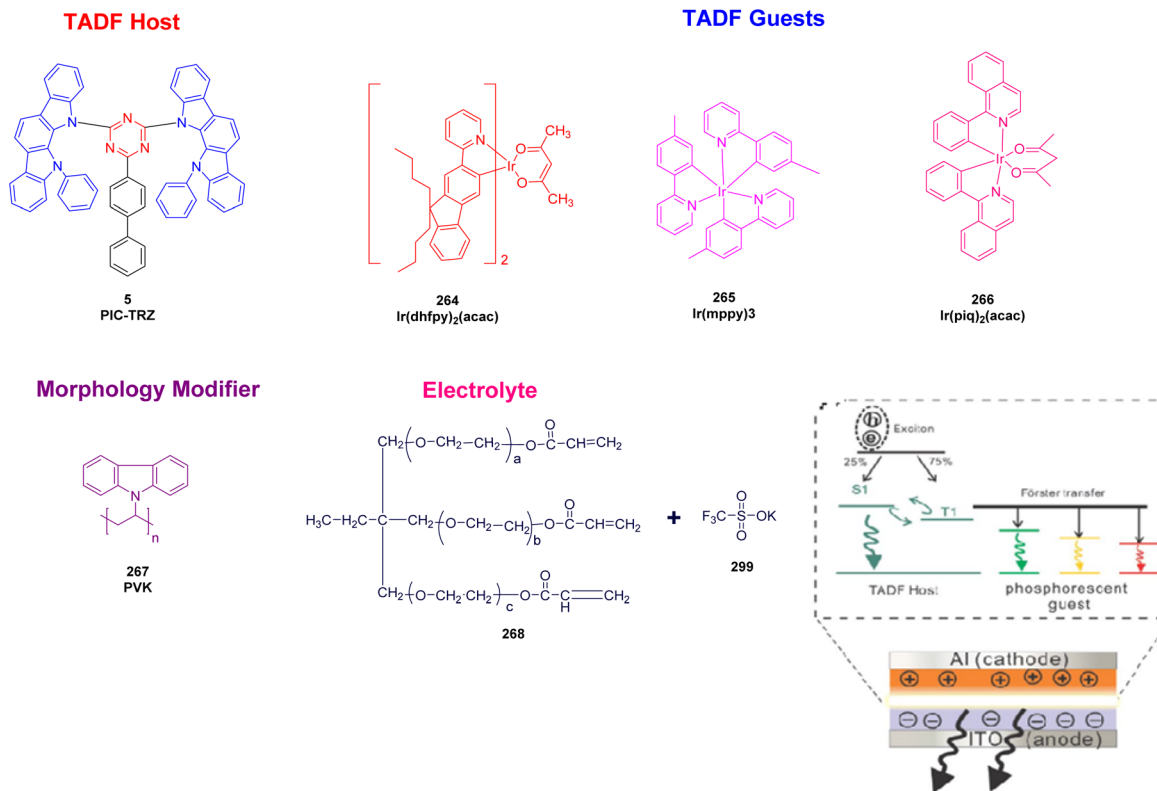
Fig. 111 Chemical structures of the TADF host (**5**), PD molecules (**264–266**), morphology modifier (**267**), and electrolyte (**268**) along with emission mechanisms in TADF-LEECs. Reproduced from ref. 331, https://doi.org/10.1038/s41598-017-01812-2, under the terms of the CC BY 4.0 license, https://creativecommons.org/licenses/by/4.0/.
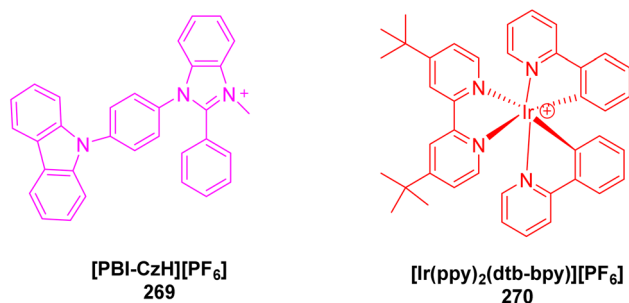

Fig. 112 Chemical structure of first-generation carbazole (Cz)-based ionic host material (**270**).[332]

90%/10% host/guest blends. Of these, the system containing PBI-CzH (**269**) host and its guest Ir(ppy)₂(dtb-bpy) (**270**) (as shown in Fig. 112), resulted in the best device performance, with an EQE of 3.80% and a luminance maximum of 624 cd m⁻².

Edman *et al.* (2019) prepared a metal-free LEEC device from a single layer of active material between air-stable electrodes that efficiently produced vivid TADF emission.[333] The active material was composed mostly of a polymeric blend host and less than 1% of the TADF-active guest emitter. Three TADF guest emitters were studied: 4CzIPN, 2-[4-(diphenylamino) phenyl]-10,10-dioxide-9H-thioxanthen-9-one (TXO-TPA), and

the orange-emitting 7,10-bis(4-(diphenylamino)phenyl)-2,3-dicyanopyrazinophenanthrene (TPA-DCPP), as shown in Fig. 113g. The host allowed for uniform film morphology, effective electronic transport and a balance of electrochemical doping, while the low guest concentration ensured optimal energy transfer from host to guest and TADF emission while reducing guest–guest aggregation. To optimize the electrochemical doping, the electrolyte tetrahexylammonium tetrafluoroborate (THABF₄) was included as part of the polymeric blend. The most efficient of the resulting TADF LEECs produced using this system was a yellow-emitting LEEC with a maximum EQE was 7.0% and peak current efficiency (CE_max), as well as a luminance of 120 cd m⁻², as shown in Fig. 113.

Shanmugasundaram *et al.* (2019) synthesized a carbazole-phenothiazine compound (CPC, **271**) as depicted in Fig. 114.[334] CPC (**271**) was shown to have high thermal stability with blue emission both in thin films and in solution. This blue emission was also observed for a LEEC with CPC as the active material, with CIE coordinates (0.16, 0.33). The incorporation of an ionic liquid improved the electroluminescent performance of the LEEC, resulting in blue emission centered at 485 nm, with a brightness of 454 cd m⁻², as well as a current efficiency of 1.33 cd A⁻¹ and an EQE of 1.76%.

Su *et al.* and coworkers designed TADF LEECs using a phosphorescent complex **272** as the host and a red TADF emitter, APDC-DTPA **273**, which emits deep-red TADF, as the guest
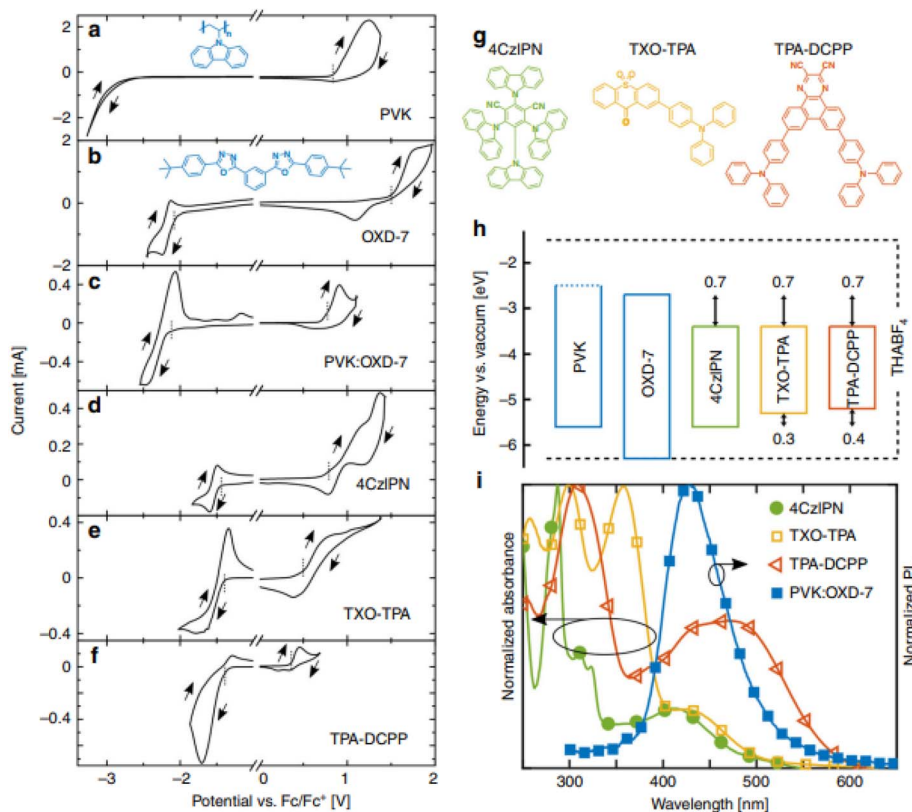
Fig. 113 Voltammograms were recorded on thin films of the host compounds (a and b), the blend host (c), and the guest compounds (d–f), as identified in the insets. (g) Structure of three TADF guest emitters. (h) Energy levels of host and guest compounds. (i) Normalized absorbance of the guest compound (left y-axis) and normalized PL of the host (right y-axis) for various films. Reproduced from ref. 333, https://doi.org/10.1038/s41598-017-01812-2 https://doi.org/10.1038/s41467-019-13289-w, under the terms of the CC BY 4.0 license, https://creativecommons.org/licenses/by/4.0/.

(Fig. 115).[335] Excitons from both the S$_1$ and T$_1$ states of 301 were involved in the Förster energy transfer between the host and guest, which was confirmed by PL and photophysical experiments. Guest triplet excitons were also recycled by Dexter energy transfer from the host to guest followed by RISC. This process was supported by the observed DF decay. The LEEC exhibited a maximum EQE of 5.11%, which the authors noted was one of the highest for deep-red emitting LEECs at the time. Thanks to the efficient energy transfer and RISC processes, the resulting LEEC was able to use over 73% of the excitons produced in the guest molecules for light emission. On the other hand, if the device current or concentration of guest doping increased, the efficiency was still limited by TTA in the guest molecules.

He *et al.* (2022) prepared two intrinsically-ionic molecules (**274**) using a donor, 3,6-di-*tert*-butylcarazole (*t*BuCAZ), and an acceptor, 2,4-diphenylpyrimidine (dPhPM),[336] in which the *t*BuCAZ and dPhPM groups were at *para*-positions for H1 and *ortho*- for H2, as described in Fig. 116. H1 displayed no TADF, as a consequence of its low triplet energy and correspondingly large ΔE_{ST}. Conversely, H2 exhibited high TADF due to higher triplet energy and correspondingly small ΔE_{ST}. Therefore, H2 was used as a host to construct blue-emitting LEECs with [Ir(buoppy)$_2$(dmapzpy)]PF$_6$ as guest material. The H2-based LEECs were color-stable and showed a peak brightness of 1078 cd m^{-2}, a peak EQE of 8.6%, and a half-lifetime ($t_{1/2}$) of 66

minutes under a constant-current driver. The addition of LiPF$_6$ as an electrolyte to the active layer improved the performance to a brightness of 918 cd m^{-2} with a $t_{1/2}$ of 2 hours.
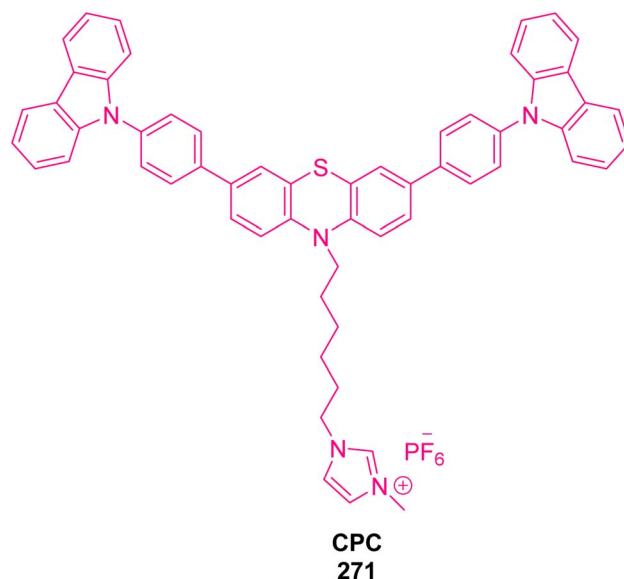
Fig. 114 Molecular structure of CPC (**271**).[334]

**Complex
272**
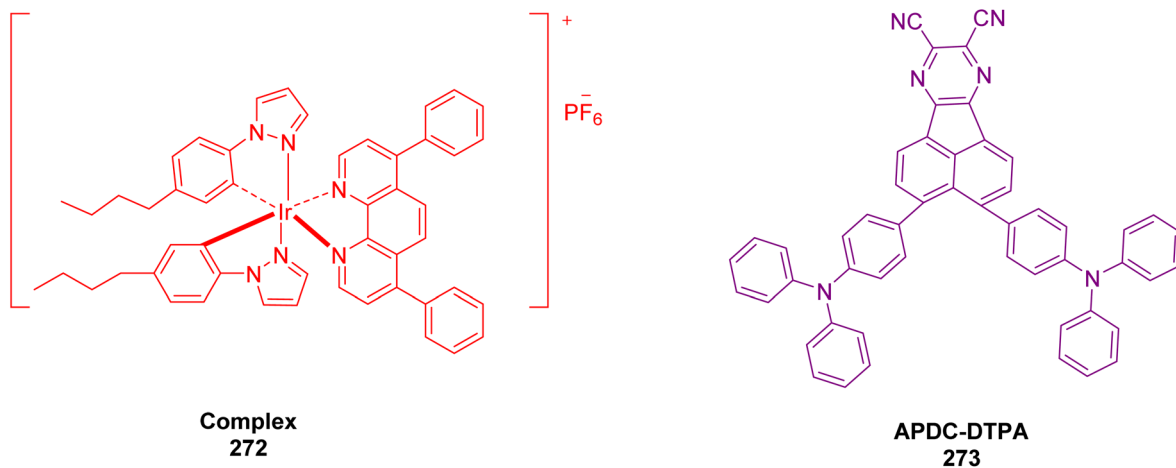
**APDC-DTPA
273**

Fig. 115 Chemical structure of phosphorescent complex **272** and APDC-DTPA (**273**).[335]

274 a

**p-tBuCAZ = H *o*-tBuCAZ = H
274**
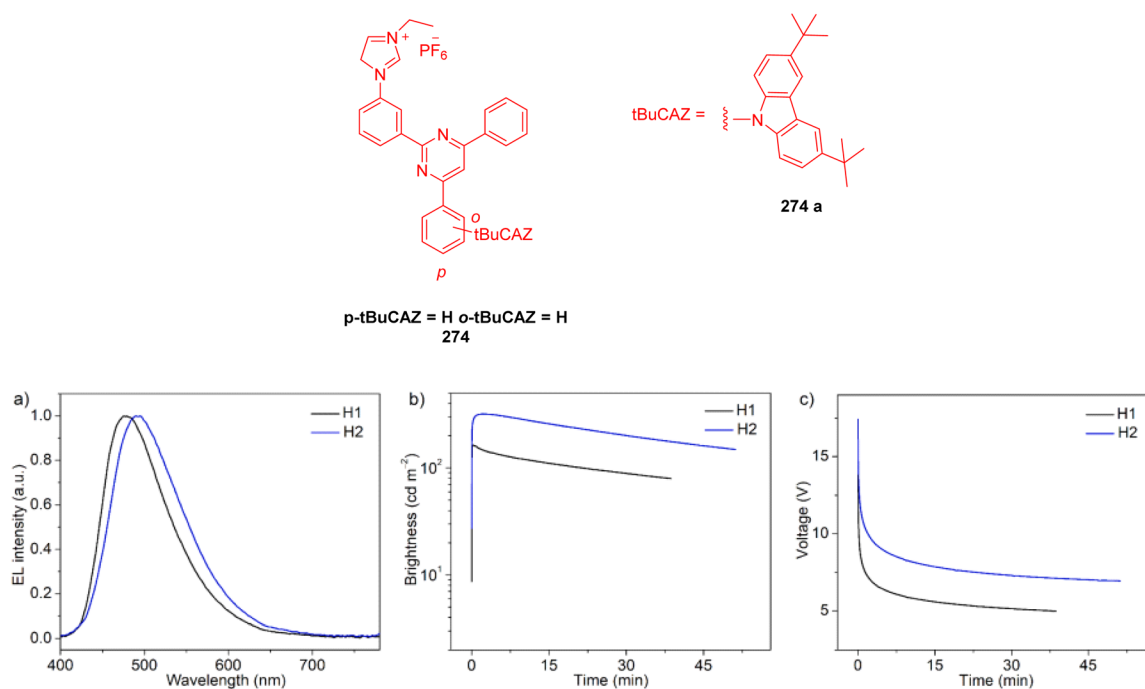
Fig. 116 (top) Chemical structure of *t*BuCAZ and (bottom) (a) peak EL intensity, (b) time-dependent brightness and (c) time-dependent voltage. Adapted from ref. 336 with permission from Elsevier, Copyright © 2022.

D =

CZ 275 a

**Pym-CZ D = CZ 275 (A)
Pym-tBuCZ D = t-BuCZ 276 (B)**

D =
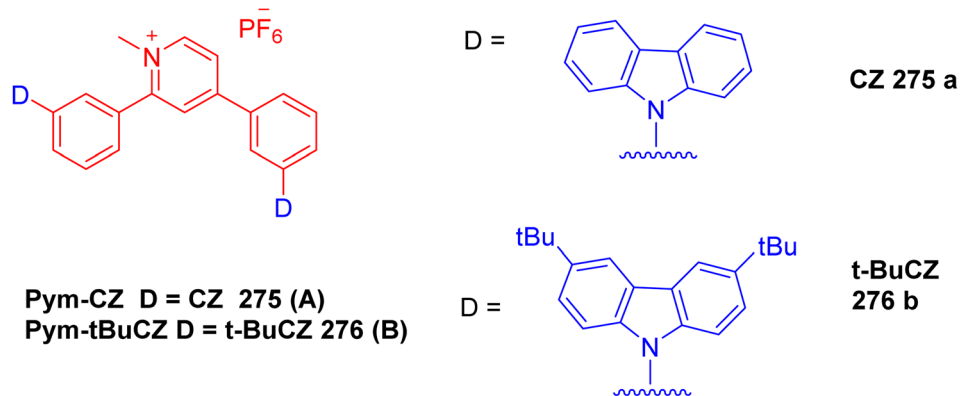
**t-BuCZ
276 b**

Fig. 117 Chemical structure of Pym-CZ (**275a**) and Pym-*t*BuCZ (**276b**).[337]

In 2022, Su *et al.* synthesized two pyridinium-based orange-red TADF emitters, Pym-CZ **275a** and Pym-*t*BuCZ **276b**, for high-efficiency LECs, as depicted in Fig. 117.[337] The pyridine moiety of the emitter was both the ionic component of the LEEC as well as the electron acceptor for TADF. The pyridine was connected to a donor, either CZ or *t*-BuCZ in a *meta*-position. TADF emission was detected by delayed fluorescence lifetimes of 2887 ns for Pym-CZ **275a** and 1746 ns for Pym-*t*BuCZ **276b**.

The LEEC containing Pym-CZ **276a** exhibited a maximum EQE of 1.2%. As the ionic component of the LEECs is pyridine, these are the first purely organic ionic TADF materials described for orange-red LEECs, which may make them useful as a new low-cost approach for the fabrication of these devices.

Zysman-Colman and coworkers (2024) synthesized TPPO-*t*Bu-DiKTa **277** and TPA-*t*Bu-DiKTa **278**, the two novel MR-TADF emitters seen in Fig. 118.[338] According to photophysical

TPPO-tBu-DiKTa
277

TPA-tBu-DiKTa
278
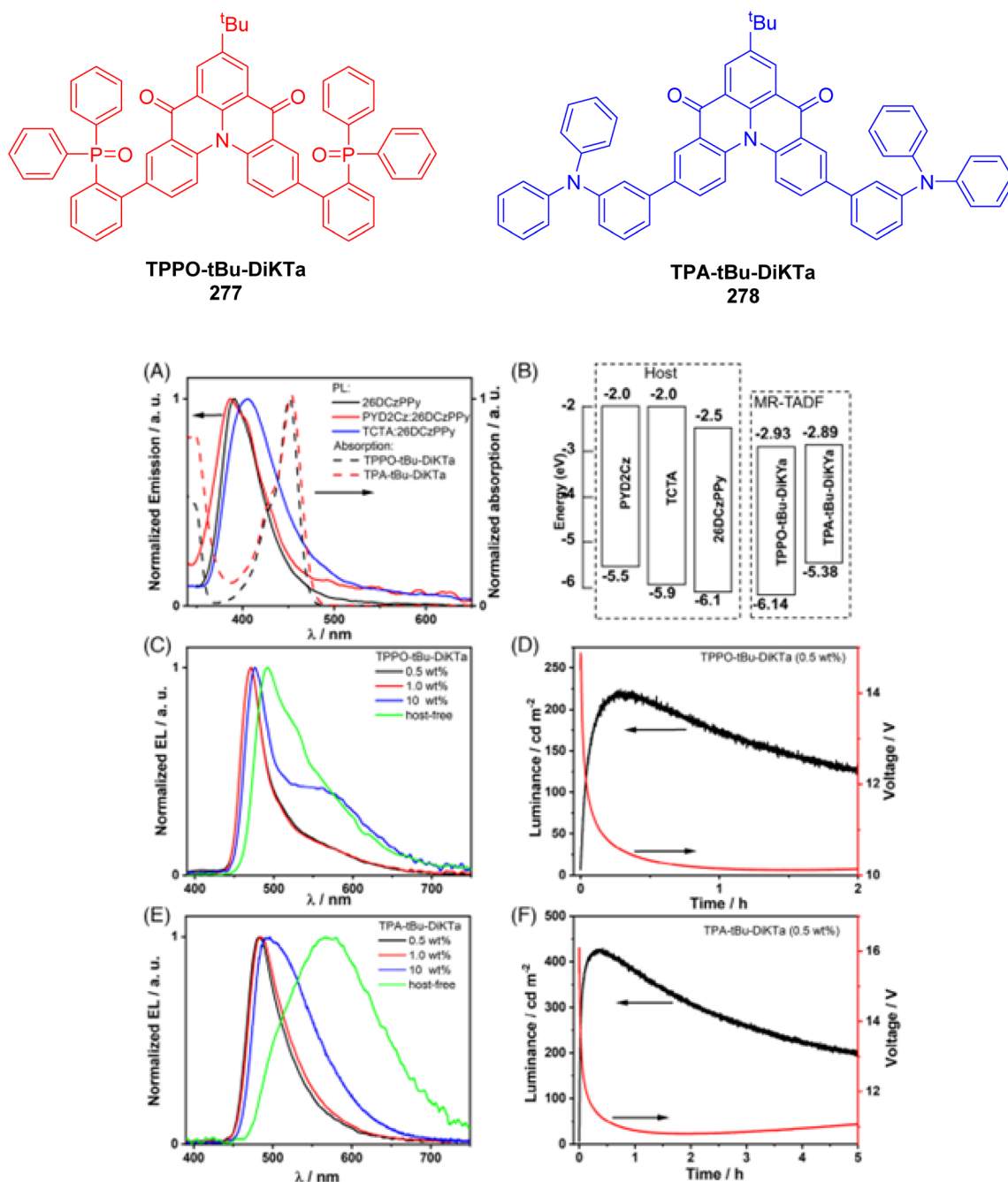
Fig. 118 (A) Normalized PL spectra of the three host systems and the normalized absorption spectra of the two MR–TADF emitters (B) electron energy diagram of the three host compounds and the two MR–TADF emitters (C) normalized EL spectra and (D) temporal evolution of luminance and the voltage of the host–free triphenylphosphine oxide (TPPO)-*t*Bu-DiKTa LECs (0.5 wt%). (E) Normalized EL spectra and (F) temporal evolution of the luminance and the voltage of the host–free triphenylamine (TPA)-*t*Bu-DiKTa LECs (0.5 wt%). Reproduced from ref. 338, https://doi.org/10.1002/agt2.571https://doi.org/10.1038/s41598-017-01812-2, under the terms of the CC BY 4.0 license, https://creativecommons.org/licenses/by/4.0/.

investigations and DFT calculations, the excited states of both TPPO-tBu-DiKTa and TPA-tBu-DiKTa exhibited short-range charge transfer (SRCT). The intermolecular charge transfer in TPA-tBu-DiKTa sped up the RISC processes, resulting in a k_{RISC} of $1.8 \times 10^4\ s^{-1}$ in a 2 wt% doped mCP film, compared to $4.0 \times 10^3\ s^{-1}$ for TPPO-tBu-DiKTa in the same film. OLEDs were produced with different concentrations of doped TPPO-tBu-DiKTa or TPA-tBu-DiKTa in a mCP:PPT cohost. The devices containing 2% TPPO-tBu-DiKTa or 5% TPA-tBu-DiKTa OLED containing 2% TPPO-tBu-DiKTa showed a blue emission at 480 nm with an EQE_{max} of 24.4%, while the OLED containing 5% TPA-tBu-DiKTa showed a green emission at 508 nm with an EQE_{max} of 31.0%. The *ortho*-substituted geometry in both emitters also prevents aggregation of DiKTa moieties leading to ACQ, even with increases in the dopant concentration. For example, a device with 25% TPA-tBu-DiKTa had a broader emission while retaining a high EQE_{max}, and reduced efficiency roll-off. The emitters were also observed to produce narrowband emission *via* the facilitation of electrochemical doping. For example, a LEEC with optimized TPA-tBu-DiKTa concentration in a 26DCzPPy:TCTA host matrix was able to produce steady narrowband blue emission with a luminance of 425 cd m^{-2} with an EQE_{max} of 2.6%.

5.   Conclusions and future outlook

Research into TADF has attracted significant global interest as an efficient method for the production of triplet excitons in pure organic molecules for EL applications. TADF materials as a host material in OLEDs the next generation of OLED technology, and have achieved high device functioning as comparable to phosphorescent OLEDs fabricated using noble metal complexes. Improvement in the functioning of TADF OLEDs, including solution-processed devices, is essential for real-world display technologies. Beyond electroluminescence, TADF materials have shown potential for photocatalysis, facilitating organic transformations under milder conditions than traditional catalytic methods. New organic photocatalysts like 4CzIPN offer advantages such as lower toxicity, cost-effectiveness, and structural diversity. While the development of TADF photocatalysts has lagged behind TADF materials for OLEDs, the field is rapidly evolving, providing valuable insights into structural design and mechanisms. TADF materials are also being explored for various applications, including TTA sensitizers, organic UVPODs, fluorescence probes for biomedical applications, and mechanoluminochromism, leveraging their small ΔE_{ST} and efficient RISC processes. Development of TADF materials is still in a nascent stage and further advances in molecular design and theoretical frameworks are needed to enhance their photophysical characteristics and move beyond D–A type systems. Future research should focus on developing new models and innovative approaches to control excitons through the TADF process, potentially expanding these materials into other research fields and applications. In conclusion, TADF materials represent a continuously advancing field of study with significant potential across various applications. The continued exploration and development of TADF materials promise to drive advancements across a spectrum of technologies, from healthcare to environmental sustainability, unlocking new potentials and innovative solutions in various scientific and industrial fields.

Data availability

All the data is provided in the manuscript file.

Conflicts of interest

The authors have no conflict of interest to declare.

Acknowledgements

References

1 R. Gao, M. S. Kodaimati and D. Yan, *Chem. Soc. Rev.*, 2021, **50**, 5564–5589.

2 N. Armaroli and H. J. Bolink, *Top. Curr. Chem.*, 2016, **374**, 1–3.

3 B. Santra, S. Pal and A. Kanjilal, *ACS Appl. Opt. Mater.*, 2024, **2**, 687–696.

4 J. Hölsä, *Electrochem. Soc. Interface*, 2009, **18**, 42.

5 A. Mesaros, *Appl. Sci.*, 2023, **13**, 11221.

6 M. G. Brik and A. M. Srivastava, *Luminescent Materials: Fundamentals and Applications*, Walter de Gruyter GmbH & Co KG, 2023.

7 E. Kim, Y. Lee, S. Lee and S. B. Park, *Acc. Chem. Res.*, 2015, **48**, 538–547.

8 J. Zhou, Q. Liu, W. Feng, Y. Sun and F. Li, *Chem. Rev.*, 2015, **115**, 395–465.

9 M. D. Allendorf, C. A. Bauer, R. Bhakta and R. Houk, *Chem. Soc. Rev.*, 2009, **38**, 1330–1352.

10 D. T. Thielemann, A. T. Wagner, E. Rösch, D. K. Kölmel, J. G. Heck, B. Rudat, M. Neumaier, C. Feldmann, U. Schepers and S. Bräse, *J. Am. Chem. Soc.*, 2013, **135**, 7454–7457.

11 S. Silvi and A. Credi, *Chem. Soc. Rev.*, 2015, **44**, 4275–4289.

12 D. Wang and B. Z. Tang, *Acc. Chem. Res.*, 2019, **52**, 2559–2570.

13 Kenry, K. C. Chong and B. Liu, *Acc. Chem. Res.*, 2019, **52**, 3051–3063.

14 S. Datta and J. Xu, *ACS Appl. Bio Mater.*, 2023, **6**, 4572–4585.

15 Y. Wang, J. Nie, W. Fang, L. Yang, Q. Hu, Z. Wang, J. Z. Sun and B. Z. Tang, *Chem. Rev.*, 2020, **120**, 4534–4577.

16 D. Barman, K. Narang, R. Parui, N. Zehra, M. N. Khatun, L. R. Adil and P. K. Iyer, *Aggregate*, 2022, **3**, e172.

17 H. Uoyama, K. Goushi, K. Shizu, H. Nomura and C. Adachi, *Nature*, 2012, **492**, 234–238.
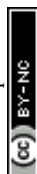
18 X. Xiong, F. Song, J. Wang, Y. Zhang, Y. Xue, L. Sun, N. Jiang, P. Gao, L. Tian and X. Peng, *J. Am. Chem. Soc.*, 2014, **136**, 9590–9597.

19 J. Mei, N. L. Leung, R. T. Kwok, J. W. Lam and B. Z. Tang, *Chem. Rev.*, 2015, **115**, 11718–11940.

20 X. Chen, L. Sun, A. A. Sukhanov, S. Doria, L. Bussotti, J. Zhao, H. Xu, B. Dick, V. K. Voronkova and M. Di Donato, *Chem. Sci.*, 2024, **15**, 10867–10881.

21 J. Perrin, *Lumière et Réactions Chimiques*, Gauthier-Villars, 1926.

22 R. Delorme and F. Perrin, *J. Phys. Radium*, 1929, **10**, 177–186.

23 D. Huang and J. M. Cole, *Sci. Data*, 2024, **11**, 80.

24 Y. Xiong, J. Gong, J. Liu, D. Wang, H. Wu, Z. Zhao, M. Fang, Z. Li, D. Wang and B. Z. Tang, *J. Mater. Chem. C*, 2022, **10**, 10009–10016.

25 F. Fang, L. Zhu, M. Li, Y. Song, M. Sun, D. Zhao and J. Zhang, *Adv. Sci.*, 2021, **8**, 2102970.

26 A. F. Suleymanova, M. Z. Shafikov, A. C. Whitwood, R. Czerwieniec and D. W. Bruce, *J. Mater. Chem. C*, 2021, **9**, 6528–6535.

27 A. F. Suleymanova, M. Z. Shafikov, X. Chen, Y. Wang, R. Czerwieniec and D. W. Bruce, *Phys. Chem. Chem. Phys.*, 2022, **24**, 22115–22121.

28 D. Chen, F. Tenopala-Carmona, J. A. Knöller, A. Mischok, D. Hall, S. Madayanad Suresh, T. Matulaitis, Y. Olivier, P. Nacke and F. Gießelmann, *Angew. Chem., Int. Ed.*, 2023, **62**, e202218911.

29 A. Farokhi, S. Lipinski, L. M. Cavinato, H. Shahroosvand, B. Pashaei, S. Karimi, S. Bellani, F. Bonaccorso and R. D. Costa, *Chem. Soc. Rev.*, 2025, (**54**), 266–340.

30 Y. Zhang, K. Aslan, M. J. Previte, S. N. Malyn and C. D. Geddes, *J. Phys. Chem. B*, 2006, **110**, 25108–25114.

31 A. Abdurahman, T. J. Hele, Q. Gu, J. Zhang, Q. Peng, M. Zhang, R. H. Friend, F. Li and E. W. Evans, *Nat. Mater.*, 2020, **19**, 1224–1229.

32 A. P. M. Reponen, G. Londi, C. S. Matthews, Y. Olivier, A. S. Romanov, N. C. Greenham and A. J. Gillett, *Angew. Chem., Int. Ed.*, 2024, **63**, e202402052.

33 Y. Feng, X. Zhuang, Y. Xu, J. Xue, C. Qu, Q. Wang, Y. Liu and Y. Wang, *Chem. Eng. J.*, 2023, **478**, 147123.

34 Y. Hu, P. Wu, H. Jiang, H. Wu, W. Li, D. Gu and T. Zhang, *Opt. Mater.*, 2022, **134**, 113071.

35 M. Mońka, P. Pander, D. Grzywacz, A. Sikorski, R. Rogowski, P. Bojarski, A. P. Monkman and I. E. Serdiuk, *ACS Appl. Mater. Interfaces*, 2025, **17**(6), 9635–9645.

36 W. Xiong, C. Zhang, Y. Fang, M. Peng and W. Sun, *Polymers*, 2022, **15**, 98.

37 V. Ferraro, C. Bizzarri and S. Bräse, *Adv. Sci.*, 2024, **11**, 2404866.

38 K. M. Rao, R. Rajavaram, D. Kolli, S. P. Vattikuti and M. Godumala, *J. Mater. Chem. C*, 2025, (**13**), 3091–3122.

39 X. Chen, X. Zhang, X. Xiao, Z. Wang and J. Zhao, *Angew. Chem., Int. Ed.*, 2023, **62**, e202216010.

40 Q. Xue and G. Xie, *Adv. Opt. Mater.*, 2021, **9**, 2002204.

41 X.-K. Chen, D. Kim and J.-L. Brédas, *Acc. Chem. Res.*, 2018, **51**, 2215–2224.

42 T. Zhang, Y. Xiao, H. Wang, S. Kong, R. Huang, V. K. -M. Au, T. Yu and W. Huang, *Angew. Chem., Int. Ed.*, 2023, **62**, e202301896.

43 Y. Bao, *Langmuir*, 2024, **40**, 3275–3282.

44 B. Cui, J. Zhou, C. Duan and H. Xu, *Adv. Opt. Mater.*, 2025, 2403295.

45 X.-F. Luo, X. Xiao and Y.-X. Zheng, *Chem. Commun.*, 2024, **60**(9), 1089–1099.

46 X. Xiaoyang, L. Meiyan, L. Chenglong, W. Xiaoming and L. Xuguang, *Chin. J. Org. Chem.*, 2023, **43**, 3826.

47 R. Wang, C.-S. Lee and Z. Lu, *J. Organomet. Chem.*, 2023, **984**, 122564.

48 J. Shi, Z. Ran, F. Peng, M. Chen, L. Li, L. Ji and W. Huang, *J. Mater. Chem. C*, 2022, **10**, 9165–9191.

49 P. Keerthika and R. K. Konidena, *Adv. Opt. Mater.*, 2023, **11**, 2301732.

50 K. P. CP, K. R. Naveen and J. Hur, *Mater. Chem. Front.*, 2024, **8**, 769–784.

51 C. Lv, X. Wang, Q. Zhang and Y. Zhang, *Mater. Chem. Front.*, 2023, **7**, 2809–2827.

52 K. Chu, Z. Ding and E. Zysman-Colman, *Chem.–Eur. J.*, 2023, **29**, e202301504.

53 P. Ledwon, *Org. Electron.*, 2019, **75**, 105422.

54 B. Wex and B. R. Kaafarani, *J. Mater. Chem. C*, 2017, **5**, 8622–8653.

55 J. Zhang, R. Chen, Z. Zhu, C. Adachi, X. Zhang and C. S. Lee, Highly Stable Near-Infrared Fluorescent Organic Nanoparticles with a Large Stokes Shift for Noninvasive Long-Term Cellular Imaging, *ACS Appl. Mater. Interfaces*, 2015, **7**(47), 26266–26274.

56 N. Jiang, C.-Y. Zhu, K.-X. Li, Y.-H. Xu and M. R. Bryce, *Macromolecules*, 2024, **57**, 5561–5577.

57 Y.-X. Che, X.-N. Qi, Q. Lin, H. Yao, W.-J. Qu, B. Shi, Y.-M. Zhang and T.-B. Wei, *J. Mater. Chem. C*, 2022, **10**, 11119–11174.

58 J.-T. Ye, L. Wang, H.-Q. Wang, H.-M. Xie and Y.-Q. Qiu, *Org. Electron.*, 2019, **70**, 193–204.

59 D.-Y. Qin, M. Zhang, Y.-N. Hu, Y.-X. Miao, J. Ye, C.-J. Zheng, J. Zhang, W. Xu, J.-C. Li and K. Wang, *Chem. Eng. J.*, 2022, **450**, 138174.

60 J.-T. Ye, H.-Q. Wang, Y. Zhang and Y.-Q. Qiu, *J. Phys. Chem. C*, 2019, **124**, 921–931.

61 S. Sharma and S. Sengupta, *Org. Chem. Front.*, 2023, **10**, 6087–6095.

62 S. Kumar, M. Kumar, H. Bhambri, S. K. Mandal and V. Bhalla, *ACS Appl. Mater. Interfaces*, 2024, **16**, 67683–67696.

63 Y.-H. Mao, M.-K. Hung, S.-T. Chung, S. Sharma, K.-W. Tsai and S.-A. Chen, *ACS Appl. Mater. Interfaces*, 2024, **16**, 60715–60731.

64 S. Garain and F. Würthner, *Chem. Commun.*, 2025, (**61**), 3081–3092.

65 N. J. Turro, V. Ramamurthy and J. C. Scaiano, *Modern Molecular Photochemistry of Organic Molecules*, University Science Books Sausalito, CA, 2010.

66 A. Köhler and H. Bässler, *Electronic Processes in Organic Semiconductors: an Introduction*, John Wiley & Sons, 2015.

67 P. L. dos Santos, M. K. Etherington and A. P. Monkman, *J. Mater. Chem. C*, 2018, **6**, 4842–4853.

68 G. Jiang, F. Li, J. Fan, Y. Song, C.-K. Wang and L. Lin, *J. Mater. Chem. C*, 2020, **8**, 98–108.

69 S. J. Yoon, J. H. Kim, W. J. Chung and J. Y. Lee, *Chem.–Eur. J.*, 2021, **27**, 3065–3073.

70 A. Danos, D. Gudeika, N. A. Kukhta, R. Lygaitis, M. Colella, H. F. Higginbotham, A. N. Bismillah, P. R. McGonigal, J. V. Grazulevicius and A. P. Monkman, *J. Mater. Chem. C*, 2022, **10**, 4737–4747.

71 Y. Olivier, M. Moral, L. Muccioli and J.-C. Sancho-García, *J. Mater. Chem. C*, 2017, **5**, 5718–5729.

72 X.-T. Liu, W. Hua, H.-X. Nie, M. Chen, Z. Chang and X.-H. Bu, *Natl. Sci. Rev.*, 2022, **9**, nwab222.

73 J. M. Kaminski, T. Böhmer and C. M. Marian, *J. Phys. Chem. C*, 2024, **128**, 13711–13721.

74 H. Miranda-Salinas, Y.-T. Hung, Y.-S. Chen, D. Luo, H.-C. Kao, C.-H. Chang, K.-T. Wong and A. Monkman, *J. Mater. Chem. C*, 2021, **9**, 8819–8833.

75 D. Zhong, Y. Yu, L. Yue, X. Yang, L. Ma, G. Zhou and Z. Wu, *Chem. Eng. J.*, 2021, **413**, 127445.

76 H.-Y. Zhang, H.-Y. Yang, M. Zhang, H. Lin, S.-L. Tao, C.-J. Zheng and X.-H. Zhang, *Mater. Horiz.*, 2022, **9**, 2425–2432.

77 T. J. Penfold and J. Gibson, *Highly Efficient OLEDs: Materials Based on Thermally Activated Delayed Fluorescence*, 2018, pp. 297–330.

78 M. Hempe, N. A. Kukhta, A. Danos, M. A. Fox, A. S. Batsanov, A. P. Monkman and M. R. Bryce, *Chem. Mater.*, 2021, **33**, 3066–3080.

79 M. K. Etherington, J. Gibson, H. F. Higginbotham, T. J. Penfold and A. P. Monkman, *Nat. Commun.*, 2016, **7**, 13680.

80 H. L. Lee, S. O. Jeon, I. Kim, S. C. Kim, J. Lim, J. Kim, S. Park, J. Chwae, W.-J. Son, H. Choi and J. Y. Lee, *Adv. Mater.*, 2022, **34**, 2202464.

81 T. J. Penfold, E. Gindensperger, C. Daniel and C. M. Marian, *Chem. Rev.*, 2018, **118**, 6975–7025.

82 N. Li, F. Ni, X. Lv, Z. Huang, X. Cao and C. Yang, *Adv. Opt. Mater.*, 2022, **10**, 2101343.

83 S. Jhulki, M. W. Cooper, S. Barlow and S. R. Marder, *Mater. Chem. Front.*, 2019, **3**, 1699–1721.

84 K. Shizu and H. Kaji, *Commun. Chem.*, 2022, **5**, 53.

85 C. Parker and C. Hatchard, *Trans. Faraday Soc.*, 1961, **57**, 1894–1904.

86 J. R. Kirchhoff, R. E. Gamache Jr, M. W. Blaskie, A. A. Del Paggio, R. K. Lengel and D. R. McMillin, *Inorg. Chem.*, 1983, **22**, 2380–2384.

87 M. N. Berberan-Santos and J. M. Garcia, *J. Am. Chem. Soc.*, 1996, **118**, 9391–9394.

88 A. Endo, M. Ogasawara, A. Takahashi, D. Yokoyama, Y. Kato and C. Adachi, *Adv. Mater.*, 2009, **21**, 4802–4806.

89 J. C. Deaton, S. C. Switalski, D. Y. Kondakov, R. H. Young, T. D. Pawlik, D. J. Giesen, S. B. Harkins, A. J. Miller, S. F. Mickenberg and J. C. Peters, *J. Am. Chem. Soc.*, 2010, **132**, 9499–9508.

90 Y. Liu, X.-L. Chen, X.-Y. Li, S.-S. Zhu, S.-J. Li, Y. Song, L.-B. Qu and B. Yu, *J. Am. Chem. Soc.*, 2020, **143**, 964–972.

91 K. Goushi, K. Yoshida, K. Sato and C. Adachi, *Nat. Photonics*, 2012, **6**, 253–258.

92 A. Endo, K. Sato, K. Yoshimura, T. Kai, A. Kawada, H. Miyazaki and C. Adachi, *Appl. Phys. Lett.*, 2011, **98**, 083302.

93 J.-H. Lee, *PhD thesis*, Seoul National University Graduate School, 2014.

94 S. Y. Kim, W. I. Jeong, C. Mayr, Y. S. Park, K. H. Kim, J. H. Lee, C. K. Moon, W. Brütting and J. J. Kim, *Adv. Funct. Mater.*, 2013, **23**, 3896–3900.

95 J. W. Sun, J. H. Lee, C. K. Moon, K. H. Kim, H. Shin and J. J. Kim, *Adv. Mater.*, 2014, **26**, 5684–5688.

96 D. R. Lee, B. S. Kim, C. W. Lee, Y. Im, K. S. Yook, S.-H. Hwang and J. Y. Lee, *ACS Appl. Mater. Interfaces*, 2015, **7**, 9625–9629.

97 C. Adachi, *Jpn. J. Appl. Phys.*, 2014, **53**, 060101.

98 Y. Tao, K. Yuan, T. Chen, P. Xu, H. Li, R. Chen, C. Zheng, L. Zhang and W. Huang, *Adv. Mater.*, 2014, **26**, 7931–7958.

99 K. Shizu, H. Noda, H. Tanaka, M. Taneda, M. Uejima, T. Sato, K. Tanaka, H. Kaji and C. Adachi, *J. Phys. Chem. C*, 2015, **119**, 26283–26289.

100 S. Hirata, Y. Sakai, K. Masui, H. Tanaka, S. Y. Lee, H. Nomura, N. Nakamura, M. Yasumatsu, H. Nakanotani and Q. Zhang, *Nat. Mater.*, 2015, **14**, 330–336.

101 K. Kawasumi, T. Wu, T. Zhu, H. S. Chae, T. Van Voorhis, M. A. Baldo and T. M. Swager, *J. Am. Chem. Soc.*, 2015, **137**, 11908–11911.

102 S. Y. Lee, T. Yasuda, I. S. Park and C. Adachi, *Dalton Trans.*, 2015, **44**, 8356–8359.

103 Y. J. Cho, S. K. Jeon, B. D. Chin, E. Yu and J. Y. Lee, *Angew. Chem., Int. Ed.*, 2015, **54**, 5201–5204.

104 T. Hatakeyama, K. Shiren, K. Nakajima, S. Nomura, S. Nakatsuka, K. Kinoshita, J. Ni, Y. Ono and T. Ikuta, *Adv. Mater.*, 2016, **28**, 2777–2781.

105 Z. Yang, Z. Mao, Z. Xie, Y. Zhang, S. Liu, J. Zhao, J. Xu, Z. Chi and M. P. Aldred, *Chem. Soc. Rev.*, 2017, **46**, 915–1016.

106 T. Mori and Y. Inoue, *Chem. Soc. Rev.*, 2013, **42**, 8122–8133.

107 S. A. Jenekhe and J. A. Osaheni, *Science*, 1994, **265**, 765–768.

108 M. Cocchi, D. Virgili, G. Giro, V. Fattori, P. Di Marco, J. Kalinowski and Y. Shirota, *Appl. Phys. Lett.*, 2002, **80**, 2401–2403.

109 S. Lee, K. H. Kim, D. Limbach, Y. S. Park and J. J. Kim, *Adv. Funct. Mater.*, 2013, **23**, 4105–4110.

110 D. Chen, G. Xie, X. Cai, M. Liu, Y. Cao and S.-J. Su, *Adv. Mater.*, 2015, **28**, 239–244.

111 D. Chen, Z. Wang, D. Wang, Y.-C. Wu, C.-C. Lo, A. Lien, Y. Cao and S.-J. Su, *Org. Electron.*, 2015, **25**, 79–84.

112 X. Jiang, R. A. Register, K. A. Killeen, M. E. Thompson, F. Pschenitzka, T. R. Hebner and J. C. Sturm, *J. Appl. Phys.*, 2002, **91**, 6717–6724.

113 M. Zhang, Z. Chen, L. Xiao, B. Qu and Q. Gong, *Appl. Phys. Express*, 2011, **4**, 082105.

114 P. Pikna, V. Skoromets, C. Becker, A. Fejfar and P. Kužel, *Appl. Phys. Lett.*, 2015, **107**, 233901.

115 H. W. Lee, H. J. Kim, Y. S. Kim, J. Kim, S. E. Lee, H. W. Lee, Y. K. Kim and S. S. Yoon, *J. Lumin.*, 2015, **165**, 99–104.

116 H.-B. Kim and J.-J. Kim, *J. Soc. Inf. Disp.*, 2019, **20**, 105–121.

117 D. Y. Zhang, Y. Zheng, H. Zhang, J. H. Sun, C. P. Tan, L. He, W. Zhang, L. N. Ji and Z. W. Mao, *Adv. Sci.*, 2018, **5**, 1800581.

118 J. F. Wang, Y. Kawabe, S. E. Shaheen, M. M. Morrell, G. E. Jabbour, P. A. Lee, J. Anderson, N. R. Armstrong, B. Kippelen and E. A. Mash, *Adv. Mater.*, 1998, **10**, 230–233.

119 Q. Wang, Q.-S. Tian, Y.-L. Zhang, X. Tang and L.-S. Liao, *J. Mater. Chem. C*, 2019, **7**, 11329–11360.

120 J. Gibson, A. P. Monkman and T. J. Penfold, *ChemPhysChem*, 2016, **17**, 2956–2961.

121 T. Hosokai, H. Matsuzaki, H. Nakanotani, K. Tokumaru, T. Tsutsui, A. Furube, K. Nasu, H. Nomura, M. Yahiro and C. Adachi, *Sci. Adv.*, 2017, **3**, e1603282.

122 J. Zhang, W. Chen, S. Kalytchuk, K. F. Li, R. Chen, C. Adachi, Z. Chen, A. L. Rogach, G. Zhu and P. K. Yu, *ACS Appl. Mater. Interfaces*, 2016, **8**, 11355–11365.

123 V.-N. Nguyen, A. Kumar, M. H. Lee and J. Yoon, *Coord. Chem. Rev.*, 2020, **425**, 213545.

124 J. Huang, J. Li, Y. Lyu, Q. Miao and K. Pu, *Nat. Mater.*, 2019, **18**, 1133–1143.

125 Q. Miao, D. C. Yeo, C. Wiraja, J. Zhang, X. Ning, C. Xu and K. Pu, *Angew. Chem.*, 2018, **130**, 1270–1274.

126 J. Zhang, S. Li, F.-F. An, J. Liu, S. Jin, J.-C. Zhang, P. C. Wang, X. Zhang, C.-S. Lee and X.-J. Liang, *Nanoscale*, 2015, **7**, 13503–13510.

127 J.-T. Hou, K.-K. Yu, K. Sunwoo, W. Y. Kim, S. Koo, J. Wang, W. X. Ren, S. Wang, X.-Q. Yu and J. S. Kim, *Chem*, 2020, **6**, 832–866.

128 F. Fang, M. Li, J. Zhang and C.-S. Lee, *ACS Mater. Lett.*, 2020, **2**, 531–549.

129 M. Lan, J. Zhang, X. Zhu, P. Wang, X. Chen, C.-S. Lee and W. Zhang, *Nano Res.*, 2015, **8**, 2380–2389.

130 T. Zhang, C. Ma, T. Sun and Z. Xie, *Coord. Chem. Rev.*, 2019, **390**, 76–85.

131 J. Zhang, R. Chen, Z. Zhu, C. Adachi, X. Zhang and C.-S. Lee, *ACS Appl. Mater. Interfaces*, 2015, **7**, 26266–26274.

132 Y. Tsuchiya, K. Ikesue, H. Nakanotani and C. Adachi, *Chem. Commun.*, 2019, **55**, 5215–5218.

133 C. Wang, Z. Chen, X. Tang, X. Liu, W. Na, W. Li and T. Liu, *Photodiagnosis Photodyn. Ther.*, 2020, **32**, 102014.

134 K. Y. Zhang, Q. Yu, H. Wei, S. Liu, Q. Zhao and W. Huang, *Chem. Rev.*, 2018, **118**, 1770–1839.

135 S. Huo, S. Jin, X. Ma, X. Xue, K. Yang, A. Kumar, P. C. Wang, J. Zhang, Z. Hu and X.-J. Liang, *ACS Nano*, 2014, **8**, 5852–5862.

136 X. H. Wang, H. S. Peng, L. Yang, F. T. You, F. Teng, L. L. Hou and O. S. Wolfbeis, *Angew. Chem.*, 2014, **126**, 12679–12683.

137 J. G. Huang, T. Leshuk and F. X. Gu, *Nano Today*, 2011, **6**, 478–492.

138 X. Ma, J. Jia, R. Cao, X. Wang and H. Fei, *J. Am. Chem. Soc.*, 2014, **136**, 17734–17737.

139 F. Fang, D. Zhao, Y. Zhang, M. Li, J. Ye and J. Zhang, *ACS Appl. Bio Mater.*, 2020, **3**, 5103–5110.

140 P. Dong, J. Stellmacher, L. M. Bouchet, M. Nieke, A. Kumar, E. R. Osorio-Blanco, G. Nagel, S. B. Lohan, C. Teutloff and A. Patzelt, *Angew. Chem., Int. Ed.*, 2021, **60**, 14938–14944.

141 G. Hong, A. L. Antaris and H. Dai, *Nat. Biomed. Eng.*, 2017, **1**, 0010.

142 J. Joo, X. Liu, V. R. Kotamraju, E. Ruoslahti, Y. Nam and M. J. Sailor, *ACS Nano*, 2015, **9**, 6233–6241.

143 R. Liu, J. Tang, Y. Xu and Z. Dai, *ACS Nano*, 2019, **13**, 5124–5132.

144 T. S. Blacker, Z. F. Mann, J. E. Gale, M. Ziegler, A. J. Bain, G. Szabadkai and M. R. Duchen, *Nat. Commun.*, 2014, **5**, 3936.

145 I. Georgakoudi, B. C. Jacobson, M. G. Muller, E. E. Sheets, K. Badizadegan, D. L. Carr-Locke, C. P. Crum, C. W. Boone, R. R. Dasari and J. Van Dam, *Cancer Res.*, 2002, **62**, 682–687.

146 H. Shi, H. Sun, H. Yang, S. Liu, G. Jenkins, W. Feng, F. Li, Q. Zhao, B. Liu and W. Huang, *Adv. Funct. Mater.*, 2013, **23**, 3268–3276.

147 F. Ni, N. Li, L. Zhan and C. Yang, *Adv. Opt. Mater.*, 2020, **8**, 1902187.

148 Y. Jiang, J. Huang, X. Zhen, Z. Zeng, J. Li, C. Xie, Q. Miao, J. Chen, P. Chen and K. Pu, *Nat. Commun.*, 2019, **10**, 2064.

149 Y. Tanigawa, J. Li, J. M. Justesen, H. Horn, M. Aguirre, C. DeBoever, C. Chang, B. Narasimhan, K. Lage and T. Hastie, *Nat. Commun.*, 2019, **10**, 4064.

150 Q. Miao, C. Xie, X. Zhen, Y. Lyu, H. Duan, X. Liu, J. V. Jokerst and K. Pu, *Nat. Biotechnol.*, 2017, **35**, 1102–1110.

151 Y. Lyu, D. Cui, J. Huang, W. Fan, Y. Miao and K. Pu, *Angew. Chem., Int. Ed.*, 2019, **58**, 4983–4987.

152 X. Zhen, Y. Tao, Z. An, P. Chen, C. Xu, R. Chen, W. Huang and K. Pu, *Adv. Mater.*, 2017, **29**, 1606665.

153 Y. Fan, P. Wang, Y. Lu, R. Wang, L. Zhou, X. Zheng, X. Li, J. A. Piper and F. Zhang, *Nat. Nanotechnol.*, 2018, **13**, 941–946.

154 Z. Zhu, B. Song, J. Yuan and C. Yang, *Adv. Sci.*, 2016, **3**, 1600146.

155 M. Delbianco, V. Sadovnikova, E. Bourrier, G. Mathis, L. Lamarque, J. M. Zwier and D. Parker, *Angew. Chem.*, 2014, **126**, 10894–10898.

156 S. M. King, S. Claire, R. I. Teixeira, A. N. Dosumu, A. J. Carrod, H. Dehghani, M. J. Hannon, A. D. Ward, R. Bicknell and S. W. Botchway, *J. Am. Chem. Soc.*, 2018, **140**, 10242–10249.

157 T. He, C. Ren, Z. Li, S. Xiao, J. Li, X. Lin, C. Ye, J. Zhang, L. Guo and W. Hu, *Appl. Phys. Lett.*, 2018, **112**, 211102.

158 Y. Liu, C. Li, Z. Ren, S. Yan and M. R. Bryce, *Nat. Rev. Mater.*, 2018, **3**, 1–20.

159 W. Hu, L. Guo, L. Bai, X. Miao, Y. Ni, Q. Wang, H. Zhao, M. Xie, L. Li and X. Lu, *Adv. Healthcare Mater.*, 2018, **7**, 1870062.

160 N. R. Paisley, C. M. Tonge and Z. M. Hudson, *Front. Chem.*, 2020, **8**, 229.

161 F. Ni, N. Li, L. Zhan and C. Yang, *Adv. Opt. Mater.*, 2020, **8**, 1902187.

162 Q. Zhang, S. Xu, M. Li, Y. Wang, N. Zhang, Y. Guan, M. Chen, C.-F. Chen and H.-Y. Hu, *Chem. Commun.*, 2019, **55**, 5639–5642.

163 R. Wei, L. Zhang, S. Xu, Q. Zhang, Y. Qi and H.-Y. Hu, *Chem. Commun.*, 2020, **56**, 2550–2553.

164 S. Gan, J. Zhou, T. A. Smith, H. Su, W. Luo, Y. Hong, Z. Zhao and B. Z. Tang, *Mater. Chem. Front.*, 2017, **1**, 2554–2558.

165 S. Qi, S. Kim, V.-N. Nguyen, Y. Kim, G. Niu, G. Kim, S.-J. Kim, S. Park and J. Yoon, *ACS Appl. Mater. Interfaces*, 2020, **12**, 51293–51301.

166 Y. Wu, L. Jiao, F. Song, M. Chen, D. Liu, W. Yang, Y. Sun, G. Hong, L. Liu and X. Peng, *Chem. Commun.*, 2019, **55**, 14522–14525.

167 Y. Wu, F. Song, W. Luo, Z. Liu, B. Song and X. Peng, *ChemPhotoChem*, 2017, **1**, 79–83.

168 S. Gan, J. Zhou, T. A. Smith, H. Su, W. Luo, Y. Hong, Z. Zhao and B. Tang, *Mater. Chem. Front.*, 2017, 2554.

169 M. Luo, X. Li, L. Ding, G. Baryshnikov, S. Shen, M. Zhu, L. Zhou, M. Zhang, J. Lu, H. Ågren, X.-d. Wang and L. Zhu, *Angew. Chem., Int. Ed.*, 2020, **59**, 17018–17025.

170 J. Jin, H. Jiang, Q. Yang, L. Tang, Y. Tao, Y. Li, R. Chen, C. Zheng, Q. Fan, K. Y. Zhang, Q. Zhao and W. Huang, *Nat. Commun.*, 2020, **11**, 842.

171 X.-L. Hao, A.-M. Ren and L. Zhou, *J. Phys. Chem. Lett.*, 2022, **13**, 11745–11752.

172 F. Ni, M. Xie, T. Liu, X. Zhou, Z. Chen, K. Zheng, Y. Wu, Q. Zhao and C. Yang, *Chem. Eng. J.*, 2022, **437**, 135396.

173 Z. Zhu, Z. Luo, Y.-Q. Xie, Y. Sun, L. Xu and Q. Wu, *Adv. Funct. Mater.*, 2024, **34**, 2313701.

174 X.-L. Hao, A.-M. Ren and L. Zhou, *J. Phys. Chem. Lett.*, 2023, **14**, 10309–10317.

175 W. L. Primrose, P. Hu and Z. M. Hudson, *ACS Appl. Nano Mater.*, 2024, 12673–12681.

176 P. W. Zach, S. A. Freunberger, I. Klimant and S. M. Borisov, *ACS Appl. Mater. Interfaces*, 2017, **9**, 38008–38023.

177 C. M. Tonge, N. R. Paisley, A. M. Polgar, K. Lix, W. R. Algar and Z. M. Hudson, *ACS Appl. Mater. Interfaces*, 2020, **12**, 6525–6535.

178 C. A. DeRosa, J. Samonina-Kosicka, Z. Fan, H. C. Hendargo, D. H. Weitzel, G. M. Palmer and C. L. Fraser, *Macromolecules*, 2015, **48**, 2967–2977.

179 C. J. Christopherson, D. M. Mayder, J. Poisson, N. R. Paisley, C. M. Tonge and Z. M. Hudson, *ACS Appl. Mater. Interfaces*, 2020, **12**, 20000–20011.

180 S. Xu, Q. Zhang, X. Han, Y. Wang, X. Wang, M. Nazare, J.-D. Jiang and H.-Y. Hu, *ACS Sens.*, 2020, **5**, 1650–1656.

181 X. Li, G. Baryshnikov, C. Deng, X. Bao, B. Wu, Y. Zhou, H. Ågren and L. Zhu, *Nat. Commun.*, 2019, **10**, 731.

182 T. J. Dougherty, C. J. Gomer, B. W. Henderson, G. Jori, D. Kessel, M. Korbelik, J. Moan and Q. Peng, *J. Natl. Cancer Inst.*, 1998, **90**, 889–905.

183 Y. Wan, G. Lu, W.-C. Wei, Y.-H. Huang, S. Li, J.-X. Chen, X. Cui, Y.-F. Xiao, X. Li and Y. Liu, *ACS Nano*, 2020, **14**, 9917–9928.

184 J. Li and K. Pu, *Chem. Soc. Rev.*, 2019, **48**, 38–71.

185 J. Zhang, Y.-C. Liang, X. Lin, X. Zhu, L. Yan, S. Li, X. Yang, G. Zhu, A. L. Rogach and P. K. Yu, *ACS Nano*, 2015, **9**, 9741–9756.

186 X. Cui, J. Zhang, Y. Wan, F. Fang, R. Chen, D. Shen, Z. Huang, S. Tian, Y. Xiao and X. Li, *ACS Appl. Bio Mater.*, 2019, **2**, 3854–3860.

187 A. P. Castano, P. Mroz and M. R. Hamblin, *Nat. Rev. Cancer*, 2006, **6**, 535–545.

188 Y. Wan, G. Lu, J. Zhang, Z. Wang, X. Li, R. Chen, X. Cui, Z. Huang, Y. Xiao and J. Chelora, *Adv. Funct. Mater.*, 2019, **29**, 1903436.

189 S. M. Mousavi, S. A. Hashemi, M. Y. Kalashgrani, N. Omidifar, S. Bahrani, N. Vijayakameswara Rao, A. Babapoor, A. Gholami and W.-H. Chiang, *Polymers*, 2022, **14**, 617.

190 X. Li, F. Fang, B. Sun, C. Yin, J. Tan, Y. Wan, J. Zhang, P. Sun, Q. Fan and P. Wang, *Nanoscale Horiz.*, 2021, **6**, 177–185.

191 D. E. Dolmans, D. Fukumura and R. K. Jain, *Nat. Rev. Cancer*, 2003, **3**, 380–387.

192 S. S. Lucky, K. C. Soo and Y. Zhang, *Chem. Rev.*, 2015, **115**, 1990–2042.

193 J. Zhao, W. Wu, J. Sun and S. Guo, *Chem. Soc. Rev.*, 2013, **42**, 5323–5351.

194 X. Cui, G. Lu, S. Dong, S. Li, Y. Xiao, J. Zhang, Y. Liu, X. Meng, F. Li and C.-S. Lee, *Mater. Horiz.*, 2021, **8**, 571–576.

195 J. Zhang, W. Chen, R. Chen, X.-K. Liu, Y. Xiong, S. V. Kershaw, A. L. Rogach, C. Adachi, X. Zhang and C.-S. Lee, *Chem. Commun.*, 2016, **52**, 11744–11747.

196 J. Zhang, F. Fang, B. Liu, J.-H. Tan, W.-C. Chen, Z. Zhu, Y. Yuan, Y. Wan, X. Cui, S. Li, Q.-X. Tong, J. Zhao, X.-M. Meng and C.-S. Lee, *ACS Appl. Mater. Interfaces*, 2019, **11**, 41051–41061.

197 Z. Liu, W. Shi, G. Hong, W. Chen, B. Song, X. Peng, X. Xiong and F. Song, *J. Contr. Release*, 2019, **310**, 1–10.

198 Z. Liu, F. Song, W. Shi, G. Gurzadyan, H. Yin, B. Song, R. Liang and X. Peng, *ACS Appl. Mater. Interfaces*, 2019, **11**, 15426–15435.

199 M. Li, J. Xia, R. Tian, J. Wang, J. Fan, J. Du, S. Long, X. Song, J. W. Foley and X. Peng, *J. Am. Chem. Soc.*, 2018, **140**, 14851–14859.

200 Y.-F. Xiao, J.-X. Chen, S. Li, W.-W. Tao, S. Tian, K. Wang, X. Cui, Z. Huang, X.-H. Zhang and C.-S. Lee, *Chem. Sci.*, 2020, **11**, 888–895.

201 Y.-F. Xiao, J.-X. Chen, W.-C. Chen, X. Zheng, C. Cao, J. Tan, X. Cui, Z. Yuan, S. Ji, G. Lu, W. Liu, P. Wang, S. Li and C.-S. Lee, *Chem. Commun.*, 2021, **57**, 4902–4905.

202 Z. Li, X.-G. Yang, H. Zhang, J.-R. Zhang, X.-K. Tian, J.-H. Qin, L.-F. Ma and D. Yan, *Inorg. Chem. Front.*, 2022, **9**, 4281–4287.

203 W. Chen, Z. Wang, M. Tian, G. Hong, Y. Wu, M. Sui, M. Chen, J. An, F. Song and X. Peng, *J. Am. Chem. Soc.*, 2023, **145**, 8130–8140.

204 J. Zhang, J. Ma, S. Zhang, X. Lou, Y. Ding, Y. Li, M. Xu, X. Xie, X. Jiao and X. Dou, *ACS Nano*, 2023, **17**, 23430–23441.

205 Y. Xu, B. Chen, D. Su, J. Li, Q. Qi, Y. Hu, Q. Wang, F. Xia, X. Lou, Z. Zhao, J. Dai, X. Dong and J. Zhou, *ACS Appl. Mater. Interfaces*, 2023, **15**, 56314–56327.

206 B. T. Luppi, W. L. Primrose and Z. M. Hudson, *Angew. Chem., Int. Ed.*, 2024, **63**, e202400712.

207 G. S. Nongthombam, D. Barman and P. K. Iyer, *ACS Appl. Bio Mater.*, 2024, **7**(3), 1899–1909.

208 M. A. Bryden and E. Zysman-Colman, *Chem. Soc. Rev.*, 2021, **50**, 7587–7680.

209 D. A. Nicewicz and D. W. MacMillan, *Science*, 2008, **322**, 77–80.

210 M. A. Ischay, M. E. Anzovino, J. Du and T. P. Yoon, *J. Am. Chem. Soc.*, 2008, **130**, 12886–12887.

211 J. M. Narayanam, J. W. Tucker and C. R. Stephenson, *J. Am. Chem. Soc.*, 2009, **131**, 8756–8757.

212 D. M. Arias-Rotondo and J. K. McCusker, *Chem. Soc. Rev.*, 2016, **45**, 5803–5820.

213 N. A. Romero and D. A. Nicewicz, *Chem. Rev.*, 2016, **116**, 10075–10166.

214 R. Marcus, *J. Phys. Chem.*, 1989, **93**, 3078–3086.

215 R. A. Marcus, *Discuss. Faraday Soc.*, 1960, **29**, 21–31.

216 D. Rehm, A. Weller and B. Bunsenges, *Phys. Chem.*, 1969, **73**, 834–839.

217 R. A. Marcus, *J. Chem. Phys.*, 1956, **24**, 966–978.

218 M. Bouzrati-Zerelli, N. Guillaume, F. Goubard, T.-T. Bui, S. Villotte, C. Dietlin, F. Morlet-Savary, D. Gigmes, J. P. Fouassier and F. Dumur, *New J. Chem.*, 2018, **42**, 8261–8270.

219 Y. Zhang, T. S. Lee, J. M. Favale, D. C. Leary, J. L. Petersen, G. D. Scholes, F. N. Castellano and C. Milsmann, *Nat. Chem.*, 2020, **12**, 345–352.

220 F. B. Dias, T. J. Penfold and A. P. Monkman, *Methods Appl. Fluoresc.*, 2017, **5**, 012001.

221 M. Y. Wong and E. Zysman-Colman, *Adv. Mater.*, 2017, **29**, 1605444.

222 Y. Im, M. Kim, Y. J. Cho, J.-A. Seo, K. S. Yook and J. Y. Lee, *Chem. Mater.*, 2017, **29**, 1946–1963.

223 V. Srivastava and P. P. Singh, *RSC Adv.*, 2017, **7**, 31377–31392.

224 A. Penzkofer, A. Beidoun and M. Daiber, *J. Lumin.*, 1992, **51**, 297–314.

225 S. Grotjahn and B. König, *Chem. Commun.*, 2024, **60**, 12951–12963.

226 L. Buzzetti, G. E. Crisenza and P. Melchiorre, *Angew. Chem., Int. Ed.*, 2019, **58**, 3730–3747.

227 M. Cismesia and T. Yoon, *Chem. sci.*, 2015, **6**(10), 5426–5434.

228 R. C. McAtee, E. J. McClain and C. R. Stephenson, *Trends Chem.*, 2019, **1**, 111–125.

229 J. R. Ochola and M. Wolf, *Org. Biomol. Chem.*, 2016, **14**, 9088–9092.

230 S. P. Pitre, C. D. McTiernan and J. C. Scaiano, *Acc. Chem. Res.*, 2016, **49**, 1320–1330.

231 J. Xuan, Z. G. Zhang and W. J. Xiao, *Angew. Chem., Int. Ed.*, 2015, **54**, 15632–15641.

232 L. M. Reid, T. Li, Y. Cao and C. P. Berlinguette, *Sustain. Energy Fuels*, 2018, **2**, 1905–1927.

233 J. Davies, L. Angelini, M. A. Alkhalifah, L. M. Sanz, N. S. Sheikh and D. Leonori, *Synthesis*, 2018, **50**, 821–830.

234 A. Noble, R. S. Mega, D. Pflästerer, E. L. Myers and V. K. Aggarwal, *Angew. Chem., Int. Ed.*, 2018, **57**, 2155–2159.

235 H. Jiang and A. Studer, *Chem.–Eur. J.*, 2019, **25**, 516–520.

236 O. Zhang and J. W. Schubert, *J. Org. Chem.*, 2020, **85**, 6225–6232.

237 N. X. Xu, B. X. Li, C. Wang and M. Uchiyama, *Angew. Chem.*, 2020, **132**, 10726–10731.

238 H. Huang, C. Yu, Y. Zhang, Y. Zhang, P. S. Mariano and W. Wang, *J. Am. Chem. Soc.*, 2017, **139**, 9799–9802.

239 S. P. Morcillo, E. M. Dauncey, J. H. Kim, J. J. Douglas, N. S. Sheikh and D. Leonori, *Angew. Chem., Int. Ed.*, 2018, **57**, 12945–12949.

240 X.-L. Lyu, S.-S. Huang, H.-J. Song, Y.-X. Liu and Q.-M. Wang, *RSC Adv.*, 2019, **9**, 36213–36216.

241 H. Huang, X. Li, C. Yu, Y. Zhang, P. S. Mariano and W. Wang, *Angew. Chem., Int. Ed.*, 2017, **56**, 1500–1505.

242 C. Shu, R. S. Mega, B. J. Andreassen, A. Noble and V. K. Aggarwal, *Angew. Chem.*, 2018, **130**, 15656–15660.

243 T. C. Sherwood, H.-Y. Xiao, R. G. Bhaskar, E. M. Simmons, S. Zaretsky, M. P. Rauch, R. R. Knowles and T. M. Dhar, *J. Org. Chem.*, 2019, **84**, 8360–8379.

244 R. Gueret, L. Pelinski, T. Bousquet, M. Sauthier, V. Ferey and A. Bigot, *Org. Lett.*, 2020, **22**, 5157–5162.

245 G. G. Pawar, F. Robert, E. Grau, H. Cramail and Y. Landais, *Chem. Commun.*, 2018, **54**, 9337–9340.

246 S. Sharma and A. Sharma, *Org. Biomol. Chem.*, 2019, **17**, 4384–4405.

247 T. C. Sherwood, N. Li, A. N. Yazdani and T. M. Dhar, *J. Org. Chem.*, 2018, **83**, 3000–3012.

248 E. W. Webb, J. B. Park, E. L. Cole, D. J. Donnelly, S. J. Bonacorsi, W. R. Ewing and A. G. Doyle, *J. Am. Chem. Soc.*, 2020, **142**, 9493–9500.

249 S. He, X. Chen, F. Zeng, P. Lu, Y. Peng, L. Qu and B. Yu, *Chin. Chem. Lett.*, 2020, **31**, 1863–1867.

250 A. N. Herron, D. Liu, G. Xia and J.-Q. Yu, *J. Am. Chem. Soc.*, 2020, **142**, 2766–2770.

251 X.-L. Huang, Y.-Z. Cheng, X. Zhang and S.-L. You, *Org. Lett.*, 2020, **22**, 9699–9705.

252 Y. Z. Cheng, X. L. Huang, W. H. Zhuang, Q. R. Zhao, X. Zhang, T. S. Mei and S. L. You, *Angew. Chem.*, 2020, **132**, 18218–18223.

253 Q.-F. Bao, M. Li, Y. Xia, Y.-Z. Wang, Z.-Z. Zhou and Y.-M. Liang, *Org. Lett.*, 2021, **23**, 1107–1112.

254 E. R. Sauvé, D. M. Mayder, S. Kamal, M. S. Oderinde and Z. M. Hudson, *Chem. Sci.*, 2022, **13**, 2296–2302.

255 E. Pinosa, E. Bassan, S. Cetin, M. Villa, S. Potenti, F. Calogero, A. Gualandi, A. Fermi, P. Ceroni and P. G. Cozzi, *J. Org. Chem.*, 2022, **88**, 6390–6400.

256 M. A. Bryden, F. Millward, T. Matulaitis, D. Chen, M. Villa, A. Fermi, S. Cetin, P. Ceroni and E. Zysman-Colman, *J. Org. Chem.*, 2022, **88**, 6364–6373.

257 G. Hong, Y. Wu, J. An, W. Chen, F. Song and X. Peng, *Sustain. Energy Fuels*, 2023, **7**, 3447–3453.

258 R. Hojo, K. Bergmann, S. A. Elgadi, D. M. Mayder, M. A. Emmanuel, M. S. Oderinde and Z. M. Hudson, *J. Am. Chem. Soc.*, 2023, **145**, 18366–18381.

259 C. Sun, Q. Zhou, C.-Y. Li, Z.-W. Hou and L. Wang, *Org. Lett.*, 2024, **26**, 883–888.

260 P. Wang, M. Ge, X. Luo, Y. Zhai, N. Meckbach, V. Strehmel, S. Li, Z. Chen and B. Strehmel, *Angew. Chem., Int. Ed.*, 2024, e202402915.

261 K. S. Yook and J. Y. Lee, *Chem. Rec.*, 2016, **16**, 159–172.

262 S. Yadav, P. Mittal and S. Negi, *Bull. Mater. Sci.*, 2022, **45**, 109.

263 S. K. Behera, R. Kainda, S. Basu and Y. S. Chaudhary, *Appl. Mater. Today*, 2022, **27**, 101407.

264 X. Fan, X. Hao, F. Huang, J. Yu, K. Wang and X. Zhang, *Adv. Sci.*, 2023, **10**, 2303504.

265 Q. Wei, N. Fei, A. Islam, T. Lei, L. Hong, R. Peng, X. Fan, L. Chen, P. Gao and Z. Ge, *Adv. Opt. Mater.*, 2018, **6**, 1800512.

266 K.-H. Kim and J.-J. Kim, *Adv. Mater.*, 2018, **30**, 1705600.

267 X.-F. Luo, X. Xiao and Y.-X. Zheng, *Chem. Commun.*, 2024, **60**, 1089–1099.

268 L. Sun, K. Di, R. Guo, Y. Wang, H. Su, Y. Tian, S. Huang and L. Wang, *Dyes Pigm.*, 2024, **222**, 111858.

269 P. Palanisamy, O. P. Kumar, H. U. Kim, K. R. Naveen, J.-Y. Kim, J.-H. Baek, M. Y. Chae and J. H. Kwon, *Chem. Eng. J.*, 2024, **481**, 148781.

270 T.-L. Wu, M.-J. Huang, C.-C. Lin, P.-Y. Huang, T.-Y. Chou, R.-W. Chen-Cheng, H.-W. Lin, R.-S. Liu and C.-H. Cheng, *Nat. Photonics*, 2018, **12**, 235–240.

271 A. Kumar, H. Y. Shin, T. Lee, J. Jung, B. J. Jung and M. H. Lee, *Chem.–Eur. J.*, 2020, **26**, 16793–16801.

272 Y. Tan, A. Ying, Y. Liu, X. Cai, L. Zhan, Z. Bin, J. You, C. Li and S. Gong, *Chem. Eng. J.*, 2024, **487**, 150618.

273 M. Cinquino, C. T. Prontera, A. Maggiore, A. Zizzari, M. Pugliese, F. Mariano, V. Valenzano, I. E. Palamà, R. Manfredi and G. Gigli, *Adv. Electron. Mater.*, 2024, **10**, 2300358.

274 W. Luo, T. Wang, Z. Huang, H. Huang, N. Li and C. Yang, *Adv. Funct. Mater.*, 2024, **34**, 2310042.

275 T. Wang, Z. Huang, H. Zhang, J. Miao and C. Yang, *Adv. Funct. Mater.*, 2024, 2408119.

276 Z. Xue, G. Chen, Z. Chen, W. Luo, N. Li, Z. Huang and C. Yang, *Adv. Funct. Mater.*, 2024, 2409244.

277 X. Cai, Y. Pan, X. Song, C. Li, Y. Pu, X. Zhuang, H. Bi and Y. Wang, *Adv. Opt. Mater.*, 2024, **12**, 2302811.

278 X. Chen, S. Bagnich, R. Pollice, B. Li, Y. Zhu, R. Saxena, Y. Yin, W. Zhu, A. Aspuru-Guzik and E. Zysman-Colman, *Adv. Opt. Mater.*, 2024, **12**, 2301784.

279 N. Peethani, N. Y. Kwon, C. W. Koh, S. H. Park, J. M. Ha, M. J. Cho, H. Y. Woo, S. Park and D. H. Choi, *Adv. Opt. Mater.*, 2024, **12**, 2301217.

280 M. K. Sit, G. S. M. Tong, T. L. Lam, G. Cheng, F. F. Hung, K. M. So, L. Du, K. O. Choy, K. H. Low and C. M. Che, *Adv. Opt. Mater.*, 2024, **12**, 2302308.

281 S. Wang, L. Peng, F. He, Y. Ming, H. Qi, Y. Liu, D. Ma, S. Ying and S. Yan, *Adv. Opt. Mater.*, 2024, **12**, 2400503.

282 X.-F. Song, S. Luo, N. Li, X. Wan, J. Miao, Y. Zou, K. Li and C. Yang, *Angew. Chem.*, 2024, e202413536.

283 S. Li, Z. Yang, Y. Xie, L. Hua, S. Ying, Y. Liu, Z. Ren and S. Yan, *Chem. Sci.*, 2024, **15**(44), 18335–18346.

284 T. Komino, H. Nomura, T. Koyanagi and C. Adachi, *Chem. Mater.*, 2013, **25**, 3038–3047.

285 C. A. Parker and E. J. Bowen, *Proc. R. Soc. London, A*, 1963, **276**, 125–135.

286 L. G. Franca, D. G. Bossanyi, J. Clark and P. L. dos Santos, *ACS Appl. Opt. Mater.*, 2024, 2476–2500.

287 Z. Chen, W. Sun, H. J. Butt and S. Wu, *Chem.–Eur. J.*, 2015, **21**, 9165–9170.

288 Y. Y. Cheng, B. Fückel, R. W. MacQueen, T. Khoury, R. G. Clady, T. F. Schulze, N. Ekins-Daukes, M. J. Crossley, B. Stannowski and K. Lips, *Energy Environ. Sci.*, 2012, **5**, 6953–6959.

289 M. Hussain, S. S. Razi, T. Tao and F. Hartl, *J. Photochem. Photobiol., C*, 2023, 100618.

290 C. Gao, W. W. Wong, Z. Qin, S. C. Lo, E. B. Namdas, H. Dong and W. Hu, *Adv. Mater.*, 2021, **33**, 2100704.

291 L. Zeng, L. Huang, J. Han and G. Han, *Acc. Chem. Res.*, 2022, **55**, 2604–2615.

292 P. Bharmoria, H. Bildirir and K. Moth-Poulsen, *Chem. Soc. Rev.*, 2020, **49**, 6529–6554.

293 T. Schloemer, P. Narayanan, Q. Zhou, E. Belliveau, M. Seitz and D. N. Congreve, *ACS Nano*, 2023, **17**, 3259–3288.

294 W. Ahmad, J. Wang, H. Li, Q. Ouyang, W. Wu and Q. Chen, *Coord. Chem. Rev.*, 2021, **439**, 213944.

295 X. Qiao and D. Ma, *Mater. Sci. Eng. R Rep.*, 2020, **139**, 100519.

296 K. V. Y. Jie, M. F. Ahmad, M. M. Ramli, S. Shaari, A. M. Ismail and Y. Sulaiman, *Int. J. Nanoelectron. Mater.*, 2022, **15**, 331–339.

297 M. Zheng, Y. Li, Y. Wei, L. Chen, S. Liu and X. Zhou, *J. Phys. Chem. C*, 2023, **127**, 2846–2854.

298 J. Li, Y. Xia, G. Li, M. Chen, J. Zhou, W. Yan, B. Zhao, K. Guo and H. Wang, *Chem. Eng. J.*, 2023, **470**, 143966.

299 X. Tang, R. Pan, X. Guan, Y. He, S. Jiang, Y. Wang, X. Zhou and Z. Xiong, *Appl. Phys. Lett.*, 2024, **124**, 123506.

300 O. Bezvikonnyi, A. Bucinskas, P. Arsenyan, A. Petrenko, Z.-Y. Wei, J.-H. Lee, D. Volyniuk, E. U. Rashid, T.-L. Chiu and J. V. Grazulevicius, *ACS Appl. Electron. Mater.*, 2024, **6**, 4489–4503.

301 F. Zhao, J. Kong, W. Zhang, Z. Kuang and M. Zhou, *J. Phys. Chem. Lett.*, 2024, **15**, 2885–2892.

302 K. V. Y. Jie, M. F. Ahmad, A. R. Mohmad, A. M. Ismail, M. N. Norizan, M. M. Ramli, S. Shaari, Y. Sulaiman, S. A. A. Rais and S. Johari, *ACS Appl. Energy Mater.*, 2024, **7**, 799–809.

303 X. Wang, D. Zhou, H. Wang, H. Jin and J. Yu, *J. Phys. D: Appl. Phys.*, 2018, **52**, 025106.

304 W. Dong, Y. Bai, Y. Wang, S. Zhao, H. Xu, Y. Miao, Q. Luo, H. Wang and J. Yu, *Sci. China Mater.*, 2024, **67**, 197–204.

305 M. A. Iqbal, X. Weng, C. Kang, N. Arif, K. Wu, W. Tang, S. Dai, X. Fang, H. Cai and Y. J. Zeng, *Laser Photon. Rev.*, 2024, **18**, 2300612.

306 M. Hesari, J. Turnbull, C. B. Khadka, F. Weigend, J. F. Corrigan and Z. Ding, *Electrochim. Acta*, 2016, **210**, 79–86.

307 R. Ishimatsu, S. Matsunami, T. Kasahara, J. Mizuno, T. Edura, C. Adachi, K. Nakano and T. Imato, *Angew. Chem., Int. Ed.*, 2014, **53**, 6993–6996.

308 T. Kasahara, S. Matsunami, T. Edura, R. Ishimatsu, J. Oshima, M. Tsuwaki, T. Imato, S. Shoji, C. Adachi and J. Mizuno, *Sens. Actuators, A*, 2014, **214**, 225–229.

309 N. Ichinohe, R. Otsuka, R. Ishimatsu, M. Kobayashi, J. Mizuno, N. Akino and T. Kasahara, *Electrochemistry*, 2024, **92**, 027004.

310 J. Zhang, X. Xu, C. Yao, J. Peng, M. Jia and L. Li, *J. Mater. Chem. C*, 2016, **4**, 4505–4511.

311 L. Zhu, M. T. Trinh, L. Yin and Z. Zhang, *Chem. Sci.*, 2016, **7**, 2058–2065.

312 Y. Sagara and T. Kato, *Nat. Chem.*, 2009, **1**, 605–610.

313 Y. Sagara, S. Yamane, M. Mitani, C. Weder and T. Kato, *Adv. Mater.*, 2016, **28**, 1073–1095.

314 Z. Chi, X. Zhang, B. Xu, X. Zhou, C. Ma, Y. Zhang, S. Liu and J. Xu, *Chem. Soc. Rev.*, 2012, **41**, 3878–3896.

315 J. Xu and Z. Chi, *Mechanochromic Fluorescent Materials: Phenomena, Materials and Applications*, Royal Society of Chemistry, 2014.

316 Z. Xie, C. Chen, S. Xu, J. Li, Y. Zhang, S. Liu, J. Xu and Z. Chi, *Angew. Chem., Int. Ed.*, 2015, **54**, 7181–7184.

317 P. Rajamalli, N. Senthilkumar, P. Gandeepan, C.-Z. Ren-Wu, H.-W. Lin and C.-H. Cheng, *J. Mater. Chem. C*, 2016, **4**, 900–904.

318 Q. Pei, *Science*, 1995, **269**, 1086.

319 Q. Pei, Y. Yang, G. Yu, C. Zhang and A. J. Heeger, *J. Am. Chem. Soc.*, 1996, **118**, 3922–3929.

320 E. Fresta and R. D. Costa, *J. Mater. Chem. C*, 2017, **5**, 5643–5675.

321 S. Tang and L. Edman, *Photoluminescent Materials and Electroluminescent Devices*, 2017, pp. 375–395.

322 K. Matsuki, J. Pu and T. Takenobu, *Adv. Funct. Mater.*, 2020, **30**, 1908641.

323 S. Kanagaraj, A. Puthanveedu and Y. Choe, *Adv. Funct. Mater.*, 2020, **30**, 1907126.

324 B. Pashaei, S. Karimi, H. Shahroosvand, P. Abbasi, M. Pilkington, A. Bartolotta, E. Fresta, J. Fernandez-Cestau, R. D. Costa and F. Bonaccorso, *Chem. Soc. Rev.*, 2019, **48**, 5033–5139.

325 B. Pashaei, S. Karimi, H. Shahroosvand and M. Pilkington, *Adv. Funct. Mater.*, 2020, **30**, 1908103.

326 A. Szlapa-Kula and S. Kula, *Energies*, 2023, **16**, 5194.

327 M. Y. Wong and E. Zysman-Colman, in *Light-Emitting Electrochemical Cells: Concepts, Advances and Challenges*, ed. R. D. Costa, Springer International Publishing, Cham, 2017, pp. 237–266, DOI: 10.1007/978-3-319-58613-7_9.

328 T.-T. Bui, F. Goubard, M. Ibrahim-Ouali, D. Gigmes and F. Dumur, *Appl. Sci.*, 2018, **8**, 494.

329 J.-H. Lee, C.-H. Chen, P.-H. Lee, H.-Y. Lin, M.-k. Leung, T.-L. Chiu and C.-F. Lin, *J. Mater. Chem. C*, 2019, **7**, 5874–5888.

330 M. Y. Wong, G. J. Hedley, G. Xie, L. S. Kölln, I. D. Samuel, A. Pertegás, H. J. Bolink and E. Zysman-Colman, *Chem. Mater.*, 2015, **27**, 6535–6542.

331 J. Liu, J. Oliva, K. Tong, F. Zhao, D. Chen and Q. Pei, *Sci. Rep.*, 2017, **7**, 1524.

332 M. D. Moore, M. H. Bowler, J. E. Reynolds III, V. M. Lynch, Y. Shen, J. D. Slinker and J. L. Sessler, *ACS Appl. Mater. Interfaces*, 2018, **10**, 24699–24707.

333 P. Lundberg, Y. Tsuchiya, E. M. Lindh, S. Tang, C. Adachi and L. Edman, *Nat. Commun.*, 2019, **10**, 5307.

334 K. Shanmugasundaram, J. C. John, S. Chitumalla, J. Jang and Y. Choe, *Org. Electron.*, 2019, **67**, 141–145.

335 Y. Chen, Y.-X. Wang, C.-W. Lu and H.-C. Su, *J. Mater. Chem. C*, 2022, **10**, 11211–11219.

336 X. Pang, K. Zhang, Y. Song, Y. Xiu, R. Yu and L. He, *Chem. Eng. J.*, 2022, **450**, 137987.

337 H.-L. Shen, P.-W. Hsiao, R.-H. Yi, Y.-H. Su, Y. Chen, C.-W. Lu and H.-C. Su, *Dyes Pigm.*, 2022, **203**, 110346.

338 J. Wang, H. Hafeez, S. Tang, T. Matulaitis, L. Edman, I. D. Samuel and E. Zysman-Colman, *Aggregate*, 2024, e571.